Circulation-Informed Seafloor Geodetic Techniques for Understanding Plate Boundary Processes

Erik K. Fredrickson

A dissertation
submitted in partial fulfillment of the
requirements for the degree of

Doctor of Philosophy
University of Washington
2023

Reading Committee:
William S. D. Wilcock, Chair
Parker MacCready
David A. Schmidt

Program Authorized to Offer Degree:
School of Oceanography

University of Washington

Abstract

Circulation-Informed Seafloor Geodetic Techniques for Understanding Plate Boundary Processes

Erik K. Fredrickson

Chair of the Supervisory Committee:
William S. D. Wilcock
School of Oceanography

Tectonic plate boundaries host a range of solid-Earth physical processes of scientific and societal interest, including the majority of the world's volcanism and earthquakes. However, these marginal systems are primarily found offshore beneath the Earth's oceans, posing significant challenge for effective observation and study. One such process is the generation of shallow slow slip events (SSEs), which in recent years have been identified in a number of subduction zones globally using observations of seafloor pressure. Such records are also sensitive to oceanographic circulation processes, which can obscure potential SSE signals and lead to false detections. In this dissertation, I present methods for understanding and eliminating oceanographic pressure signals so that tectonic signals may be more readily identified and characterized. In Chapter 2, I use data from the 2011-2015 Cascadia Initiative Experiment to show that the oceanographic noise on tidally filtered, detrended seafloor pressure records can be reduced from >6 cm to ≤1 cm root-mean-square (RMS) by correcting with a reference pressure record from a comparable depth and further show that such corrections enable the detection of a range of Mw ~6 synthetic SSE scenarios. In Chapter 3, I use data from the 2018-2019 Alaska Amphibious Community Seismic Experiment to compare a variety of oceanographic pressure proxies and demonstrate that correcting seafloor pressure records with the first Complex

Empirical Orthogonal Function (CEOF) and differencing with a depth-matched pressure record yield the greatest signal RMS reduction and enable the detection of ≥2 cm SSE signals on the continental slope and ≥4 cm SSE signals on the continental shelf. In Chapter 4, I calculate seafloor pressure from a regional oceanographic model of the Cascadia region and show that mesoscale eddies traveling over the continental margin can generate SSE-like signals in pressure records, which may lead to false detections. Finally, in Chapter 5, I present seafloor and on-land observations from a novel tiltmeter design that provides a means of recording and correcting instrumental drift, with parallels to comparable drift issues in standard pressure sensors.

TABLE OF CONTENTS

Page

List of Figures…………………………………………………………………………….………… v

List of Tables………………………………………………………………………….……….. xiv

Acknowledgements……………………………………………………………….………….…..xv

Chapter 1: Introduction and Organization of the Dissertation ………………...………… 1

Chapter 2: Optimizing Sensor Configurations for the Detection of Slow-Slip Earthquakes in Seafloor Pressure Records, Using the Cascadia Subduction Zone as a Case Study 6

- 2.0 Abstract……………………………………………………………….……….… 6
- 2.1 Introduction……….……………………………………………………...……..… 7
- 2.2 Methods……………………………………...….………………….……… 12
  - 2.2.1 APG Data……….……………………………………………………… 12
  - 2.2.2 Physical Oceanographic Circulation Models……….…………..……… 16
  - 2.2.3 Geophysical Slow-Slip Modeling……….……………………...……… 18
- 2.3 Results……….…………………………………………………………….…… 23
  - 2.3.1 Differencing of APG Data……………………………..….….……… 23
  - 2.3.2 Hindcast Seafloor Pressure from Circulation Models…….….……… 29
  - 2.3.3 SSE Deformation Modeling…….………………………………….……… 35
- 2.4 Discussion……….…………………………………………………...…… 45
  - 2.4.1 Detection of Slow-Slip Events in Observational Data…….….………… 45
  - 2.4.2 Oceanographic Signal Reduction in Seafloor Pressure Data…………… 49
  - 2.4.3 Idealized Sensor Geometry for Slow-Slip Detection Off Oregon……… 51
  - 2.4.4 Slow-Slip Detectability in the CI Experiment…………….….……… 58

2.5 Conclusions……………………………………………………………………… 59

2.6 Acknowledgements……………………………………………………………… 62

Chapter 3: Slow Slip Detectability in Seafloor Pressure Records Offshore Alaska ……… 63

3.0 Abstract………………………………………………………………………… 63

3.1 Introduction……………………………………………………………………. 64

3.2 Geologic and Oceanographic Setting…………………………………………… 69

3.3 Methods………………………………………………………………………… 73

3.3.1 Pressure, temperature, and altimetry data………………………………… 73

3.3.2 Corrections to remove non-tectonic long-period signals………………… 75

3.3.3 Proxies for oceanographic pressure, P_O……………………………… 80

3.3.4 Synthetic SSE detection and characterization…………………………… 81

3.4 Results………………………………………………………………………… 84

3.4.1 Seafloor Pressure characteristics………………………………………… 84

3.4.2 Proxy efficacy for correcting for oceanographic pressure signals……… 88

3.4.3 Identification and characterization of SSE transients…………………… 90

3.4.3.1 Known onset time…………………………………………………… 90

3.4.3.2 Unknown onset time………………………………………………… 93

3.5 Discussion……………………………………………………………………… 98

3.5.1 RMS as a metric for SSE detectability…………………………………… 98

3.5.2 Implications of observed seafloor pressure spatial coherence…………… 99

3.5.3 Maximizing SSE detectability in pressure records……………………… 103

3.5 Conclusions…………………………………………………………………… 106

3.7 Acknowledgements……………………………………………………………… 107

Chapter 4: Demonstrating the Generation of Slow Slip-Like Seafloor Pressure Signals by Mesoscale Eddies in a Regional Oceanographic Modeling System for the Cascadia Margin……… 109

4.0 Abstract……… 109

4.1 Introduction……… 109

4.2 Methods……… 113

4.2.1 Regional oceanographic model……… 113

4.2.2 Approach……… 116

4.2.2 Approach……… 117

4.3 Results……… 118

4.3.1 Bottom pressure anomaly characteristics……… 118

4.3.2 Pressure effects from mesoscale eddies……… 123

4.4 Discussion……… 129

4.4.1 The impact of eddies as a function of water depth……… 129

4.4.2 Pressure component differences……… 129

4.4.3 Relevance for SSE studies……… 132

4.5 Conclusions……… 133

4.6 Acknowledgements……… 134

Chapter 5: A Method for Observing Tilt and Correcting Drift with a Triaxial Accelerometer……… 135

5.0 Abstract……… 135

5.1 Introduction……… 135

5.2 Instrumental Approach……… 139

5.2.1 Calibration principle……………………………………………...……… 139

5.2.2 SCTA design………………………………………………………..…… 142

5.3 Field Tests……………………………………………………...……… 143

5.3.1 Axial Seamount………………………………………………...… 144

5.3.2 Pinon Flat Observatory…………………………………...……… 147

5.4 Results…………………………………………………………………… 149

5.4.1 Calibration Measurements………………………………..……… 149

5.4.2 Applying calibrations and data stitching………………….……… 154

5.5 Discussion……………………………………………………...……… 162

5.5.1 Calibration technique…………………………………………..… 162

5.5.2 Axial Seamount tilt observations……………………………………… 163

5.5.3 Pinon Flat Observatory tilt observations……………………….…… 164

5.5.4 Future steps……………………………………………………..…… 165

5.6 Acknowledgements…………………………………………….………… 165

Chapter 6: Summary and Future Work …………………………………………………… 167

Bibliography……………………………………………………………...………… 170

Appendix 1: Supplementary Materials for Chapter 2…………………………….……… 192

Appendix 2: Supplementary Materials for Chapter 3……………………………..……… 210

Appendix 3: Supplementary Materials for Chapter 5…………………………………..… 228

LIST OF FIGURES

Figure 2.1 Map of the study area, depicting bathymetry and station locations. Thin black contours at 300 m and 2000 m differentiate near-shelf, slope, and abyssal plain regimes, dotted lines show the LiveOcean and WCOFS model domains, black bold line depicts trench axis as per McCrory et al. (2012), and dashed black lines at 44°N and 46°N depict the approximate bounds of the region of partial locking offshore northern Oregon (Burgette et al., 2009; Schmalzle et al., 2014). Pressure gauge instrument locations are displayed with symbols and colors corresponding to experiment years and are unfilled for those which did not yield useable data. The 2013-2014 experiment year is excluded because it had only one useable quality station. The 2014-2015 instruments include cabled pressure gauges from the OOI Cabled Array and a benchmark sensor offshore central Oregon (OBPR), which are denoted by rotated triangles. Red and blue contours show the 1.5 cm uplift and subsidence areas, respectively, from our base SSE model. 13

Figure 2.2 The pressure data used in these analyses, offset for display purposes, alongside maps of instrument locations for (a) 2011-2012, (b) 2012-2013, and (c) 2014-2015. For each time series, the first two weeks of data are discarded, a Godin 24-24-25 filter (Godin, 1972) is applied, and a third-order polynomial fit is removed. Data from below 2000 m depth are plotted in dark blue, depths 300-2000 m in light blue, and depths above 300 m in green. Station name and depth are listed next to each time series. The start and end times of the data vary, according to deployment/recovery and scheduled ship time. 15

Figure 2.3 (a) Parameterization of the Juan de Fuca slab surface into triangular elements, used in our deformation modeling, with elements color coded according to slip amplitude for the base model. The trench is depicted by the westernmost boundary of the slab, the coastline is shown in bold white, thin white contours show 300 m and 2000 m depth, and dashed white lines at 44°N and 46°N depict the approximate bounds of the region of partial locking offshore northern Oregon (Burgette et al., 2009; Schmalzle et al., 2014). The black line at 44.7°N indicates the cross section line for (b)-(e). (b) Cross section of plate interface depth versus longitude with the region of slip highlighted in red. The dotted and dashed red curves below and above show the slip region for updip and downdip model variations, respectively, offset vertically for display purposes. Note that depth is given relative to the seafloor and does not go to zero at the trench due to significant sediment coverage in Cascadia. c) Slip versus longitude, with updip and downdip variations shown by dotted and dashed curves, respectively. d) Surface vertical deformation versus longitude. e) Surface horizontal deformation versus longitude. Vertical bars in (b-d) represent the locations of the deformation front and coastline in the cross-section. 19

Figure 2.4 Example comparisons (upper panels) and differences (lower panels) of APG time series at similar depths. (a) Comparison of continental shelf stations from 2012-2013. (b) Comparison of continental slope stations from 2012-2013. c) Comparison of stations on the abyssal plain from 2011-2012. The legend in the upper panels indicates the names of instruments, their separation from the top-most instrument, and the water depth of their location. Bold curves indicate the two stations used to generate the differences in the lower panels. In the difference plots, the black curve depicts the time series obtained by differencing the APG data, the red curve depicts the difference from the WCOFS model at the same locations, and the blue curve depicts the difference obtained after correcting the data with the model. RMS are listed for each. All curves are offset for display purposes. Instrument locations are mapped in Figure 2.2. ……25

Figure 2.5 Pressure difference RMS versus lateral separation and depth difference. Triangles represent observed differences from the APG data, color coded by RMS. Contours show predictions from the WCOFS oceanographic model, using the same color scale but faded for display purposes. (a) Instruments between 1400-3000 m depth and model reference location at 2581 m. (b) Instruments between 500-1400 m depth and model reference location at 1103 m. (c) Instruments between 250-500 m depth and model reference location at 394 m. Note that one difference at large separation is excluded from the APG data for display purposes. (d) Instruments between 100-250 m depth and model reference location at 121 m. Note that two differences at large separation are excluded from the APG data for display purposes. (e) Instruments less than 100 m depth and model reference location at 57 m. The model reference locations are shown by open symbols in Figure 2.6a. We use the convention that ΔDepth is positive when the reference location is deeper than the location from which it is subtracted and negative when it is shallower. For the APG data, the reference station is chosen to be that which is most similar to the model reference for that depth bin, for consistency in our sign convention. ……30

Figure 2.6 (a) Contours of modeled bottom pressure RMS from 2013-2014 of the LiveOcean model, with a Godin 24-24-25 filter (Godin, 1972) applied and a third-order polynomial fit removed. Open circles indicate the model locations used in Figure 2.5. (b)-(d) Contours of RMS of modeled differences relative to the starred reference locations for all grid points in the model, with depth indicated in legend, for an abyssal plain, continental slope, and continental shelf location, respectively. Black contours show 300 m and 2000 m isobaths. ……31

Figure 2.7 Comparison of APG data and modeled bottom pressure for the 2012-2013 year at select locations. (a-c) Pressure time series (top panel) and differences (bottom panel) for the data and WCOFS model for continental shelf, slope, and abyssal plain locations. (d-f) Amplitude spectra of the time series at the same locations. Grayed areas indicate frequencies of 0.07, 0.035, and 0.2-0.33 day^{-1}, where APG amplitudes are consistently larger than predicted by the model. ……33

Figure 2.8 (a) R^2 of the fit of the 2011-2013 WCOFS modeled bottom pressure to the observed APG data as a function of instrument depth. A positive R^2 signifies that variance is reduced by differencing, while a negative R^2 signifies that variance is increased. (b) Comparison of RMS versus depth of APG pressure time series before (open circles) and after (filled circles) correcting with the WCOFS model, as a function of instrument depth. ……35

Figure 2.9 Synthetic SSE modeling results for our base model, a mid-slope M$_w$ 6.4 event of two-week duration, beginning on 1 June 2013. (a) Contours of seafloor deformation beginning at

5 mm with an interval of 10 mm on a regional map, overlain with modeled stations (squares and circles) running through the site of peak deformation and reference locations for subsequent differencing plots. Bold contours indicate vertical deformation of ±15 mm. Instrument spacing is 12 km along isobaths and 10 km across isobaths. Coastal and near-coast GPS instrument locations are labeled as inverted triangles and modeled horizontal deformation is color coded at the coastline. Bold black lines show the trench and coastline, thin black lines show 300 m and 2000 m isobaths, and the partially-locked Oregon region is demarked by the dashed lines. (b) Time series plots of modeled seafloor pressure differences of the strike-perpendicular station locations, relative to the red star location in (a). Differences from the stations overlying the uplift lobe (>15 mm) are displayed in red while those overlying the subsidence lobe (<-15 mm) are displayed in blue. (c) Time series as in (b) but for the depth-matched stations and red triangle reference location. Time series are offset for display purposes and station depths are indicated next to each.
……………………………………………………………………………………………37

Figure 2.10 As in Figure 2.9, but for a trench-adjacent SSE. Note that deformation occurs on the incoming plate due to the 3 km of sediment cover above the updip terminus of our modeled plate interface.
……………………………………………………………………………………………40

Figure 2.11 As in Figure 2.9, but for a SSE with a stress drop of $\Delta\sigma_E = 0.014$ MPa. Infilled station markers in (a) are those for which modeled pressure differences are shown in (b) and (c).
……………………………………………………………………………………………42

Figure 2.12 As in Figure 2.9, but for a Mw 5.9 SSE. Infilled station markers in (a) are those for which modeled pressure differences are shown in (b) and (c).
……………………………………………………………………………………………44

Figure 2.13 Example of the standard differencing technique producing a significant false SSE detection between instruments J25D and MJ01A from the 2014-2015 year (locations shown in Figure 2.2c). The dashed vertical line indicates the perceived onset time of the SSE. The horizontal gray lines mark the average pressure before and after the event, with the difference between these given in the bottom right of each figure. (a) The difference time series using polynomial-corrected pressure records. (b) The difference time series from applying a polynomial correction to the reference station and detrending the second station using the linear fit to only the three months of data preceding the presumed SSE (Wallace et al., 2016). (c) Recreation of (b) using the LiveOcean model in place of APG records. (d) Hindcast wind speed and wave height from NOAA Wavewatch III (Tolman, 2009) during the same time interval, low-pass filtered (0.2 day^{-1} cutoff) to emphasize long-period signals.
……………………………………………………………………………………………48

Figure 2.14 A possible configuration for an idealized APG network for detecting shallow SSEs offshore central Oregon. Bold black curves show the coastline and trench as per McCrory et al. (2012), fine lines show 300 m and 2000 m isobaths, and dashed horizontal lines demark the extent of the partially locked zone (Burgette et al., 2009; Schmalzle et al., 2014). The triangles indicate our recommended station locations. The vertical deformation from the base model

(Figure 2.9) is shown by the solid ellipsoids in the north, the low-stress variation (Figure 2.11) is shown by the solid ellipsoids in the south, and the low M_w variation (Figure 2.12) is shown by the dashed ellipsoids. All have been offset from their modeled locations for display purposes. Thin ellipsoids contour 1 cm deformation, while bold ellipsoids contour 1.5 cm deformation, with red indicating uplift and blue indicating subsidence. Note that the low M_w model produces only a small region of 1.5 cm uplift and no region of 1.5 cm subsidence. ……54

Figure 3.1 Map of the experiment area offshore the Alaska Peninsula. Filled triangles indicate the absolute pressure gauges (APGs) used in this study, colored by the RMS of their tidally filtered, drift corrected data. 'X' markers indicate APGs that did not return data. Square markers indicate other OBS from the AACSE in the region and circles indicate proximal GNSS stations active during the AACSE deployment. Bold depth contours at 300 m and 5000 m approximate the shelf break and trench, respectively. Inset shows broader geographic context and major circulation features. AC = Alaska Current. ACC = Alaska Coastal Current. AS = Alaska Stream. ……70

Figure 3.2 Time series of tidally filtered, drift corrected pressure, tidally filtered SSH, and tidally filtered temperature (blue), along with corresponding 1st pressure-, SSH-, and temperature-CEOFs (red), vertically offset with shallowest station at the top for display purposes. Winter months, when signals are anomalously large across observables, are labeled in bold. A) Shelf pressure. B) Shelf SSH. C) Shelf temperature. D) Slope pressure. E) Slope SSH. F) Slope temperature. ……76

Figure 3.3 Time series of a representative subset of tidally filtered, drift and sinusoidal-corrected shelf pressure data (blue), scaled proxies (red), and proxy-corrected data (black), vertically offset with shallowest station at the top for display purposes. Winter months, when signals are anomalously large across observables, are labeled in bold. A) No proxy. B) Reference station pressure (P_{ref}). C) Depth-matched pressure (P_{match}), with matched station labeled in red text. D) Network average pressure (P_{avg}). E) Temperatures, lagged to maximize correlation (P_{temp}). F) Sea surface height (P_{SSH}). ……79

Figure 3.4 Demonstration of SSE signal detector for a 10 cm, 14 day ramp beginning on September 09, 2018 applied to sinusoidally- and proxy-corrected pressure records from station LT16 for A) the case of known onset and B) unknown onset. Each proxy-corrected time series is offset vertically for display purposes, from top to bottom: none, P_{ref}, P_{match}, P_{avg}, P_{temp}, and P_{ssh}. The vertical lines indicate the true synthetic event duration. Thin black curves show where the detector identifies the event and how it is characterized. ……84

Figure 3.5 Plots of difference RMS for all station combinations as a function of separation and depth difference, after tidal filtering, drift correction, and sinusoidal seasonal correction. Symbol shapes correspond to individual stations and colors scale with RMS. Negative depth differences mean that the station indicated by the marker is shallower than the station that has been

subtracted from it. A) All shelf pairs (depths 83-262 m). B) Shelf pairs at depths 83-125 m. C) Shelf pairs at depths 156-262 m. We highlight station pairs that include LT11 and/or LT20, which may be anomalous (see text), by outlining them in bold black. D) All slope pairs (depths 1564-4612 m). E) Slope pairs at depths 1564-2130 m. F) Slope pairs at depths 2622-4612 m. Vertical dashed lines in (D-E) mark the depth range limits considered in (A), highlighting the difference in scale. As the only station beyond the trench, LA21 is excluded from these comparisons.
....87

Figure 3.6 Proxy-corrected pressure RMS improvements for sinusoidally corrected A) shelf and B) slope data, and pressure-CEOF (p-CEOF) corrected C) shelf, and D) slope data. The empty, black-outlined bars in the background show the RMS of the seasonally corrected pressure record prior to applying any proxy, while the thin colored bars show the RMS of each proxy corrected time series.
....89

Figure 3.7 Histograms showing amplitude recovery error from the synthetic SSE detection analysis on the continental shelf, when known onset time is assumed, using sinusoidal (black), and pressure-CEOF (p-CEOF, translucent gray) seasonal corrections, for each of the proxies considered. The results from all synthetic ramp amplitudes considered (0, 2, 4, 6, 8, and 10 cm) were combined, with ramp duration held at 14 days and onset times varied weekly from August 2018 through April 2019. A) No proxy. B) P_{ref}. C) P_{match}. D) P_{avg}. E) P_{temp}. F) P_{SSH}. Vertical solid lines indicate the desired result ($A_{pred}–A_{known} = 0$), vertical dotted lines show the median and ±MAD of the error for the sinusoidal case, and vertical dashed lines show the same for the pressure-CEOF case.
....91

Figure 3.8 Histograms displaying SSE onset errors and amplitude predictions as a function of input ramp amplitude from synthetic detection analysis on the shelf, for unknown onset times, for sinusoidal (black) and pressure-CEOF (p-CEOF, translucent gray) seasonal corrections, using only our best-preforming proxy, P_{match}. Synthetic ramp duration was held constant at 14 days and onset times were varied weekly from August 2018 through April 2019 to generate the composite distributions shown. A-F) Timing recovery for synthetic ramps of 0, 2, 4, 6, 8, and 10 cm amplitude. Vertical dotted lines show the median and ±MAD for the sinusoidal case, while vertical dashed lines show the same for the pressure-CEOF case. G-L) Amplitude recovery for synthetic ramps of 0, 2, 4, 6, 8, and 10 cm amplitude. Vertical solid lines show the input synthetic amplitude, vertical dotted lines show the median and ±MAD for the sinusoidal case, and vertical dashed lines show the same for the pressure-CEOF case.
....94

Figure 4.1 Map view of the study region with contours of (a) the RMS of the bottom pressure anomaly at each point in the model domain, (b) the RMS of the eustatic component, (c) the RMS of the steric component, (d) the cross correlation coefficient of the bottom pressure anomaly and the eustatic component, (e) the cross correlation coefficient of the bottom pressure anomaly and the steric component, and (f) the cross correlation of the steric and eustatic components. All panels use model output from the period December 16, 2017–December 15, 2018. In (a) the

yellow filled triangle indicates the location of the 200 m extraction and the yellow filled star indicates the location of the 2000 m extraction. The yellow open triangle indicates the 200 m reference location and the yellow open star indicates the 2000 m reference location for calculating the differences plotted in Figure 4.2. The red curve marks the track of the warm core eddy plotted in Figure 4.3, with the red 'X' as its terminus and the red circles indicating the location of the extractions. The white curve, 'X', and circles mark the same for the cold core eddy plotted in Figure 4.4.
……………………………………………………………………………………………115

Figure 4.2 a) Bottom pressure anomaly (red), eustatic component (yellow), and steric component (blue) from December 16, 2018 – December 15, 2019 for a shelf location at 200 m depth, marked by the yellow triangle in Figure 4.1a. Curves with a positive offset have been high-pass filtered with a 30 day cutoff and curves with a negative offset have been low-pass filtered with a 30 day cutoff. b) The same pressure components for a near-trench location at 2000 m depth, marked by the yellow triangle in Figure 4.1a. c) The unfiltered differences in bottom pressure anomaly and components for the 200 m depth location relative to another location at the same depth, marked by the yellow triangles in Figure 1a. Gray shaded intervals mark the presence of ramp-like signals in the total pressure anomaly difference, as discussed in the text. d) Unfiltered pressure differences for the 2000 m location relative to another location at the same depth, marked by the yellow stars in Figure 4.1a.
……………………………………………………………………………………………121

Figure 4.3 Total pressure anomaly and component extractions from select locations along the track of a warm-core eddy, which originates on February 11, 2019 and terminates on April 04, 2019, with track and moorings shown with red markers in Figure 4.1a. a-d) Time series of total pressure anomaly (red), eustatic component (yellow), and steric component (blue) at the locations marked in Figure 4.1a for the entire model year. The location depth is listed above each panel, the gray shaded region marks the time interval of the eddy's entire duration, and the vertical black bar indicates the time at which the eddy overlies the location. e-g) Differences in total pressure anomaly (red), eustatic difference (yellow), and steric difference (blue) of (b-d) relative to (a) for a narrower time window that extends only 30 days before/after the start/end of the eddy period. The depth difference as an absolute value is listed above each panel, the gray shaded region marks the time interval of the eddy's entire duration, and the vertical black bar indicates the time at which the eddy overlies the location. Arrows indicate example intervals during which SSE-like ramps are seen in the total pressure anomaly differences.
……………………………………………………………………………………………125

Figure 4.4 As in Figure 4.3, but for a cold-core eddy that originates on August 31, 2018 and terminates on December 04, 2018, with track and moorings shown with red markers in Figure 4.1a.
……………………………………………………………………………………………128

Figure 4.5 Maps of the model's sea surface height field at the times indicated above each panel, corresponding to the passage of the warm-core eddy in a) Figure 4.3b, b) Figure 4.3c, and c) Figure 4.3d, and the passage of the cold-core eddy in d) Figure 4.4b, e) Figure 4.4c, and f) Figure 4.4d. In each panel, the corresponding extraction location and letter are colored gray.

……………………………………………………………………………………………131

Figure 5.1. (a) Notation used to indicate accelerometer orientations when making tilt measurements (b) Schematic of the 3-orientation rotation sequence used during calibrations prior to August 9, 2021. The colors correspond to the same axes throughout the sequence. Arrows indicate the sense of rotation applied to get to the next orientation. (c) As in (b), but for the 5-orientation rotation sequence used for all calibrations on and after August 9, 2021. Gray shading indicates the orientations common to the sequence shown in (b). We use notation of the form +X and -X to indicate whether the positive or negative X channel is positively upwards. ……………………………………………………………………………………………141

Figure 5.2. (a) Schematic of SCTA design showing the stepping motors that rotate the accelerometer, the motor control, Paroscientific Nano-Resolution frequency counting, the microprocessor and power boards. (b) Axial Seamount SCTA attached to the end cap before insertion into the pressure housing, (c) Axial Seamount SCTA on the seafloor at Location 1 showing the orientation of the X and Y channels (X at an azimuth of 355°). The leg that we inferred to be subsiding is on the left. At Location 2, the X channel was at an azimuth of 340° (d) Piñon Flat SCTA in the vault showing the orientations (X is north). ……………………………………………………………………………………………143

Figure 5.3. (a) Map showing the location of Axial Seamount and Piñon Flat Observatory. (b) Bathymetric map of the Axial Seamount summit caldera (courtesy of Deborah Kelley) showing the location the OOI RCA cables (white for the trunk line to the red primary node and yellow lines for cables to secondary infrastructure), cabled pressure sites (black circles), the approximate surface locations of inward and outward dipping faults (Hefner et al., 2021), and the center of inflation for two models of volcano/inflation deflation; inflation center A assumes no fault motion (Nooner & Chadwick, 2016) and inflation center B assume motion on an outward dipping ring fault (Hefner et al., 2020). A square box about the Central Caldera site shows the area of (c). (c) Map of the OOI RCA infrastructure at the Central Caldera site (courtesy of the OOI RCA) showing the deployment location of the SCTA and LILY tiltmeter. ……………………………………………………………………………………………145

Figure 5.4. (a) Representative 6-days of data from Axial Seamount with the SCTA in the measurement orientation (with the Z channel in the vertical) at Location 1 (before relocating the instrument) starting 05/06/2019 12:00 GMT, showing X-, Y-, and Z-channel observations are plotted in blue, red, and black, respectively, after removing the mean and linear trend and decimating to 1 sample/minute. Vertical offsets are for display purposes only. (b) Associated power spectral density for the three channels, calculated without decimating the data and plotted with the same colors. (c-d) As in (a-b), but at Location 2 (after relocating the instrument) starting from 7/01/2018 12:00 GMT. ……………………………………………………………………………………………147

Figure 5.5. (a) X (blue) and Y channel (red) acceleration observations during a 5-orientation calibration sequence at Axial Seamount Location 2, with calibration orientations labeled. Gray shaded area indicates the time interval plotted in (b). (b) Total acceleration observed during the interval indicated in (a), after the sensor has stabilized in the +X1 orientation and prior to

beginning the next rotation. Gray shaded area indicates the interval over which the acceleration is averaged to get a calibration value. The dark gray horizontal line indicates the calculated calibration value during the interval.
....150

Figure 5.6. Calibration observations and model values for the Axial Seamount SCTA at Location 2. (a) Calibration results for +X1 (black) and +X2 (red). (b) Calibrations results for -X. (c) Span defined as +X1 or +X2 minus -X. (d) Misfit of the exponential linear model (equation 5) for the +X1, +X2 and -X calibrations. (e-h) As for (a-d) except for Y calibrations. Vertical dotted lines in (a-b) and (e-f) indicate where anomalous calibrations have been excluded (see text).
....153

Figure 5.7. Calibration observations and model values, and temperatures for Piñon Flat Observatory. (a) Calibration results for +X1 (black) and +X2 (red) with temperature shown by purple on the righthand axis. (b) Calibrations results for -X. (c) Span defined as +X1 or +X2 minus -X. (d) Misfit of the exponential linear model (equation 5) for the +X1, +X2 and -X calibrations. (e-h) As for (a-d) except for Y calibrations.
....154

Figure 5.8. Demonstration of the stitching process with scale exaggerated for display purposes. There are three key components to stitching a continuous tilt time series: the tilt offset between data segments, the time offset between data segments (i.e., the calibration interval $t_{s,k}$–$t_{e,k-1}$) and the post-calibration transient (δa_X (δt)). Each data segment is corrected for its transient, extrapolated to time $t_{e,k-1}$, and then corrected for the tilt offset.
....157

Figure 5.9. Transient accelerations (black lines) observed after the calibrations for (a) the X channel and the three-orientation sequence, (b) the X channel and the five-orientation sequence, (c) the Y channel and the three-orientation sequence and (d) the Y channel and the five-orientation sequence. The transients determined after first decimating the observed accelerations to a 1-minute time series and then by averaging the detrended accelerations observations after each calibration type. The standard deviation (red lines) will be a combination of any variation in the post-calibration transient and environmental variations in the 1-minute averaged acceleration.
....158

Figure 5.10. Time series of one-minute averaged tilt for Piñon Flat Observatory from 2018 to 2020 for the (a) east (-Y) and (b) north (+X) directions. The curves show the drift-corrected stitched data with $\delta t = 0$ hours in equation (9) (red) and the stitched data fit after adjusting for linear temperature dependence (black) and with both a linear temperature dependence and a step at the 46-day gap (gray). The temperature is also shown (purple). The sign convention is positive for a downward tilt.
....160

Figure 5.11. Time series of 1-minute averaged tilt for Axial Seamount Location 2 from 2020 to 2021 for the (a) east and (b) north directions. Each plot shows the drift corrected stitched SCTA data with $\delta t = 2$ hours in equation (9) with the assumption of no transient acceleration after 5 hours (red), the LILY tile meter data (blue) and the difference (LILY – SCTA) (black). The sign convention is positive for a downward tilt. ………………………………………………………………………………………………161

LIST OF TABLES

Table 2.1 Slow Slip Earthquake Modeling Scenarios…………………………………………...22

Table 2.2 RMS Reduction from Depth Matched Differencing……………………………….....27

Table 3.1 Summary of synthetic detectability results when onset is assumed known…………..92

Table 3.2 Summary of synthetic detectability results when onset is assumed unknown……..…96

Table 5.1. Calibration model parameters for equations (5) and (6) and misfit by location and orientation……………………………………………………………………………………152

ACKNOWLEDGEMENTS

I have received an immense amount of support during my time in the School of Oceanography and, if left to it, could use as many words in dedication to the community as to the dissertation itself. Instead, I will simply state that this doctoral program was one of the most challenging undertakings of my life and my success would not have been possible without the support of my committee, a number of faculty mentors – both formal and informal – and the School's truly incredible staff. Foremost in my mind, though, are my fellow graduate students. Their compassion, sincerity, and dedication are truly astonishing and inspired me to be better both academically and personally.

To The Touch Tank

For teaching me that a good story writes itself

Chapter 1:
Introduction and Organization of the Dissertation

The majority of the Earth's plate boundaries lie offshore. The subduction end of these systems hosts the planet's largest earthquakes and the spreading end generates oceanic plates that record the recent history of Earth's evolution and ultimately become the material fed into subduction. Near-shore processes in subduction zones are critical to understanding the full subduction cycle and particularly relevant to society because they produce large megathrust earthquakes and tsunamis. In these systems, observations of offshore slow slip earthquakes (SSEs) and secular strain, if they can be resolved, can inform us about the accumulation and release of strain on and around subduction thrusts (Dixon et al., 2014; Holtkamp & Brudzinski, 2010; Radiguet et al., 2014). SSEs are well-studied downdip of the seismogenic zone in many subduction zones (Dragert et al., 2001; Lowry et al., 2001; Obara et al., 2002) and are capable of releasing significant strain energy, up to at least M_w~7, making them an important component of the earthquake cycle (Schwartz & Rokosky, 2007). In recent years, SSEs have been observed offshore in several subduction zones, including New Zealand (Wallace et al., 2016), Japan (Ito et al., 2013), Costa Rica (Davis et al., 2015), Mexico (Radiguet et al., 2016), and Chile (Ruiz et al., 2014). Offshore SSEs also seem to be important parts of the seismic cycle in several subduction zones globally, releasing significant strain energy (e.g., Wallace & Beavan, 2010) and in some cases possibly acting as triggering mechanisms for large megathrust earthquakes (Ito et al., 2013; Uchida et al., 2016).

On land, geodetic measurements have proven an essential complement to seismic measurements, which in combination provide a comprehensive view of tectonic processes (e.g., Bevis et al., 2001; Bock et al., 1993; Feigl et al., 1993; Kreemer et al., 2014; Massonnet et al., 1993; McCaffrey, 2005). However, geodetic measurements in the offshore are much less common, owing largely to the difficulty and cost of working in this setting, and the fact that methods dependent on the propagation of electromagnetic waves (e.g., GNSS, InSAR) are not easily adapted to work beneath the sea surface (Burgmann & Chadwell, 2014). Further, while onshore geodetics such as InSAR and GNSS provide high-resolution areal coverage and incredibly precise signal resolution, respectively (Bock & Melgar, 2016; Hu et al., 2014), seafloor geodetic measurements remain sparse and relatively coarse, complicated by the presence of oceanographic and instrumental signals (Ballu et al., 2009; DeSanto et al., 2016; Freymueller et al., 2019; Polster et al., 2009; Spiess 1985). The combination of limited quality, density, and duration for offshore geodetic experiments has resulted in an incomplete understanding of fundamental plate boundary processes on the seafloor. As such, it is essential to optimize the spatially and temporally limited deployments to maximize the information gathered. With the growing likelihood of expanded, more ambitious deployments, these efforts will help us sensibly organize our sensor networks and meaningfully interpret the data produced.

This dissertation seeks to address the optimization of seafloor geodetic measurements, with a focus on bottom pressure and tilt data, with the goal of improving our ability to observe tectonic deformation in the offshore environment. Better understanding offshore tectonic processes is not as simple as applying existing land-based techniques to the seafloor. This environment presents a unique set of challenges that are prohibitive to making observations at the level of sensitivity required. Thus, for the science to move forward we need new techniques and strategies to make sense of the data available and prepare for future endeavors. This dissertation's principal aim aligns with this need for methods development, providing extensive data exploration and robustness testing. Seafloor pressure processing techniques identified in Chapter 2 using data from the Cascadia Subduction Zone have proven equally effective in other settings, including the Hikurangi Subduction Zone (Inoue et al., 2021) and the Alaska margin (Chapter 3). These techniques are further refined and expanded in Chapter 3, allowing for the detection of increasingly smaller events. Likewise, the development of the Self Calibrating Tilt Accelerometer (SCTA) provides opportunities for observing subtle deformation signals in a range of settings, in particular those which produce small amplitude signals over long periods of time. These improved geodetic techniques, along with other ongoing developments in the field, have the potential to critically inform our understanding of plate boundary processes in the near future. A clear conclusion is that the effects of oceanographic circulation simply cannot be ignored in this environment. Efforts to mitigate ocean signals without understanding them will see only limited gains. Instead, an integrated approach is needed.

In Chapter 2, I present seafloor pressure records, oceanographic models, and geophysical deformation simulations from 2011-2015 from the Cascadia Subduction Zone and show that the oceanographic component of seafloor pressure can be reduced to ≤1 cm RMS by differencing against a reference record from a similar depth over >100 km separation (termed "depth-matched differencing"). In addition, I generate synthetic slow slip observational records from modeled seafloor pressure and simulated deformation to show that a range of slip scenarios produce resolvable signals when using depth-matched differencing. The contents of this chapter are published in *The Journal of Geophysical Research: Solid Earth* under the title "Optimizing Sensor Configurations for the Detection of Slow-Slip Earthquakes in Seafloor Pressure Records, Using the Cascadia Subduction Zone as a Case Study" (Fredrickson et al., 2019).

In Chapter 3, I use seafloor pressure and temperature data from the Alaska margin, along with sea surface height data from satellite altimetry to evaluate the efficacy of various seasonal and oceanographic pressure corrections, conducting synthetic tests to determine their impact on the timing and amplitude prediction of ramp-like signals typical of SSEs. I show that subtracting out the first mode of the complex empirical orthogonal functions of the pressure records on either the shelf or slope, then additionally correcting with a scaled version of depth-matched differencing, yields signal RMS reductions up to 83% or 93%, respectively. The detectability tests show that when using these same corrections, the timing and amplitude of synthetic SSE-like ramps can be well constrained for ramp amplitudes ≥4 cm on the shelf and ≥2 cm on the slope, using a fully automated detector. The contents of this chapter are currently published in the *Journal of Geophysical Research: Solid Earth* under the title "Slow slip detectability in seafloor pressure records offshore Alaska" (Fredrickson, et al., 2023)

In Chapter 4, I use 2017-2021 hindcasts from a Regional Ocean Modeling System encompassing the Cascadia margin to explore the relationships between mesoscale ocean circulation processes and seafloor pressure. I show that on the Cascadia margin, the eustatic and steric components of bottom pressure largely anticorrelate on the lower continental slope and near the trench, but above the shelf break their relationship becomes more complicated with the eustatic component the predominant driver of total pressure and the steric component mostly contributing to long period fluctuations. I also demonstrate that depth-matched differencing results in large-amplitude eustatic and steric differences, despite producing expected low-amplitude differences in the total pressure. Finally, I present case studies of mesoscale eddies generated in the region, showing that these are responsible for at least some of the observed large-amplitude component differences and that these are frequently linked with ramp-like signals in the total pressure difference – a feature of particular concern for the false detection of slow-slip deformation. This work is being prepared for publication in a peer reviewed journal.

In Chapter 5, I present observations from a novel tiltmeter, the Self-Calibrating Tilt Accelerometer (SCTA), designed to diminish the instrumental drift typical of such sensors. Using data from a land-based field deployment at Pinon Flats Observatory in southern California and a seafloor deployment from Axial Seamount on the Juan de Fuca Ridge, I demonstrate that the SCTA accurately records the drift of its channels of 20~100 μrad/yr and can correct these to a residual standard deviation better than 5 μrad and as good as 1 μrad. The SCTA tests suggest marked improvement over traditional short-baseline tiltmeters and show promise for even further performance improvements if deployed in a borehole observatory. This work is being prepared for publication in *Earth and Space Science*.

In Chapter 6, I consider the prior chapters as a whole in the broad context of the field and highlight key areas for future work.

Chapter 2:

Optimizing Sensor Configurations for the Detection of Slow-Slip Earthquakes in Seafloor Pressure Records, Using the Cascadia Subduction Zone as a Case Study

Erik K. Fredrickson[1], William S. D. Wilcock[1], David A. Schmidt[2], Parker MacCready[1], Emily Roland[1], Alexander L. Kurapov[3], Mark A. Zumberge[4], Glenn S. Sasagawa[4]

[1]School of Oceanography, University of Washington, Seattle, Washington, USA
[2]Department of Earth and Space Sciences, University of Washington, Seattle, Washington, USA
[3]Coast Survey Development Laboratory, National Oceanic and Atmospheric Administration, Silver Spring, Maryland, USA
[4]Institute of Geophysics and Planetary Physics, Scripps Institution of Oceanography, University of California, San Diego, La Jolla, California, USA

2.0 Abstract

We present seafloor pressure records from the Cascadia Subduction Zone, alongside oceanographic and geophysical models, to evaluate the spatial uniformity of bottom pressure and optimize the geometry of sensor networks for resolving offshore slow slip transients. Seafloor pressure records from 2011-2015 show that signal amplitudes are depth-dependent, with tidally filtered and detrended root mean squares (RMSs) of <2 cm on the abyssal plain and >6 cm on the continental shelf. This is consistent with bottom pressure predictions from circulation models and comparable to deformation amplitudes from offshore slow slip observed in other subduction zones. We show that the oceanographic component of seafloor pressure can be reduced to ≤1 cm RMS by differencing against a reference record from a similar depth, under restrictions that vary with depth. Instruments at 100-250 m require depths matched within 10 m at separations of <100 km, while locations deeper than 1400 m are broadly comparable over separations of at least 300 km. Despite the significant noise reduction from this method, no slow slip was identified in the dataset, possibly due to poor spatiotemporal instrument coverage, non-ideal deployment geometry, and limited depth-matched instruments. We use forward predictions of deformation

from elastic half-space models and hindcast pressure from circulation models to generate synthetic slow slip observational records and show that a range of slip scenarios produce resolvable signals under depth-matched differencing. For future detection of offshore slow slip in Cascadia, we recommend a geometry in which instruments are deployed along isobaths to optimize corrections for oceanographic signals.

2.1 Introduction

Subduction zones are the sites of the world's largest earthquakes, with high potential for damaging shaking and tsunamigenesis. The locked region of subduction zones, where megathrust earthquakes occur, is often located offshore and has historically been difficult to observe. As such, the slip behavior of offshore seismogenic zones on subduction thrusts is not well understood. The archetypical subducting plate boundary is divided from depth to surface into a zone of stable sliding at depth, a transition zone of slow slip earthquakes (SSEs) and tremor, a locked or partially locked seismogenic zone, and an uncoupled region extending up to the trench (e.g. Hyndman, 2013). This view has been amended in recent years to include, at some subduction zones, another transition zone updip of the sesismogenic zone that hosts slow slip (shallow SSEs) and tremor (Araki et al., 2017; Obara & Kato, 2016). However, it is not known if these features are ubiquitous or particular to specific subduction regimes. Resolving this ambiguity has important implications for subduction zone hazards, particularly the determination of likely megathrust rupture locations and tsunami amplitudes, as interseismic deformation will influence stress accumulation and potentially coseismic displacements on the updip edge of the megathrust.

SSEs downdip of the seismogenic zone have been well-studied in subduction zones worldwide, particularly in Nankai (Hirose et al., 1999; Obara et al., 2002), Cascadia (Dragert et al., 2001), Costa Rica (Dixon et al., 2014), New Zealand (Wallace & Beavan, 2010), and Mexico (Lowry et al., 2001). During slow slip, displacement occurs along the fault over much longer periods of time than in a normal earthquake. Although they vary in size, SSEs are capable of releasing considerable strain energy, up to M_w 7.0 or greater (Schwartz & Rokosky, 2007). SSEs sometimes occur in the same fault region as tremor and low frequency earthquakes, though they are not always found concurrently (Rogers & Dragert, 2003; Shelly et al., 2007) and the updip extent of slow slip may consistently occur beyond that of tremor (Hall et al., 2018; Wang et al., 2008). SSEs appear to obey scaling laws akin to, but different from, those of regular earthquakes, including a relationship between seismic moment and fault area in which stress drops are generally found to be between 0.01-0.10 MPa (Gao et al., 2012), though there are exceptions above and below this range (e.g. Brodsky & Mori, 2007). There is also evidence that SSE and regular earthquakes obey the same moment-duration scaling, which is bimodal as a function of slip area (Gomberg et al., 2016). SSE durations vary broadly, ranging from days to years, leading to the categorization of long-term and short-term events (Fu & Freymueller, 2013; Radiguet et al., 2011).

In the past decade, studies in other subduction zone settings that incorporate offshore measurements, such as seafloor pressure, borehole formation pressure, or ocean bottom seismometers (Araki et al., 2017; Davis et al., 2015; Ito et al., 2013; Wallace et al., 2016), or where the trench is in close proximity to land (Dixon et al., 2014; Ozawa et al., 2007; Radiguet et al., 2016; Ruiz et al., 2014; Vallée et al., 2013; Wallace & Beavan, 2010) have identified shallow SSEs within and updip of the seismogenic zone. Measuring SSE signals on the seafloor is challenging, as there is added difficulty in instrument design and deployment, and the ocean is a significant source of noise. Nonetheless, some of those events successfully observed show consistency in fault size, slip magnitude, and duration. Shallow SSEs recorded on seafloor pressure instruments in Hikurangi (Wallace et al., 2016) and the Japan Trench (Ito et al., 2013) measured 1.5-6 cm vertical deformation at the seafloor over periods of 1-2 weeks and areas of 40-60 km across-strike and 75-80 km along-strike, which were inverted for 10-25 cm peak slip at depths of 15 km up to the trench. The Japan Trench SSEs were separated by 27 months, while Hikurangi shallow SSEs have been observed in the onshore geodetic record to recur at intervals of 18-24 months (Wallace et al., 2012). Davis et al. (2015) used borehole and seafloor pressure to identify near-trench slow slip near Costa Rica's Nicoya Peninsula with comparable vertical deformation, but with only 2 instrument sites could not infer detailed fault parameters.

Similarly, repeating shallow SSEs have been identified in offshore borehole pressure and low-frequency tremor records in the Nankai Subduction Zone (Araki et al., 2017). These events seem to occur over smaller areas, typically 20-40 km, and produce less deformation. The existence of such low-magnitude SSEs suggests the possibility of their occurrence elsewhere, and motivates the development of improved observational methods and techniques for increasing detection capabilities. Yamashita et al. (2015) also measured a shallow, migrating tremor episode in southern Japan on an ocean bottom seismometer network and inferred a coincident SSE with an along-strike extent of up to 150 km. There is global evidence that these shallow slip processes may be capable of triggering megathrust earthquakes (Ito et al., 2013; Ruiz et al., 2014; Uchida et al., 2016).

The Cascadia Subduction Zone exists between the North American Plate and the converging Juan de Fuca Plate, which subducts obliquely at a variable rate that increases from

3.0 cm/yr off California in the south to 4.5 cm/yr off Vancouver Island in the north (Schmalzle et al., 2014). This subduction zone has historically produced M_w~9.0 megathrust earthquakes with a recurrence interval of ~500 years (Atwater, 1987), the last of which occurred in 1700 (Atwater et al., 2015). Sedimentary records indicate that smaller (M_w~8), partial ruptures occur more frequently in the south, at an interval of ~240 years (Goldfinger et al., 2012). As such, the Cascadia Subduction Zone poses a significant seismic hazard to western U.S. and Canadian regions.

There is limited information in Cascadia regarding the presence or absence of SSEs and tremor updip of the seismogenic zone. Current land-based seismic and geodetic measurements are not able to fully resolve the state of locking in the offshore segment of the subduction zone (Wang & Tréhu, 2016), though there are indications that there is a lesser degree of locking offshore northern and central Oregon (Burgette et al., 2009; Schmalzle et al., 2014). Until recent ocean-bottom instrument deployments, such as the Cascadia Initiative (Toomey et al., 2014) and SeaJade experiment (Scherwath et al., 2011), information on seismicity was also limited. One recent study combining onshore and Cascadia Initiative seismic data identified several hundred earthquakes between 2011-2015 of $M_w<4$ (most less than 2) in the vicinity of the megathrust, which may provide additional constraints on locking (Stone, I. et al., 2018). Increased offshore observations would provide a better understanding of the stress state of the subduction zone and possibly give clues as to where the next megathrust earthquake may occur.

In the Cascadia Subduction Zone, though we lack any information about offshore slip processes, a range of recurrence behavior is observed in the record of downdip SSEs. There is significant along-strike segmentation in recurrence interval, which is approximately 10 months beneath northern California, 19 months beneath central and northern Oregon, and 14 months beneath Washington and Vancouver Island (Brudzinski & Allen, 2007). This segmentation in Cascadia is manifested in other properties of the subduction zone (e.g. Porritt et al., 2011), and may also apply to any shallow SSE behavior. There is also across-strike variation in slip behavior, with smaller, more frequent events occurring further downdip and larger, less frequent events occurring further updip (Wech & Creager, 2011).

Offshore instrumentation is important for the measurement of shallow SSEs in Cascadia because the large distance between shoreline and trench (from ~90 km in the south to >150 km in the north) limits the detection of offshore deformation and seismicity by onshore GPS and seismometers. Seafloor absolute pressure gauges (APGs) provide a measure of the overlying atmospheric and oceanic mass and are therefore sensitive to the vertical deformation of the seafloor from SSEs. The major contributions to seafloor pressure are the average water depth, tides, non-tidal oceanographic effects, and geophysical signals. Quartz pressure sensors, which produce high-resolution data, are subject to an instrumental drift that adds an additional term to the measured pressure. This drift can be fit with an initial exponential term that has a characteristic time of weeks to months superimposed upon a linear trend (Polster et al., 2009; Watts & Kontoyiannis, 1990). To isolate the geophysical signals, pressures from APGs are generally filtered for tides, detrended for sensor drift, then subjected to station differencing, wherein a reference pressure record is subtracted from all others (e.g. Wallace et al., 2016). This reference, located away from the deformation, is assumed to capture the regional oceanographic pressure signal, and after its subtraction any remaining signals are assumed attributable to vertical geophysical deformation.

In this paper, we search for evidence of offshore SSEs in the available Cascadia seafloor pressure data between 2011-2015, present a method for best reducing oceanographic pressure signals, and assess the sensitivity of APGs to the deformation signals produced by SSEs, using data from seafloor sensors and models of oceanographic circulation and crustal deformation. We assess the spatial scales of significant oceanographic noise reduction in these data and models to infer the optimal sensor configurations for the purpose of detecting SSEs in the offshore setting.

2.2 Methods

2.2.1 Absolute pressure gauge data

We use data from seafloor APGs deployed between 2011 and 2015 (Figure 2.1) to search for evidence of SSEs in Cascadia. The bulk of these data come from the Cascadia Initiative (CI) experiment (Toomey et al., 2014), an ocean bottom seismometer deployment aimed at recording regional and teleseismic earthquakes on the Juan de Fuca plate and Cascadia forearc. Instruments were recovered and replaced each summer, alternating between northern (> 44° N) and southern locations (< 45° N) every year. This results in the division of these data into the experiment years 2011-2012, 2012-2013, 2013-2014, and 2014-2015. The experiment was not designed with the purpose of detecting offshore SSEs, so deployment geometries were not idealized for this purpose. A total of 70 instruments were used for this experiment. All the instruments had 4 channels: a 3-component seismometer and a 4th channel to measure pressure. The 4th channel for 40 instruments from Scripps Institution of Oceanography and Woods Hole Oceanographic Institution was equipped with a differential pressure gauges (Cox et al., 1984), which could not be used in this study due to their inability to measure pressure changes at periods greater than ~1000 s. The remaining 30 instruments from Lamont-Doherty Earth Observatory used Paroscientific resonant quartz crystal APGs. Of these, 20 were specifically designed with trawl-resistant housings and deployed at depths less than 1000 m. The Cascadia Initiative APGs collected data at 125 Hz, which we down-sampled to 1 sample/hour with a zero-phase filter before performing our analysis. APGs on the Ocean Observatories Initiative (OOI) Cabled Array (Smith et al., 2018) and a pressure benchmark from offshore central Oregon (Cook et al., 2017) provide additional data in the 2014-2015 year.

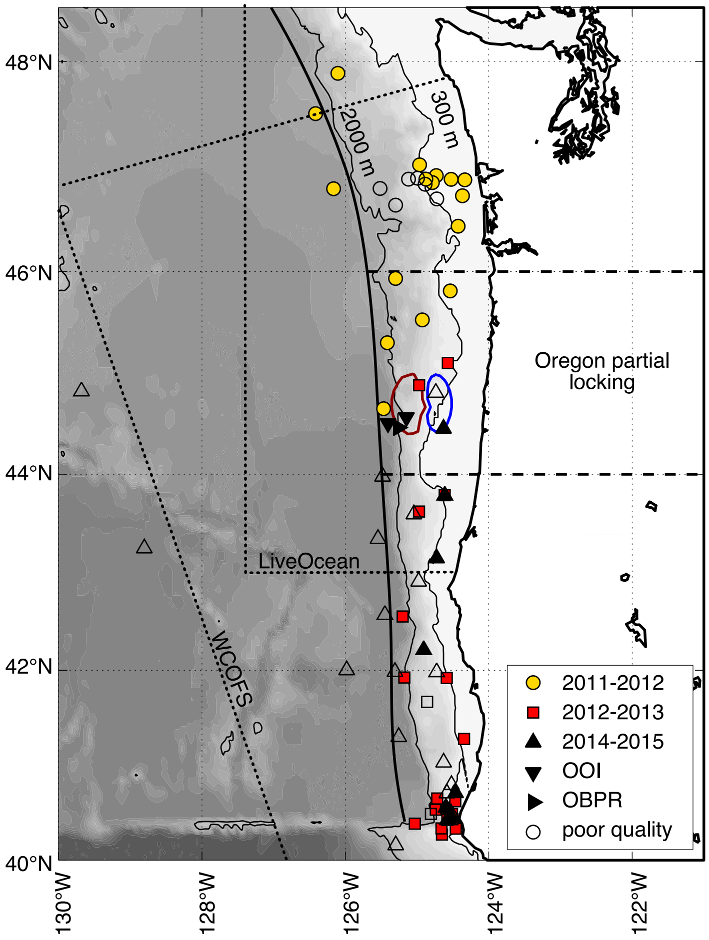

Figure 2.1 Map of the study area, depicting bathymetry and station locations. Thin black contours at 300 m and 2000 m differentiate near-shelf, slope, and abyssal plain regimes, dotted lines show the LiveOcean and WCOFS model domains, black bold line depicts trench axis as per McCrory et al. (2012), and dashed black lines at 44°N and 46°N depict the approximate bounds of the region of partial locking offshore northern Oregon (Burgette et al., 2009; Schmalzle et al., 2014). Pressure gauge instrument locations are displayed with symbols and colors corresponding to experiment years and are unfilled for those which did not yield useable data. The 2013-2014 experiment year is excluded because it had only one useable quality station. The 2014-2015 instruments include cabled pressure gauges from the OOI Cabled Array and a benchmark sensor offshore central Oregon (OBPR), which are denoted by rotated triangles. Red and blue contours show the 1.5 cm uplift and subsidence areas, respectively, from our base SSE model.

In total there are 16 pressure records useable for this study in 2011-2012, 19 in 2012-2013, and 11 in 2014-2015. No useable data was recorded in 2013-2014. Data quality issues associated with the excluded instruments are discussed in Text A1.1. Many of the instruments in each year are located on or near the continental shelf (defined here as depth < 300 m): 9 in 2011-2012, 8 in 2012-2013, and 7 in 2014-2015. Few instruments are located on the continental slope (defined here as 300 m < depth < 2000 m): 3 in 2011-2012, 8 in 2012-2014, and 2 in 2014-2015. The remaining 4, 3, and 2 instruments in each year are located on or near the abyssal plain (defined here as depth > 2000 m).

To recover the geophysical signals from these data, the highest amplitude portion of exponential sensor drift was removed by discarding the first two weeks of data. The pressure records were then detided using a lowpass Godin filter, in which three running averages are applied at 24, 24, and 25 hours (Emery & Thomson 2004; Godin, 1972), and a third order polynomial was fit and subtracted from each time series to remove the mean and any long period signal. A polynomial of third order, the minimum to remove the seasonal signal seen in many oceanographic observables (e.g. Giddings et al., 2014), was chosen to balance RMS reduction and the risk of overfitting, including the fitting of any transient deformation signal (see Text A1.2 and Figure A1.1 of Appendix 1). These processed data are shown in Figure 2.2. Here and throughout this paper, changes in pressure are given in equivalent centimeters of seawater (at $\rho = 1026$ kg/m^3). Detided and polynomial-corrected pressure time series were then analyzed for SSEs by using station differencing and by inspecting visually for steps that might be due to deformation.

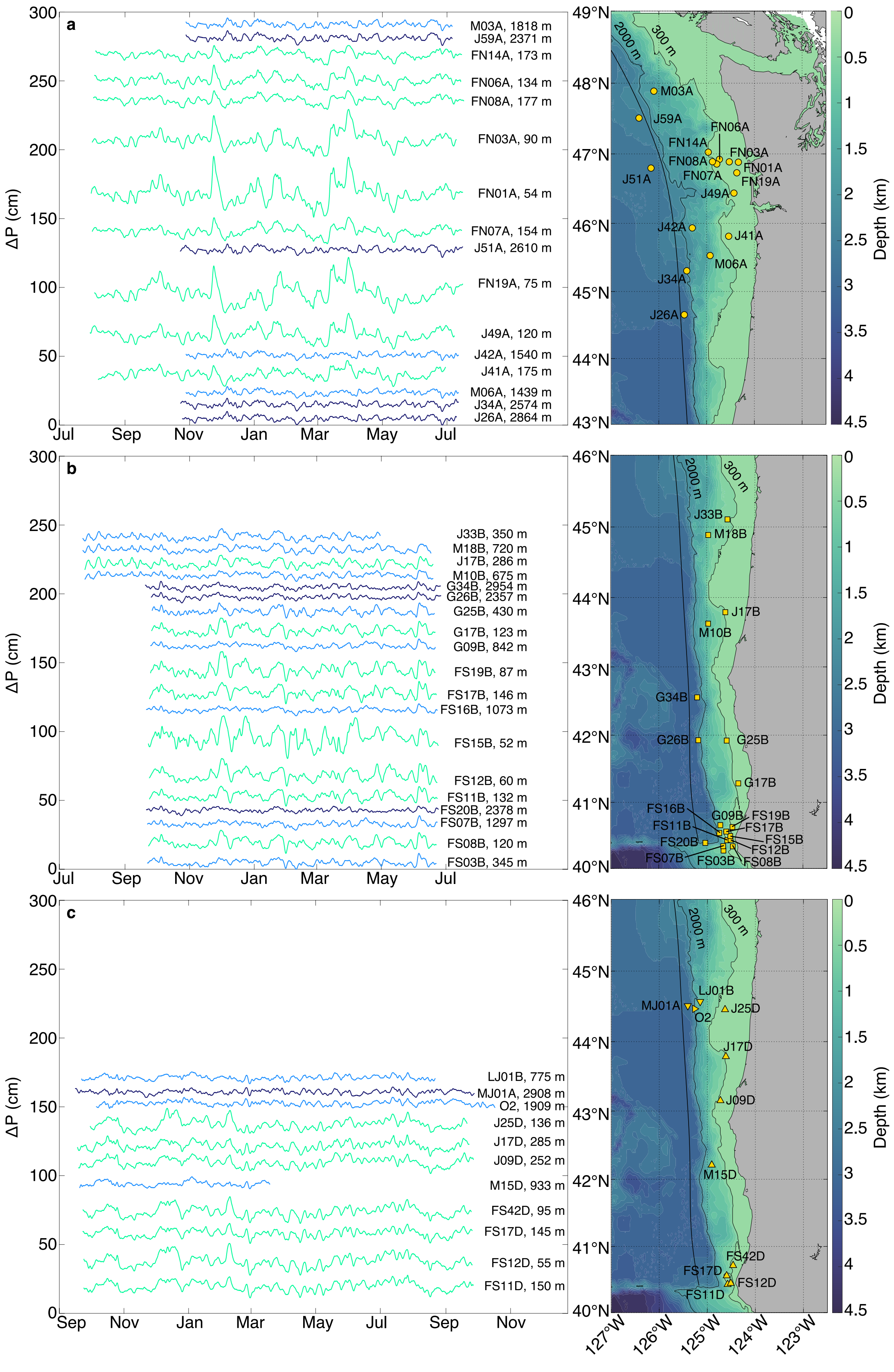
a
b
c
ΔP (cm)
300
250
200
150
100
50
0
Jul
Sep
Nov
Jan
Mar
May
Jul
Sep
Nov
M03A, 1818 m
J59A, 2371 m
FN14A, 173 m
FN06A, 134 m
FN08A, 177 m
FN03A, 90 m
FN01A, 54 m
FN07A, 154 m
J51A, 2610 m
FN19A, 75 m
J49A, 120 m
J42A, 1540 m
J41A, 175 m
M06A, 1439 m
J34A, 2574 m
J26A, 2864 m
J33B, 350 m
M18B, 720 m
J17B, 286 m
M10B, 675 m
G34B, 2954 m
G26B, 2357 m
G25B, 430 m
G17B, 123 m
G09B, 842 m
FS19B, 87 m
FS17B, 146 m
FS16B, 1073 m
FS15B, 52 m
FS12B, 60 m
FS11B, 132 m
FS20B, 2378 m
FS07B, 1297 m
FS08B, 120 m
FS03B, 345 m
LJ01B, 775 m
MJ01A, 2908 m
O2, 1909 m
J25D, 136 m
J17D, 285 m
J09D, 252 m
M15D, 933 m
FS42D, 95 m
FS17D, 145 m
FS12D, 55 m
FS11D, 150 m
49°N
48°N
47°N
46°N
45°N
44°N
43°N
42°N
41°N
40°N
127°W
126°W
125°W
124°W
123°W
2000 m
300 m
Depth (km)
0
0.5
1
1.5
2
2.5
3
3.5
4
4.5
M03A
J59A
FN06A
FN14A
FN03A
FN08A
FN01A
FN07A
FN19A
J51A
J49A
J42A
J41A
M06A
J34A
J26A
J33B
M18B
J17B
M10B
G34B
G26B
G25B
G17B
FS16B
G09B
FS19B
FS11B
FS17B
FS15B
FS20B
FS12B
FS07B
FS03B
FS08B
LJ01B
MJ01A
O2
J25D
J17D
J09D
M15D
FS42D
FS17D
FS12D
FS11D

Figure 2.2 The pressure data used in these analyses, offset for display purposes, alongside maps of instrument locations for (a) 2011-2012, (b) 2012-2013, and (c) 2014-2015. For each time series, the first two weeks of data are discarded, a Godin 24-24-25 filter (Godin, 1972) is applied, and a third-order polynomial fit is removed. Data from below 2000 m depth are plotted in dark blue, depths 300-2000 m in light blue, and depths above 300 m in green. Station name and depth are listed next to each time series. The start and end times of the data vary, according to deployment/recovery and scheduled ship time.

2.2.2 Physical oceanographic circulation models

To better understand the effects of physical oceanographic processes on seafloor pressure, and to assess the effectiveness of station differencing, we utilized two ocean circulation models that overlapped our study region, the domains of which are shown in Figure 2.1. One is the LiveOcean model developed by the University of Washington Coastal Modeling Group (Giddings et al., 2014; Stone, H.B. et al., 2018), which extends from 43°N to 50°N. The other is the West Coast Ocean Forecast System (WCOFS) developed at the National Oceanic and Atmospheric Administration (NOAA) Coast Survey Development Laboratory (Kurapov et al., 2017), which extends along the North American coast from 24°N to 54°N. The LiveOcean model has 1.5 km resolution near the coast, decreases to 4.5 km resolution offshore, and at all points has 40 vertical layers optimized for determining surface and bottom conditions. The WCOFS model has a uniform 2 km resolution with 40 vertical layers, at least 10 of which are in the top 50 m of the water column. Both models are constructed using the Regional Ocean Modeling System (ROMS) framework, which uses the seawater equation of state and conservation of tracers, within the Boussinesq approximation. The pressure is hydrostatic and equations are solved to generate full 3D fields of physical oceanographic parameters, optimized for integrated conservation and constancy preservation given a free ocean surface and realistic bathymetry (Shchepetkin & McWilliams, 2005). Forcings come from atmospheric, tidal, and river inputs, in addition to model boundary conditions from the U.S. Navy HYCOM (Chassignet et al., 2007). The calculated fields are validated against observational data, including temperature, salinity, and tide gauges.

Such models are typically used to study regional ocean circulation processes, such as major currents or regions of upwelling, that can be tied to the transport of biological and chemical tracers of interest. These models were not developed for the purpose of calculating seafloor pressure, but they contain the necessary fields to do so. Global-scale barotropic models have previously been used to this end (Inazu et al., 2012; Ito et al., 2013; Muramoto et al., 2019). Herein, modeled bottom pressures were calculated hourly, averaged daily, and subjected to the same filtering and polynomial fitting as the APG data to ensure comparability. We use the LiveOcean model from January 2013 (its inception) to December 2015 (the end of our APG dataset) and the WCOFS model from January 2011 (the start of our APG dataset) to December 2014 (its latest available date). The combined spatiotemporal model domain overlaps with all but one instrument in the 2011-2012 and 2012-2013 APG datasets, but provides only partial spatial overlap with the 2014-2015 data. Though the two models show some differences in their common year (2013-2014), particularly off the continental shelf, we determine that they predict bottom pressures similar enough to be used interchangeably (see Text A1.3 and Figures A1.2-A1.4 of Appendix 1).

We quantified the comparability between models and data by calculating the R^2 of the fit of the modeled bottom pressure to the observed pressure at the same location, given by:

$$R^2 = 1 - \frac{\sigma_{y-x}^2}{\sigma_y^2} \qquad (1)$$

where σ_y^2 is the variance in the observed data, and σ_{y-x}^2 is the variance in the model-corrected signal. This relation is similarly used to assess the agreement of the two models. As the relationship between the model and observations is non-linear, the calculated R^2 values do not have an easily interpretable meaning (e.g. Kvalseth, 1985) but do provide a quantitative assessment of the goodness of fit at a given location and can be compared to one another. A positive R^2 signifies that variance is reduced by differencing, while a negative R^2 signifies that variance is increased.

2.2.3 Geophysical slow slip modeling

We also present elastic slip models of representative SSEs to understand the nature of expected signals in the region and the ability of an APG network to detect them. We model the Cascadia Subduction Zone fault surface as 5729 planar, triangular elements following the slab model of McCrory et al. (2012), adjusting depth to be relative to the seafloor rather than to sea level, as shown in Figure 2.3. Green's functions were then calculated for each element in an elastic half-space using the boundary element code Poly3D (Thomas, 1993), allowing the determination of vertical displacement, among other parameters, for a given slip geometry. We use a Poisson's ratio of $\nu = 0.38$ and a Shear Modulus of $\mu = 10$ GPa, consistent with the physical properties of the accretionary prism (Jeppson et al., 2018). Modeled displacements are incorporated into modeled oceanographic bottom pressure time series from LiveOcean to generate synthetic time series of various SSE scenarios in Cascadia from which detectability can be assessed. These synthetics were detided and corrected with a third-order polynomial after incorporating SSE displacement, but before differencing, to mimic the handling of real observational data. Though not the focus of this study, we also assess detectability from on-land GPS by calculating predicted horizontal deformation at the coast. These predictions should be viewed as coarse approximations because our modeling space does not account for the complex structure and associated rheological changes at and near the coast.

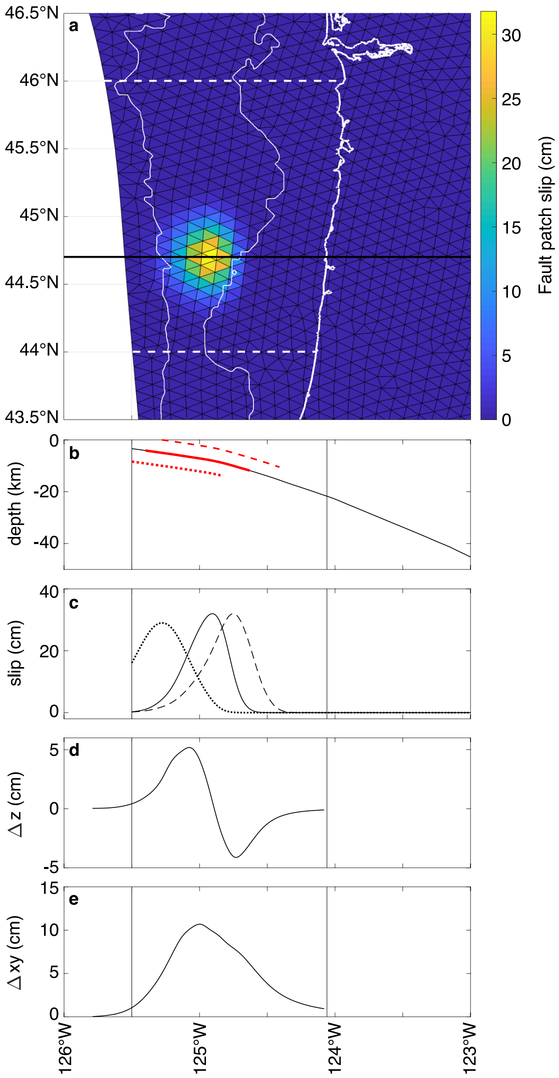

Figure 2.3 (a) Parameterization of the Juan de Fuca slab surface into triangular elements, used in our deformation modeling, with elements color coded according to slip amplitude for the base model. The trench is depicted by the westernmost boundary of the slab, the coastline is shown in bold white, thin white contours show 300 m and 2000 m depth, and dashed white lines at 44°N and 46°N depict the approximate bounds of the region of partial locking offshore northern Oregon (Burgette et al., 2009; Schmalzle et al., 2014). The black line at 44.7°N indicates the cross section line for (b)-(e). (b) Cross section of plate interface depth versus longitude with the region of slip highlighted in red. The dotted and dashed red curves below and above show the slip region for updip and downdip model variations, respectively, offset vertically for display purposes. Note that depth is given relative to the seafloor and does not go to zero at the trench due to significant sediment coverage in Cascadia. c) Slip versus longitude, with updip and downdip variations shown by dotted and dashed curves, respectively. d) Surface vertical deformation versus longitude. e) Surface horizontal deformation versus longitude. Vertical bars in (b-d) represent the locations of the deformation front and coastline in the cross-section.

Slip geometries were based on measurements of offshore SSEs in other settings, predominantly Ito et al. (2013) and Wallace et al. (2016), who report M_w 6.8 events near the Japan and Hikurangi trenches, respectively. Spatial extents of both are elongated along-strike compared to across-strike, though the Japan trench event is not as well constrained along-strike due to the deployment geometry of that experiment. Neither SSE has a reported stress drop, but from the information provided for each an approximate value of $\Delta\sigma = 0.1$ MPa can be calculated. Given earthquake scaling laws, smaller events likely occur more regularly but there are limited reports of smaller offshore SSEs in the literature, likely due to the difficulty in detecting these events. Araki et al. (2017) report offshore SSEs in Nankai of M_w 5.0-5.6, with displacement inferred from borehole formation pressures and spatial extent inferred from concurrent tremor. Other small-amplitude shallow SSE signals have been reported from borehole pressure measurements (e.g. Davis et al., 2015), but limited instrument coverage inhibits inferences about event size.

The base slip geometry used in our model is a two-dimensional Gaussian with 32 cm peak slip, constrained by depth and length along strike and centered beneath the continental slope offshore central Oregon (Figure 2.3a and Table 2.1), chosen for the inferred partial locking there (Burgette et al., 2009; Schmalzle et al., 2014). The Gaussian has a 19 km halfwidth in the north-south direction and 1.5 km halfwidth in the z-direction (approximately corresponding to an east-west halfwidth of 12 km). To reduce the effects of our models' smoothness, which causes many elements to have very small, non-zero slip, in all models we reassign elements with <1 cm slip to instead have zero slip. The peak uplift generated by this event is 5.5 cm, consistent with values measured in Hikurangi and the Japan Trench. The fault slip in this setting corresponds to a minimum recurrence interval of 8.4 years, given the convergence rate of 3.8 cm/yr at this location. We chose the slip to occur uniformly over 14 days, based off observations elsewhere. Our model results in a M_w 6.4 event, lower than reported in Hikurangi and Japan, a result of the significantly lower Shear Modulus used in our modeling, which was selected to accurately reflect the low rigidity of Cascadia's accretionary prism, while inversion modeling in Hikurangi and the Japan Trench assumed parameters consistent with continental crust.

Table 2.1

Slow Slip Earthquake Modeling Scenarios

Model Name	M_w	$\Delta\sigma_E$ (MPa)	$\Delta\sigma_M$ (MPa)	Dist. to shore (km)	L (km)	W (km)	Max slip (cm)	Δz_{max} (cm)	Δz_{min} (cm)	$L_{+\Delta z}$ (km)	$W_{+\Delta z}$ (km)	$L_{-\Delta z}$ (km)	$W_{-\Delta z}$ (km)	$\Delta\ xy_{coast}$ (cm)
Base (Figure 2.9)	6.4	0.057	0.031	72	96	60	32	5.5	-4.1	65	36	61	26	0.9
Time shifted (Figure A1.5)														
30-day (Figure A1.6)														
Near-Trench (Figure 2.10)	6.4	0.057	0.036	100	90	55	28	5.1	-2.8	56	30	48	24	0.3
Near-Shelf (Figure A1.7)	6.4	0.057	0.029	58	89	62	31	6.8	-3.9	67	38	60	27	1.7
Low $\Delta\sigma$ (Figure 2.11)	6.4	0.014	0.010	72	248	51	11	2.0	-1.7	80	18	52	7	0.5
High $\Delta\sigma$ (Figure A1.8)	6.4	0.217	0.104	72	37	62	78	10.6	-7.1	40	44	43	31	1.0
Low M_w (Figure 2.12)	5.9	0.022	0.016	72	65	47	9	1.5	-1.1	1	1	--	--	0.2
High M_w (Figure A1.9)	6.9	0.057	0.026	72	342	70	65	12.0	-9.9	240	48	237	43	3.4
Very low slip (Figure A1.10)	6.2	0.006	0.005	137	260	45	4	0.8	-0.5	--	--	--	--	0.1

Note. M_w – moment magnitude, $\Delta\sigma_E$ – energy averaged stress drop, $\Delta\sigma_M$ – moment-based stress drop, Dist. to shore – E-W distance from site of peak slip to shoreline, L – N-S total length of slip region, W – E-W total width of slip region, Max slip – maximum slip, Δz_{max} – peak uplift at seafloor, Δz_{min} – peak subsidence at seafloor, $L_{+\Delta z}$ – N-S length of uplift ≥ 1.5cm, $W_{+\Delta z}$ – E-W width of uplift ≥ 1.5cm, $L_{-\Delta z}$ – N-S length of subsidence ≤ -1.5cm, $W_{-\Delta z}$ – E-W width of subsidence ≤ -1.5cm, Δxy_{coast} – horizontal displacement at the coast

We recognize that there is ambiguity in calculating the stress drop for a heterogeneous slip distribution (Noda et al., 2013). Herein, we present stress drops using the energy-based averaging approach of Noda at al. (2013, equation 10), which in the case of our discretized fault model is given by:

$$\Delta\sigma_E = \frac{\sum \Delta\sigma_i D_i A_i}{\sum D_i A_i} \qquad (2)$$

where $\Delta\sigma_i$, D_i, and A_i are the stress drop, slip, and area of a given patch, respectively, and the sum is performed over all slipping patches. However, much of the literature for recorded SSEs report a simplified stress drops that assumes an average slip over the entire slipping area, analogous to the moment-based approach Noda et al. (2013, equation 4), so in Table 2.1 we also report this value. In the text, we will explicitly denote each calculation as $\Delta\sigma_E$ and $\Delta\sigma_M$. This allows us to most accurately describe the nature of the slip distribution in our models while still giving a meaningful comparison to the literature (e.g. Gao et al., 2012). Our base model results in a stress drop of $\Delta\sigma_E = 0.057$ MPa, lower than estimated for Hikurangi and Japan due to our use of smaller elastic parameters.

To investigate a broader range of potential SSE behavior, we consider additional models in which we change the timing and duration of slip to reflect the broad range of observations elsewhere, the slip location along dip to explore trenchward and landward deformation, the stress drop to simulate endmembers of a given moment release, and the moment magnitude to assess how observational parameters scale.

2.3 Results

2.3.1 Differencing of absolute pressure gauge data

The detided and polynomial-corrected APG data used in our study, shown in Figure 2.2, have signal amplitudes that decrease with water depth, from a mean of 5 cm RMS over the deployment interval for instruments at depths shallower than 100 m down to a mean of 1.5 cm RMS for instruments at depths below 1400 m. The largest amplitudes come from the shallow, northern APGs in 2011-2012, with RMS ~1 cm larger than southern instruments from 2012-2013 and 2014-2015 at comparable depths. Pressure amplitudes increase in the winter across all stations and years, but the difference is most pronounced for shallow locations.

With the limited number of available instruments in each year, it was possible to apply station differencing to every combination of pressure time series. In all of the differences generated, no static step clearly indicative of SSE-induced deformation was found; however, the residual oceanographic noise varied greatly among these differences, from <1 cm to >7.5 cm RMS, so detectability varied similarly. The greatest reduction in non-tidal oceanographic signal was achieved by differencing instruments at comparable depths. Examples of bottom pressure time series for instruments with comparable depths are shown in the upper panels of Figure 2.4 and their differences are shown as black curves in the lower panels. Inspected visually, the pressure time series at each depth show a high degree of similarity and upon differencing, residual RMS of these examples are <1 cm. The differences do not, generally, have consistent RMS through time but instead have discrete segments of increased amplitude, on time scales of weeks.

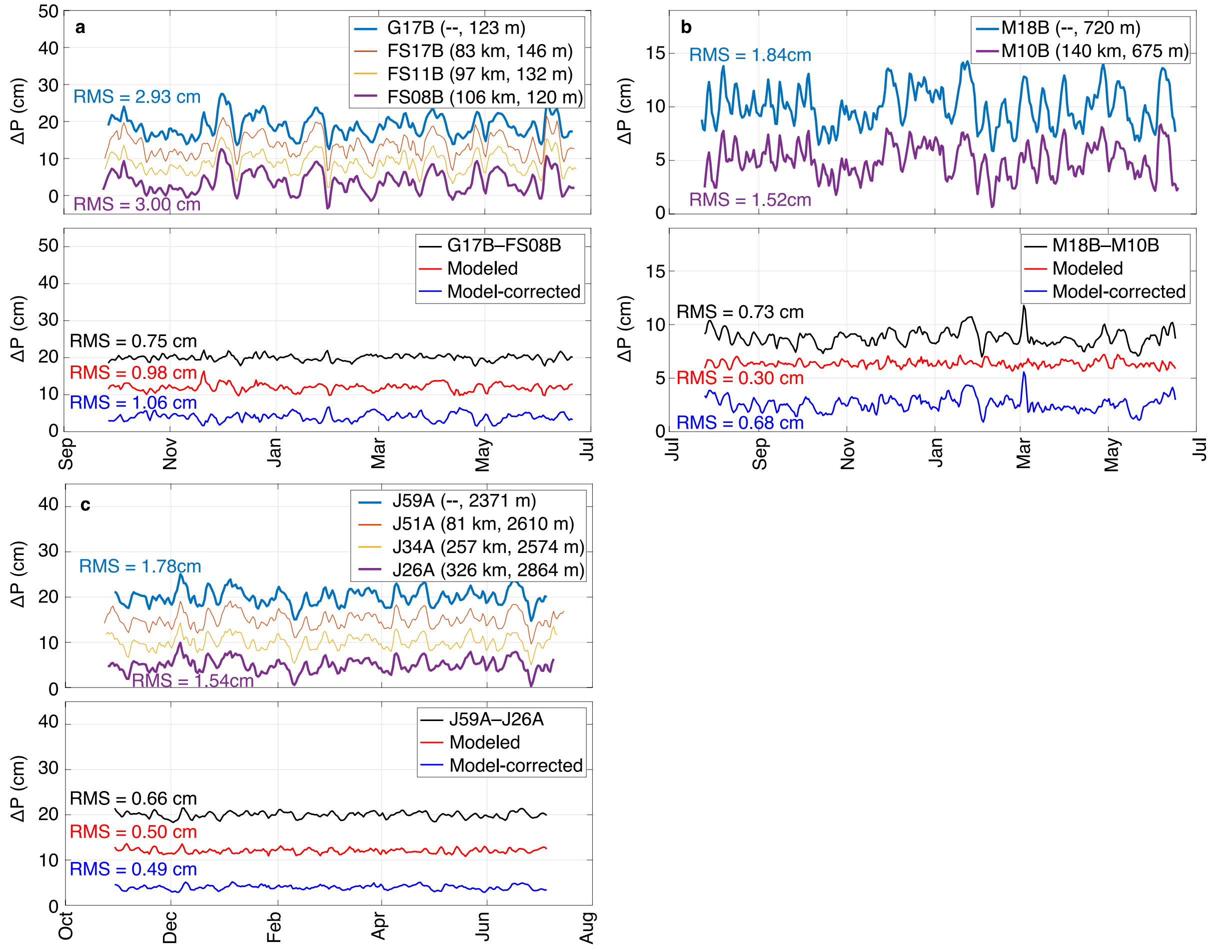

Figure 2.4 Example comparisons (upper panels) and differences (lower panels) of APG time series at similar depths. (a) Comparison of continental shelf stations from 2012-2013. (b) Comparison of continental slope stations from 2012-2013. c) Comparison of stations on the abyssal plain from 2011-2012. The legend in the upper panels indicates the names of instruments, their separation from the top-most instrument, and the water depth of their location. Bold curves indicate the two stations used to generate the differences in the lower panels. In the difference plots, the black curve depicts the time series obtained by differencing the APG data, the red curve depicts the difference from the WCOFS model at the same locations, and the blue curve depicts the difference obtained after correcting the data with the model. RMS are listed for each. All curves are offset for display purposes. Instrument locations are mapped in Figure 2.2.

Table 2.2 gives the RMS of differences for all groups of two or more stations at similar depths throughout experiment years, relative to the northernmost or southernmost station in the group. This was done to provide a representative range of separations and to minimize redundant information. A comprehensive list of all difference combinations for instruments at similar depths is given in Table A1.1. In Figure 2.5 we explore all of the matched-depth differences further by separating instruments into depth bins and plotting the difference RMS between pairs of sensors versus the depth difference and lateral distance between sensors. These bins contain 25 differences at depth > 1400 m (Figure 2.5a), 11 at 1400 m > depth > 500 m (Figure 2.5b), 7 at 500 m > depth > 250 m (Figure 2.5c), 24 at 250 m > depth > 100m (Figure 2.5d), and 7 at depth < 100 m (Figure 2.5e) and were selected because the differences of instruments between bins had uniformly high RMS, in part because the depths are not evenly distributed within those bins. With the notable exception of instruments at <100 m depth, the majority of the depth-matched differences at separations <100 km from Figure 2.5 and Table 2.2 have ≤1 cm RMS. We therefore find a vertical deformation amplitude of 1.5 cm to be an unambiguous SSE detection threshold for this dataset and use this threshold in the subsequent geophysical modeling scenarios.

Table 2.2

RMS Reduction from Depth Matched Differencing

		Depth	Depth dif.	Separation	Observations		Model		Model corrected obs.	
Year	Station	z (m)	Δ z (m)	Δ xy (km)	RMS (cm)	Dif. RMS (cm)	RMS (cm)	Dif. RMS (cm)	RMS (cm)	Dif. RMS (cm)
2011-2012	**J26A**	**2864**	**--**	**--**	**1.5**	**--**	**1.3**	**--**	**1.6**	**--**
	J34A	2574	-290	72	1.5	0.6	1.4	0.2	1.8	0.6
	J51A	2610	-254	244	1.7	0.8	1.4	0.4	1.9	0.8
	J59A	2371	-493	326	1.8	0.7	1.4	0.5	1.8	0.5
	M06A	**1439**	**--**	**--**	**1.5**	**--**	**1.4**	**--**	**1.6**	**--**
	J42A	1540	-101	53	1.5	0.4	1.4	0.2	1.7	0.4
	M03A	1818	+379	277	1.7	0.5	n/a [a]	n/a [a]	n/a [a]	n/a [a]
	J41A	**175**	**--**	**--**	**3.1**	**--**	**2.5**	**--**	**2.7**	**--**
	FN08A	177	+2	123	2.6	1.7	1.8	1.1	2.3	1.7
	FN14A	173	-2	139	2.7	1.7	1.7	1.2	2.5	1.8
	FN06A	**134**	**--**	**--**	**3.1**	**--**	**3.0**	**--**	**2.2**	**--**
	FN07A	154	+20	8	3.3	0.7	2.5	0.6	2.5	1.0
	J49A	120	-14	59	4.3	1.7	3.5	0.7	2.7	1.5
	FN03A	**90**	**--**	**--**	**5.3**	**--**	**4.2**	**--**	**3.4**	**--**
	FN01A	54	-36	14	6.9	2.5	5.5	1.6	3.3	1.9
	FN19A	75	-15	21	7.1	3.8	4.8	0.8	5.2	3.8
2012-2013	**FS20B**	**2378**	**--**	**--**	**1.3**	**--**	**1.2**	**--**	**1.4**	**--**
	G26B	2357	-21	171	1.3	0.3	1.2	0.3	1.4	0.3
	G34B	2954	-576	241	1.2	0.5	1.2	0.3	1.4	0.5
	FS16B	**1073**	**--**	**--**	**1.4**	**--**	**1.1**	**--**	**1.4**	**--**
	FS07B	1297	+224	23	1.5	0.6	1.1	0.1	1.6	0.6
	M10B	**675**	**--**	**--**	**1.5**	**--**	**1.3**	**--**	**1.4**	**--**
	M18B	720	+45	140	1.8	0.7	1.4	0.3	1.5	0.7
	G09B	842	+167	331	1.5	0.8	1.1	0.5	1.4	0.8

Table 2.2 cont.

		Depth	Depth dif.	Separation	Observations		Model		Model corrected obs.	
Year	Station	z (m)	Δ z (m)	Δ xy (km)	RMS (cm)	Dif. RMS (cm)	RMS (cm)	Dif. RMS (cm)	RMS (cm)	Dif. RMS (cm)
2012-2013	**J33B**	**350**	**--**	**--**	**1.9**	**--**	**1.7**	**--**	**1.6**	**--**
	J17B	286	-64	146	2.3	0.9	1.8	0.5	1.8	0.9
	G25B	430	+80	354	2.0	1.3	1.5	0.9	1.7	1.4
	FS03B	345	-5	537	1.8	1.3	1.3	1.1	1.5	1.2
	FS08B	**120**	**--**	**--**	**3.0**	**--**	**1.8**	**--**	**2.2**	**--**
	FS11B	132	+12	14	2.7	0.6	1.6	0.5	2.2	0.7
	FS17B	146	+26	27	3.0	0.9	2.1	0.5	2.1	1.1
	G17B	123	+3	106	2.9	0.7	2.4	1.0	1.9	1.1
	FS12B	**60**	**--**	**--**	**3.7**	**--**	**3.1**	**--**	**2.3**	**--**
	FS15B	52	-8	6	5.8	3.6	2.9	0.3	4.5	3.6
	FS19B	87	+27	21	3.9	1.5	2.1	1.5	2.9	2.3
2014-2015	**MJ01A**	**2908**	**--**	**--**	**1.4**	**--**	**2.7**	**--**	**2.6**	**--**
	O2	1909	-999	12	1.6	0.8	2.4	0.8	2.5	1.2
	LJ01B	**775**	**--**	**--**	**1.6**	**--**	**1.9**[b]	**--**	**2.0**[b]	**--**
	M15D	933	+158	263	1.7	1.0	1.8[b]	0.4[b]	2.1[b]	1.0[b]
	J09D	**252**	**--**	**--**	**3.0**	**--**	**1.8**	**--**	**2.9**	**--**
	J17D	285	+32	71	2.8	1.1	1.8	0.4	2.6	1.1
	FS11D	**150**	**--**	**--**	**3.2**	**--**	**2.2**[b]	**--**	**3.1**[b]	**--**
	FS17D	145	-5	15	2.9	1.1	2.9[b]	1.1[b]	2.7[b]	1.7[b]
	J25D	136	-14	448	3.6	2.0	3.6[b]	2.1[b]	4.1[b]	2.6[b]
	FS42D	**95**	**--**	**--**	**3.5**	**--**	**3.3**[b]	**--**	**3.3**[b]	**--**
	FS12D	55	-40	30	4.2	1.2	3.9[b]	0.8[b]	4.1[b]	1.2[b]

Note. We include here only differences for which depths are reasonably well matched: within 10s of m for instruments on or near the continental shelf, within 100s of m for instruments on the mid to lower slope, and within ~1000m for instruments on the abyssal plain. The first station in each group acts as the reference, against which all others were differenced ("Observations"). Values from the WCOFS model at the same locations are also included ("Model"), as are those obtained by applying the model as a correction to the data prior to differencing ("Model corrected obs."). In the 2014-2015 year, the LiveOcean model is used for those instruments within its domain, while the remainder use a truncated WCOFS model (which ends in December 2014). z – depth, Δxy – horizontal separation, RMS – RMS of pressure time series, Dif. RMS – RMS of difference.

[a] Model unavailable for station M03A

[b] WCOFS model available only until 12/31/2014

2.3.2 Hindcast seafloor pressure from circulation models

The LiveOcean and WCOFS oceanographic models were used to assess how patterns identified in the APG dataset scale to a regional coverage area. Figure 2.6a contours bottom pressure RMS for all grid points in the WCOFS model for the 2013-2014 year, showing significant depth dependence for locations above mid-slope depths of about 1000 m. This depth-dependence is comparable to the scaling identified in the APG data: for the same APG locations shallower than 100m, the model predicts a mean 4 cm RMS while for the same locations below 1400 m the model predicts a mean of 1.5 cm. Shallow, northern locations have the highest RMS, just as with the APG data.

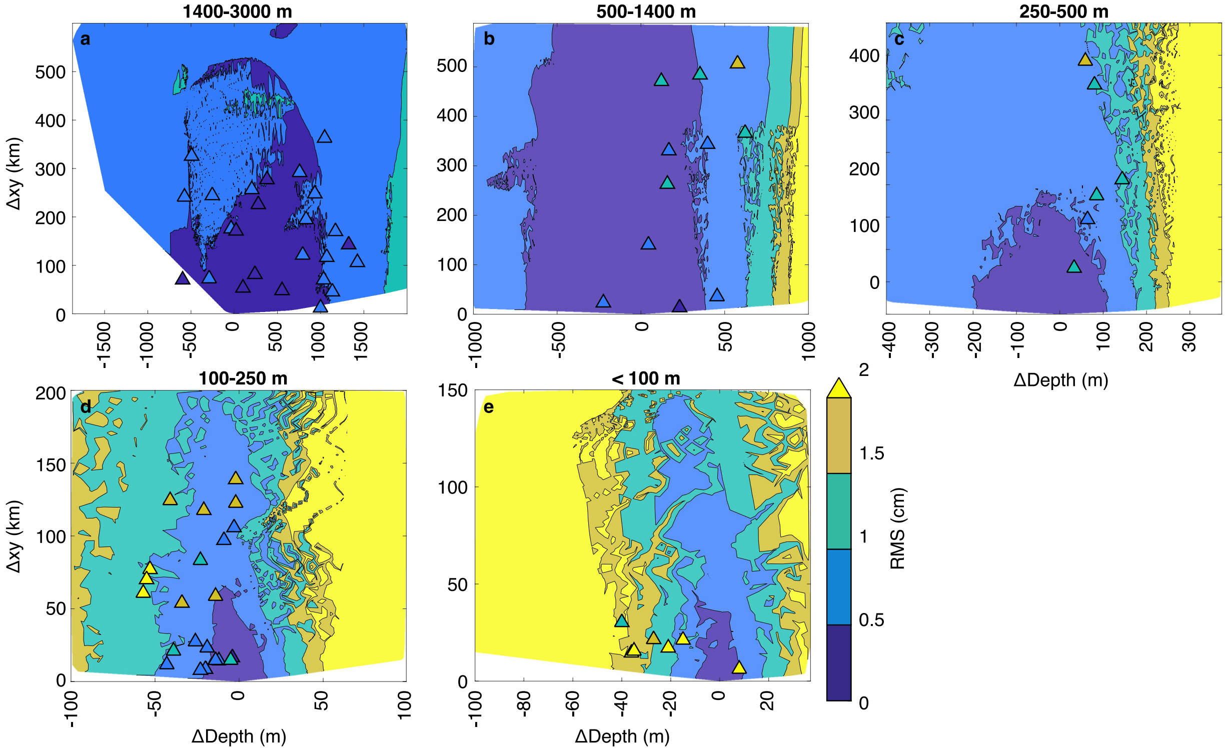

Figure 2.5 Pressure difference RMS versus lateral separation and depth difference. Triangles represent observed differences from the APG data, color coded by RMS. Contours show predictions from the WCOFS oceanographic model, using the same color scale but faded for display purposes. (a) Instruments between 1400-3000 m depth and model reference location at 2581 m. (b) Instruments between 500-1400 m depth and model reference location at 1103 m. (c) Instruments between 250-500 m depth and model reference location at 394 m. Note that one difference at large separation is excluded from the APG data for display purposes. (d) Instruments between 100-250 m depth and model reference location at 121 m. Note that two differences at large separation are excluded from the APG data for display purposes. (e) Instruments less than 100 m depth and model reference location at 57 m. The model reference locations are shown by open symbols in Figure 2.6a. We use the convention that ΔDepth is positive when the reference location is deeper than the location from which it is subtracted and negative when it is shallower. For the APG data, the reference station is chosen to be that which is most similar to the model reference for that depth bin, for consistency in our sign convention.

Select pressure time series from the WCOFS oceanographic model are shown alongside pressure data from collocated CI APGs in Figure 2.7. The model accurately captures certain elements of the measured seafloor pressure signal, particularly in shallow, near-shore locations, as can be seen in the time series plotted in the upper panels of Figure 2.7a-c, but consistently underpredicts RMS. The longest- and shortest-period pressure signals are generally well-predicted but those in the days to weeks range do not match the APG data well. This results in differences between observation and model pressure time series with significant RMS – often of the same order as the original pressure time series and large enough to obscure deformation signals of at most a few centimeters characteristic of shallow SSEs in other settings, as shown in the differences in the lower panels of Figure 2.7a-c.

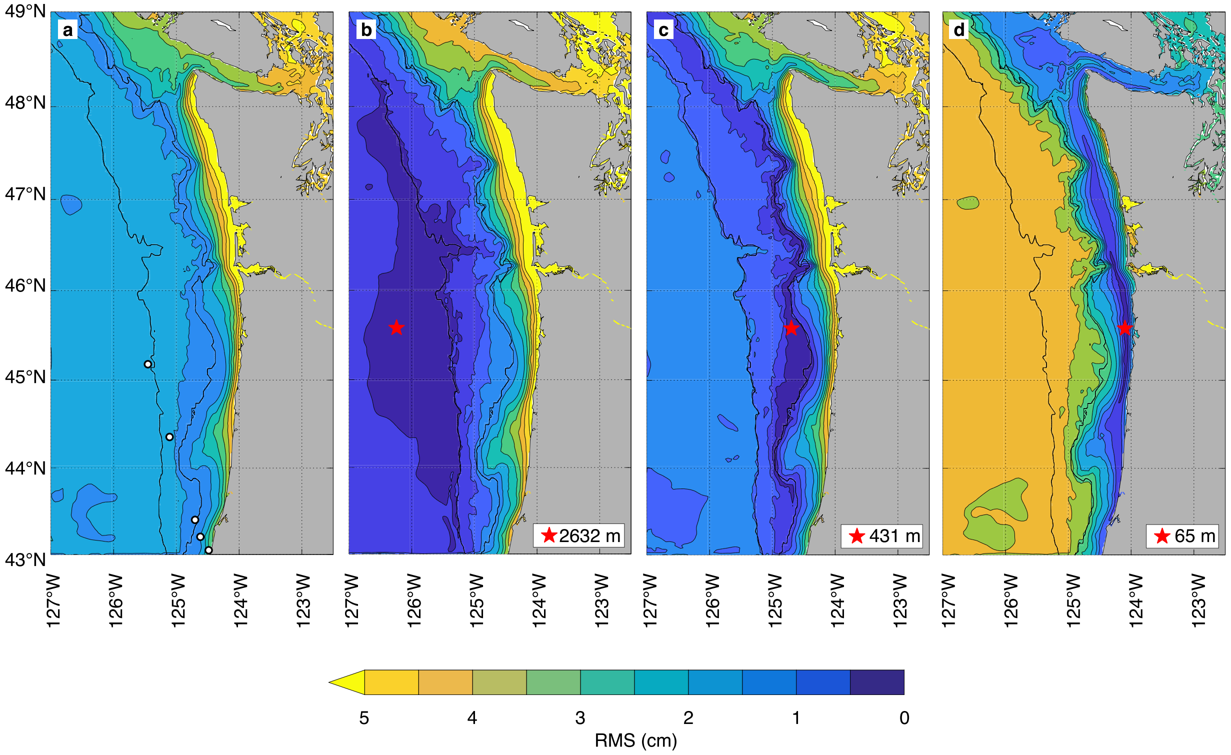

Figure 2.6 (a) Contours of modeled bottom pressure RMS from 2013-2014 of the LiveOcean model, with a Godin 24-24-25 filter (Godin, 1972) applied and a third-order polynomial fit removed. Open circles indicate the model locations used in Figure 2.5. (b)-(d) Contours of RMS of modeled differences relative to the starred reference locations for all grid points in the model, with depth indicated in legend, for an abyssal plain, continental slope, and continental shelf location, respectively. Black contours show 300 m and 2000 m isobaths.

Frequency spectra of the APG data and model are plotted together in Figure 2.7d-e. As with the time series comparisons, the model closely matches the frequency content of the APGs on or near the shelf but does worse for the instruments on the slope and abyssal plain, particularly at frequencies of 0.07 and 0.035 day^{-1} (periods of 14 and 27 days), where the APG data have larger amplitudes. Across all experiment years, the amplitude at these periods is about twice as large for the APGs than for either of the models, suggesting that the instruments are capturing some oceanographic process that the models do not accurately account for. Instruments off the continental shelf also tend to have elevated amplitudes at higher frequencies when compared to the models, particularly between 0.2 and 0.33 day^{-1} (periods of 5 and 3 days).

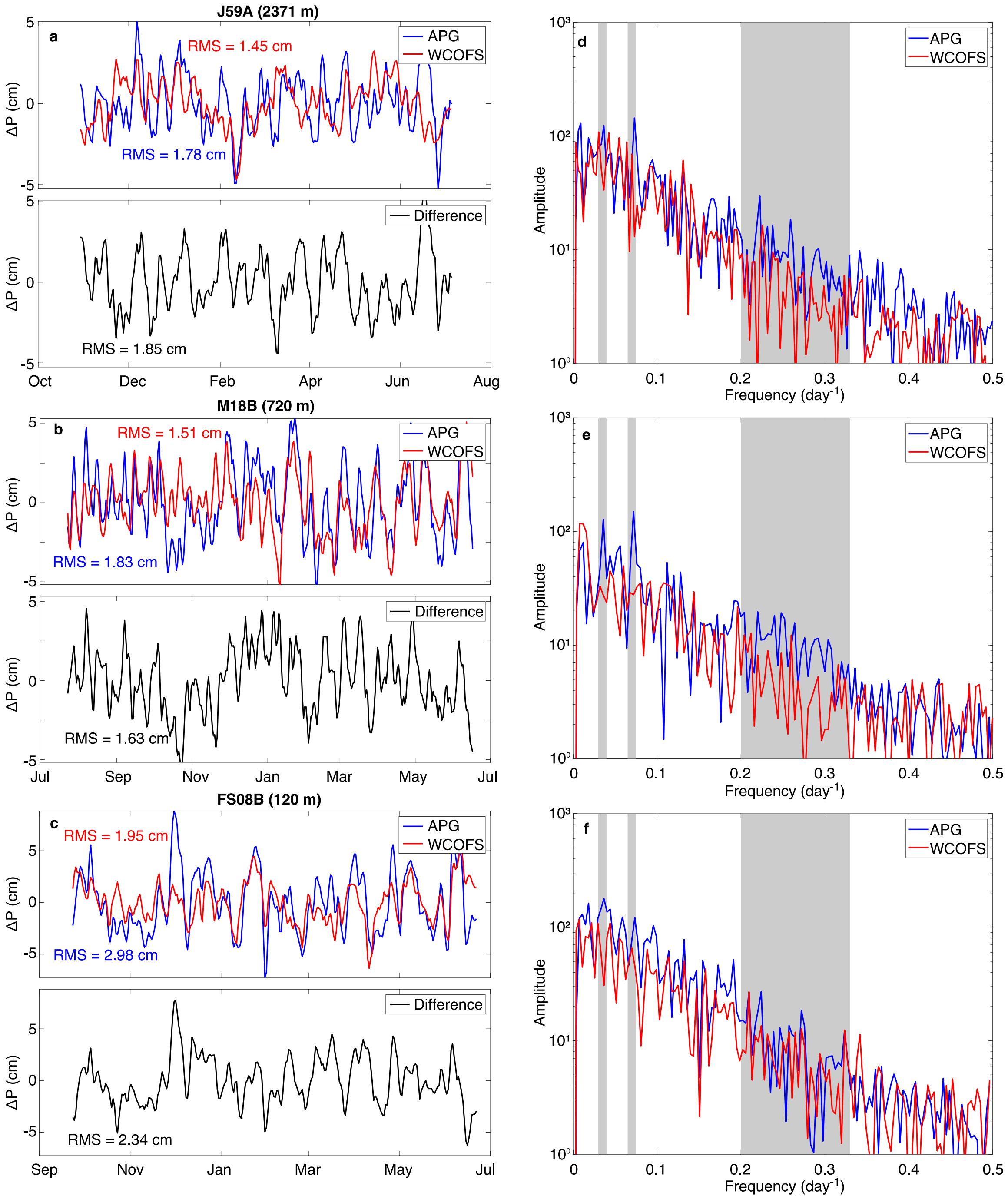

Figure 2.7 Comparison of APG data and modeled bottom pressure for the 2012-2013 year at select locations. (a-c) Pressure time series (top panel) and differences (bottom panel) for the data and WCOFS model for continental shelf, slope, and abyssal plain locations. (d-f) Amplitude spectra of the time series at the same locations. Grayed areas indicate frequencies of 0.07, 0.035, and 0.2-0.33 day^{-1}, where APG amplitudes are consistently larger than predicted by the model.

Example pressure time series differences predicted by the WCOFS oceanographic model are shown in Figure 2.4 (red curve in lower panels) for the same locations as the observations and have a very similar character and RMS as the observed differences. These modeled difference RMS values are given for all of the station pairs in Tables 2.2 and A1.1. Differences obtained from model-corrected observations, wherein the model is subtracted from the observation, are plotted in the blue curves of the lower panels of Figure 2.4 and the difference RMS are also reported in Tables 2.2 and A1.1. Applying the model as a correction to the data does not significantly change the RMS of the differences, consistent with the results of Muramoto et al. (2019), who found the variance reduction from subtraction of a barotropic model to generally be less than that achieved through reference station differencing.

The models best predict signals on or near the continental shelf, where R^2 values (equation 1) of the fit to the pressure time series are as high as 0.6 (Figure 2.8a). The models have a poorer fit in mid to lower continental slope and abyssal plain locations, with generally negative R^2 values. Despite the better predictability at shallow locations, those locations are left with larger RMS than the more poorly-predicted deep locations (Figure 2.8b) when model-corrected because of the significantly larger amplitudes of pressure signals in shallow water.

The circulation models capture a significant portion of localized oceanographic processes and may therefore be used to better understand those processes. We assessed the signal similarity between locations, and thereby the effectiveness of differencing, by selecting grid points within the model domains and differencing their predicted pressure time series against those of all other grid points in the domain, then calculating the RMS of the differenced signals. Results of this analysis are shown in Figure 2.6b-d, where difference RMS are contoured for reference locations on the abyssal plain, continental slope, and continental shelf in the WCOFS model. The oceanographic models suggest broadly similar oceanographic characteristics along isobaths, within 0.5 cm RMS over 100s of kilometers, while RMS changes rapidly across isobaths, as seen most clearly on the upper slope and shelf. These characteristics of the oceanographic models mirror those seen in the APG dataset, suggesting that the models accurately predict the regionality of seafloor pressure signals and their comparability between locations. To directly compare APG observations and model output, we contour modeled difference RMS against depth difference and separation for a sample location within each of the depth bins in Figure 2.5. This shows that the model predicts a lower RMS is achievable over greater separation and depth difference than seen in the observations, which is unsurprising given that the model underpredicts signal amplitudes and is missing certain spectral content.

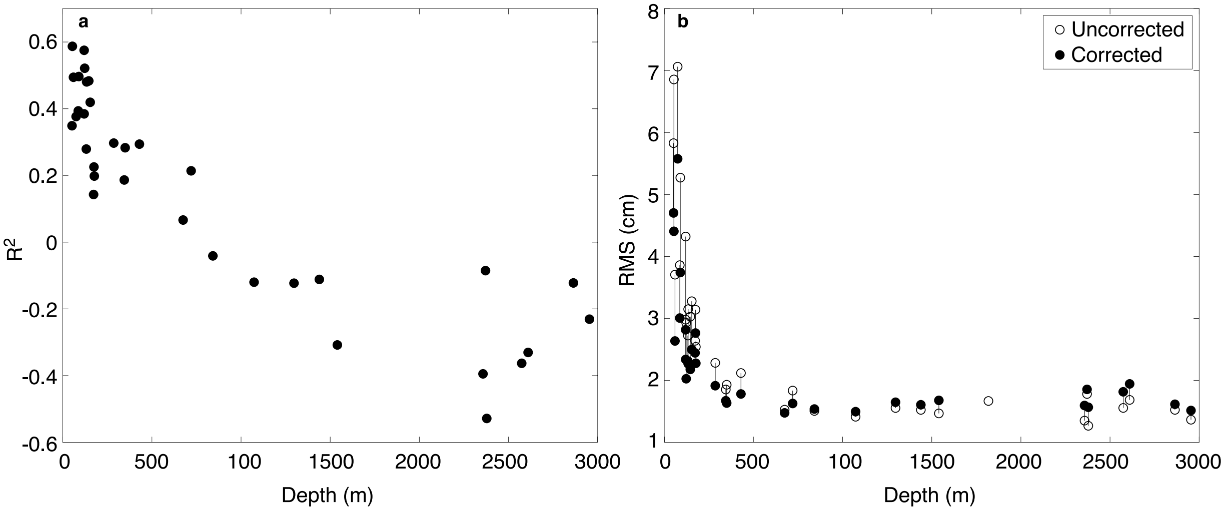

Figure 2.8 (a) R^2 of the fit of the 2011-2013 WCOFS modeled bottom pressure to the observed APG data as a function of instrument depth. A positive R^2 signifies that variance is reduced by differencing, while a negative R^2 signifies that variance is increased. (b) Comparison of RMS versus depth of APG pressure time series before (open circles) and after (filled circles) correcting with the WCOFS model, as a function of instrument depth.

2.3.3 Slow slip earthquake deformation modeling

Our base model emulates the characteristics of shallow SSEs from Hikurangi and the Japan Trench. The parameters for this model and the variations we explore are presented in Table 2.1. The Mw 6.4, $\Delta\sigma_E = 0.057$ MPa base model (Figures 2.3 and 2.9a), with 32 cm peak slip centered 72 km offshore from the coastline at 8 km depth below the seafloor, results in two lobes of vertical seafloor deformation: a trenchward zone of up to 5.5 cm uplift and a landward zone of up to 4.1 cm subsidence, with a total area of deformation greater than ±1.5 cm of approximately 4000 km^2. This two-lobed deformation pattern is found in all our models, with the subsidence lobe consistently smaller in both area and amplitude. As a whole, the region of deformation scales with the dimensions of the slip patch; deformation does not extend much beyond the along-strike limits of slip but the combined deformational area does extend tens of kilometers beyond the up- and down-dip extent of slip.

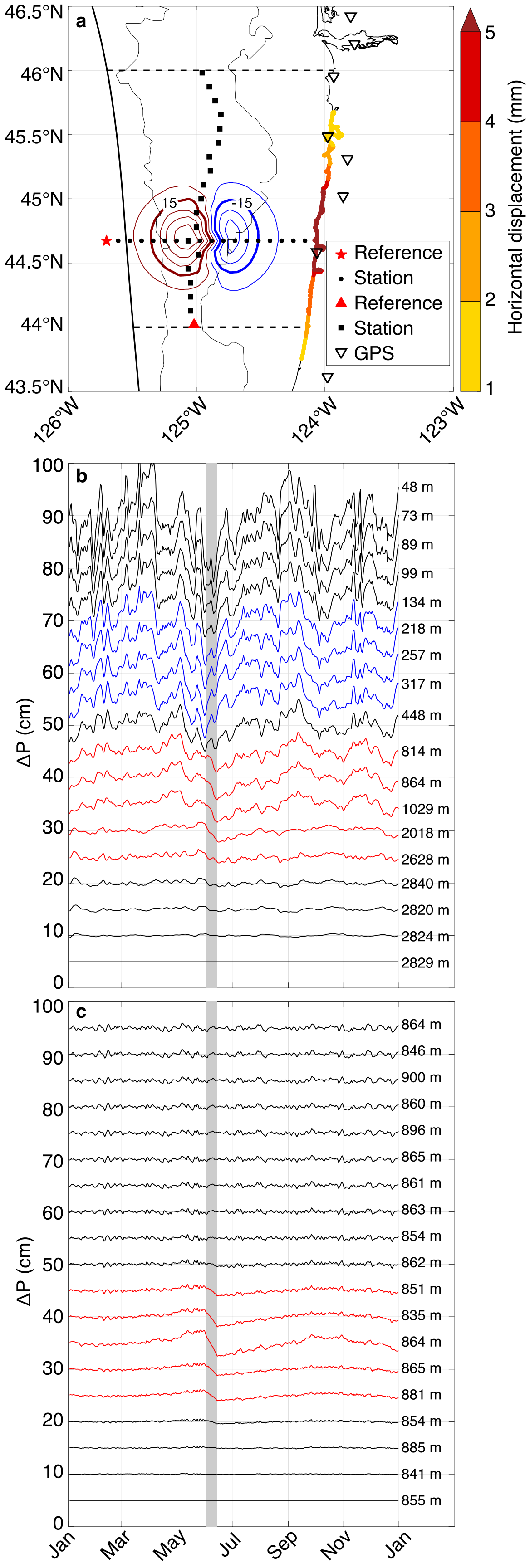
a
46.5°N
46°N
45.5°N
45°N
44.5°N
44°N
43.5°N
126°W
125°W
124°W
123°W
15
-15
★ Reference
• Station
▲ Reference
■ Station
▽ GPS
Horizontal displacement (mm)
1
2
3
4
5
b
ΔP (cm)
100
90
80
70
60
50
40
30
20
10
0
48 m
73 m
89 m
99 m
134 m
218 m
257 m
317 m
448 m
814 m
864 m
1029 m
2018 m
2628 m
2840 m
2820 m
2824 m
2829 m
c
ΔP (cm)
864 m
846 m
900 m
860 m
896 m
865 m
861 m
863 m
854 m
862 m
851 m
835 m
864 m
865 m
881 m
854 m
885 m
841 m
855 m
Jan
Mar
May
Jul
Sep
Nov
Jan

Figure 2.9 Synthetic SSE modeling results for our base model, a mid-slope M_w 6.4 event of two-week duration, beginning on 1 June 2013. (a) Contours of seafloor deformation beginning at 5 mm with an interval of 10 mm on a regional map, overlain with modeled stations (squares and circles) running through the site of peak deformation and reference locations for subsequent differencing plots. Bold contours indicate vertical deformation of ±15 mm. Instrument spacing is 12 km along isobaths and 10 km across isobaths. Coastal and near-coast GPS instrument locations are labeled as inverted triangles and modeled horizontal deformation is color coded at the coastline. Bold black lines show the trench and coastline, thin black lines show 300 m and 2000 m isobaths, and the partially-locked Oregon region is demarked by the dashed lines. (b) Time series plots of modeled seafloor pressure differences of the strike-perpendicular station locations, relative to the red star location in (a). Differences from the stations overlying the uplift lobe (>15 mm) are displayed in red while those overlying the subsidence lobe (<-15 mm) are displayed in blue. (c) Time series as in (b) but for the depth-matched stations and red triangle reference location. Time series are offset for display purposes and station depths are indicated next to each.

We assessed the detectability of our models by generating two idealized lines of stations, with pressure time series extracted from the LiveOcean model, from which to detect the SSE: one running roughly perpendicular to strike with 10 km spacing and the other running roughly parallel to strike along a contour of constant depth with 12 km spacing (Figure 2.9a). The modeled deformation at each station location was added linearly to that station's modeled pressure over the event duration of 14 days. Both lines pass through the point of maximum uplift and each station was differenced against a reference station at the end of its respective line. In the case of the depth-matched station line, the reference location was sometimes moved from one end of the line to the other, to avoid overlapping the deformation region. In the differences, uplift results in a decrease in pressure and is expressed as a negative offset, while subsidence is expressed as a positive offset. For both lines, the uplift signal is clearly visible above the noise in the difference time series (Figure 2.9b-c). This is especially true for the depth-matched station line, for which oceanographic noise has been largely eliminated. Subsidence signals are more difficult to detect in the strike-perpendicular line, as they occur high on the continental slope and on the shelf, where oceanographic noise is high and dissimilar to that of the reference station on the abyssal plain. Changing the onset time of slip to coincide with an oceanographic signal of opposite sign (Figure A1.5) obscures deformation in the strike-perpendicular line for all but one record and illustrates the utility of depth-matched differencing. Extending the duration of slip to 30 days (Figure A1.6) makes deformation more closely resemble an oceanographic signal and is more susceptible to partial removal by a polynomial correction, again illustrating the importance of the noise-reduction obtained by our method.

Figure 2.10a shows the modeled deformation that results from an event of the same magnitude and stress drop as the base SSE, shifted updip so as to occur adjacent to the trench, with 28 cm peak slip centered 100 km offshore at 5 km depth below the seafloor. This shift results in both deformation lobes similarly shifting to deeper waters, which provides a more uniform oceanographic setting for the uplift lobe, which is easily identified on difference plots for either station line (Figure 2.10b-c). Much of the subsidence lobe, including the site of peak negative deformation, is still on the mid to upper slope and so these signals are not readily distinguished in the strike-perpendicular line, given the significant residual noise in the differences. Moving slip downdip, with 31 cm peak slip centered 58 km offshore at 10 km depth below the seafloor (Figure A1.7), shifts deformation into shallower waters, in which larger oceanographic signals obscure deformation on the strike-perpendicular line for both uplift and subsidence lobes. In both the updip and downdip scenarios, deformation is clearly identifiable on the depth-matched line.

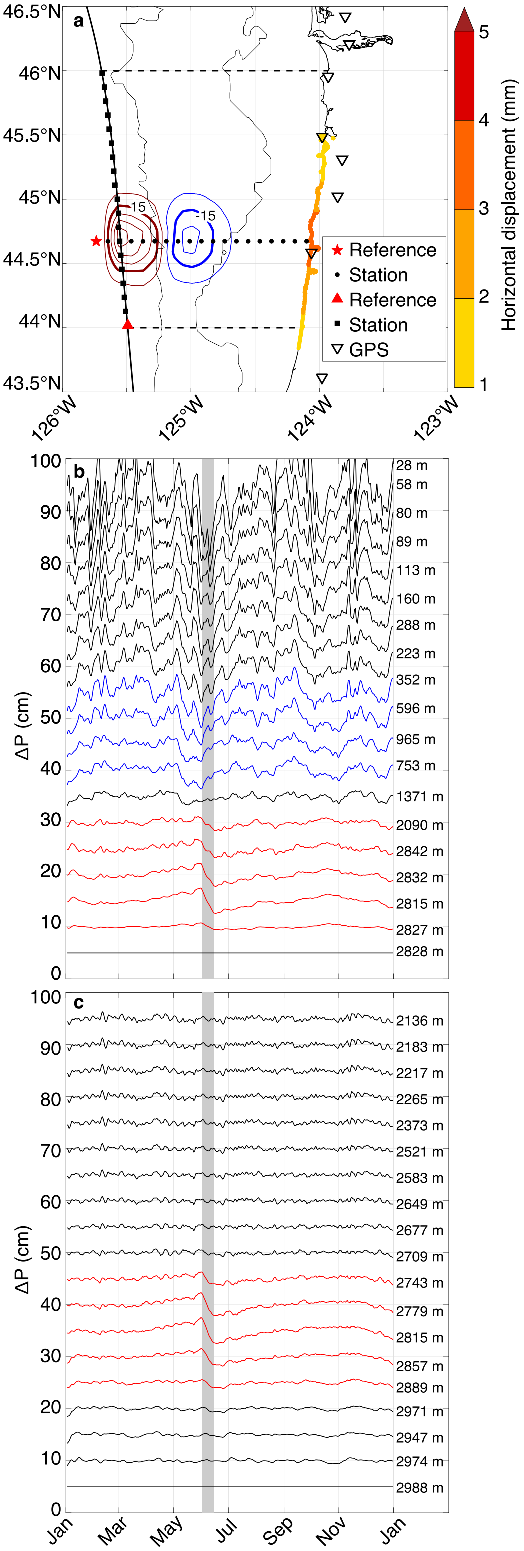

Figure 2.10 As in Figure 2.9, but for a trench-adjacent SSE. Note that deformation occurs on the incoming plate due to the 3 km of sediment cover above the updip terminus of our modeled plate interface.

Another model variation held the magnitude of the SSE constant and reduced the stress drop to $\Delta\sigma_E = 0.014$ MPa (Figure 2.11a). This corresponds to $\Delta\sigma_M = 0.010$ Mpa, the lower limit of stress drop scaling for SSEs reported by Gao et al. (2012). We accomplished this by increasing the along-strike halfwidth of our Gaussian from 19 km to 58 km, holding the up-and down-dip extent of the fault patch constant, and decreasing the peak slip to 11 cm. The resulting deformational pattern is elongated along-strike, with decreased amplitudes in both positive and negative lobes and a significant region of non-detectable deformation between lobes. The area of uplift >1.5 cm is approximately 1400 km^2, while the area of subsidence >1.5 cm is approximately 350 km^2. For the strike-perpendicular differences (Figure 2.11b), this deformation is too small to be distinguished from the oceanographic noise. For the depth-matched differences (Figure 2.11c), on the other hand, the signal is larger than the residual noise and is captured on a large number of stations, which would lend confidence that it is a real geophysical signal. We also increased the stress drop of the base model to $\Delta\sigma_E = 0.22$ Mpa (Figure A1.8), or $\Delta\sigma_M = 0.10$ MPa, the upper stress drop limit of Gao et al. (2012), by decreasing the along-strike halfwidth to 7.3 km and increasing the peak slip to 82 cm. This results in larger-amplitude deformation lobes, but with areas slightly smaller than those of the base model, with approximately 3000 km^2 of deformation greater than ±1.5 cm.

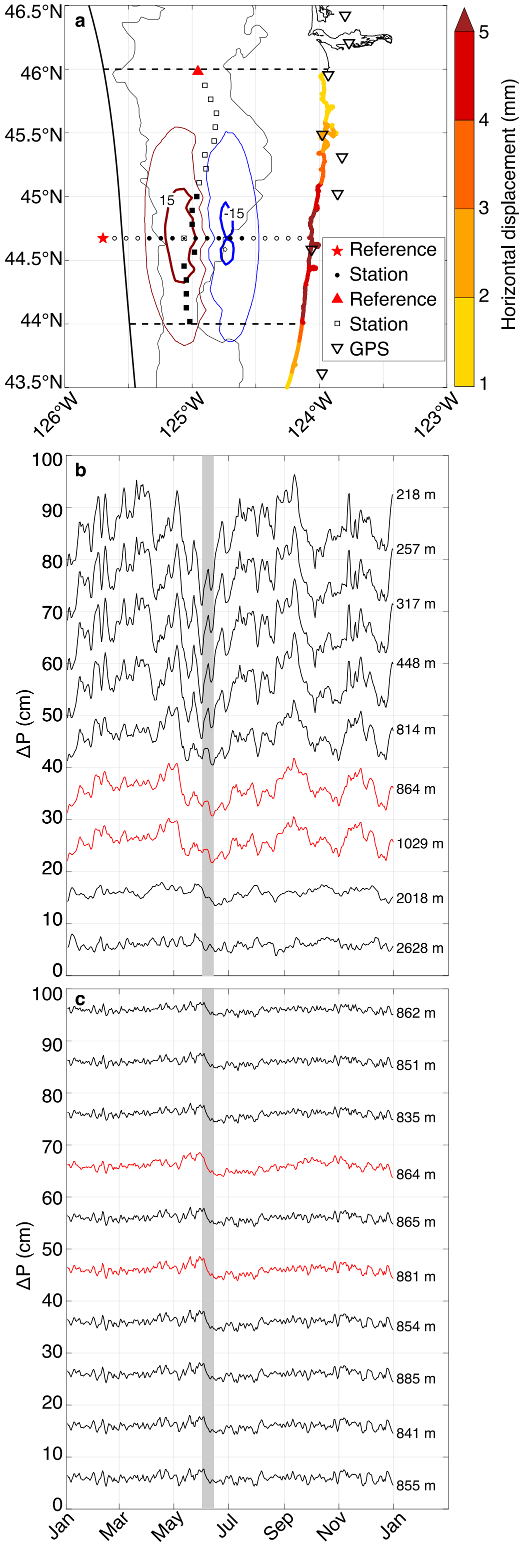

Figure 2.11 As in Figure 2.9, but for a SSE with a stress drop of $\Delta\sigma_E = 0.014$ MPa. Infilled station markers in (a) are those for which modeled pressure differences are shown in (b) and (c).

A low-magnitude model was also explored (Figure 2.12a) with M_w 5.9 and $\Delta\sigma_E = 0.022$ MPa by decreasing the along-strike halfwidth of our slip Gaussian to 17 km and the maximum slip to 9 cm. This leads to a very small area of deformation on the seafloor, approximately 1 km^2 of >1.5 cm uplift and no subsidence >1.5 cm. The deformation is indistinguishable from oceanographic noise on the strike-perpendicular station line (Figure 2.12b) and is visible on only one station in the depth-matched line (Figure 2.12c) and thus, near the detection limit of our method. Another variation increased the magnitude to M_w 6.9 and $\Delta\sigma_E = 0.022$ MPa (Figure A1.9), near the upper limit of what has been observed in Cascadia deep SSEs (e.g. Hall et al., 2018), by increasing the along-strike halfwidth to 60 km and increasing the peak slip to 65 cm. This model has significantly increased area and amplitude of deformation greater than ±1.5 cm relative to the base model. Regardless, the strike-perpendicular line is still unable to clearly resolve the subsidence signal on and near the continental shelf.

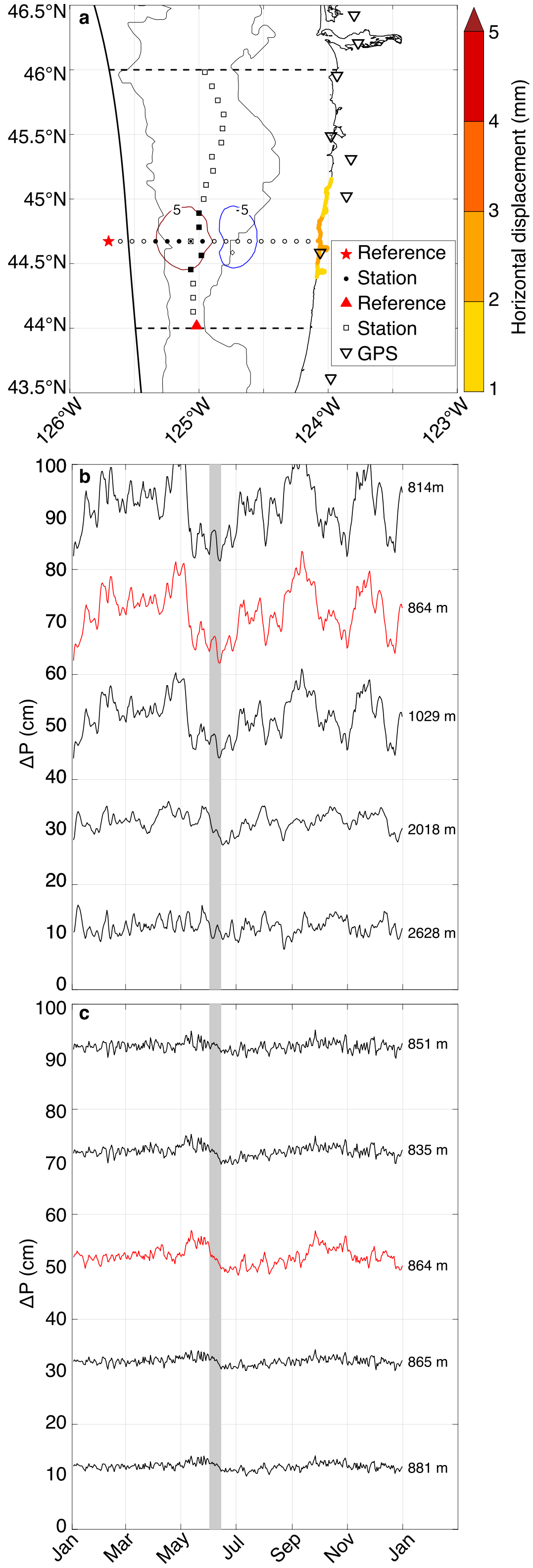

Figure 2.12 As in Figure 2.9, but for a Mw 5.9 SSE. Infilled station markers in (a) are those for which modeled pressure differences are shown in (b) and (c).

The stress drop range given by Gao et al. (2012) is derived from observations of deep SSEs in Cascadia and it is possible that shallow SSEs may have stress strops lower than $\Delta\sigma_M$ = 0.01 MPa, as suggested by the small amount of slip reported in the events of Araki et al. (2017). To this end, we model a near-trench M_w 6.2 SSE with maximum 4 cm slip and a stress drop of $\Delta\sigma_E$ = 0.006 MPa ($\Delta\sigma_M$ = 0.005 MPa; Figure A1.10a). Such an event produces no vertical deformation greater than 1.5 cm. Both station lines are effectively depth-matched over the small deformation area produced by this event, and in both sets of differences (Figure A1.10b-c) the uplift signal is of the same amplitude as the residual noise. Given that the synthetic time series come from the LiveOcean model, which does not contain the full complexity of the observational data (Figure 2.7), and that the deformation signal is comparable with the noise floor, this event is clearly below the detection limit of our method.

2.4 Discussion

2.4.1 Detection of slow slip events in observational data

In order to be confidently detected in the available APG data, a shallow SSE would need to 1) be concurrent and collocated with the sensor network, 2) be of sufficient geographic extent to cause deformation at more than one station, and 3) produce sufficient vertical seafloor displacement to be resolvable above the residual noise in the APG differences. Ideally, sensors would resolve both the trenchward uplift and shoreward subsidence signals, as their relative positions are diagnostic.

Under these qualifications, we found no evidence of a shallow SSE in the four years of our dataset. To our knowledge, there are no published reports of related activity recorded on CI seismometers or land-based instruments during this interval. While it is possible, perhaps likely, that no SSE comparable to those seen at Hikurangi and the Japan Trench occurred during the study period, we infer that the pressure data used in the study were insufficient to confidently identify such a SSE, should it have taken place. The CI APG network was not designed with the intention of measuring SSE deformation. Stations were clustered offshore Washington and California, where the subduction zone may not be slipping, according to current models of plate locking (Burgette et al., 2009; Schmalzle et al., 2014). Outside of these clusters, instruments were broadly spaced, and the deformation produced in any of our SSE modeling scenarios would not likely cover multiple instruments. Instruments also shifted between northern and southern domains between experiment years, so only about half of the margin was instrumented at any given time. Additionally, the sensitivity of the differencing method depends upon the availability of depth-matched stations for differencing, which were not consistently available. As shown in Figure 2.5 and Table 2.2, instruments below 1400 m depth can be effectively differenced to ≤1 cm RMS even in the absence of a closely depth-matched pair, but such instruments represent only some 35% of all instruments and have limited spatial coverage outside of the 2011-2012 year, while instruments shallower than 250 m require depth matching to avoid RMS as high as 5 cm. The OOI and Oregon benchmark instruments used to supplement these data help increase coverage near Oregon, but overlap in time with the CI data for only one year of the experiment.

Some oceanographic bottom pressure signals have timescales and amplitudes similar to those of SSE deformation. Such signals, if not properly corrected, have the potential to be misidentified as geophysical deformation. This is explored in Figure 2.13, for which the standard differencing technique using a reference instrument on the incoming plate (e.g. Wallace et al., 2016), is applied to a pressure record from 2014-2015 in Cascadia that has previously been speculated to have recorded a SSE transient signal (Bletery et al., 2017). A near-trench reference pressure record at 2908 m depth, presumed to have experienced little or no deformation, is fit with a third-order polynomial to remove instrument drift and act as the regional oceanographic correction. A pressure record from the upper plate, 62 km away at 136 m depth, presumed to have undergone deformation during a specific time, is detrended using three months of data prior to the event, meant to represent the linear component of the sensor drift. The two pressure records are then differenced (Figure 2.13a) and the offset due to deformation is determined by calculating the mean pressure before and after the event. This processing method produces an offset well above the noise. However, applying the same method to predicted pressures from the same locations in the LiveOcean model (Figure 2.13b), which contains no deformation signal, results in a comparable perceived offset. Conversely, when no assumptions are made about event timing and the same two instruments are both corrected with polynomials then differenced (Figure 2.13c), the offset between the same time intervals is well below the residual noise. Comparing the pressure time series to wind and wave hindcasts from NOAA's Wavewatch III (Tolman, 2009) reveals a significant change in these surface observables concurrent with the perceived SSE (Figure 2.13d), suggesting that storm events can generate seafloor pressure signals that may easily be mistaken for geophysical deformation due to their similar amplitude and duration. Further, these storm signals can be seen over large areas and across multiple sensors, with varying amplitudes, again resembling qualities of a SSE. However, Figure 2.13 also shows that these storm signals are present in the oceanographic models and in observations of sea surface conditions, so by examining these data false detection of SSEs can be minimized.

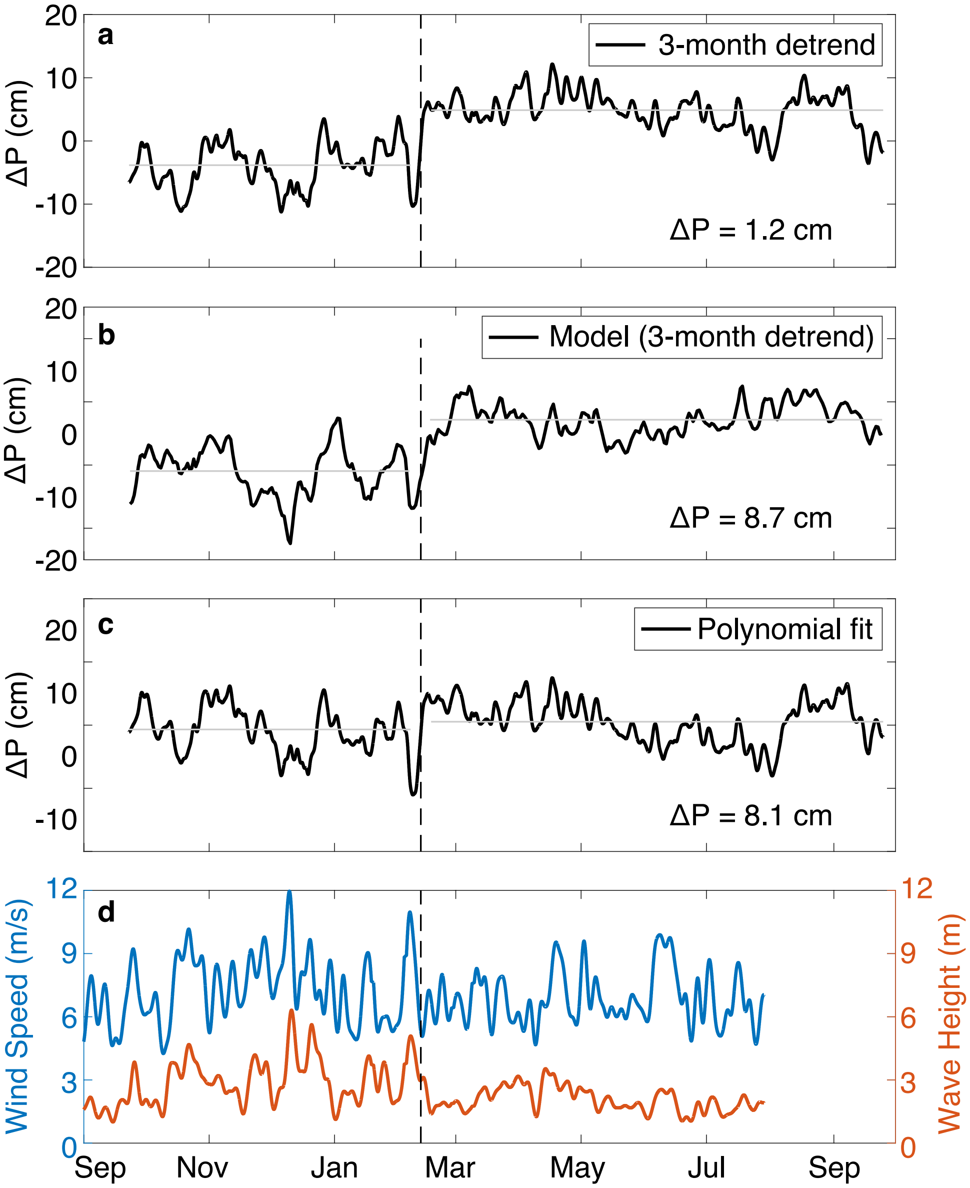

Figure 2.13 Example of the standard differencing technique producing a significant false SSE detection between instruments J25D and MJ01A from the 2014-2015 year (locations shown in Figure 2.2c). The dashed vertical line indicates the perceived onset time of the SSE. The horizontal gray lines mark the average pressure before and after the event, with the difference between these given in the bottom right of each figure. (a) The difference time series using polynomial-corrected pressure records. (b) The difference time series from applying a polynomial correction to the reference station and detrending the second station using the linear fit to only the three months of data preceding the presumed SSE (Wallace et al., 2016). (c) Recreation of (b) using the LiveOcean model in place of APG records. (d) Hindcast wind speed and wave height from NOAA Wavewatch III (Tolman, 2009) during the same time interval, low-pass filtered (0.2 day^{-1} cutoff) to emphasize long-period signals.

2.4.2 Oceanographic signal reduction in seafloor pressure data

Although the oceanographic circulation models reproduce much of the fluctuations in observed seafloor pressure time series, they are not sufficiently accurate at this time to act as a correction for oceanographic signals on observational data, consistent with the results of Muramoto et al. (2019). The largest disagreement occurs at periods of 14 and 27 days, which closely match the spring-neap tidal cycle and the anomalistic month, the period over which the moon goes from apogee to apogee. Both cycles modulate tidal amplitudes at these periods, possibly in part in the form of internal tides generated outside of the model domains and not included in the boundary conditions. Comparisons of model and APG time series also show that pressures at deep locations are not predicted as well as pressures at shallow locations, particularly at periods of 3 to 5 days (Figure 2.7). This is not surprising, as the majority of the observations through which these models are validated are located on the continental shelf (Giddings et al., 2014; Kurapov et al., 2017) and shelf physics are more deterministic due to the heavy influence of sea surface forcings and bottom boundary dampening. At depth, unstable processes like mesoscale eddies and cuddies (California Undercurrent eddies) are proportionally larger contributors to circulation and energy transfer (e.g. Collins et al., 2004), making pressure inherently less predictable on the slope and abyssal plain. Given that these oceanographic models were not designed for calculating seafloor pressures, further studies are needed to understand how models could be optimized for this purpose, such as by accurately determining the physical properties of near-bottom waters and using available seafloor pressure data for validation.

Despite the differences between model and observation, amplitude and frequency characteristics are sufficiently similar to be used for studying the propagation and comparability of seafloor pressure between locations. The oceanographic models suggest that seafloor pressure differences with ≤1 cm RMS can be achieved between locations at the same depth separated by hundreds of kilometers, as demonstrated in Figures 2.5 and 2.6. The continuity in oceanographic seafloor pressure at constant depth is consistent with patterns identified by Hughes et al. (2018), who found seafloor pressure to closely reflect basin-scale circulation processes while being largely unaffected by mesoscale eddy effects that typically have significant impact on physical oceanographic observables. They additionally suggest that measurements of ocean bottom pressure, along with observations of bottom density and currents, could lead to improvements in models of global oceanographic processes. Such improvements could in turn improve the comparability between modeled and observed pressures as these models become closer approximations to the real ocean system.

Differencing of depth-matched instruments is highly effective at reducing the non-tidal oceanographic component of bottom pressure time series for any instrument depth. The degree to which low RMS can be maintained over increasing separation is a function of the depths of the stations being compared, as seen in Figure 2.5, Table 2.2, and Table A1.1, where the shallowest stations require the most similar depths. All of the 25 differences for instruments at depths greater than 1400 m (Figure 2.5a) have RMS < 1 cm, with a mean of 0.6 cm, at separations as large as 360 km and up to 1400 m depth difference. For instruments at 1400 m > depth > 500 m (Figure 2.5b), the differences restricted to a depth difference less than 456 m and separation less than 344 km have a mean RMS of 0.7 cm, with 6 of 7 having RMS < 1 cm. The mean depth difference for these restricted differences is 240 m and the mean separation is 164 km. For instruments at 500 m > depth > 250 m (Figure 2.5c), there are very few data points to draw from, with 5 of the 7 total differences coming from instruments separated by more than 150 km (Figure

2.5c). Of the remaining two differences, one at a depth difference of 64 m and separation of 146 km has an RMS of 0.9 cm while the other at a depth difference of 33 m and a separation of 71 km has an RMS of 1.1 cm. For instruments at 250 m > depth > 100 m (Figure 2.5d), the differences restricted to a depth difference less than 44 m and separation less than 106 km have a mean RMS of 1.0 cm, with 10 of 15 having RMS < 1 cm. The mean depth difference for these restricted differences is 19 m and the mean separation is 37 km. At instrument depth < 100 m, no differences yield RMS ≤1 cm (Figure 2.5e). Thus, Cascadia APG data provide evidence that at depths > 100 m distal locations at comparable depths experience highly similar pressure fluctuations, and suggest that effective differencing under our method does not act as a significant constraint on distance between instruments for a deployment.

Given the above relationships, we suggest the following restrictions on depth difference and separation to enable effective differencing to better than 1 cm RMS. Instruments at 250 m > depth > 100 m should be depth matched to within ~10 m and separated by less than ~100 km. There are limited data from instruments at 500 m > depth > 250 m, so conservatively these should also be depth matched to within ~10 m and separated by less than ~100 km. Instruments at 1400 m > depth > 500 m should be depth matched to within ~200 m and separated by less than ~200 km. Instruments deeper than 1400 m can differ in depth by ~1000 m and separated by ~300 km.

2.4.3 Idealized sensor geometry for slow slip detection off Oregon

The above difference relationships show that the standard differencing technique, which uses a reference station, or stations, on the incoming plate is effective at removing oceanographic noise only for other stations on the abyssal plain and lower continental slope. Moving up the slope and onto the shelf, the oceanographic signals vary too much between locations for differencing with an abyssal plain station to provide an accurate correction. This complication can be overcome by designing networks of depth-matched instruments over a range of depths so that all pressure data are paired with a suitable reference for correction. For such a network, we prescribe a 1.5 cm threshold for the unambiguous detection of deformation signals, based on the 49 depth- and range-restricted differences discussed above. For these data, a threshold of 1.5 cm represents >1.5 times the standard deviation for 86% of our depth- and separation-restricted differences. For 57% of these differences (predominantly instruments deeper than 500 m) this threshold is > 2 times the standard deviation, so our detection threshold for this network likely represents a conservative overestimation.

The region of Cascadia offshore central Oregon is a good location to search for shallow SSEs in Cascadia because the coupling offshore is inferred to be lower than for the rest of the subduction zone (Burgette et al., 2009; Schmalzle et al., 2014). For this reason, we use our geophysical modeling results to recommend an optimized station configuration for the detection of SSEs in this region. The geometry of any deployment is dependent upon the size of event that needs to be measured; smaller SSEs should occur frequently but produce less deformation while larger SSEs will produce more deformation but occur less often. Additionally, for a given moment release, a lower stress drop SSE produces smaller amplitude deformation and requires more sensitive observation, while a higher stress drop SSE has a smaller footprint and requires a denser network.

The base SSE model (Figure 2.9) produces absolute deformation greater than 1.5 cm of differential signal (combined uplift and subsidence lobes) in an approximate ellipsoid with a 65 km N-S axis and 66 km E-W axis, though there is a narrow, ~6 km, region between uplift and subsidence where non-resolvable deformation occurs. For such dimensions, instrument spacing of approximately 30 km is sufficient to ensure the identification of a significant deformation signal on more than one instrument. This spacing would serve as a bare minimum for detection but would not provide sufficient data points for a detailed slip inversion.

For the purpose of detecting a SSE off central Oregon comparable to our base model, we recommend 22 instruments in four depth-matched sets (Figure 2.14), which together ensure a resolvable signal on multiple instruments. Our geometry has 6 instruments just landward of the trench at 2000-3000 m, 7 on the lower slope at 1100-1600 m, 3 on the upper slope at 450-700 m, and 6 below the shelf break at 300 m. The shelf-break locations were selected to have precisely matched depths (readily achievable with current ship-based technologies), while the trench-adjacent stations, which require less restrictive depth matching, were instead chosen to parallel the trench of McCrory et al. (2012). The intermediate lines were similarly allowed to vary in depth, within the limits described in this work, and were selected to evenly fill the distance between the shallow and deep lines. Each set of instruments has 44 km N-S spacing, but the lines are staggered to minimize the gaps that would result from a regular grid. In Cascadia the distance between shelf break and trench varies with latitude, resulting in nearest-neighbor station spacing as small as 17.5 km and as large as 31 km, dense enough to pick up multiple resolvable signals, regardless of where the SSE should occur. The density of this recommended network also increases the likelihood of capturing the diagnostic relative positioning of uplift and subsidence. Such a geometry would also ensure that multiple instruments record resolvable deformation from a larger magnitude SSE (e.g. Figure A1.9) as well as for a high stress drop event, for which the area of deformation does not decrease significantly relative to the base model (e.g. Figure A1.8). To resolve deformation on multiple instruments during a low stress drop SSE (Figure 2.11), a denser E-W network would be required, on the order of 15 km spacing. This is because the areas of deformation greater than ±1.5 cm in the low stress drop model are significantly narrower, particularly the subsidence lobe, and there is a ~20 km region of non-resolvable deformation between uplift and subsidence lobes, resulting in a much narrower footprint overall for this event.

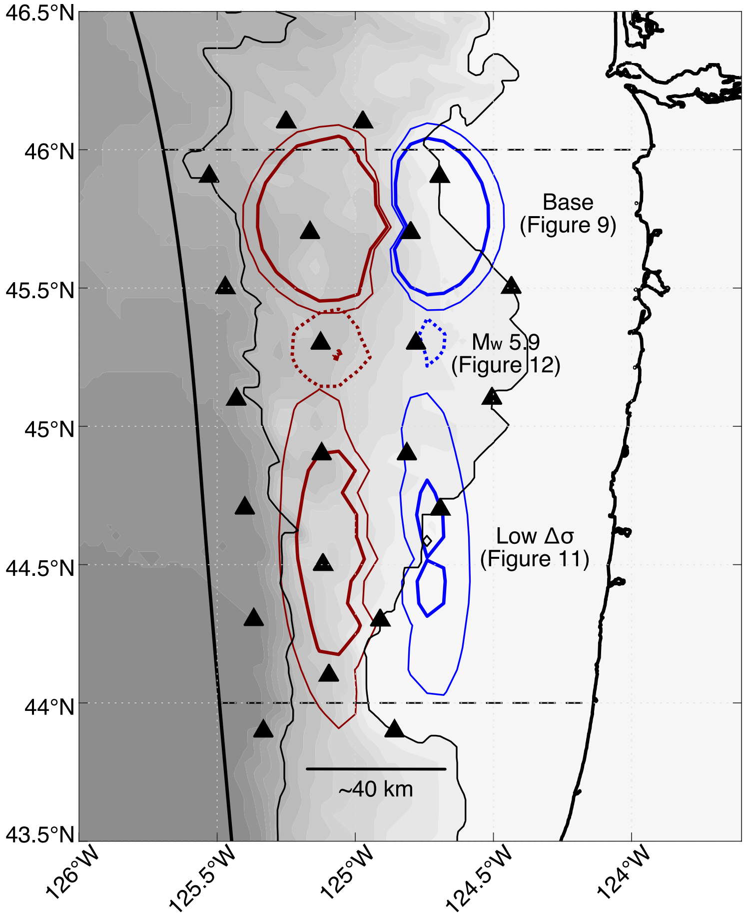

Figure 2.14 A possible configuration for an idealized APG network for detecting shallow SSEs offshore central Oregon. Bold black curves show the coastline and trench as per McCrory et al. (2012), fine lines show 300 m and 2000 m isobaths, and dashed horizontal lines demark the extent of the partially locked zone (Burgette et al., 2009; Schmalzle et al., 2014). The triangles indicate our recommended station locations. The vertical deformation from the base model (Figure 2.9) is shown by the solid ellipsoids in the north, the low-stress variation (Figure 2.11) is shown by the solid ellipsoids in the south, and the low M_w variation (Figure 2.12) is shown by the dashed ellipsoids. All have been offset from their modeled locations for display purposes. Thin ellipsoids contour 1 cm deformation, while bold ellipsoids contour 1.5 cm deformation, with red indicating uplift and blue indicating subsidence. Note that the low M_w model produces only a small region of 1.5 cm uplift and no region of 1.5 cm subsidence.

We view the network described here as the sparsest array that ensures resolvable deformation signals on multiple instruments for SSEs of Mw ≥ 6.4. Denser networks would allow for better characterization of the slip, at the cost of either a smaller instrumented area or the need for more instruments. However, the $\Delta\sigma_E = 0.014$ MPa (Figure 2.11) and M_w 5.9 (Figure 2.12) models suggest that increased density will not significantly aid the detection of lower-magnitude or lower-stress drop SSEs, as events smaller than these do not produce significant regions of ±1.5 cm vertical deformation (e.g. Figure A1.10). This scenario is demonstrative of the importance of further exploring the effectiveness of depth-matched differencing. If oceanographic noise can be reduced to allow a lower detection threshold of 1 cm, the area of resolvable deformation increases drastically, as shown in Figure 2.14. The oceanographic models, though they tend to underpredict signal amplitudes, suggest that difference RMS less than 0.5 cm can be achieved throughout the margin with sufficiently well-matched depths and the station spacing recommended here (Figure 2.5). Similarly, the APG differences reported in Tables 2.2 and A1.1 include a few difference RMS values ≤ 0.5 cm, though there are limited similar-depth, closely-spaced instruments from which to draw conclusions.

A sufficiently large offshore SSE, or one occurring sufficiently far downdip, will produce deformation resolvable on land-based GPS stations. GPS records of deep SSEs in Cascadia show that horizontal displacements of only a few mm are readily resolved at a single station (e.g. Rogers & Dragert, 2003; Szeliga et al., 2008), but these offsets are meaningfully interpreted only with concurrent signals on multiple instruments. The detectability of offshore slow slip on land-based systems is also inhibited by the increased noise levels and prevalence of anomalous signals at coastal GPS stations, effects infrequently discussed in the literature, particularly on horizontal components. However, Tian (2011) identifies anomalous horizontal signals in the Crustal Motion Observation Network of China and points to complex oceanic loading at coastal sites. Similarly, Nordman et al. (2015) generate models of non-tidal loading to explain anomalous horizontal signals on instruments bordering the Baltic Sea, on the order of a few mm, consistent with displacements calculated by Geng et al. (2012) for instruments bordering the North Sea during a large storm surge. Thus, we assume a detection threshold for horizontal displacement on a single coastal instrument to be ~4-5 mm, though even a large signal would be inherently uncertain if not corroborated by a concurrent measurement. There is also the issue of instrument density relative to expected coastal deformational areas, with spacing between coastal instruments ranging from 20-130 km (https://www.unavco.org/instrumentation/networks/map/map.html). Horizontal displacements decay rapidly inland, reaching near-zero values within <50 km, so only those instruments nearest the coastline would be expected to record resolvable deformation. Current interest in Earthquake Early Warning and tsunami modeling will likely lead to increased density of coastal GPS in the near future; under such conditions it becomes more likely for a SSE signal to be captured on multiple instruments and a detection threshold of ~2 mm is more reasonable.

For our base model M_w 6.4 event (Figure 2.9; peak slip 72 km offshore), coastal horizontal displacement > 4 mm (peak 9 mm) occurs over ~80 km N-S (Table 2.1). A similar event occurring downdip (Figure A1.8; peak slip 58 km offshore) of our base model produces coastal horizontal displacement > 4 mm (peak 17 mm) over ~100 km N-S, while a similar updip event (Figure 2.10; peak slip 100 km offshore) generates no coastal horizontal displacement > 4 mm (peak 3 mm). The low stress drop model ($\Delta\sigma_E$ = 0.014 MPa; Figure 2.11) produces coastal horizontal displacement >4 mm (peak 5 mm) over ~100 km N-S, and the high stress drop model

($\Delta\sigma_E$ = 0.217 MPa; Figure A1.8) produces <4 mm (peak 10 mm) over ~80 km N-S. The M_w 5.9 model (Figure 2.12) and $\Delta\sigma_E$ = 0.006 MPa model (Figure A1.10) produce a peak 2 mm and 1 mm coastal horizontal displacement, respectively. The M_w 6.9 model (Figure A1.9) produces coastal deformation >5 mm (peak 34 mm) over at least 280 km N-S. We would then expect the base, downdip, high and low stress drop models to produce a resolvable signal, should they occur at a similar latitude to a coastal GPS station. The M_w 6.9 model produces a resolvable GPS signal regardless of its latitude. The updip, Mw 5.9, and $\Delta\sigma_E$ = 0.006 MPa models are expected not to be detectable on coastal GPS alone. Thus, our models suggest that a combination of on- and offshore instrumentation is ideal for the detection of a M_w 6.4 or larger SSE. Further, these models show that any SSE that produces a significant region of resolvable deformation on the continental slope will also produce a resolvable signal on land, suggesting that, from a detection standpoint, it is not necessary to instrument the continental shelf with APGs for the purpose of detecting SSEs of this size. Under the assumption of increased coastal GPS density, all of our modeled SSEs except for the $\Delta\sigma_E$ = 0.006 MPa model produce horizontal deformation <2 mm over regions of 50 km N-S or greater and would therefore likely be detectable. Even so, offshore instrumentation would prove valuable in precisely locating and characterizing offshore SSEs to an extent not possible with the limited resolution of purely onshore measurements.

An idealized APG network also has a time-dependent component: the instruments must be active for a sufficient time for a SSE to occur. The M_w 6.4 base event modeled here is expected to recur at a minimum of approximately every 8.4 years, given its peak slip 32 cm, the local convergence rate offshore central Oregon of ~3.8 cm/yr, and assuming complete strain release by slow slip. This minimum recurrence interval decreases to ~7 years in the north of Cascadia and increases to ~10.5 years in the south. Our low stress drop model, with a peak slip of 11 cm, is expected to occur no more than every 2.9 years and requires nearly all of the partially locked Oregon segment to rupture. Similarly, lower magnitude SSEs may have lower recurrence intervals but will be more difficult to detect. In the absence of any information as to when and where the last SSE occurred, a decadal-scale instrumentation effort is necessary to determine if and where detectable shallow SSEs occur in Cascadia.

2.4.4 Slow slip detectability in the Cascadia Initiative experiment

The difficulty of detecting SSEs with the available seafloor pressure data is visualized in Figure 2.1. The resolvable deformation footprint for the base SSE model covers approximately 4000 km^2, which represents 15.1% of the approximately 26500 km^2 between trench and shore offshore central Oregon. The northern segment of this partially locked region was reasonably instrumented in 2011-2012 with 5 APGs, and in 2014-2015 3 APGs provided some coverage for the southern part of the region. This is far fewer instruments than our recommended geometry and the limited instruments present in a given year lacked proximal depth-matched instruments for eliminating oceanographic noise. The 8.4 year recurrence interval of the modeled SSE is longer than the 4-year observational period of the CI experiment and significantly longer than the ~1 year deployment period of a given sensor configuration, so it is unlikely that such an SSE would have occurred while instruments were in place to be able to measure it.

Offshore SSEs identified in other settings (Davis et al., 2015; Wallace et al., 2016) have typically had the advantage of previous datasets, such as onshore GPS or previously recorded tremor, guiding where to deploy instruments and when to look for subtle signals. The Cascadia Subduction Zone is characterized by a wide continental shelf and there are a wide range of SSE scenarios that would not produce resolvable horizontal deformation on coastal GPS instruments

(Table 2.1). In the absence of any data on shallow SSE occurrence, it is necessary in Cascadia to monitor the entire partially locked Oregon region, requiring a minimum of ~20 instruments deployed in a decadal scale experiment to observe a M_w 6.4 or greater event. This geometry could be expanded into a network spanning the entire subduction zone, with an emphasis on those regions with the least constrained locking, namely the northern-most and southern-most extents of the subduction zone (Schmalzle et al., 2014). Smaller SSEs could be detected with a denser array, but sufficiently small events do not produce any deformation greater than ±1.5 cm (Figure 2.12) and would therefore be difficult to detect without improvements in resolution.

2.5 Conclusions

We show that by utilizing depth-matched differencing, seafloor pressure records are a viable tool for detecting offshore SSEs in Cascadia of similar magnitude to what has been observed at subduction zones globally. Locations at depths from 100-250 m require very strict depth matching, within ~10 m, while deeper stations can vary on the order of 1000 m depth and still achieve significant reductions in RMS. The shallowest available data, though limited, suggest that ≤1 cm RMS cannot be achieved for locations at depths < 100 m. In all cases, the best RMS reduction is achieved by the closest depth matches over separations <100 km. It is important to test this method in other subduction zone settings, as varying modes of regional circulation may impact the efficacy of depth-matched differencing. Further, Cascadia is a relatively shallow system and we cannot distinguish if the degree of depth matching required is a function of total instrument depth or depth relative to the abyssal plain; it may be that Cascadia is a particularly difficult environment for differencing.

Oceanographic circulation models, though insufficiently accurate to act as a direct correction to pressure records, contain a significant portion of the measured oceanographic signal and are important for understanding the continuity of these pressure signals through the region. These models support the depth difference and separation relationships seen in the APG data, tending to underpredict difference RMS. Because of the temporal heterogeneity of noise in even closely depth-matched differences (lower panels in Figure 2.4), there is the potential, in using APG data, for misidentifying oceanographic pressure signals as SSEs in the absence of redundant observation of deformation, as these signals manifest similarly in amplitude, duration, and spatial distribution (Figure 2.13). However, the largest of these such signals are predicted by the oceanographic models, which can be used to avoid their misidentification. As these models are improved in resolution and validation, they will become increasingly useful in assessing the comparability of bottom pressure between locations and may become practical for use as a correction to oceanographic pressure effects.

No offshore SSEs were found in the 4 years of the Cascadia Initiative experiment, supplemented by the OOI cabled instruments and an Oregon benchmark, but we determine that the configuration of these APGs was not optimized for the detection of seafloor deformation. A lack of depth-matched stations, the movement of instruments between experiment years, and the limited deployment timeframe restrict the utility of this experiment for SSE detection. Another disadvantage in this setting is that the width of the accretionary prism limits the detectability of offshore slow slip on land-based geodetic networks, so these networks cannot, at their current density, be used to guide seafloor deployments. As such, there is no evidence for an SSE comparable to those observed in Hikurangi and the Japan Trench during this study period.

Our SSE modeling efforts suggest that events with a magnitude comparable to those recorded in other offshore settings could be detected and characterized using 22 APGs arranged in four depth-matched sets, spaced evenly between the trench and shelf break, at 44 km N-S spacing. This is true across a broad range of possible stress drops. Such a system takes advantage of depth-matched instruments to reduce the oceanographic pressure signal to 1 cm RMS or less. Smaller magnitude SSEs could be detected by this system so long as they produce over 1.5 cm of vertical deformation across a region with dimensions on the order of 65 km. However, with decreasing magnitude, low stress drop events will cease to produce a resolvable signal while high stress drop events will produce resolvable signals only over increasingly small areas. A network capable of detecting small M_w and low stress drop SSEs is impractical unless the deformation detection threshold can be reduced to 1 cm or less. Our oceanographic models and limited depth-matched differences at separations <100 km suggest that this may be possible, but more observational data are needed to verify this. Even with a 1 cm SSE detection threshold, our modeled areas of significant deformation rapidly fall off with decreasing magnitude, so increasingly dense networks are needed to detect smaller events, which becomes impractical over a regional scale. Improved oceanographic models that more closely predict observed pressures would be valuable in determining the lowest achievable RMS through differencing and thereby determining the smallest possible detectable events using seafloor pressure.

Due to the long recurrence intervals of our modeled SSEs, a consequence of the local convergence rate, any observational network would require a decadal-scale monitoring effort to have a high likelihood of detecting an event. Such a long-term deployment has the added benefit of simplified drift, which becomes stable and linear after several months, allowing for better characterization of signals as non-instrumental. Additionally, our SSE modeling suggests that resolvable horizontal deformation may occur onshore over limited areas for various M_w>6.4 scenarios, so increasing the density of coastal GPS instruments would help better identify and characterize shallow SSEs in Cascadia. An increase in density would also lower the detection threshold, were a signal to be observed on multiple instruments, enabling the detection of smaller SSEs. The payoff for this observational endeavor would be significant, as the detection and characterization of shallow SSEs in Cascadia may lead to a better understanding of the mechanical properties of the plate boundary and the stress release process leading up to large magnitude megathrust earthquakes.

2.6 Acknowledgments

Cascadia Initiative APG data was made possible by the Ocean Bottom Seismograph Instrument Pool (OBSIP) (www.obsip.org) and acquired from the Incorporated Research Institutions for Seismology (IRIS) (www.iris.edu). Additional APG data came from the Ocean Observatories Initiative (OOI) Cabled Array (www.oceanobservatories.org/array/cabled-array). We thank Laura Wallace and an anonymous reviewer for inciteful reviews and Rose Wade and Christian Baillard for useful discussions on the analysis presented herein. This research was supported by NSF grant OCE1558477.

Chapter 3:

Slow Slip Detectability in Seafloor Pressure Records Offshore Alaska

Erik K. Fredrickson[1], Joan S. Gomberg[2], William S. D. Wilcock[1], Susan L. Hautala[1], Albert J. Hermann[3,4], H. Paul Johnson[1]

[1]School of Oceanography, University of Washington, Seattle, Washington, USA
[2]U.S. Geological Survey, Seattle, Washington, USA
[3]Joint Institute for the Study of the Atmosphere and Ocean, University of Washington, Seattle, Washington, USA
[4]NOAA Pacific Marine Environmental Laboratory, Seattle, Washington, USA

3.0 Abstract

In subduction zones worldwide, seafloor pressure data are used to observe tectonic deformation, particularly from megathrust earthquakes and slow slip events (SSEs). However, such measurements are also sensitive to oceanographic circulation-generated pressures over a range of frequencies that conflate with tectonic signals of interest. Using seafloor pressure and temperature data from the Alaska Amphibious Community Seismic Experiment, and sea surface height data from satellite altimetry, we evaluate the efficacy of various seasonal and oceanographic pressure signal proxy corrections and conduct synthetic tests to determine their impact on the timing and amplitude prediction of ramp-like signals typical of SSEs. We find that subtracting out the first mode of the complex empirical orthogonal functions of the pressure records on either the shelf or slope yields signal root-mean-square error (RMS) reductions up to 73% or 80%, respectively. Additional correction with proxies that exploit the depth-dependent spatial coherence of pressure records provides cumulative variance reductions up to 83% and 93%, respectively. Our detectability tests show that the timing and amplitude of synthetic SSE-like ramps can be well constrained for ramp amplitudes ≥4 cm on the shelf and ≥2 cm on the slope, using a fully automated detector. The principal limits on detectability are residual abrupt changes in pressure that occur as part of the transition to and from summer to winter conditions

but are not adequately characterized by our seasonal corrections, as well as the inability to properly account for instrumental drift, which is not readily separated from the seasonal signal.

3.1 Introduction

The world's largest faults, subduction zone plate-interfaces, are found mostly offshore. An increasing body of work has shown that the offshore segments of subduction faults slip both seismically in earthquakes and aseismically in transient slow slip events (SSEs) (Dixon et al., 2014; Ozawa et al., 2007; Radiguet et al., 2016; Ruiz et al., 2014; Vallée et al., 2013; Wallace & Beavan, 2010). In addition to adding to the global inventory of slow slip phenomena and understanding of their relation to tectonic environmental conditions, SSEs provide key constraints on slip that occurs as damaging earthquakes. Such implications have led to the increased use of absolute pressure gauges (APGs) to detect and measure vertical deformation caused by SSEs. However, a principal complication of these observations is that ocean circulation generates significant seafloor pressure signals that resemble, obscure, and/or interfere with potential geodetic signals. The need for approaches to reliably detect and characterize SSEs in seafloor pressure records motivates this study and others (Fredrickson et al., 2019; Gomberg et al., 2019; He et al., 2020; Inoue et al., 2021; Muramoto et al, 2019; Woods et al., 2020).

Here we focus on assessing the efficacy of various observational proxies to correct for the ocean circulation-generated component of bottom pressure, as quantified by variance reduction and by the ability to detect and characterize a suite of synthetic SSE deformation signals on a single station. We begin by providing a framework for our approach and noting that on the seafloor, APGs measure the change in the weight of the overlying water column that is due to changes in the sea surface height (SSH), water column density structure, and seafloor vertical position changes. In functional form, the measured seafloor pressure, *P,* may be considered as a linear combination of signals (e.g., Gomberg et al., 2019), denoted as:

$$P(x,t) = P_T + P_O + P_G + P_D + \varepsilon$$

in which all terms vary with location, *x,* and time, *t,* and represent pressure changes due to ocean and Earth tides (P_T), non-tidal ocean circulation (P_O), geodetic deformation (P_G), instrumental drift (P_D), and unmodeled signal (ε). Herein, we are concerned with isolating and reliably characterizing P_G, specifically for the case of offshore SSE deformation. A first-order functional representation of P_G is a ramp with amplitude of 1.5-6 hPa and rise-times of 1-4 weeks, observed over regions of 40-80 km diameter (Davis et al., 2015; Ito et al., 2013; Wallace et al., 2016), though only a limited number of offshore SSEs have been observed to date. 1 hPa is roughly equal to 1 cm of water column height, and herein we use cm.

P_T is the largest of the component terms in most observations, on the order of 10^2 cm and variable with location, but is readily removed with standard methods, including low-pass filtering or fitting with a tidal model (e.g. Foreman, et al., 2000; Polster et al., 2009). P_D for the most precise and widely used APGs is reasonably characterized as a combined exponential and linear trend (Polster et al., 2009) but both terms are unpredictable prior to deployment. P_D is typically accounted for by least-squares fitting with the assumed functional form, or by removing the first month(s) of data and assuming purely linear drift thereafter. Thus, this signal is particularly problematic for deployments with relatively short durations of months to a year, as is typical of most large-scale deployments to date (e.g., Barcheck et al., 2020; Todd et al., 2018; Toomey et al., 2014). P_O contains a complex suite of signals, with variations typically exceeding those of P_G, including seasonal variation, oscillatory effects such as seasonal fluctuations and weather band energy (periods of 5~14 days), and stochastic processes that include meso-scale eddies and coastal trapped waves (e.g., Hughes et al., 2018; Wang & Mooers, 1976). While oscillatory signals in P_O are theoretically distinguishable from the non-oscillatory P_G, even in the absence of any explicit knowledge of the local circulation, the typical limited duration of seafloor pressure time series complicates this distinction.

The traditional proxy for P_O is a reference pressure, P_{ref}, recorded close to the trench on the incoming plate and assumed to be representative of the network oceanographic pressure fluctuations and to contain no deformation signal. This proxy has been used in the Japan Trench by Ito et al. (2013) and in Hikurangi by Wallace et al. (2016) to identify SSE deformation signals. The assumptions inherent in P_{ref} are broadly consistent with the current state of knowledge of seafloor pressure from physical oceanography on the time-scales important to SSE detection. For example, Hughes et al. (2018) demonstrated with a global ocean model the coherence of seafloor pressure throughout the entire Atlantic basin at nominal continental slope depths of 100-3200 m. Additionally, for periods of several days to about two weeks, the ocean response is largely barotropic (i.e., depth-independent) with spatial coherence over 1000 km scales, reflecting the footprint of atmospheric forcing in the so-called "weather band" (Luther et al., 1990). Recent work in Cascadia and Hikurangi has demonstrated that P_{ref} has mixed effectiveness that depends on the network geometry and performs particularly poorly on the shelf (Fredrickson et al., 2019; Gomberg et al., 2019; Inoue et al., 2021).

Another proxy that also relies on the spatial coherence of the ocean-generated pressure field – in this case expected along-margin coherence (Hughes & Meredith, 2006) – uses a pressure record at a site far from the posited SSE deformation at approximately the same depth (i.e., 'depth-matched'), independently selected for each station. We refer to this proxy as P_{match}. This approach was suggested by Fredrickson et al. (2019) from work in Cascadia and confirmed to work well in Hikurangi by Inoue et al. (2021). Both studies demonstrated that for strict depth matching criteria (tens of meters) on the shelf and much more lenient matching on the lower slope and abyssal plain, P_{match} is capable of reducing signal root-mean-square error (RMS) amplitude to better than 1 cm, over station separations of hundreds of kilometers in Cascadia, and at least 80 km in Hikurangi where instruments were deployed over a much smaller region. Previously observed shallow SSEs (Araki et al., 2017; Ito et al., 2013; Wallace et al., 2016) and the forward modelling of Fredrickson et al. (2019) show that SSEs of Mw < 7.0 generally produce deformation fields with dimensions smaller than 100 km, and therefore P_{match} should be effective if it is selected from distances beyond likely SSE dimensions.

The spatial coherence of the seafloor pressure field may also be exploited using complex empirical orthogonal functions (CEOFs) (e.g., Thomson & Emery, 2014), which capture not only the synchronously coherent component of the pressure field, but also allow for propagating oceanographic signals; effectively a CEOF decomposition is a principal component analysis that allows for phase-shifts between input signals. CEOFs have previously been used in Cascadia to derive a correction for seasonal and non-seasonal P_O signals (Watts et al., 2021) and comparable principal component analysis has been used to analyze megathrust earthquake deformation recorded by bottom pressure sensors during the 2011 Tohoku-Oki event (Hino et al., 2014). In the context of this study, we refer to the 1st CEOF as a seasonal correction, but recognize that it captures higher frequency features as well. Herein, we derive CEOFs from a collection of contemporaneous seafloor pressure records and we can assume that oceanographic signals dominate the first mode because it captures the lowest frequency pattern that is shared among the greatest number of stations. CEOFs derived from combined records of pressure and other data types that are sensitive to the same oceanographic processes, or multivariate CEOFs, also may be used. The inclusion of additional data that are insensitive to geodetic deformation may reduce the potential for it to be represented in the CEOFs and eliminated when applied as a proxy.

Non-pressure observables measured on co-located sensors have been used as proxies for ocean pressures, and benefit from not relying on spatial coherence assumptions. Hydrostatic pressure at the seafloor is related to both sea surface height and integrated water column density variations, although information about the latter is typically limited to seafloor temperature. Baba et al. (2006), Gomberg et al. (2019), and Itoh et al. (2019) examined correlations between seafloor pressure and temperature in the Japan and Hikurangi subduction zones. Assuming a linear relationship between pressure and temperature fluctuations, as well as negligible influence on the temperature field by tectonic deformation, the proxy P_{temp} can be constructed from scaled and possibly time-lagged temperatures. Likewise, the correlation between SSH and bottom pressure is well-documented, particularly in shallow water (e.g., Siegismund et al., 2011), but to our knowledge this has never been used in the study of offshore tectonic processes. However, in deeper locations water column structure acts to compensate pressure perturbations caused by changing SSH (e.g., Dobashi & Inazu, 2021) and so we hypothesize P_{SSH} to be more effective on the shelf than on the slope and abyss. Similarly, previous studies (Dobashi & Inazu, 2021; Fredrickson et al., 2019; Inoue et al., 2021; Muramoto et al., 2019) have constructed proxies from collocated hindcasts of seafloor pressure from numerical models of oceanographic circulation but have shown that such simulations are not accurate enough to provide useful corrections.

In this study, we use observations from the Alaska margin to systematically compare pressure correction techniques for minimizing the instrumental and oceanographic components of *P(x,t)* in an oceanographically challenging setting and evaluate the detectability of synthetic single-station SSE signals in these corrected data. Although subtle evidence for a single SSE in the same pressure data has been reported by He et al. (2021), these pressure data are clearly dominated by oceanographic signals and thus suitable for a study that compares various techniques for assessing the detectability of synthetic signals for various processing approaches.

3.2 Geologic and Oceanographic Setting

This study focuses on the Alaska Peninsula Subduction Zone (Figure 3.1), where the Pacific Plate subducts beneath the North American Plate, which has historically hosted numerous large megathrust earthquakes. This region was the focus area for the 2018-2019 Alaska Amphibious Community Seismic Experiment (AACSE), which was aimed at understanding along-strike variability in geodetic and seismic deformation processes, through seismic and geodetic (APG) observation and subsurface structural imaging (Abers et al., 2019; Barcheck et al., 2020). Within this footprint, the region roughly between 158° and 161° W, known as the Shumagin gap, had not ruptured in a Mw > 8.0 earthquake within the period of instrumental records (Davies et al., 1981). The available onshore data suggest this segment is weakly locked and is presumed to accommodate a significant fraction of plate convergence aseismically, though resolution near the trench is poor (Fournier & Freymueller, 2007; Li & Freymueller, 2018). Recently, in July and October of 2020, the gap was partially ruptured by two $M_w>7.5$ earthquakes (Crowell & Melgar, 2020) and in July of 2021 a Mw 8.2 earthquake occurred just east of the gap, likely triggered by the previous year's events (Elliott, et al., 2021). Although this subduction zone has hosted several documented SSEs and tremor episodes down dip of the seismogenic zone (Brown et al., 2013; Li & Freymueller, 2018; Rousset et al., 2019), to date there is only limited evidence for SSEs within or updip of the seismogenic zone (He et al., 2021).

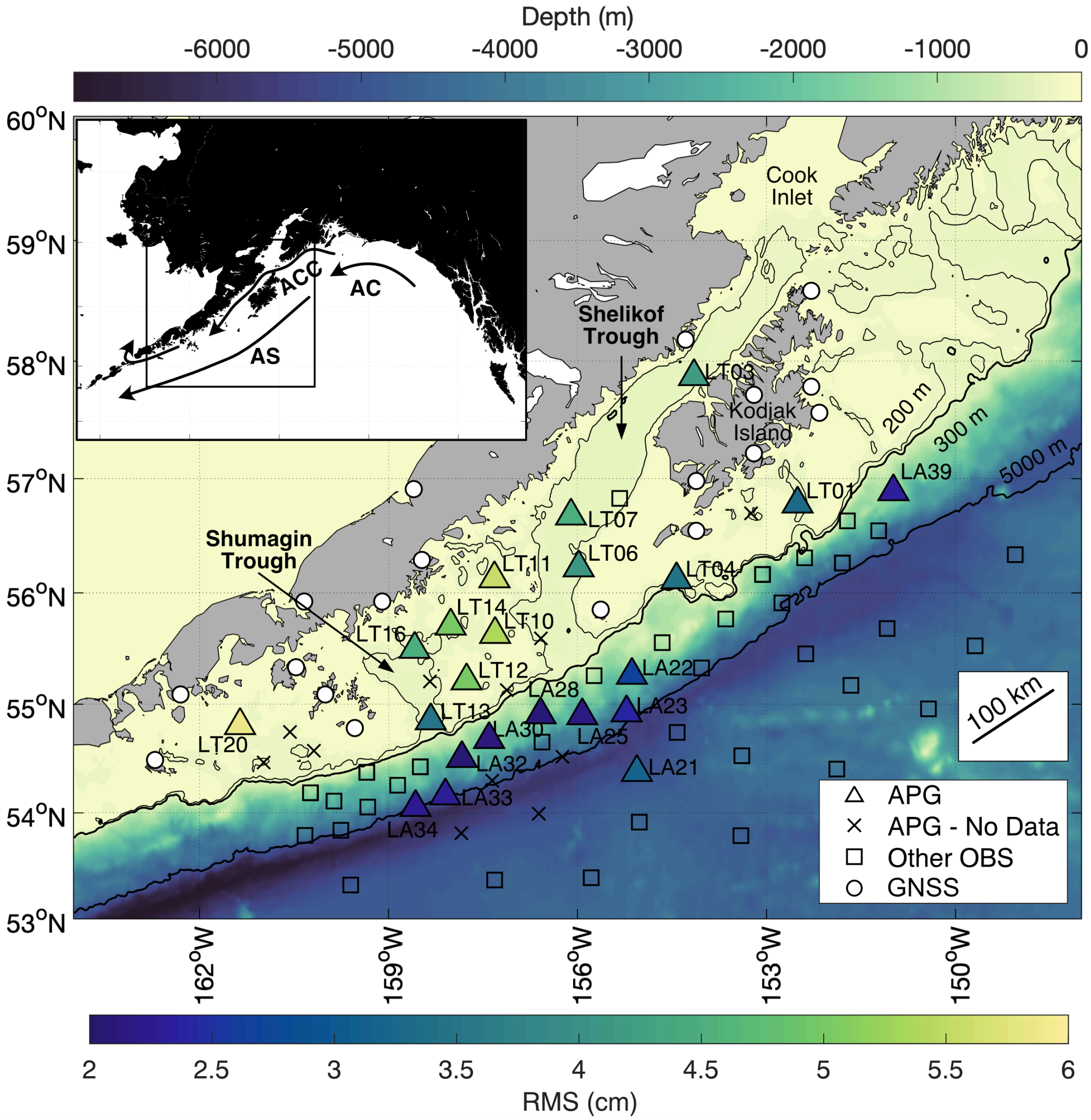

Figure 3.1 Map of the experiment area offshore the Alaska Peninsula. Filled triangles indicate the absolute pressure gauges (APGs) used in this study, colored by the RMS of their tidally filtered, drift corrected data. ‘X’ markers indicate APGs that did not return data. Square markers indicate other OBS from the AACSE in the region and circles indicate proximal GNSS stations active during the AACSE deployment. Bold depth contours at 300 m and 5000 m approximate the shelf break and trench, respectively. Inset shows broader geographic context and major circulation features. AC = Alaska Current. ACC = Alaska Coastal Current. AS = Alaska Stream.

In addition to the barotropic weather band response highlighted earlier, ocean circulation has a significant effect on seafloor pressure and here we summarize some of its distinguishing features offshore of Alaska. On a gross scale the circulation is dominated by the Alaska Current, a boundary current at the northern rim of the counterclockwise Pacific subarctic gyre (Figure 3.1 inset). Following the geography of the Alaska Peninsula, the Alaska Current narrows to ~50 km and strengthens, becoming a western boundary current: the Alaskan Stream. The Alaska Stream extends to depths >3000 m and flows southwest along the lower continental slope, overlying a deep northeastward current directly along the Alaska Trench (Warren & Owens, 1988). Changes in wind-forced subarctic Ekman pumping affect regional sea level patterns and the strength of the Alaska Stream (Capotondi et al., 2009), which is in geostrophic balance with the cross-stream pressure gradient – the along-stream pressure gradient being much weaker. Relatively strong mesoscale (~100 km) variability occurs, consistent with its dynamics as a western boundary current. These shifts in the intensity and location of the Alaskan Stream relative to the slope, on the timescales of several weeks to several months (Reed & Stabeno, 1989), are expected to lead to coherent pressure changes at the seafloor. This region is also characterized by coastally trapped waves that propagate southwestward along the slope associated with locally and remotely forced SSH variations on time scales ranging from weeks to years (Hermann et al., 2009) and that propagate pressure variations efficiently along isobaths. Thus, for a wide range of time scales relevant to the detection of SSEs, we expect pressure signals on the lower slope to show coherence along isobaths, as observed in Cascadia by Fredrickson et al. (2019) and in Hikurangi by Inoue et al. (2021). A large part of the mesoscale variability in the Alaskan Stream is due to baroclinic eddies propagating to the southwest at speeds of a few km/day (Ladd et al., 2014), which may interrupt along-slope coherence or introduce lags, although the depth of penetration of associated pressure anomalies is uncertain.

Ocean circulation on the shelf and coast is dominated by the Alaska Coastal Current but is less organized than further offshore, being affected by significant freshwater input, flows strongly steered by regional-scale bathymetric features, and wind forcing that can lead to daily-averaged surface currents that may exceed 100 cm/s (Stabeno et al., 2016a). Onshore/offshore Ekman transport that rapidly adjusts to changes in the along-shore wind leads to significant SSH changes over the shelf (Capotondi et al., 2009). All these factors lead to larger, less spatiotemporally coherent seafloor pressure variations and most geodetic studies elsewhere have simply avoided incorporating shelf observations. However, avoiding the shelf offshore of Alaska would make most of the AACSE's geodetic goals unachievable, given the ~150 km width of the shelf.

In summary, oceanographic signals related to both tidal and non-tidal processes are large offshore of the Alaska Peninsula. The array of non-tidal processes includes the high rate of meso-scale (~100 km diameter) eddies generated both locally and propagating in from the eastern Gulf of Alaska (Ladd et al., 2007; Reed & Stabeno, 1989), the presence of strong wind-driven boundary currents that extend over the shelf and continental slope (Stabeno et al., 2016b), complex bottom topography, strong storms, seasonal cycles (that tend to be stronger in the west), laterally meandering currents and eddies, upwelling and downwelling (Stabeno et al., 2004), the variable strength and cross-slope location of the Alaska Stream (Stabeno & Hristova, 2014), and abyssal boundary currents (Warren & Owens, 1988). Thus, we anticipate that oceanographic corrections for pressure geodesy may be particularly challenging in this setting.

At the same time, seafloor pressure observations are sparse, not just in Alaska but globally and extrapolation is limited by the immense range of spatial and temporal scales involved in ocean circulation (e.g., Wunsch, 2016). The circulation processes described above are expected to influence the bottom pressure field but have not been comprehensively studied or verified observationally, particularly those that have been invoked to affect pressure on the ~100 km scale.

Despite these challenges, our preliminary explorations indicate that regional ocean model hindcasts of the northern Gulf, forced with observed atmospheric conditions but assimilating no ocean data internally (e.g. Coyle et al. 2019, extended through the time period of this study), can faithfully reproduce some of the large-scale, wind-forced pressure variations associated with upwelling/downwelling and coastal-trapped wave signals on the shelf and upper slope. However, in the absence of dense oceanic data simulation, a much weaker correspondence with pressure variations is observed on the lower slope, partly due to the inevitable model/data mismatch in the timing and location of the (fundamentally chaotic, nonlinear) mesoscale eddies and current meanders – with ~100-km length and weekly to several month time scales – which populate the Alaskan Stream region. Further, even where greater correspondence is seen on the shelf, these model hindcasts do not capture a significant portion of the finer-scale spatiotemporal variability in the observational data.

3.3 Methods

3.3.1 Pressure, temperature, and altimetry data

The pressure and temperature data used in this study come from the offshore component of the AACSE (see Data Availability section), which included 75 ocean-bottom instrument packages deployed for 15 months from May 2018 through September 2019, roughly between Kodiak and the Shumagin Islands, from the near-shore out to the abyssal plain. 35 of the AACSE instruments were equipped with Paroscientific APGs, and of these 25 were recovered and yielded usable data for this study (Figure 3.1). Of these, three sensors stopped recording midway through the deployment and are excluded from this study for the sake of consistency between records in our analysis. Thus, we present pressure data from each of 9 slope sites (depth ≥ 1564 m), 12 shelf sites (depth ≤ 262 m), and 1 site on the incoming plate. Note that between network design and failed instrument recoveries, no seafloor data were available for this study for depths between 262–1564 m. A combination of Antares, Star-Oddi DST CTD, and HOBO TidbiT temperature loggers were attached externally to many of the AACSE instruments and returned data for all but two of the pressure-recording instruments used in this study. For these two instruments (LA21 and LA28), data from the internal temperature sensor of the Paroscientific APG were used instead. Time series of SSH were obtained for all station locations, compiled as a Jason-3 satellite product by the Copernicus Programme (Taburet et al., 2019; see Data Availability section). All data were truncated as necessary so that all time series were of the same duration, beginning on June 8, 2018, and ending on June 20, 2019, for a duration of 377 days.

As our interest lies in signals with periods of a few days or longer, we down-sample the pressure and temperature data to 1 sample/hour and apply a 24-24-25 Godin lowpass “tide-elimination” filter (Thomson & Emery, 2014). The SSH data are provided at a daily sample rate pre-corrected for tides. Throughout this study, we separate the data into shelf and slope groupings, based on the coherence of data in each that is apparent visually, and consistent with previous studies (e.g., Fredrickson et al., 2019; Wallace et al., 2016), water column dynamics (Hughes & Meredith, 2006), and corroborated in this study.

3.3.2 Corrections to remove non-tectonic long-period signals

The instrumental drift, P_D, is unique to each sensor and in some cases may be as large or larger than the seasonal variation. For all our analyses we solve for P_D using a least-squares inversion, linearized by solving repeatedly assuming exponential time constants ranging from 1 day to 6 months. Non-linear sensor drift was not generally apparent in the temperature data, evidenced by comparing temperature records from the sites with multiple different temperature sensor types, and only linear trends were fit and subtracted from them. We assumed there is no drift in the SSH data, which were also given only a linear correction. The tidally filtered, drift-corrected data are shown in Figure 3.2a-c for shelf instruments and in Figure 3.2d-f for slope and abyss instruments.

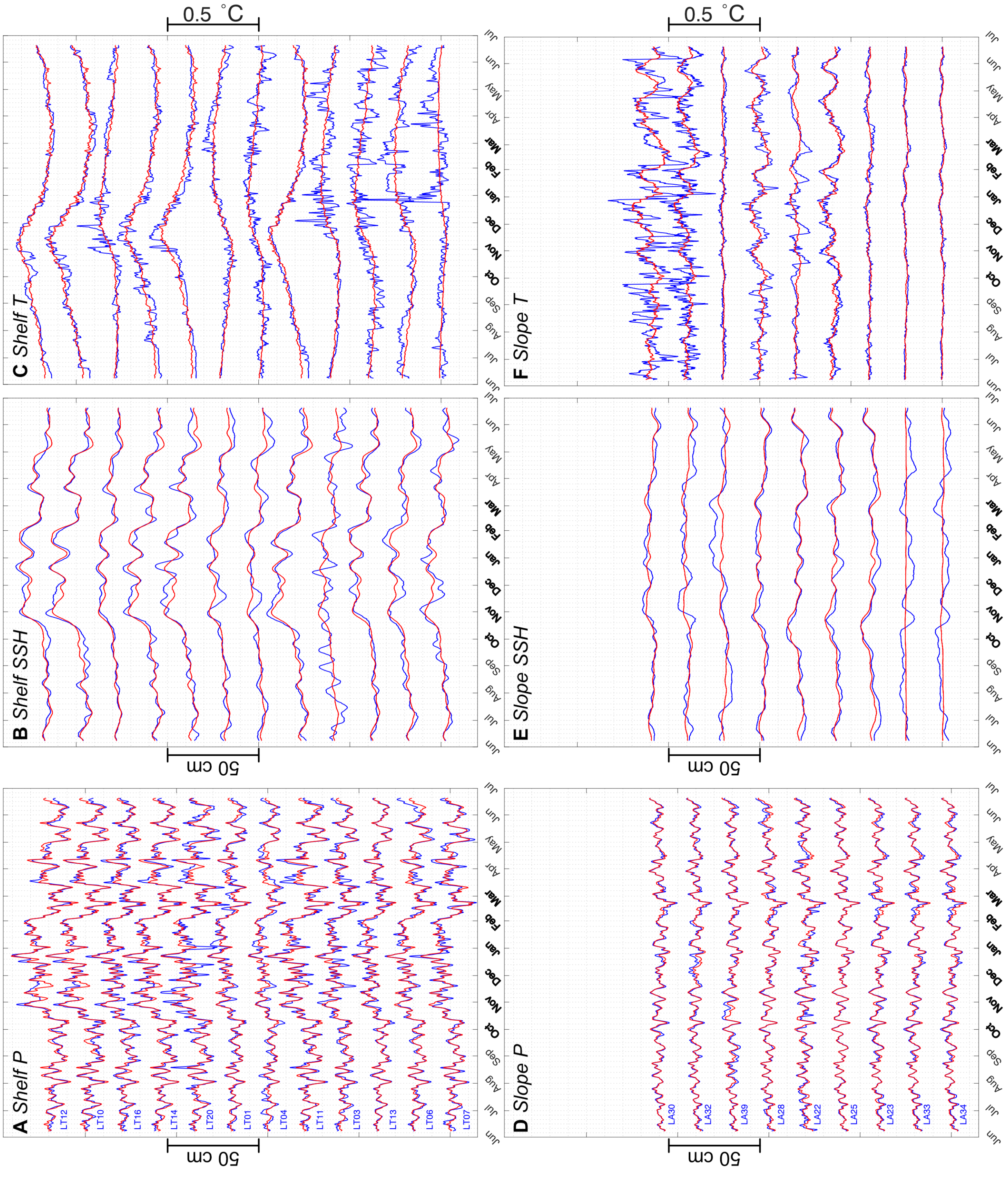

Figure 3.2 Time series of tidally filtered, drift corrected pressure, tidally filtered SSH, and tidally filtered temperature (blue), along with corresponding 1st pressure-, SSH-, and temperature-CEOFs (red), vertically offset with shallowest station at the top for display purposes. Winter months, when signals are anomalously large across observables, are labeled in bold. A) Shelf pressure. B) Shelf SSH. C) Shelf temperature. D) Slope pressure. E) Slope SSH. F) Slope temperature.

As seen in other studies, the AASCE data exhibit a spatially variable seasonal signal. This is a component of P_O but we treat it separately as part of our processing. This seasonal signal can obscure SSE deformation signals, if present, and we explored several methods for removing it. First, we tested fitting two separate functional forms, a sinusoid (365.25 day period) and a third order polynomial – conducting all analyses for both alternatives to assess robustness. Though there is inherent risk in aliasing and removing some of P_G with these functional-form corrections, the fits determined for the AACSE pressures are modest in amplitude so any such effect is expected to be small (Figure A2.1). The sinusoidally- and polynomially-corrected data exhibit variability in individual time series, but do not produce substantially different results in aggregate. So, in the main text we present and discuss only the sinusoidal results, while the polynomial equivalents are provided in the Supplementary Materials. A representative subset of the tidally filtered, drift- and sinusoidally-corrected pressure data from the shelf is shown in blue in Figure 3.3a, with all data shown in Figures A2.2a (shelf) and A2.3a (slope and abyss). We also tested using two forms of corrections calculated from CEOFs, which are the complex principal components of Hilbert transformed input data (see Thomson & Emery (2014) for details). One of these corrections is the 1st CEOF of the combined pressure data on either the shelf or slope, which we will refer to as the pressure-CEOF (p-CEOF). Similar CEOFs may be derived for the temperature or SSH data, and the 1st CEOFs for each data type are shown in red in Figure 3.2. As seen in the figure, the largest fluctuations in the 1st CEOFs are generally the seasonal fluctuations, but significant higher frequency content is also represented. The other correction considered is the 1st CEOF of the combined dataset of pressure, temperature, and SSH data, again for either the shelf or slope We refer to this as the multivariate-CEOF (m-CEOF) and we explore it because of the visually apparent, though complex relationships between the pressure, temperature, and SSH data. In either case, the CEOFs are sensitive to whatever signals contribute the greatest variance across all input data and thus are inherently insensitive to site-specific signals. In particular, incorporating P_G into the 1st CEOF is of the greatest concern for this study, but the dispersed network geometry and expected spatial scales of SSE deformation limit the possibility of capturing P_G on more than one or two sensors. Further mitigation is provided by the multivariate approach since deformation has no expression in temperature and SSH observations. Ultimately, the pressure-CEOF method outperformed the multivariate-CEOF method, so we present only the prior in the main text and show equivalent results for the latter in the Supplementary Materials (Figures A2.4, A2.6, and A2.8).

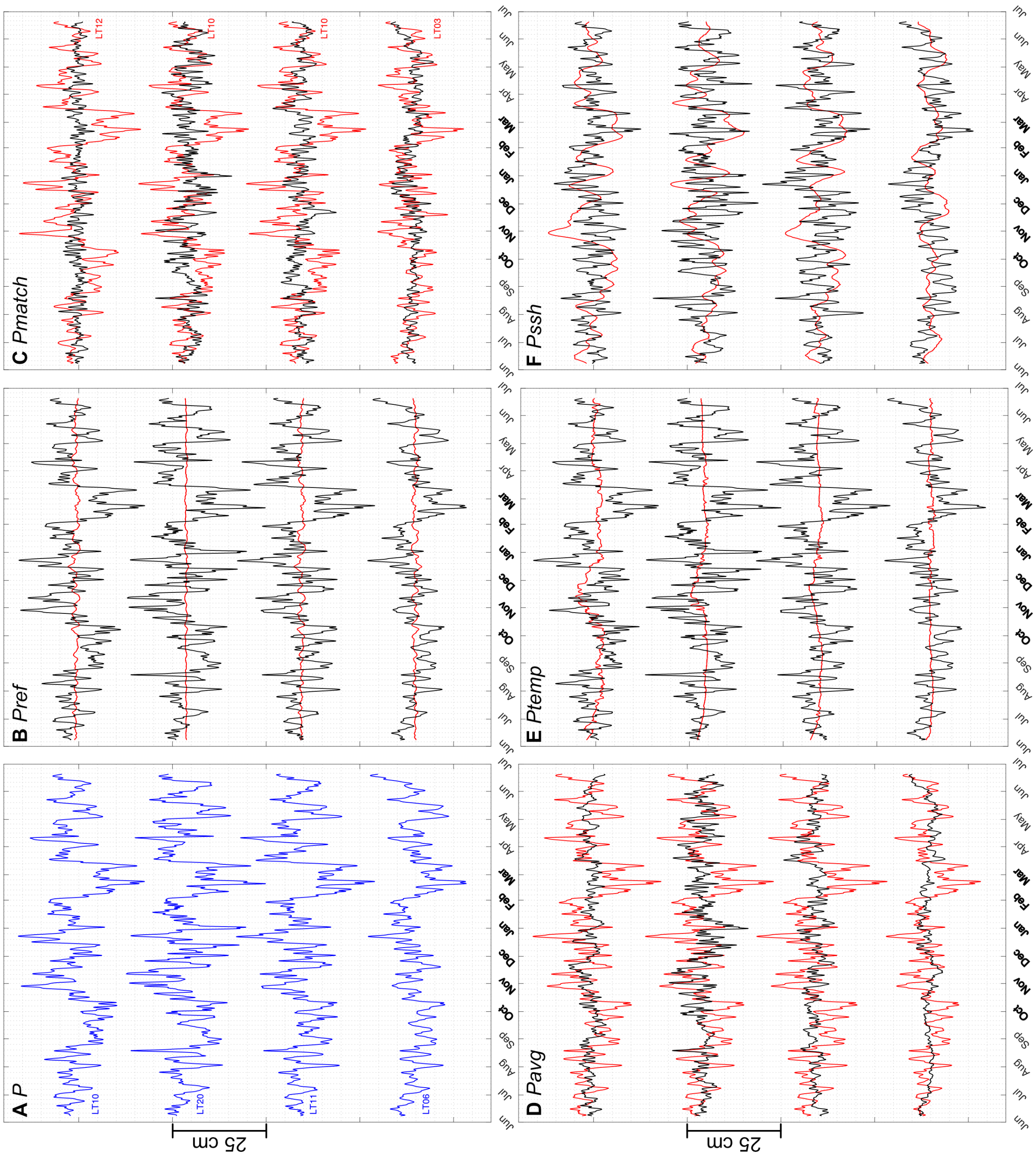

Figure 3.3 Time series of a representative subset of tidally filtered, drift and sinusoidal-corrected shelf pressure data (blue), scaled proxies (red), and proxy-corrected data (black), vertically offset with shallowest station at the top for display purposes. Winter months, when signals are anomalously large across observables, are labeled in bold. A) No proxy. B) Reference station pressure (P_{ref}). C) Depth-matched pressure (P_{match}), with matched station labeled in red text. D) Network average pressure (P_{avg}). E) Temperatures, lagged to maximize correlation (P_{temp}). F) Sea surface height (P_{SSH}).

3.3.3 Proxies for oceanographic pressure, P_O

We explored a range of proxies for correcting the non-seasonal components of P_O, the first class of which are those derived from observations of pressure at other locations. Such pressure-derived proxies assume that P_O is coherent over spatial scales at least the size of the network – or subnetwork – being considered. Further, to avoid removing any or all of P_G when the proxy is applied, the coherent region must be larger than the region affected by an SSE. Only a single APG, LT21, was placed seaward of the trench and is therefore used as the incoming plate reference pressure, P_{ref} for all other sites (red curves, Figures 3.3b, A2.2b and A2.3b). Depth match station pairs, P_{match} (red curves, Figures 3.3c, A2.2c and 3.3c), were determined empirically, choosing the proxy pressures yielding the smallest signal RMS and separated by >80 km where possible and >50 km otherwise (Tables A2.1 and A2.2 list pair RMS values), to avoid subtracting out any potential common P_G signal. Given the limitations of working with a network of finite size, there were inherently tradeoffs between optimizing depth differences and separations. Further, we chose to avoid repeat station pairs (e.g., LT04-LT01 and LT01-LT04) when a comparably effective station pair was available to demonstrate the robustness of the method. Finally, we use a sub-network average pressure, P_{avg}, which we derive by normalizing each pressure record by its RMS and calculating an average. Though no spatial limitations comparable to those of P_{match} were used in the calculation of P_{avg}, this method is inherently less susceptible to contamination by common Pg signals since it will be scaled by the number of stations and since the majority of the network falls outside any expected deformation area. A separate P_{avg} is calculated for each of the shelf and slope regions (red curves, Figures 3.3d, A2.2d and A2.3d).

The second class of proxies are derived from independent, collocated measurements of ocean properties that respond to the same forces that drive the pressure changes, or are driven by the pressure gradients themselves, but that are not affected by SSE deformation. These proxies are derived from bottom temperatures (P_{temp}, red curves, Figures 3.3e, A2.2e and A2.3e), and from SSH (P_{SSH}, red curves, Figures 3.3f, A2.2f and A2.3f) recorded at or above each instrument site.

All proxies are applied as corrections by scaling to achieve best fit and subtracting them from the pressure record of interest to achieve the lowest RMS difference. We justify this scaling even for the P_{ref} and P_{match} proxies since oceanographic pressure signals are known to scale with depth and may also be influenced by other local factors. The scale factors for P_{ref} varied from 0.72-1.04 on the shelf and from 0.84-1.11 on the slope, while those for P_{match} varied from 0.03-0.2 on the shelf and from 0.34-0.58 on the slope. P_{temp} was also lagged to account for delayed advective and wave adjustment of the density field and to achieve highest correlation. We assume that temperature should always lag pressure because changing seafloor pressure gradients should drive bottom currents, tracked by their temperature signatures. However, since such gradients could result in the advection of either warmer or colder water, we search for the maximum absolute correlation. We also limited the lag to a 30-day maximum, with the optimal lags ranging from 7-24 days and generally being larger on the shelf than on the slope. We ascribe no physical meaning to the variation in these lags in terms of circulation processes, as the relationship between seafloor pressure and temperature is demonstrably complex. Lagging was unnecessary for all other proxies.

3.3.4 Synthetic SSE detection and characterization

We assessed the efficacy of the candidate proxies to improve the detection and characterization of possible SSEs by adding synthetic deformation signals to the tidally filtered (but otherwise unprocessed) AACSE pressures and quantifying the accuracy with which those signals' onset times and amplitudes were estimated with each type of seasonal and proxy correction. We perform our analyses in the absence of, and then assuming, known SSE onset timing to evaluate the benefit of independent information about events (e.g., from onshore GNSS data). Unlike other synthetic detectability studies for offshore deformation (e.g., Agata et al., 2019; Ariyoshi et al., 2014; Fredrickson et al., 2018), this analysis focuses on evaluating the detection threshold of an observed signal rather than assuming one and assessing the slip scenarios that could generate such signals.

Representative SSE deformation transients were generated as simple ramps with amplitudes ranging from 0 to 10 cm and durations ranging from 1 day to 90 days so as to include the SSE characteristics observed elsewhere as well as to explore end member cases. Weekly onset times ranged from July 8, 2018 to May 19, 2019, which intentionally excluded the first and last 30 days of data (out of 377 days total) to reduce complications near the edges. For each amplitude considered, the duration was held at 14 days and for each duration considered the amplitude was fixed at 8 cm for shelf sites and 6 cm for slope sites, to assess the effect of duration on a large, readily detectable signal. The full range of onset times was used for every amplitude/duration combination to minimize any bias resulting from either positive or negative coherence of concurrent oceanographic signals with the synthetic ramp. Synthetics were added to only one pressure record at a time, then those modified data were put through the detrending and seasonal correction processing described above prior to attempting detection under the various proxy corrections. On the shelf this analysis yielded 552 detection results per amplitude or duration per proxy (12 stations and 46 onsets considered) and on the slope it yielded 414 (9 stations and 46 onsets considered).

We opted for a fully-automated approach to detect and characterize ramps to ensure the comparability of results between methods (Figure 3.4). For sinusoidal and polynomial seasonal corrections, the onset of an event was estimated by iteratively inverting, for every time step, the best-fit seasonal correction while allowing for an instantaneous offset in pressure at that time. We considered the time that yielded the lowest post-correction RMS value to indicate the center of the ramp. For the case of assumed known event onset, this step was unnecessary. To estimate the ramp amplitude, we then masked the 7 days before and after the estimated onset (for 14 days total) and re-inverted for the seasonal fit, again allowing for an offset in pressure on either side of the masked time period and considered that offset as equal to the ramp amplitude.

For the CEOF based seasonal corrections, we endeavored to estimate the event onset similarly; however, the CEOF calculation does not allow for undefined offsets, unlike the inversions described above. Instead, at each time step we inverted the CEOF corrected pressure for a linear fit with arbitrary offset at that time and again used the lowest RMS residual to determine the center of the ramp. In estimating the amplitude, we likewise endeavored to mirror the sinusoidal/polynomial scheme to the extent possible, given that the CEOF calculation does not allow for masking, while also recognizing that the presence of the synthetic ramp contaminated the CEOF calculation and could then lead to its partial or entire removal. Instead, for the determined (or assumed) onset time, we iteratively recalculated the CEOFs after subtracting out a 14-day ramp of variable amplitude from -20 to 20 cm. The CEOFs that yielded the lowest post-correction RMS value were then considered to be uncontaminated by the presence of the ramp and were used as a replacement seasonal correction for the original input data (i.e., those for which no attempt to subtract out the ramp had been made). Finally, to estimate the ramp amplitude by the same method as the polynomial and sinusoidal cases, the newly CEOF-corrected data were masked for the 7 days before and after the estimated onset (for 14 days total) and inverted for a linear fit, again allowing for an offset in pressure on either side of the masked time period, with the offset considered to be the ramp amplitude.

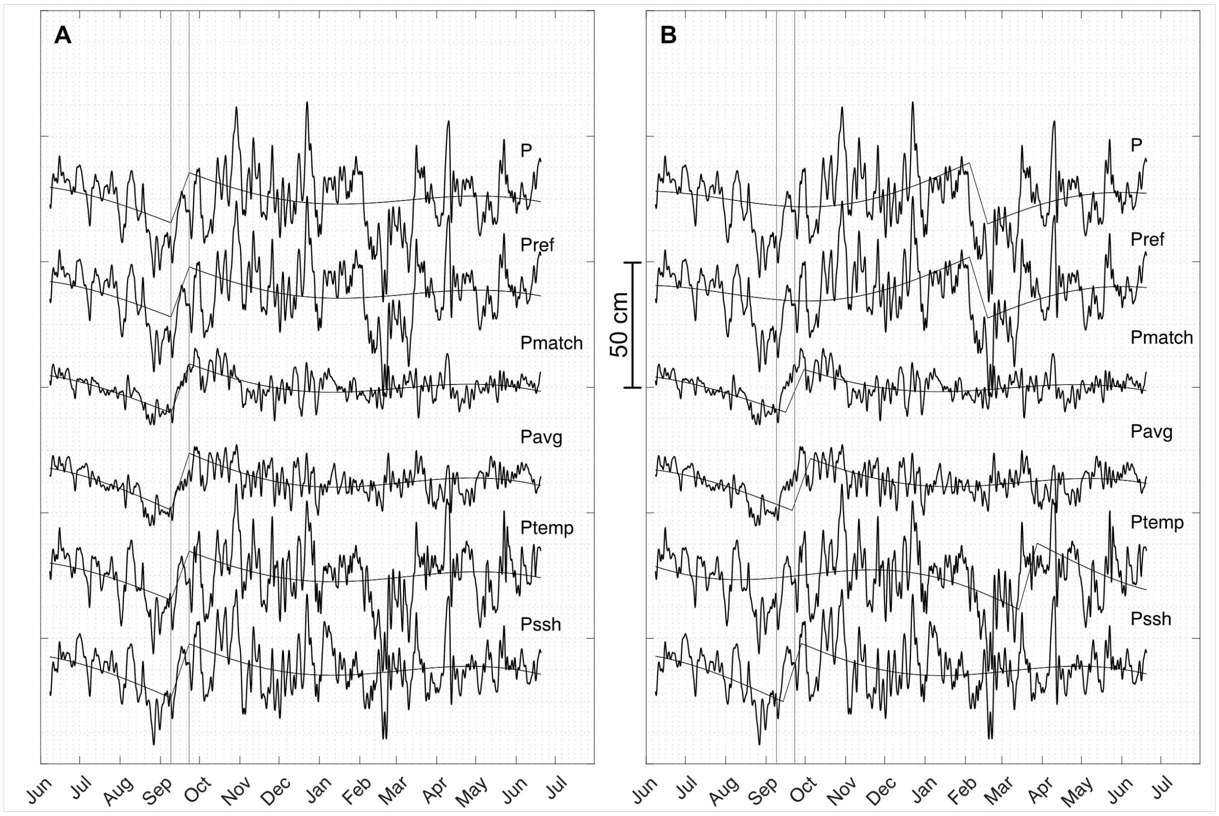

Figure 3.4 Demonstration of SSE signal detector for a 10 cm, 14 day ramp beginning on September 09, 2018 applied to sinusoidally- and proxy-corrected pressure records from station LT16 for A) the case of known onset and B) unknown onset. Each proxy-corrected time series is offset vertically for display purposes, from top to bottom: none, P_{ref}, P_{match}, P_{avg}, P_{temp}, and P_{ssh}. The vertical lines indicate the true synthetic event duration. Thin black curves show where the detector identifies the event and how it is characterized.

3.4 Results

3.4.1 Seafloor pressure characteristics

Tidally filtered pressure data from the AACSE for the period of June 8, 2018 to June 20, 2019 (377 days) show complex residual oceanographic signals of varying amplitude. After filtering out the tides, correcting for sensor drift, and detrending (Figures 3.2a, A2.2a and A2.3a), signal amplitudes are seen to broadly scale inversely with station depth, decreasing from the continental shelf to the continental slope and abyssal plain (Figure 3.1). There is little variation in the signal amplitudes of the slope pressures despite the depth range of 1564-4612 m, for which signal RMS varies from 2.2 to 2.9 cm. The pressure record from the deepest instrument, LA21 (5113 m) on the incoming Pacific Plate, has a notably larger RMS of 3.6 cm. Greater variability is seen on the shelf, where signal amplitudes do not vary systematically over the depth range of 83-262 m, but instead relate to broad-scale bathymetric features (Figure 3.1). Pressure RMS is lowest near the shelf break, at 3.7-4.3 cm, increasing to 4.7-5.2 cm within the Shelikof and Shumagin Troughs, and largest at the bathymetric high between the Shelikof and Shumagin Troughs and the one location west of the Shumagin Islands (LT20), at 6.2-6.9 cm. Despite these amplitude differences, the pressure data are remarkably coherent within the shelf and slope groupings, over separations of hundreds of kilometers, at both short and long periods (Figures 3.2a, A2.2a and A2.3a). This is particularly striking at periods of a few weeks or less, where pressures are not only coherent but synchronous within the hourly sample rate considered here, suggesting a barotropic response that is corroborated by the visual coherence between pressure and SSH (Figure 3.2b,e).

This domain-wide coherence in bottom pressure results in non-uniqueness in determining the proxy P_{match}. Figure 3.5 and Table A2.1 consider every combination of scaled station pair differences within the shelf and slope groupings. We do this for sinusoidally-corrected pressure data, with the aim of assessing signal similarity without drift, tidal, or seasonal signals, but prior to any proxy correction. Note that we consider symmetric differences (e.g., LT01–LT04 and LT04–LT01) and that because of the scaling described in Section 3.3 these do not necessarily yield the same RMS difference. Every station on the shelf has two or more stations that can be differenced with to achieve RMS ≤ 2 cm – down from the 3.7-6.9 cm noted above – with the exception of LT20 and LT11, which have no such pairs. Likewise, all stations on the continental slope have two or more stations that they can be differenced with to achieve RMS ≤ 1 cm – down from the 2.2-2.9 cm noted above – except LA22, which has none. Given the broad geographic footprint and relative sparsity of the AACSE network, it is difficult to discern precise limits on depth difference and range between station pairs to yield a given RMS threshold. However, some tentative correlation scales can be gleaned from the station pair differences. On the shelf, to yield signal RMS ≤ 2 cm over separations as large as 422 km there may be two distinct regimes; for stations at depths ≥ 156m depth differences can be as large as 120 m and for those at ≤ 125 m depths differences must be ≤ 42 m. On the slope, to achieve RMS ≤ 1 cm differences over separations as large as 470 km there may be a deeper regime (depths ≥ 2622 m) where depth differences can be as large as 1990 m, and a shallower regime (depths ≤ 2130 m) where depth differences are limited to 1058 m. These limits are dependent on the spatially sparse data available from the AACSE. It should also be noted that there are station pairs within these bounds that do not result in the RMS thresholds given, suggesting more complexity in the constraints on depth-matched pressure coherence.

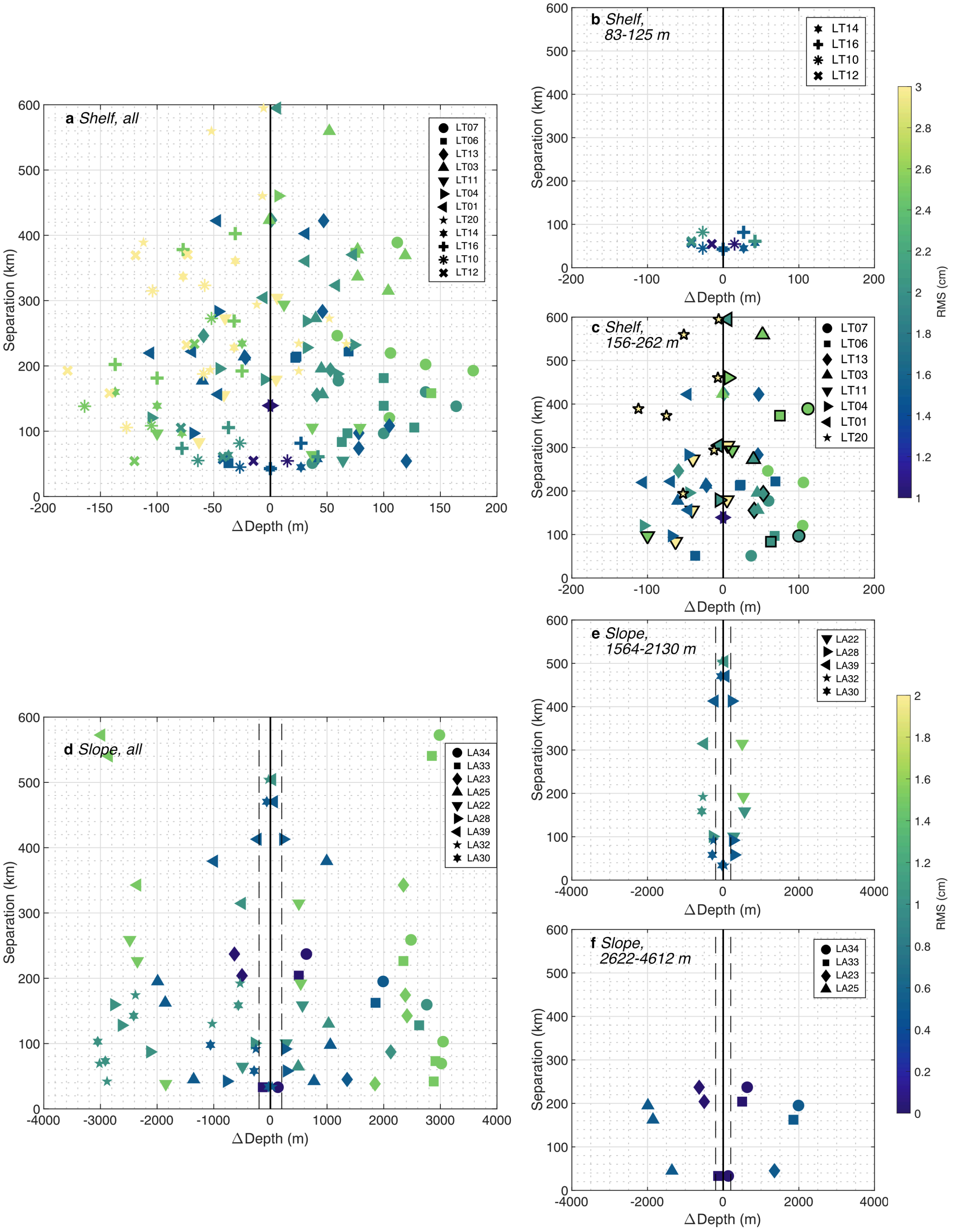

Figure 3.5 Plots of difference RMS for all station combinations as a function of separation and depth difference, after tidal filtering, drift correction, and sinusoidal seasonal correction. Symbol

shapes correspond to individual stations and colors scale with RMS. Negative depth differences mean that the station indicated by the marker is shallower than the station that has been subtracted from it. A) All shelf pairs (depths 83-262 m). B) Shelf pairs at depths 83-125 m. C) Shelf pairs at depths 156-262 m. We highlight station pairs that include LT11 and/or LT20, which may be anomalous (see text), by outlining them in bold black. D) All slope pairs (depths 1564-4612 m). E) Slope pairs at depths 1564-2130 m. F) Slope pairs at depths 2622-4612 m. Vertical dashed lines in (D-E) mark the depth range limits considered in (A), highlighting the difference in scale. As the only station beyond the trench, LA21 is excluded from these comparisons.

3.4.2 Proxy efficacy for correcting for oceanographic pressure signals

We consider RMS reduction as a measure of the extent to which a given seasonal correction and/or proxy can remove oceanographic signals, again noting that this measure may not strictly correspond to increased detectability of SSE-like signals. RMS reduction is defined as:

$$RMS\ reduction = 1 - \frac{RMS(corrected\ data)}{RMS(uncorrected\ data)}$$

The RMS reduction depends on the site and all forms of corrections considered herein, so we provide only a summary here and present full data in Figure 3.6 (sinusoidal and pressure-CEOF corrections), Figure A2.4 (polynomial and m-CEOF corrections), and Tables A2.3 & A2.4. For the shelf sites, the sinusoidal correction alone (Figure 3.6a & Table A2.3) yields RMS reductions of 6-24%. The net RMS reductions achieved with subsequent proxy applications are similar for P_{match} and P_{avg} at 53~80%, for P_{SSH} they generally increase with decreasing station depth and range from 12-54%, and P_{temp} makes negligible improvement. Application of the pressure-CEOF correction alone on the shelf (Figure 3.6c & Table A2.4) reduces the RMS by 54-73%, and further application of P_{match} or P_{avg} raises the upper limit of net RMS reduction to 83% and 80%, respectively. Interestingly, though P_{ref} generally does not further reduce RMS, the two shallowest stations (LT10 and LT12) prove an exception.

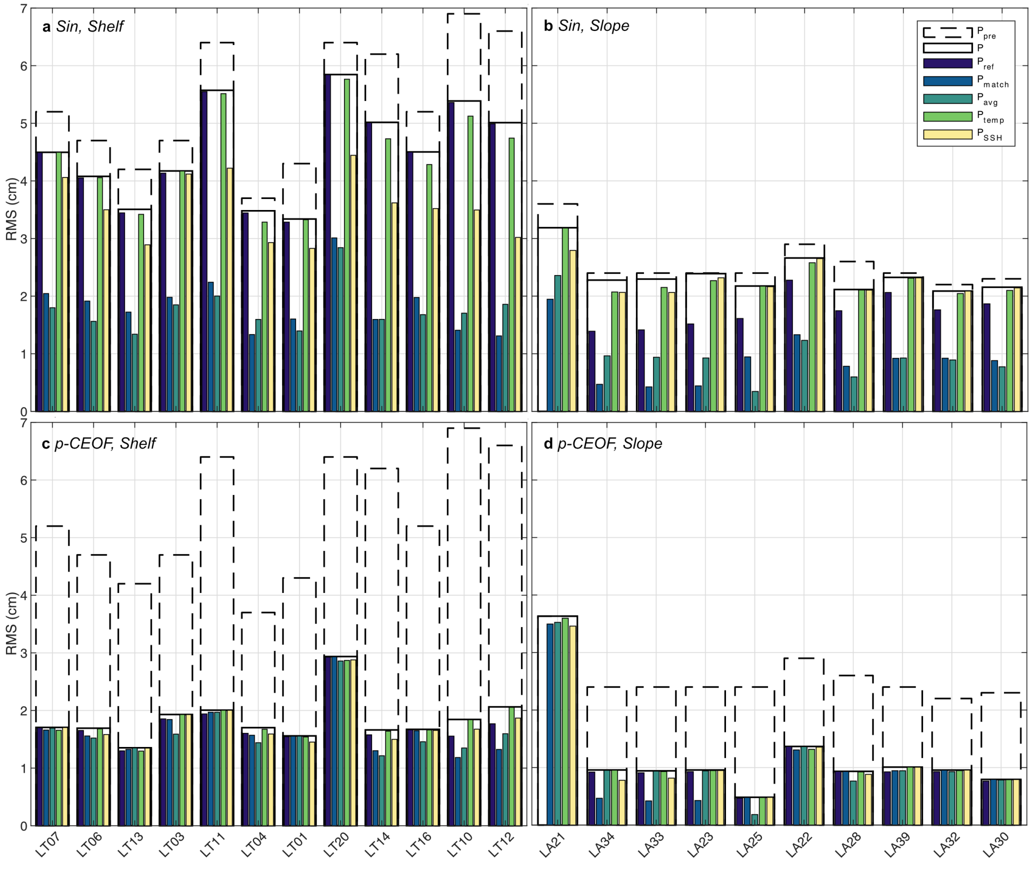

Figure 3.6 Proxy-corrected pressure RMS improvements for sinusoidally corrected A) shelf and B) slope data, and pressure-CEOF (p-CEOF) corrected C) shelf, and D) slope data. The empty, black-outlined bars in the background show the RMS of the seasonally corrected pressure record prior to applying any proxy, while the thin colored bars show the RMS of each proxy corrected time series.

For the slope sites, the sinusoidal correction (Figure 3.6b & Table A2.3) yields RMS reductions from 2-17%, and again P_{match} and P_{avg} perform comparably with a net reduction to 54~86%. The net RMS achieved with P_{ref} roughly scales with station depth, from 13% at one of the shallower sites to 41% for the deepest site. Pressure-CEOF corrected slope pressures (Figure 3.6d & Table A2.4) have RMS reductions of 53-80%. P_{match} and P_{avg} are the only proxies to provide a notable further RMS reduction, but only for a few sites where they achieve maximum reductions of 83% and 93%, respectively.

Figure A2.4 summarizes proxy RMS reduction for polynomial and multivariate-CEOF corrected data. The polynomial results are highly comparable to the sinusoidal results, while the multivariate-CEOF results fall somewhere between those of the pressure-CEOF and the functional corrections. Across all locations and seasonal corrections, the proxies P_{match} and P_{avg} tend to yield the greatest RMS reductions.

3.4.3 Identification and characterization of SSE transients

3.4.3.1 Known onset time

The seasonal and proxy corrections considered herein yield a large number of combinations from which to assess detectability. For simplicity, we focus on the sinusoidal and pressure-CEOF methods, noting that the sinusoidal and polynomial results are comparable and the pressure-CEOF results yield better overall detectability than the multivariate-CEOF results. A summary of the full results is provided in Table 3.1.

Figure 3.7 shows the amplitude recovery error from our detectability analysis for shelf stations when onset timing is assumed known, as might be the case if constrained by coastal GNSS data or other observables (e.g., Wallace et al., 2016). With known onset timing, our detector does not depend on the synthetic SSE amplitude because it is masked out (see Section 3.4). With the exceptions of multivariate-CEOF + P_{ref} on the shelf and pressure-CEOF + P_{avg} on the slope, all processing and proxy methods yield amplitude recovery results with medians within 1 cm of the known value, but with significant differences in distribution around the median (Figures 3.7, A2.5 and A2.6). To meaningfully compare correction techniques, we present results in terms of median plus or minus the median absolute deviation (MAD).

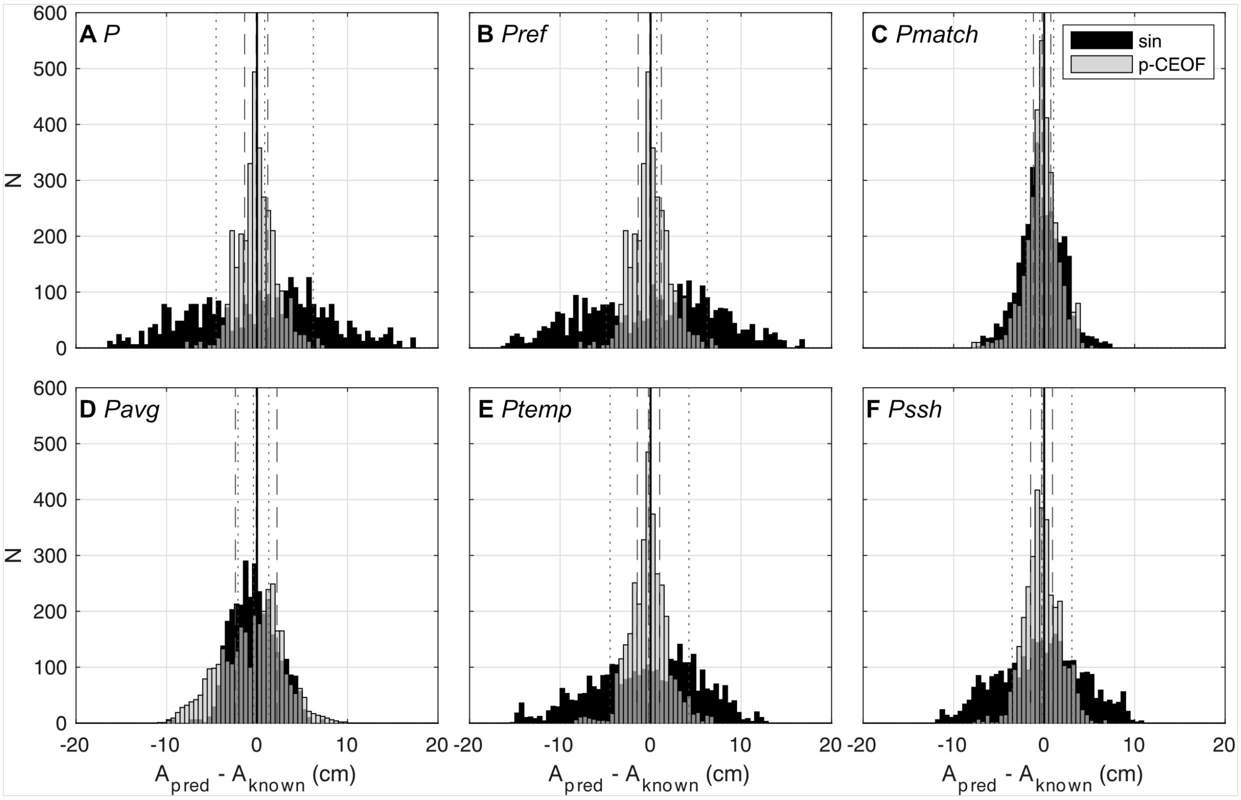

Figure 3.7 Histograms showing amplitude recovery error from the synthetic SSE detection analysis on the continental shelf, when known onset time is assumed, using sinusoidal (black), and pressure-CEOF (p-CEOF, translucent gray) seasonal corrections, for each of the proxies considered. The results from all synthetic ramp amplitudes considered (0, 2, 4, 6, 8, and 10 cm) were combined, with ramp duration held at 14 days and onset times varied weekly from August 2018 through April 2019. A) No proxy. B) P_{ref}. C) P_{match}. D) P_{avg}. E) P_{temp}. F) P_{SSH}. Vertical solid lines indicate the desired result ($A_{pred}–A_{known} = 0$), vertical dotted lines show the median and ±MAD of the error for the sinusoidal case, and vertical dashed lines show the same for the pressure-CEOF case.

On the shelf, the pressure-CEOF yields significantly tighter distributions than the other three seasonal correction methods, and notably the application of proxy corrections results in negligible improvement relative to the no-proxy cases and regardless of the varying RMS reductions associated with each proxy (Figures 3.7 & A2.6, Table 3.1). The tightest distributions, for the pressure-CEOF case, have median ± MAD ranges within -1.5 to 1.5 cm of the known value for the no-proxy, P_{ref}, P_{match}, P_{temp}, and P_{SSH} (light gray shading in Table 3.1). P_{avg} is the only exception here, with an anomalously large median ± MAD range of -2.8 to 2.2 cm, while the multivariate-CEOF method with P_{avg} yields the smallest range of -1.6 to 0.8 cm (Table 3.1). Across polynomial, sinusoidal, and multivariate-CEOF seasonal corrections, the tightest distributions result from P_{match} and P_{avg}, with median ± MAD ranges of -2.2 to 1.7 cm or better.

Table 3.1 Summary of synthetic detectability results when onset is assumed known

Proxy		Amplitude Recovery Error (cm)			
		Shelf		Slope	
		median	mad	median	mad
POLY	P	0.8	5.4	-0.4	1.4
	Pref	0.8	5.4	-0.4	1.4
	Pmatch	-0.5	1.6	-0.2	0.6
	Pavg	-0.5	1.7	-0.2	1.1
	Ptemp	0.2	4.9	-0.5	1.1
	Pssh	-0.7	2.7	-0.7	1.1
SIN	P	0.9	5.4	-0.3	1.6
	Pref	0.7	5.6	-0.3	1.7
	Pmatch	-0.5	1.5	-0.2	0.6
	Pavg	-0.4	1.7	-0.1	1.5
	Ptemp	-0.1	4.4	-0.6	1.1
	Pssh	-0.2	3.3	-0.6	1.1
m-CEOF	P	-1.8	3.1	-0.6	1.0
	Pref	-2.1	2.0	-1.2	1.2
	Pmatch	-1.8	1.3	-1.2	1.0
	Pavg	-1.9	1.4	-1.2	1.1
	Ptemp	-2.3	2.4	-1.3	1.2
	Pssh	-2.2	2.4	-1.4	1.2
p-CEOF	P	-0.1	1.3	-0.1	1.0
	Pref	-0.1	1.3	-0.6	1.0
	Pmatch	-0.2	1.0	-0.5	0.6
	Pavg	-0.1	2.3	-1.9	1.8
	Ptemp	-0.2	1.2	-0.2	0.9
	Pssh	-0.3	1.2	-0.4	0.9

Note. Amplitude recovery error for the known onset case is summarized as median and MAD values for the combined predictions from all ramp amplitudes considered herein, for all combinations of seasonal and proxy corrections considered in this study, with shelf and slope presented separately. The values for each seasonal/proxy pair result from 552 synthetic detection results on the shelf and 414 results on the slope. Light gray cells indicate median ± MAD ranges that fall within -1.5 to +1.5 cm of the known value. Dark gray cells indicate a range of -1.0 to +1.0 cm. m-CEOF = multivariate-CEOF, p-CEOF = pressure-CEOF.

On the slope (Figure A2.5 & A2.6), the differences in results between methods are similar but more subtle, with all yielding MADs ≤1.8 cm. Here also, the pressure-CEOF seasonal correction consistently yields the most favorable median ± MAD ranges, -1.5 to 1.5 cm or better for no proxy, P_{match}, P_{temp}, and P_{SSH} (Table 3.1). Unlike the shelf, the application of the P_{match} proxy consistently reduces the MAD relative to using none. Poor performance is again seen for pressure-CEOF with P_{avg}, yielding a range of 0.0 to 3.6 cm. Comparing all methods, polynomial, sinusoidal, and multivariate-CEOF seasonal corrections with P_{match}, as well as pressure-CEOF with no proxy, yield the best ranges, at -1.0 to 1.0 cm or better (dark gray shading in Table 3.1).

3.4.3.2 Unknown onset time

For unknown onset timing, we consider each proxy's efficacy in predicting the ramp onset time (Figure 3.8a-f) as well as its amplitude (Figure 3.8g-l). Though our detector still assumes the presence of a ramp, in the absence of known timing the ramp amplitude does affect the detectability. For simplicity, in Figure 3.8 we display only two detectability distributions on the shelf: the sinusoidal and pressure-CEOF seasonal corrections with P_{match}. These two correction methods were chosen because of both their high degree of RMS reduction (Tables A2.3 & A2.4) and for the accuracy of their known-time detection distributions (Figures 3.7c & A2.5c, Table 3.1) Summary results for all seasonal corrections and for the proxies P_{match}, P_{avg}, and no proxy are detailed in Table 3.2.

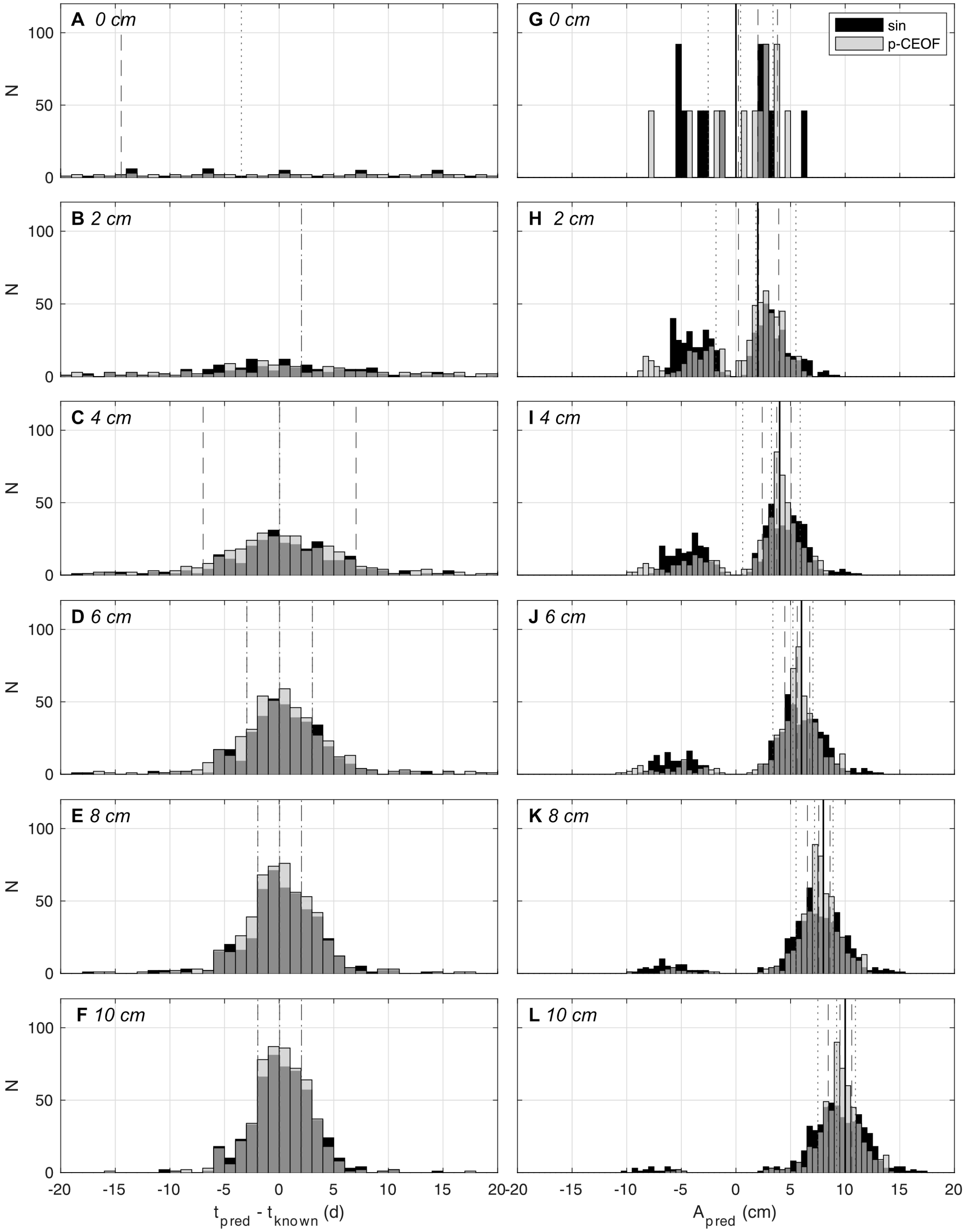

Figure 3.8 Histograms displaying SSE onset errors and amplitude predictions as a function of input ramp amplitude from synthetic detection analysis on the shelf, for unknown onset times,

for sinusoidal (black) and pressure-CEOF (p-CEOF, translucent gray) seasonal corrections, using only our best-preforming proxy, P_{match}. Synthetic ramp duration was held constant at 14 days and onset times were varied weekly from August 2018 through April 2019 to generate the composite distributions shown. A-F) Timing recovery for synthetic ramps of 0, 2, 4, 6, 8, and 10 cm amplitude. Vertical dotted lines show the median and ±MAD for the sinusoidal case, while vertical dashed lines show the same for the pressure-CEOF case. G-L) Amplitude recovery for synthetic ramps of 0, 2, 4, 6, 8, and 10 cm amplitude. Vertical solid lines show the input synthetic amplitude, vertical dotted lines show the median and ±MAD for the sinusoidal case, and vertical dashed lines show the same for the pressure-CEOF case.

As with the detectability distributions in the known timing case, we assess ramp detectability under the various scenarios by the median ± MAD. We first summarize results on the shelf and for the pressure-CEOF seasonal correction. For a 4 cm ramp, pressure-CEOF with P_{match} is the only method that can meaningfully localize the onset, yielding estimated median ± MAD ranges of -6 to 8 days and of 2.1 to 5.1 cm (Figure 3.8c,i & Table 3.2). A 3.5 cm ramp was also tested, but its onset could not be constrained by any method (Table A2.5). For 6 cm ramps, several processing combinations yield distributions that are well localized in time, the best among these being pressure-CEOF with either no proxy or P_{match} providing median ± MAD ranges of -3 to 3 days (Figure 3.8d) and 4.3 to 7.1 cm or better (Figure 3.8j). Notably, using the P_{match} proxy provides negligible improvement relative to the no-proxy case. For 8 and 10 cm ramps, predicted onset distributions become increasingly comparable between seasonal and proxy correction methods – as good as -2 to 2 days with amplitude MADs of 1.2 cm – with the exceptions of no-proxy polynomial and sinusoidal seasonal corrections performing significantly worse. This reflects both the tendency for functional seasonal corrections to incorporate some of the ramp signal and the simplification of treating the CEOF corrections as purely seasonal. Detection results for the polynomial and mulitvariate-CEOF seasonal corrections are shown in Figure A2.8. Across all processing techniques and input amplitudes, when the onset time is estimated accurately, the detector tends to underpredict ramp amplitude.

Table 3.2 Summary of synthetic detectability results when onset is assumed unknown

Aknown (cm)	Proxy		Shelf				Slope			
			Onset Recovery Error (d)		Amplitude Recovery (cm)		Onset Recovery Error (d)		Amplitude Recovery (cm)	
			median	mad	median	mad	median	mad	median	mad
0	POLY	P	--	--	-12.4	2.4	--	--	1.9	1.1
		Pmatch	--	--	0.4	2.7	--	--	0.5	2.3
		Pavg	--	--	0.3	3.6	--	--	3.0	0.8
	SIN	P	--	--	-12.0	2.0	--	--	3.3	1.5
		Pmatch	--	--	0.4	3.0	--	--	-0.8	2.4
		Pavg	--	--	3.9	1.5	--	--	3.7	0.9
	m-CEOF	P	--	--	4.4	1.4	--	--	-0.5	1.3
		Pmatch	--	--	-1.4	1.0	--	--	0.5	0.9
		Pavg	--	--	-1.1	1.1	--	--	1.7	0.5
	p-CEOF	P	--	--	2.8	2.3	--	--	-0.7	1.4
		Pmatch	--	--	2.0	1.8	--	--	1.5	1.3
		Pavg	--	--	3.7	3.2	--	--	0.8	0.6
2	POLY	P	36.0	84.0	-12.5	2.3	14.0	58.0	2.7	1.1
		Pmatch	-2.0	78.0	-1.5	3.6	0.0	34.0	1.8	1.3
		Pavg	-5.5	72.5	2.9	2.1	2.0	61.0	2.9	1.1
	SIN	P	43.0	84.0	-11.3	2.5	8.0	58.0	2.8	1.3
		Pmatch	2.0	74.5	1.8	3.7	0.0	25.5	1.8	1.9
		Pavg	-2.0	79.0	3.4	2.2	-1.0	52.0	3.1	1.7
	m-CEOF	P	37.5	89.5	4.3	1.5	-7.0	77.5	0.4	1.8
		Pmatch	1.5	65.5	-0.7	2.3	0.0	7.0	1.5	0.8
		Pavg	2.0	60.5	-0.2	1.9	5.0	63.5	1.5	1.2
	p-CEOF	P	1.5	79.0	3.0	2.1	-7.0	77.5	0.6	2.3
		Pmatch	2.0	75.0	2.1	1.8	-1.0	7.0	2.0	0.5
		Pavg	2.0	84.0	1.3	3.7	-3.0	84.5	0.0	2.2
4	POLY	P	30.0	84.0	-12.6	2.5	2.0	30.5	3.4	1.5
		Pmatch	-1.0	29.0	2.7	3.7	0.0	3.0	3.7	0.7
		Pavg	-1.0	58.0	3.4	2.5	0.0	9.0	3.6	1.4
	SIN	P	36.0	84.0	-11.6	2.9	1.5	18.5	3.6	1.7
		Pmatch	0.0	23.5	3.2	2.6	0.0	3.0	3.8	0.8
		Pavg	-1.0	51.0	3.8	2.7	0.0	6.5	4.1	1.9
	m-CEOF	P	13.5	77.5	4.3	2.4	0.0	20.0	2.0	2.7
		Pmatch	3.0	46.0	1.8	2.4	0.0	3.0	2.7	0.9
		Pavg	3.0	51.5	1.3	2.5	3.0	10.0	2.6	1.2
	p-CEOF	P	0.0	12.0	4.0	1.6	0.0	20.0	2.8	2.8
		Pmatch	0.0	7.0	3.7	1.3	0.0	2.0	3.6	0.7
		Pavg	0.0	12.0	2.7	3.5	1.0	20.0	0.5	2.9
6	POLY	P	23.0	83.0	-12.8	3.0	0.0	8.0	4.8	1.9
		Pmatch	0.0	4.0	4.7	2.4	0.0	2.0	5.7	0.7
		Pavg	0.0	7.0	4.6	2.2	0.0	2.0	5.5	1.2
	SIN	P	29.5	80.5	-11.6	3.8	0.0	5.0	5.4	2.0
		Pmatch	0.0	3.0	5.2	1.8	0.0	1.0	5.8	0.6
		Pavg	0.0	6.0	5.1	2.4	0.0	2.0	6.0	1.6
	m-CEOF	P	4.0	59.0	4.6	2.7	0.0	3.0	4.8	1.4
		Pmatch	2.0	12.0	3.1	1.9	0.0	2.0	4.3	0.9
		Pavg	2.0	33.0	2.6	2.0	1.0	5.0	4.2	1.1
	p-CEOF	P	0.0	4.0	5.8	1.4	0.0	3.0	5.5	1.4
		Pmatch	0.0	3.0	5.6	1.1	0.0	1.0	5.5	0.6
		Pavg	0.0	4.0	4.7	3.0	0.0	3.0	3.1	2.1
8	POLY	P	20.5	75.5	-12.5	3.7	0.0	3.5	7.2	1.8
		Pmatch	0.0	2.0	7.0	1.9	0.0	1.0	7.7	0.6
		Pavg	0.0	3.0	6.5	2.1	0.0	1.0	7.6	1.3
	SIN	P	22.5	66.5	-10.6	6.0	0.0	3.0	7.3	1.8
		Pmatch	0.0	2.0	7.2	1.7	0.0	1.0	7.7	0.6
		Pavg	0.0	3.0	7.0	2.1	0.0	1.0	8.0	1.5
	m-CEOF	P	2.0	25.5	5.5	2.8	0.0	2.0	6.9	1.1
		Pmatch	1.0	4.0	4.4	1.7	0.0	1.0	5.8	1.0
		Pavg	1.0	5.0	4.0	1.6	0.0	4.0	5.9	1.0
	p-CEOF	P	0.0	2.0	7.9	1.3	0.0	2.0	7.9	1.0
		Pmatch	0.0	2.0	7.6	1.0	0.0	1.0	7.3	0.7
		Pavg	0.0	3.0	7.4	2.3	0.0	2.0	5.1	1.9
10	POLY	P	16.0	71.0	-12.3	4.7	0.0	3.0	9.3	1.7
		Pmatch	0.0	2.0	9.0	1.8	0.0	1.0	9.7	0.6
		Pavg	0.0	2.0	8.5	2.0	0.0	1.0	9.6	1.2
	SIN	P	17.5	53.5	-7.3	12.1	0.0	2.0	9.4	1.7
		Pmatch	0.0	2.0	9.2	1.7	0.0	1.0	9.7	0.6
		Pavg	0.0	2.0	9.0	1.9	0.0	1.0	9.9	1.5
	m-CEOF	P	0.0	5.5	6.3	2.9	0.0	1.5	8.8	1.1
		Pmatch	0.0	3.0	5.8	1.5	0.0	1.0	7.4	1.0
		Pavg	0.0	3.0	5.3	1.4	0.0	3.0	7.5	1.1
	p-CEOF	P	0.0	2.0	9.9	1.3	0.0	1.5	9.9	1.0
		Pmatch	0.0	2.0	9.5	1.1	0.0	1.0	9.1	0.7
		Pavg	0.0	2.0	9.4	2.1	0.0	2.0	6.6	2.1

Note. Onset recovery error and amplitude recovery for the unknown onset case is summarized as median and MAD errors for each ramp amplitude considered herein for all seasonal corrections, and the proxy corrections P, P_{match}, and P_{avg}, with shelf and slope presented separately. Light gray cells indicate onset prediction median ± MAD ranges that fall within -8 to +8 days of the known value. Dark gray cells indicate ranges that fall within -4 to +4 days of the known value. m-CEOF = multivariate-CEOF, p-CEOF = pressure-CEOF.

For the slope, a summary of the full detectability analysis for unknown onset timing is given in Table 3.2, while Figure A2.7 plots the detection distributions for the sinusoidal and pressure-CEOF seasonal corrections with P_{match} proxy applied. In this setting, a 2 cm ramp can only be meaningfully constrained by either of the pressure- or multivariate-CEOF seasonal corrections, in conjunction with P_{match}, yielding median ± MAD range of -7 to 7 days or better and -1.0 to 2.6 cm or better (Figure A2.7b,h & Table 3.2). A 1.5 cm ramp was also tested, but its onset could not be constrained by any method (Table A2.5). For amplitudes 4 cm and above, timing accuracy improves rapidly and equalizes across seasonal and proxy corrections. At 4 cm, all seasonal corrections with P_{match} have median ± MAD ranges of -2.0 to 2.0 days and 2.7 to 4.3 cm or better. By 6 cm, all methods except polynomial and sinusoidal with no proxy and pressure-CEOF with P_{avg} yield median ± MAD ranges of -3 to 3 days and 3.8 to 7.2 cm or better. Detection results for the polynomial and multivariate-CEOF seasonal corrections are shown in Figure A2.9. Even when the timing is estimated well, the amplitude tends to be underpredicted, though to a lesser degree than is seen on the shelf.

Tests for the null case (i.e. a 0 cm synthetic ramp) provide some insight on false detections (Figure 3.8g). In the absence of a ramp on the shelf, the pressure-CEOF seasonal correction with P_{match} yields the tightest distributions, with a median ± MAD of 1.9 ± 1.7 cm. On the slope, the pressure-CEOF seasonal correction and P_{avg} yield the tightest distributions, with a median ± MAD of 0.0 ± 0.5 cm, but we deem this to be anomalous and instead infer ~1 ± 1 cm to be more probable, given the values seen across other processing methods. False detections appear significantly more probable with the functional form seasonal corrections and no proxy, yielding shelf and slope median ± MADs of ~-12 ± ~2 cm and ~4 ± ~1 cm, respectively.

For both shelf and slope locations, the worst onset time predictions are seen to arise from the detector misidentifying signals unrelated to the synthetic ramps (Figure A2.12). On the shelf, most of these poor detections arise in September–October, mid January–early February, at the end of the time series, and predominantly from a subset of stations. On the slope, the worst predictions are more broadly dispersed in time, but again principally occurring at only a subset of stations.

The detectability results described above hold for ramps as short as 1 day (Figure A2.10, shelf; Figure A2.11, slope). When attempting to detect longer ramps, the distributions broaden, to a greater extent in time than in amplitude, and amplitude distributions also shift toward greater underprediction (Figures A2.10- A2.11).

3.5 Discussion

3.5.1 RMS as a metric for SSE detectability

Our results permit us to assess the applicability of pressure record RMS as a predictor of the accuracy of SSE detection and characterization. RMS reduction is commonly used in pressure geodesy as a measure of a proxy's ability to reduce oceanographic signals, but its sensitivity to oscillatory signals in addition to ramp-like SSE signals suggests it may not represent a proxy's potential to improve SSE detection and characterization, as is generally assumed. Indeed, a significant component of pressure signals, particularly on the shelf, result from highly oscillatory weather-band energy (Luther et al., 1990), as has been observed in seafloor pressures offshore New Zealand and Japan (Gomberg et al., 2019; Johnson et al., 2017).

Further, signal RMS changes with time, becoming notably elevated in the winter months. Our results suggest that RMS is only a first order measure of SSE detectability and that RMS differences of a few millimeters are not predictive. For example, when assuming known onset timing, the corrections that yield the greatest RMS reduction (Tables A2.3 & A2.4) likewise tend to yield the best constrained amplitude predictions (gray shading in Table 3.1), but the differences between these predictions are small and do not correlate with RMS reduction. Notably, pressure-CEOF with P_{match} yields better RMS reductions on the slope than pressure-CEOF with no proxy and yet the latter ostensibly outperforms the former in its amplitude predictions. When onset timing is unknown, the corrections that yield the greatest RMS reduction (Tables A2.3 & A2.4) yield the best timing predictions for ramps just above the threshold of predictability, but these timing predictions and the resultant amplitude predictions equalize across processing methods as larger ramps are considered (gray shading in Table 3.2).

3.5.2 Implications of observed seafloor pressure spatial coherence

The efficacy of the CEOF-based seasonal corrections and the proxies P_{match} and P_{avg} for removing non-tidal oceanographic signals (Figure 3.6, Tables A2.2 & A2.3) is a consequence of the remarkable coherence of the bottom pressure anomaly field over the ~970 km span of the AACSE network. Such broad spatial scales are characteristic of water column processes (e.g., Hughes and Meredith 2006). While this signal similarity holds across the shelf and slope regimes, it is strongest within broad, coherent bathymetric features such as the Shelikof Trough (Figure 3.1). In addition, the breakdown of this coherence in the case of LT20 (the only shelf station west of the Shumagin Islands) and LA21 (the only deep station outboard of the lower slope Alaska Boundary Current) suggests that distinct coherent oceanographic domains exist beyond the simple shelf/slope demarcation described here.

The seafloor pressure coherence seen in Alaska can be compared to similar studies in Cascadia (Fredrickson et al., 2019) and Hikurangi (Inoue et al., 2021), bearing in mind the observational sparsity in all three settings. It should first be noted that, on a broad scale, pressure data have larger amplitudes in Alaska than in either Cascadia or Hikurangi and as a result, even the most effective seasonal and proxy corrections yield larger RMS values. At shelf sites in Alaska (83-262 m depth), RMS ≤ 2 cm and as low as 1.3 cm can be – but is not always – achieved between sites with depth differences $\lesssim$100 m with no consistent improvement when the depth difference is reduced to $\lesssim$50 m. In contrast, on the Cascadia shelf for 120-177 m depth, RMS of ≤ 1.7 cm and as low as 0.7 cm can be obtained from sites with depth differences $\lesssim$50 m, with some exceptions. Analysis of Hikurangi shelf pressure records are not available in the literature. Thus, to first order the available data suggest that the proxy P_{match} can be more flexibly defined on the shelf in Alaska but proves to be a more effective correction on the shelf in Cascadia.

At slope sites in Alaska, RMS values of ≤ 1 cm may be achieved for station pairs at 1564-2130 m depth over the full ~500 m depth difference range, with some exceptions, and RMS values of ≤ 1 cm may be achieved for sites at 2622-4612 m depth for depth differences of ~2000 m. In Cascadia, differences between upper slope sites (675-1297 m) yield RMS values ≤ 1 cm for depth differences $\lesssim$ 400 m, and all differences for sites at depths 1400-2908 m yield RMS values ≤ 0.9 cm with many ≤ 0.5 cm (Fredrickson et al., 2019). For upper slope sites in Hikurangi (651-1031 m depth), RMS values ≤ 1 cm are seen when depth differences are $\lesssim$ 350 m, while for lower slope and abyss sites (1246-3538 m depth), RMS values ≤ 1 cm (many ≤ 0.5

cm) are seen for depth differences up to ~2000 m (Inoue et al., 2021). Thus, given the limited extent of the networks in each location, the appropriate depth difference and separation scales for shallow slope sites are approximately the same across localities to minimize difference RMS to ≤ 1 cm. On the lower slope, these scales are likewise comparable between localities, but with evidence for Cascadia and Hikurangi having a lower noise floor than is seen in Alaska. We also note that in the Nankai Trough, RMS values averaging 1.1 cm were obtained for DONET pressures at ~1500-4500 m depth (e.g., Kawaguchi et al., 2015) recorded on sensors grouped in busnets of five instruments spaced ~20 km apart, after subtracting the mean pressure record for the respective subnet (Suzuki et al., 2018). It is notable that only in Alaska do we see a distinct incoherence between abyssal plain and lower slope sites, regardless of depth difference or separation. In Alaska and Cascadia, all of the above relationships hold true over site separations of hundreds of kilometers and in Hikurangi over separations of at least 80 km (the diameter of the network). Overall, these comparisons suggests that across multiple margins, the circulation processes that contribute significantly to seafloor pressures are temporally and spatially uniform along isobaths, within the hourly sampling considered here and subject to some linear scaling factor between sites.

The proxies based on other water column properties (seafloor temperature and SSH) at sites collocated with the pressures, seafloor temperature and SSH herein, do not appear to serve as effective proxies when used in the analyses employed here. However, their use warrants further investigation because they do not rely on multiple recording sites nor assumptions about spatial coherence, and they may provide qualitative indicators of oceanographic signals that could be misconstrued as tectonic in origin. For example, on the shelf, P_{SSH} yields only modest reductions in signal RMS (Figure 3.6, Table A2.3), likely because of the difference in frequency content when compared with the more continuously sampled seafloor records. However, it nonetheless tracks the abrupt seasonal transitions in October and February (Figure 3.3a,f). This observation is consistent with model simulations and published information on climatic and oceanographic patterns in the region, which show that during the winter months, strong winds transport water onto the shelf and cause downwelling of warmer water, creating winter-time peaked elevated sea levels, seafloor warming and pressure increases (Stabeno et al., 2004). Any potential deformation that occurs during the transitions between summer and winter is prone to conflation with that seasonal shift, making it difficult to isolate empirically. We observe that these seasonal shifts differ enough between locations to not be reliably corrected during differencing (Figure 3.3c,d). Thus, if not carefully accounted for, climatically-driven seasonal variations in P_O and proxy data may mask or lead to a misleading amplitude prediction for P_G, particularly when only a single or incomplete seasonal cycle is recorded (Gomberg et al., 2019). A benefit of the SSH data is the fact that they are routinely collected and readily available globally. Further, the spatial resolution of SSH grid requires interpolation to station locations, but nonetheless yields promising results. Future increases in spatial and temporal resolution of these satellite products may prove to be increasingly effective predictors of seafloor pressure.

There is very little RMS reduction provided by P_T (Figure 3.7), consistent with prior studies by Baba et al. (2006), Gomberg et al. (2019), and Itoh et al. (2019). However, qualitatively inspecting and comparing the time series reveals that there are certain frequencies and time periods at which the two signals correlate well, particularly on the shelf. This indicates that, as one might expect, there is a physical relationship between bottom temperature and pressure, but that it is temporally and spatially variable. As with SSH, this relationship has the potential to provide an additional means of differentiating tectonic and oceanographic signals and warrants further study. Additional independent measurements warrant exploration as P_O proxies, but require a deeper understanding of ocean circulation processes that may be region-specific.

3.5.3 Maximizing SSE detectability in pressure records

We summarize some of the limitations associated with the detectability analysis presented herein. Firstly, we have assumed that there is only one SSE signal present on a single station in the network at any time, which is reasonably consistent with the AACSE network geometry and the anticipated spatial scale of SSE deformation based on other studies. However, the higher site density in the western end of the AACSE or in other networks does not preclude the possibility of recording SSE deformation at multiple sites, as reported by He et al. (2021). Secondly, the methods that assume spatially coherent oceanographic pressures at multiple sites may inadvertently correct out some component of P_G, particularly those using the CEOF seasonal corrections and proxy P_{avg}, and P_{match} for poorly chosen site pairs. We minimized this possibility by masking out deformation signals prior to calculating the CEOFs and by excluding the station containing the synthetic deformation signal from the calculation of P_{avg}, but in a real scenario this would not be as straightforward. In smaller aperture networks or those with larger instrument density (e.g. Woods et al., 2022), these concerns are amplified as it may be difficult or impossible to exclude proximal stations. However, in such settings the pressure-CEOF seasonal correction and P_{avg} proxy have the benefit of being sensitive to sign and so in a well-recorded SSE the records of uplift and subsidence would tend to cancel one another out in their P_G terms. Further, in the case of known onset time or even known approximate location SSEs, efforts could be made to exclude particular stations from calculations or to mask the P_G period of the signal. We also caution that with all of the seasonal corrections considered here there is risk of correcting out or aliasing some part of P_G, so none should be used blindly. Finally, the detector is designed to perform optimally when the SSE ramp is the only significant signal present, which as noted in section 4.3.2 is not always the case even with our best-corrected pressure data.

Our detectability results show that there is a significant benefit to having independent information about the onset time (e.g., coastal GNSS deformation signals), particularly for smaller SSEs. In the end-member case of a 0 cm (null) SSE ramp, knowing the event onset a priori yields a median ± MAD range as good as -1.3–0.9 cm on the shelf (pressure-CEOF and P_{match}, Table 3.1), as compared to 0.2–3.6 cm when event timing is unknown (pressure-CEOF and P_{match}, Table 3.2). For larger ramps, onset constraint improves for the unknown timing case and consequently amplitude predictions more closely compare to those from the known timing case, though general amplitude underprediction remains. This underprediction results in part from the bimodal distributions of the recovered amplitudes when timing is unknown (Figure 3.8 for the shelf and Figure A2.7 for the slope). The bimodality of the amplitude recovery arises from spurious detections often associated with days- to weeks-scale large pressure fluctuations that occur as part of the transition between winter and summer seasons. All correction techniques assessed in this study are based on least squares regression, so the offsets that result when the detector misses ramps will necessarily be accompanied by a comparable decrease elsewhere in the corrected pressure record to minimize the residuals. Figure 3.4b is demonstrative of this effect for the P_{ref} and no proxy corrections, though it occurs with varying frequency across all proxy corrections.

Whether on the shelf or slope, pressure data corrected with pressure-CEOF seasonal corrections and P_{match} yield the best or among the best constraints on onset and amplitude (gray shading in Tables 3.1 & 3.2). The smallest SSEs that may be detected and characterized with these corrections have amplitudes of 4 cm on the shelf and 2 cm on the slope, comparing favorably with deformation amplitudes observed from SSEs in other studies. The difference in the threshold of detectability between shelf and slope is also roughly consistent with the ratio of post-correction RMS amplitudes between the two regions (Figure 3.6, Tables A2.3 & A2.4). Nearly all processing methods systematically underpredict ramp amplitudes and distributions are notably bimodal for small amplitudes (Figure 3.8), but the use of the pressure-CEOF and P_{match} minimize these complications. Thus, our results provide evidence that CEOFs can be used to provide seasonal and higher-frequency corrections to seafloor pressure data without significantly impacting the determination of P_G amplitude, as compared to other seasonal correction methods. The timing accuracy that results from this preferred processing method should enable meaningful time-dependent SSE slip inversions, given the cm-scale SSE deformation amplitudes observed elsewhere. The potential to detect and characterize SSE deformation on the shelf is particularly important for the AACSE study area and much of Alaska, given the shelf's width of hundreds of kilometers and sparse onshore geodetic network. In a broader view, it is also significant in that it has generally been assumed previously that shelf pressure data are too noisy to be used in the detection of SSE deformation.

Longer deployments will help with correcting sensor drift and in the absence of known event timing, it would allow for sufficient data on either side of an SSE to adequately detect and characterize it. Going forward, extending deployment duration to include multiple seasonal cycles would have multiple benefits for geodetic studies, to improve the preprocessing corrections for instrumental drift and seasonal variation. The former can be difficult to constrain due to the exponential component of unknown duration at the beginning of the deployment, which becomes decreasingly problematic with increasing observation duration. Seasonal signals and interannual variability can be better characterized with each additional year of data. The latter has not been extensively studied to date, but may be significant noting that La Nina & El Nino have been observed to influence seafloor pressure records on the U.S. west coast (e.g., Wilcock et al., 2021).

3.6 Conclusions

Our analyses quantify the patterns of significant coherence in seafloor pressure records from the Alaska margin over distances of hundreds of kilometers, controlled largely by location above or below the shelf break, and then secondarily by regional scale bathymetric features such as troughs and rises. We exploit this coherence to remove oceanographic signals from seafloor pressure records, thereby reducing the RMS of these records by as much as 83% on the shelf and 93% on the slope. The most effective approach to this involves first subtracting out the 1st CEOF of the combined pressure dataset from either shelf or slope sites, and then using depth matched differencing (the proxy P_{match}) to further correct the data. Most pressure records corrected in this way can be reduced to ≤1 cm RMS on the slope and ≤2 cm on the shelf. The separation and depth differences required to achieve those lowest RMS values are to first order consistent with what has been reported in Cascadia and Hikurangi margins, though the RMS values themselves are higher than what has been observed in those external locations.

We also demonstrate, through a synthetic detectability analysis, that the same combination of pressure-CEOF and P_{match} corrections enable the greatest detectability of SSE deformation signals, allowing for statistically repeatable detection of 4 cm SSE signals on the shelf and 2 cm signals on the slope when no additional SSE constraints exist. Our analyses show that it is highly advantageous to have a priori information about event onset, perhaps provided by deformation observed on coastal GNSS stations. With known event timing, ramp amplitudes can be constrained to the ± 1 cm level on the shelf and the ± 0.5 cm level on the slope, while without this knowledge ramps are systematically underpredicted and MADs are generally larger, particularly for small amplitude ramps.

Even with oceanographic signal corrections applied, significant residual pressure fluctuations occur at the transitions between winter and summer seasons and can be misidentified as SSE deformation, particularly when using an automated SSE detector. While collocated SSH data are highly predictive of these seasonal signals for stations on the shelf, they still fail to adequately predict other oceanographic signals and thus do not yield dramatic improvements to pressure RMS values or to SSE detectability. Nonetheless, this relationship warrants further exploration, as does the time- and frequency-dependent correlation between seafloor temperature and pressure. Additional improvements to oceanographic corrections and SSE detectability are likely to arise from longer, multi-year observational records.

Our results demonstrate that seafloor pressure records properly corrected for oceanographic pressure effects may be powerful tools for identifying SSE and other small-amplitude transient tectonic deformation. In particular, we show that observations from the shelf, which have previously been neglected or simply not made, can be adequately corrected to reliably detect SSE deformation.

3.7 Acknowledgments

We thank David Schmidt and Parker MacCready of the University of Washington for their input and feedback on the detectability analysis and oceanographic interpretations, respectively. We also thank the Associate Editor and two anonymous reviewers for their valuable feedback on the original manuscript. This research was supported by NSF grant OCE1951071. *Any use of trade, firm, or product names is for descriptive purposes only and does not imply endorsement by the U.S. Government.*

Chapter 4:
Demonstrating the Generation of Slow Slip-Like Seafloor Pressure Signals by Mesoscale Eddies in a Regional Oceanographic Model of the Cascadia Margin

4.0 Abstract

4.1 Introduction

In recent years, there has been increasing interest and investment in the study of offshore subduction processes (Burgmann & Chadwell, 2014; Wang & Trehu, 2016). Many such processes have been found to occur on the updip end or even updip of the locked megathrust – where large, catastrophic earthquakes nucleate – suggesting their importance for the earthquake cycle, but placing them far from land-based observation networks. While offshore technologies are rapidly evolving, such as GNSS-Acoustic and Distributed Acoustic Sensing (DAS), and deployments are increasing in frequency and scope (Barcheck et al., 2020; Kawaguchi et al., 2015; Toomey et al., 2014; Yarce et al., 2019), presently, a major challenge in the study of offshore tectonic processes is the significant noise generated by ocean circulation.

Phenomena that have recently been observed on offshore subduction thrusts include tremor (e.g., Yamashita et al, 2015), low- and very low-frequency earthquakes (e.g, Chaudhuri & Gosh, 2022), and slow slip events (SSEs; e.g. Wallace & Beaven, 2010), as well as associated inferences about the locked state of the subduction thrust (Lindsey et al., 2021). In some subduction zones, the full plate interface is sufficiently close to shore to observe with land-based sensors (Dixon et al., 2014; Ozawa et al., 2007; Radiguet et al., 2016; Ruiz et al., 2014; Vallée et al., 2013; Wallace & Beavan, 2010), but in many settings the distance from shore to trench is prohibitive and such phenomena have instead been observed on ocean bottom instrumentation (Araki et al., 2017; Davis et al., 2015; Ito et al., 2013). Even where observation from land is possible, there is great benefit from direct seafloor observation (e.g., Wallace et al., 2016; Woods et al., 2022).

In addition to the added cost and logistical complexity associated with offshore deployments, circulation-related processes continuously generate signals of significant magnitude in comparison to solid-Earth processes of interest, which are generally not well understood and characterized (see Chapters 2 & 3; Gomberg et al., 2019; Hilmo et al., 2020; Janiszewski et al., *in prep*). Of greatest relevance to this study, a widely-used method for observing shallow SSEs exploits the sensitivity of bottom pressure records to changes in the overlying water column thickness to identify the uplift and/or subsidence of the seafloor that results from these events (e.g., Wallace et al., 2016). However, pressure records are equally sensitive to changes in sea surface height and water column density, which presents a significant challenge when it comes to reliably identifying and characterizing SSE deformation. Some efforts and progress have been made on this front by exploiting spatial coherence of seafloor pressure signals (see Chapters 2 & 3; Inoue et al., 2021; Woods et al., 2022), using additional observations from Current meters and Pressure recording Inverted Echosounders (CPIES; Watts et al., 2021), correcting with oceanographic circulation models (Dobashi & Inazu, 2021; Muramoto et al, 2019), and training machine learning models to distinguish tectonic signals (He et al., 2020). Primarily though, such efforts have been focused on correcting the signals rather than understanding the ocean physics that dictate them.

In the field of physical oceanography, bottom pressure has not historically been an area of focus, though there are exceptions such as in the study of major current systems (e.g., Nagano et al., 2021; Pickart & Watts, 1990). Additionally, the coherence of seafloor pressure has been noted and examined, though at different spatiotemporal scales than those of interest for offshore

SSE studies. For example, Hughes & Meredith (2006) explored the coherence of sub-surface pressure – sea surface height corrected for the inverse barometer effect – along the global continental slope. They noted that a stratified ocean with vertical boundaries will generate Kelvin waves that propagate rapidly along the boundaries while an unstratified ocean with sloping boundaries will generate Rossby waves that propagate towards the ocean interior. Thus, a realistic ocean will generate hybrid waves that are strongly Kelvin-like (i.e., tend to propagate rapidly along boundaries) at continental margins where stratification is high and topography steep. Their analysis ultimately showed significant coherence in sub-surface pressure signals at periods of >15 days over broad regions of the global continental slope, particularly so for the North Pacific where lateral coherence spatial scales span thousands of kilometers. In a more recent study, Hughes et al. (2018) used a global oceanographic model spanning 1958-2012 at 1/12° resolution to demonstrate that mesoscale variability is much weaker in bottom pressure than in other observables, particularly on the continental slope. With a focus on the Atlantic continental slope at depths from 100-3200 m, they showed that the first 2 empirical orthogonal functions (EOFs) in depth-time space calculated independently for each group of model points within 50 km of one another explained 90% of the variance seen in those modeled bottom pressures. They further demonstrated that these first 2 EOFs strongly correlate between groups at periods of 1.5-10 years over distances of thousands if not tens of thousands of kilometers and strongly correlate at periods of <1.5 years over distances of hundreds of kilometers.

At lower periods (<1 month), it is generally assumed that seafloor pressure is essentially barotropic (i.e., determined purely by SSH). However, in any real system with bottom topography and water column structure, barotropic motions result in the displacement of isopycnals, meaning the physics is in fact baroclinic. Further, limited observations and the coarseness of ocean models have resulted in a limited understanding of how topography influences seafloor pressure. An analysis by Androsov et al. (2020) of ~4 years worth of bottom pressure data and 4 circulation models in the Southern Ocean between South Africa and Antarctica showed significant influence of Agulhas eddies in the variability of seafloor pressure. The interaction of deep-reaching eddies with bottom topography may play an important role in energy dispersal at the mesoscale (Zhang et al., 2016). In a study of the subsurface structure of eddies on the Kyushu-Palau Ridge, Andres et al. (2019) showed that mesoscale eddies perturb the thermocline – shallowing in cold-core eddies and a deepening in warm-core eddies – and observed bottom pressure perturbations on CPIES at depths from 2600–4300 m. Further, Yuan et al. (2021) developed a 3D eddy tracking algorithm based purely on bottom pressure expression and were able to compile over 21,000 eddy trajectories from 5 years of HYCOM output in a 20°Nx15°E focus area of the Kuroshio Extension.

Using a 50 year global ocean model with 1° resolution, Vinogradova et al. (2007) show that bottom pressure and sea level are highly correlated at periods of <30 days, dominated by essentially barotropic modes. At longer periods of ~100 days high correlation occurs only at high latitudes >60° and shallow depths <200 m, with baroclinic modes dominating elsewhere. Bingham & Hughes (2008) explored these relationships at finer scales in an eddy-permitting model, showing that eddies can interrupt the correspondence between SSH and bottom pressure, even on short timescales of 10-20 days.

All of this points to bottom pressure being reflective and correlative to identifiable ocean circulation processes, including mesoscale eddies. We want to integrate this knowledge into the solid-Earth side of bottom pressure studies. Ocean bottom pressure observations have been identified as a key physical oceanographic observational need (Levin et al., 2019). Such measurements are important for understanding mass-related sea level rise (regional and global), validation of satellite products (e.g., GRACE), monitoring global-scale circulation processes, tsunami early warning, and more. OBP is sensitive to barotropic tides, internal waves, infragravity waves, and storm surges. Thus, there are shared goals and interests between the fields.

Models of ocean circulation have proven to be useful tools in the study of seafloor pressure, but by nature of the stochastic processes that govern much of circulation at the mesoscale are insufficiently accurate to serve as direct corrections. In this study, we leverage a regional oceanographic model that encompasses the Cascadia Margin as a tool to understand the processes dictating seafloor pressure by assessing how seafloor pressure characteristics differ throughout the region and identifying processes that generate significant pressure signals that are not readily corrected by current processing methods and may ultimately be confused for SSE deformation signals.

4.2 Materials and Methods

4.2.1 Regional oceanographic model

We use the LiveOcean model, which employs the Regional Oceanographic Modeling System (ROMS; Shchepetkin & McWilliams, 2005), to extract the seafloor pressure data presented herein. LiveOcean, developed by the University of Washington Coastal Modeling Group (e.g., Liu et al., 2009), covers a broad region including the Salish Sea and the coastal Eastern Pacific Ocean offshore Oregon and Washington states, and Vancouver Island, with variable resolution no lower than 3 km at open boundaries and increasing inland. The model is described extensively in MacCready et al. (2021) and has been validated against a range of biological, chemical, and physical observables (Giddings et al., 2014; MacCready et al., 2021). Most pertinent to this study, LiveOcean is nested within the U.S. Navy HYCOM (Chassignet et al., 2007), from which it takes its boundary conditions and has 30 vertical layers whose spacing is closest at the top and bottom of the water column. The model state variables are salinity and potential temperature and the Boussinesq approximation (incompressibility) is assumed, from which in-situ density and pressure are ultimately calculated using the seawater equation of state. The model is hydrostatic and optimized for integrated conservation of tracers and constancy preservation. Forcings come from atmospheric, tidal, and river inputs, a free ocean surface is assumed, and realistic – albeit smoothed – bathymetry is used. The model configuration used for this study was initialized to run from December 15, 2016 through the present with regular updates.

As the focus of this study lies in the bottom pressure of the Cascadia Margin, we use only a subdomain of the full Cascadia domain. This focus area is bounded at 48° and 44° N to the north and south and at -127º E and the coastline to the west and east, as shown in Figure 4.1. Further, only model output from December 16, 2017–December 15, 2021 was used in this study, sufficiently long to be representative for typical seafloor pressure sensor deployments. We here define three primary zones of interest: the continental shelf, from 0–300 m depth, the continental slope, from 300–2000 m depth, and the near-trench at >2000 m depth. The boundaries between these regions are marked in bold in Figure 4.1 and throughout. Using this subdomain, we also avoid regions near the open boundaries where nudging to HYCOM fields makes the dynamics difficult to interpret (MacCready et al., 2021).

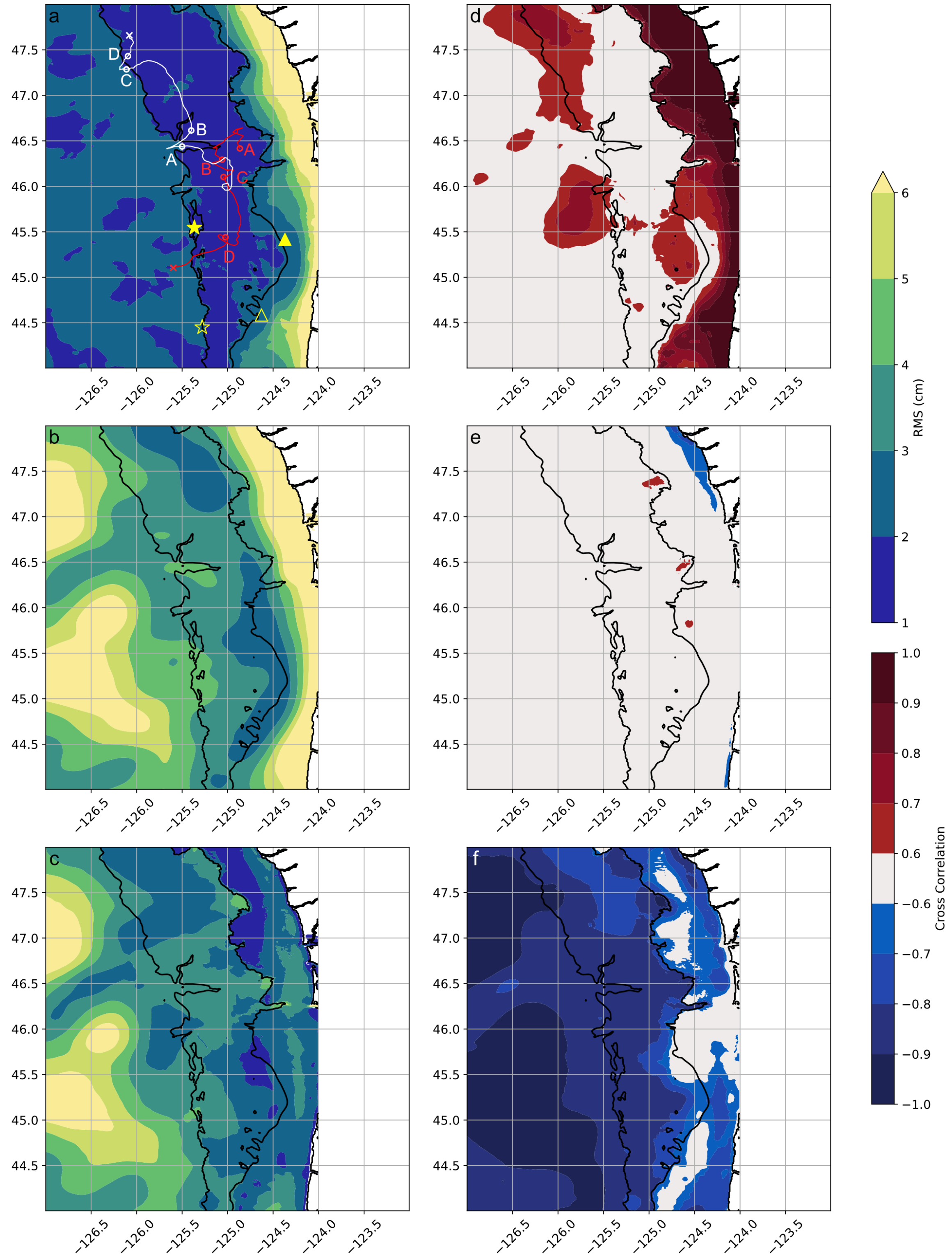

Figure 4.1 Map view of the study region with contours of (a) the RMS of the bottom pressure anomaly at each point in the model domain, (b) the RMS of the eustatic component, (c) the RMS of the steric component, (d) the cross correlation coefficient of the bottom pressure anomaly and

the eustatic component, (e) the cross correlation coefficient of the bottom pressure anomaly and the steric component, and (f) the cross correlation of the steric and eustatic components. All panels use model output from the period December 16, 2017–December 15, 2018. In (a) the yellow filled triangle indicates the location of the 200 m extraction and the yellow filled star indicates the location of the 2000 m extraction. The yellow open triangle indicates the 200 m reference location and the yellow open star indicates the 2000 m reference location for calculating the differences plotted in Figure 4.2. The red curve marks the track of the warm core eddy plotted in Figure 4.3, with the red 'X' as its terminus and the red circles indicating the location of the extractions. The white curve, 'X', and circles mark the same for the cold core eddy plotted in Figure 4.4.

4.2.2 Bottom pressure anomalies

We calculate pressure at the seafloor from the model's hourly output as the sum of pressure contributions of the model's 30 vertical layers:

$$P_{total} = \sum_{i=1}^{30} \rho_i \; g \; \Delta Z_i$$

Where ρ_i is the in-situ density of the layer, g is gravitational acceleration, and ΔZ_i is the thickness of the layer. ρ_i and ΔZ_i vary in model space and time, while g is constant 9.81 m/s^2 throughout.

We divide the total pressure into two parts: its eustatic component, which results from the addition of water and is observed in the sea surface height field, and its steric component, which results from changes in the structure of the water column (namely, its density). Mathematically, these components are approximated by:

$$P_{eustatic} = \rho_0 \; g \; Z$$

$$P_{steric} = \sum_{i=1}^{30} (\rho_i - \rho_0) \; g \; \Delta Z^*{}_i$$

with: $P_{total} \cong P_{eustatic} + P_{steric}$

Where ρ_0 is set to a nominal constant 1025 kg/m^3, Z is the total water column height, and ΔZ^* is the model layer thickness assuming an unperturbed sea surface height (i.e., the vertical distance between the bottom boundary of the top layer and the mean sea surface height). As we are only concerned with pressure anomalies and not the absolute pressure, all formulations are converted to anomalies by subtracting the time mean for each grid point:

$$p_t = P_{total} - \overline{P}_{total}$$

$$p_e = P_{eustatic} - \overline{P}_{eustatic}$$

$$p_s = P_{steric} - \overline{P}_{steric}$$

These anomalies are detided using a Godin 24-24-25 moving-average filter (Emery & Thomson, 2004; Godin, 1972) and decimated to daily values at 12:00 UTC each day.

The formulations for p_e and p_s rely on approximations. The eustatic seafloor pressure assumes a constant water density; however even the largest density excursions are limited to ~1000 kg/m^3 for freshwater and ~1040 kg/m^3 for cold, saline water, limiting the approximation's error to ~2.5%. Further, these extreme variations have temporally and/or spatially limited extent, while the bulk of the water mass is much closer to the assumed constant value, making this a reasonable approximation. The steric seafloor pressure, in ignoring fluctuations in sea surface height, excludes the density anomaly introduced by any additional water at the very top of the water column, but again this is a reasonable approximation since the deviation is inherently small and relevant only to a small fraction of the total water column height.

4.2.3 Eddy tracking

We manually tracked a small subset of the eddies generated in and propagated through the model subdomain, with a focus on those which traversed the continental margin over a sustained period of time (>50 days). Our tracking process was as follows. Candidate eddies were identified visually in map-view plots of the daily SSH field and, once identified, their centers were manually picked for each day of their duration. These centers were then modified with a simple algorithm that updated the eddy center to instead be the local extrema in the SSH field within 15 model grid points of the user pick. Two warm-core (positive SSH anomaly) and two cold-core (negative SSH anomaly) eddies were tracked in this way for each of the four model years analyzed in this study.

4.3 Results

4.3.1 Bottom pressure anomaly characteristics

Broadly, signal amplitudes in the ROMS bottom pressure anomaly increase with shallowing bathymetry, with amplitudes as low as 2 cm RMS near the trench and in excess of 7 cm RMS near the coast (Figure 4.1a), consistent with the findings of Fredrickson et al. (2019) for an earlier iteration of the model. This result is expected from theory, since waves and various circulation effects interact with the bottom in shallow waters but do not do so in deeper waters. The result is also consistent with direct observations of bottom pressure in continental margin environments around the globe (e.g., Dobashi & Inazu, 2021; Inoue et al., 2021). Between the trench and the coast, the eustatic component of bottom pressure also follows this pattern, with the largest signal amplitudes (>10 cm RMS) seen in the shallowest waters (Figure 4.1b). This is again consistent with theory and observations, in which the shallowing bathymetry increases wave amplitudes and the presence of the coastal barrier can result in water piling up on the continental shelf. Present in the eustatic field are also broad regions beyond the trench with large amplitudes, which are not static between model years but are always present in some broad region west of the margin. The steric pressure anomaly field is more complex, with fewer consistent features through time. However, signal amplitudes are consistently low near the shelf break, elevated near the mouth of the Columbia River, and highest out beyond the trench (Figure 4.1c). To a degree not seen in the total pressure anomaly and the eustatic component, regions of high and low signal amplitude are dynamic between model years.

Over the period of a year at daily sampling, the eustatic component is strongly positively correlated with total pressure anomaly almost everywhere on the shelf, but to a lesser degree in the south of the domain (Figure 4.1d). While some regions of high correlation exist on the slope and abyss, these are not static through model years. There is virtually no anticorrelation between the eustatic component and total pressure anomaly anywhere in the domain, even at finer levels than those displayed in Figure 4.1. The steric component of bottom pressure shows very little strong correlation with the total bottom pressure over the period of a year (Figure 4.1e). The steric and eustatic components, on the other hand, show spatially broad anticorrelation (Figure 4.1f). This relationship is persistent below the shelf break across all model years, though there is temporal variability in the spatial pattern of the cross correlation coefficient amplitude. On the shelf, the anticorrelation between the two components is not as strong nor as temporally consistent.

The broad relationships seen in the cross correlation maps can be understood in greater detail by looking at the time series from individual locations. On the shelf, the bottom pressure anomaly tracks the eustatic component very closely over a broad range of frequencies, as shown for a representative location in Figure 4.2a. In particular, large-amplitude, abrupt changes in the eustatic component – several centimeters over periods of a few days – are well reflected in the total anomaly. The relationship between the total anomaly and the steric component is less apparent visually, as expected from the low cross correlation coefficients throughout the model subdomain. On close inspection, the total anomaly is seen to track the steric component at low frequencies, on the order of approximately a month or longer. This relationship is dynamic through time, with the two signals going in and out of phase over periods of a few months. Further, depending on time and location, the correlation is seen to be both positive and negative. Higher frequency signals of a few days or weeks are rarely coherent between the two, though there are occasional exceptions. The relationship between the eustatic and steric components is most obvious during periods of sustained deviation from the mean, with the steric component exhibiting the opposite sign of the eustatic behavior, acting to compensate the effects of significant SSH deviations at the seafloor. This behavior is reflected across frequencies, though at high frequencies of a few days to weeks amplitudes and phase are not consistently matched.

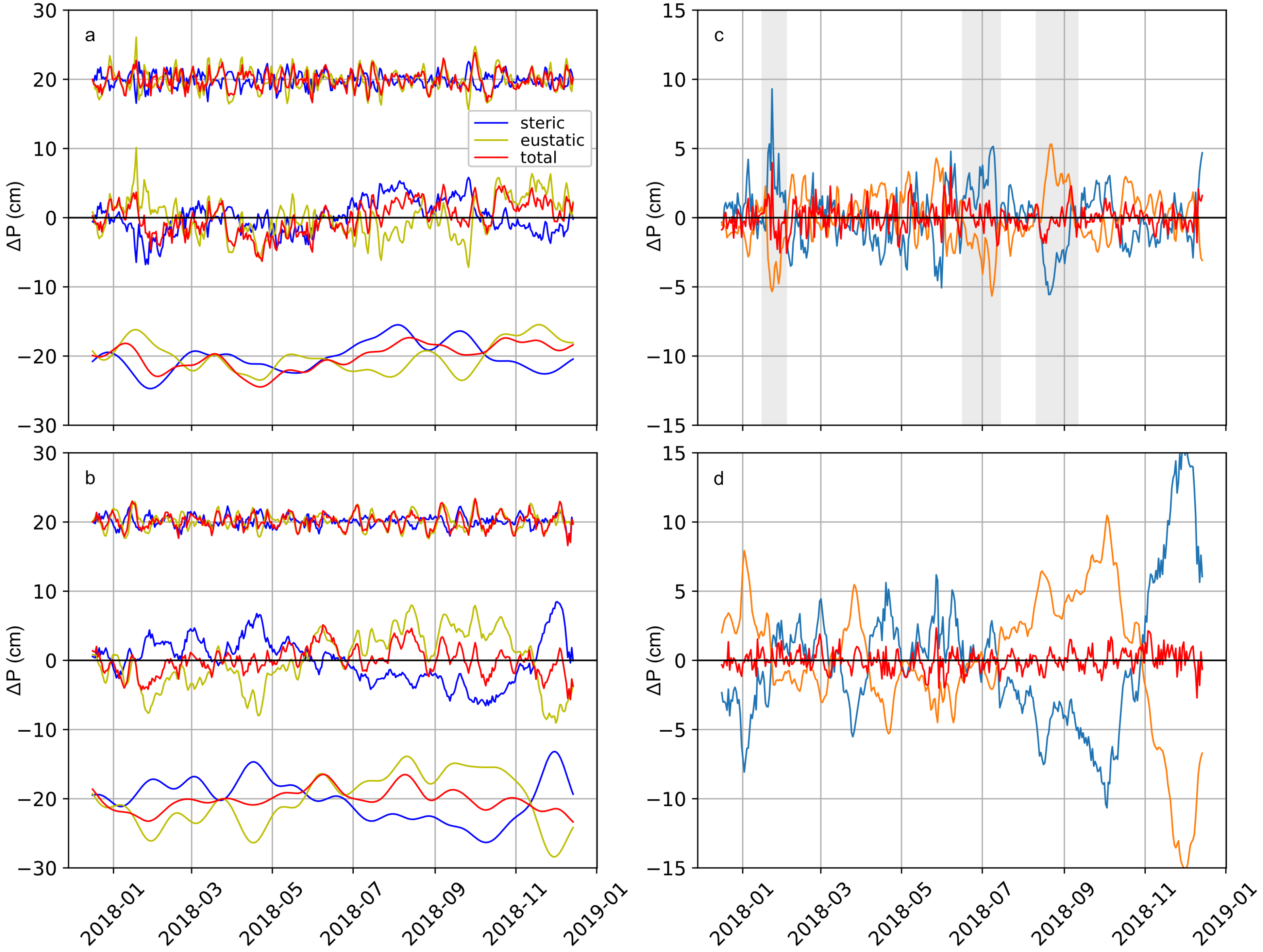
a
b
c
d
steric
eustatic
total
ΔP (cm)
ΔP (cm)
ΔP (cm)
ΔP (cm)
30
20
10
0
−10
−20
−30
15
10
5
0
−5
−10
−15
2018-01
2018-03
2018-05
2018-07
2018-09
2018-11
2019-01

Figure 4.2 a) Bottom pressure anomaly (red), eustatic component (yellow), and steric component (blue) from December 16, 2018 – December 15, 2019 for a shelf location at 200 m depth, marked by the yellow triangle in Figure 4.1a. Curves with a positive offset have been high-pass filtered with a 30 day cutoff and curves with a negative offset have been low-pass filtered with a 30 day cutoff. b) The same pressure components for a near-trench location at 2000 m depth, marked by the yellow triangle in Figure 4.1a. c) The unfiltered differences in bottom pressure anomaly and components for the 200 m depth location relative to another location at the same depth, marked by the yellow triangles in Figure 1a. Gray shaded intervals mark the presence of ramp-like signals in the total pressure anomaly difference, as discussed in the text. d) Unfiltered pressure differences for the 2000 m location relative to another location at the same depth, marked by the yellow stars in Figure 4.1a.

On the lower slope and near the trench, the steric component mostly acts to compensate the eustatic component, with only limited exceptions. This is visible in the pressure component time series from a representative 2000 m depth location shown in Figure 4.2b, wherein low-frequency signals dominate and the eustatic and steric components are nearly sign changed versions of one another, with the total anomaly emphasizing the differences between the two where it deviates from zero. At this greater depth, the pressure components also distinguish themselves in having clear, coordinated intervals of deviations from zero, whereas shelf locations exhibit more consistent fluctuations about zero. For depths in between these two end members (i.e., locations along the continental slope), a hybrid behavior is observed, with the lower slope more resembling the trench behavior and the upper slope more resembling the shelf behavior.

For the detection of SSEs using the methods of Fredrickson et al. (2019) and similar (Chapter 2), it is important to consider the pressure differences between two locations at comparable depths. Thus, in Figure 4.2c we plot the difference in total anomaly, the eustatic difference, and the steric difference between two locations at 200 m depth. As anticipated from previous studies, the difference in total pressure anomaly is low amplitude and fluctuates around zero. For the most part, the eustatic and steric differences also have modest amplitudes, but there are coherent intervals for which this is not the case. In the example shown in Figure 4.2c, the clearest of these intervals occur in February, June-July, and again in August. Of particular relevance to the misidentification of SSEs (Chapters 2 & 3), these intervals of elevated amplitude in the eustatic and steric differences correspond to ramp-like signals in the difference of the total pressure anomaly, which steadily decreases in the February event, decreases again in the June-July event, and then increases in the August event.

At 2000 m depth, the difference of the total pressure anomaly is again seen to have a low amplitude that fluctuates about zero (Figure 4.2d). Excursions in the eustatic and steric differences are more dramatic than seen on the shelf, some in excess of 10 and even 15 cm, and these two differences anticorrelate even more strongly than seen in the components at their respective sites. Assessing these more frequent and longer lived excursions presents a complex picture as to when these events do or don't correspond to a ramp-like signal in the total pressure difference. Those sustained for the longest durations observed, on the order of 2 months or longer, do not produce distinctive ramps, while shorter examples on the order of a week to a month often, but not always, do.

4.3.2 Pressure effects from mesoscale eddies

Some instances of large eustatic and steric differences between matched-depth locations can be linked to the presence of an eddy at one of the locations. Figure 4.3 shows total pressure anomaly and component extractions for select locations along the path of a warm-core eddy that originated on the mid slope at ~46.5º N on February 11, 2019, traveled south along the slope, and terminated beyond the trench at ~45º N on April 22, 2019, as depicted in Figure 4.1a. The total pressure anomalies along the track (Figure 4.3a-d) do not show any distinctive characteristics reflecting the presence of this eddy. However, the eustatic components exhibit positive anomalies around the time of the eddy’s passing – as expected – with the amplitude and duration a function of the eddy’s size, trajectory, and speed at that time. These eustatic anomalies (i.e., the pressure generated by the eddy’s SSH expression) are largely compensated by steric anomalies of comparable magnitude. This behavior is consistent not only between locations along the eddy track considered in Figure 4.3, but also between other warm core eddies on the Cascadia margin considered throughout all model years used in this study.

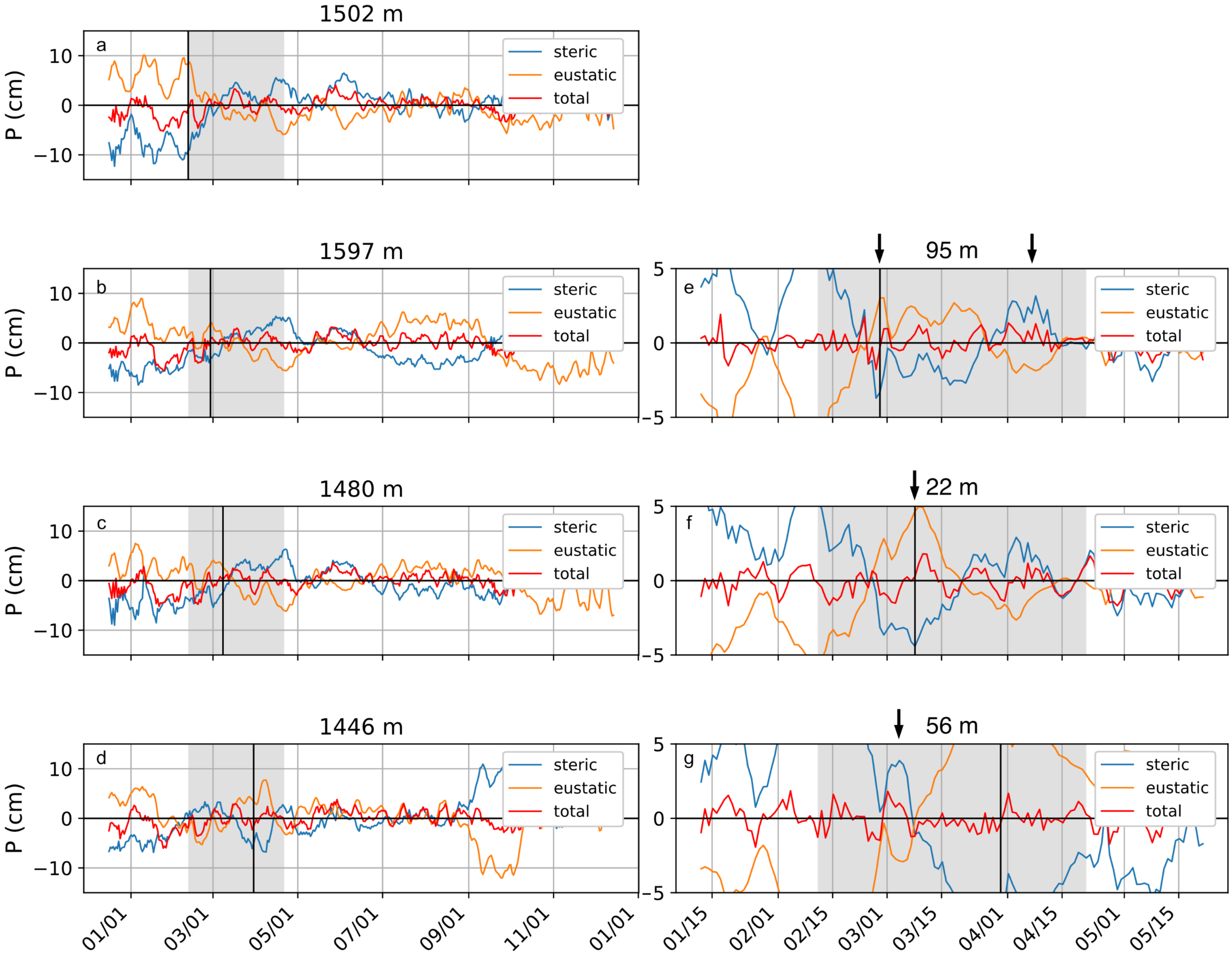
1502 m
a
1597 m
b
1480 m
c
1446 m
d
95 m
e
22 m
f
56 m
g
steric
eustatic
total
P (cm)
10
0
−10
5
0
−5
01/01
03/01
05/01
07/01
09/01
11/01
01/01
01/15
02/01
02/15
03/01
03/15
04/01
04/15
05/01
05/15

Figure 4.3 Total pressure anomaly and component extractions from select locations along the track of a warm-core eddy, which originates on February 11, 2019 and terminates on April 04, 2019, with track and moorings shown with red markers in Figure 4.1a. a-d) Time series of total pressure anomaly (red), eustatic component (yellow), and steric component (blue) at the locations marked in Figure 4.1a for the entire model year. The location depth is listed above each panel, the gray shaded region marks the time interval of the eddy's entire duration, and the vertical black bar indicates the time at which the eddy overlies the location. e-g) Differences in total pressure anomaly (red), eustatic difference (yellow), and steric difference (blue) of (b-d) relative to (a) for a narrower time window that extends only 30 days before/after the start/end of the eddy period. The depth difference as an absolute value is listed above each panel, the gray shaded region marks the time interval of the eddy's entire duration, and the vertical black bar indicates the time at which the eddy overlies the location. Arrows indicate example intervals during which SSE-like ramps are seen in the total pressure anomaly differences.

Considering instead the differences in pressure anomaly and components for the same locations along the eddy track relative to a matched-depth location (marked as 'A' in Figure 4.1a), ramp-like signals are frequently seen concurrent with the eddy's presence at a given location (Figure 4.3e-g). While the steric and eustatic differences still oppose one another, the eustatic difference consistently leads the steric difference – only by a few days, but enough to drive the total anomaly difference and generate a ramp. In the case of the representative warm-core eddy in Figure 4.3, the eustatic difference is positive because of the presence of the eddy at the time and location of interest and its absence at the reference location. In turn, the ramps generated in the total anomaly differences are also positive.

In Figure 4.4, a cold-core eddy is instead considered, which originated on the mid slope at ~46° N on August 30, 2018, traveled north along the mid and lower slope, and terminated in the north of the subdomain at ~47.5° N on December 04, 2018. As with the warm-core eddy example, there are not any distinctive signals in the total pressure anomaly that might indicate the eddy's passing. Again as anticipated, the eustatic component shows a negative excursion at the times of the eddy's passing that is consistent with a cold-core eddy's SSH depression and is in large part compensated by the steric component. In the pressure differences – relative to a matched-depth location – there are dramatic excursions in the eustatic and steric components, which mostly cancel each other out but leave behind a negative amplitude ramp in the total pressure anomaly.

Inspecting the pressure extractions outside the period of the eddy's passing (Figures 4.3 & 4.4), one can identify a number of different coherent signals in the eustatic and steric components, and their differences. Likewise, the broader SSH fields are highly dynamic in time and space (Figure 4.5), demonstrating a complex, interactive circulation field that is oversimplified by focusing on one eddy at a time. For example, in the pressure extractions and differences from the first two moorings of the cold-core eddy example, beginning in the first week of November and ending in early December, when a positive eustatic excursion arises (Figure 4.4a,b). In the corresponding SSH snapshots (Figure 4.5e,f), one can see a warm core eddy beginning to spin up, fluctuating in amplitude. And in the pressure difference (Figure 4.4e) the eustatic component is initially larger at the first mooring before being overtaken by the eustatic component at the second location. The steric component difference lags the eustatic behavior slightly, with opposite sign, resulting in first a negative and then a positive ramp in the total anomaly difference.

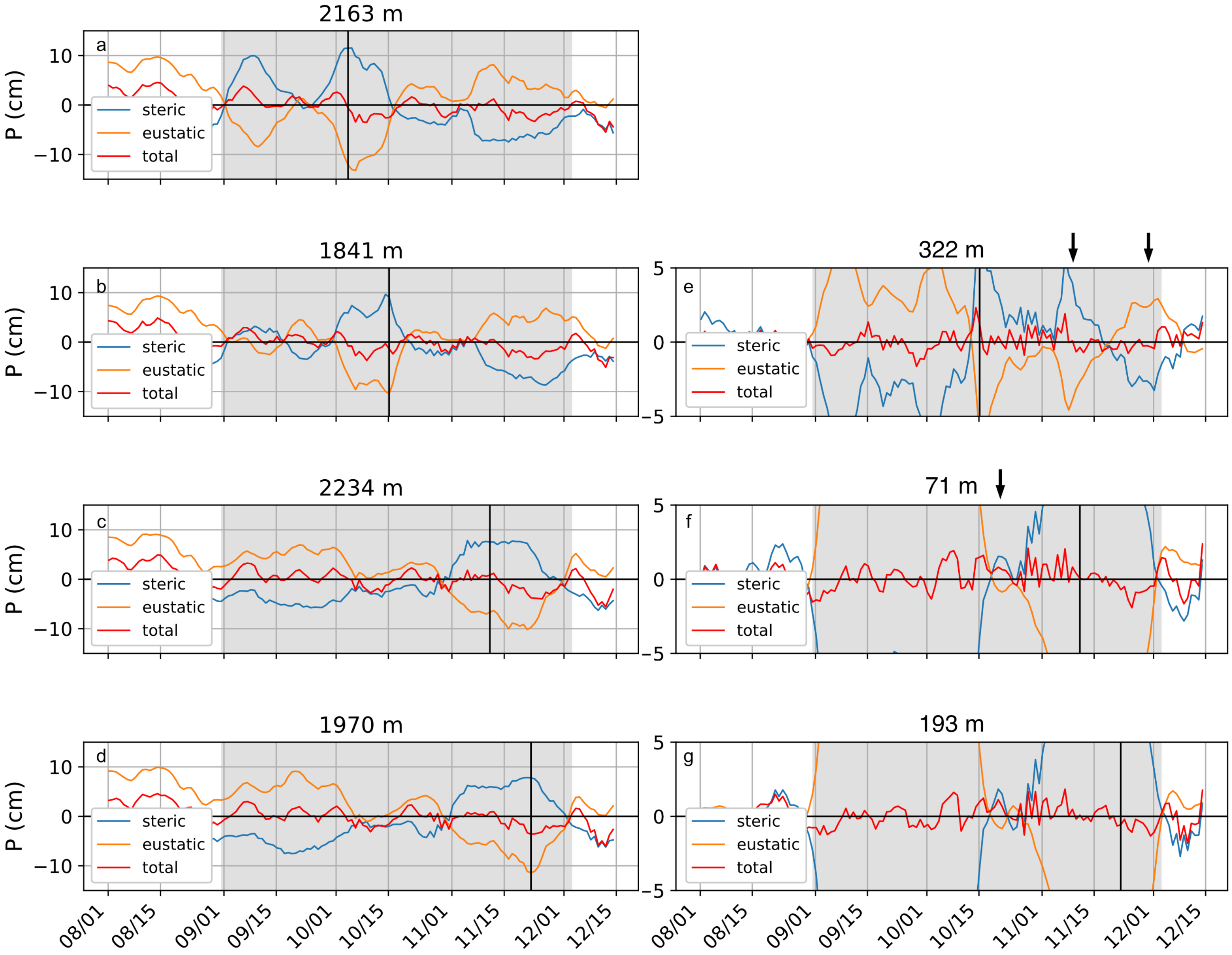
2163 m
a
1841 m
b
2234 m
c
1970 m
d
322 m
e
71 m
f
193 m
g
P (cm)
10
0
−10
5
−5
steric
eustatic
total
08/01
08/15
09/01
09/15
10/01
10/15
11/01
11/15
12/01
12/15

Figure 4.4 As in Figure 4.3, but for a cold-core eddy that originates on August 31, 2018 and terminates on December 04, 2018, with track and moorings shown with red markers in Figure 4.1a.

4.4 Discussion

4.4.1 The impact of eddies as a function of water depth

The strong relationship between the eustatic pressure component and the total anomaly seen in Figure 4.1d (particularly on the shelf) and in Figure 4.2a,b is evidence of the direct impact sea surface height anomalies have on the bottom pressure over a range of depths. However, we see that in deeper waters off the shelf this relationship becomes more complicated, with long period SSH changes not well reflected in the total pressure. The relationship between steric pressure and total anomaly is restricted to low periods only and is strongest on the shelf. Even so, the strength of the relationship fluctuates through time.

Eddies on the shelf seem to largely act to disrupt the relationship between the eustatic component and total anomaly, triggering a steric response (Figure 4.2a). On the slope and near the trench, where this relationship has already broken down, the effect is instead to amplify the anticorrelation between the eustatic and steric components, resulting in a total anomaly with far lower signal amplitudes than do the components at the time of the eddy’s passing (Figure 4.2b). In conjunction with the temporally-variable correlation apparent visually between the total pressure anomaly and the steric component at periods > 30 days, this suggests the steric pressure anomaly to be strongly linked to spatiotemporally dynamic circulation processes, such as eddies, which seem to notably alter the water column structure as they advect through the domain. What other processes may induce these steric responses warrants further study.

4.4.2 Pressure and component differences

The differences in eustatic and steric components between matched-depth locations are remarkable for their large amplitudes relative to the total pressure anomaly differences. This shows that despite dramatic differences in water column structure (steric) and SSH (eustatic) between two sites at comparable depths, those component differences are nonetheless strongly anticorrelated over distances of hundreds of kilometers and ultimately cancel out to produce a nearly net zero total pressure anomaly. Further, for matched-depth locations, this anticorrelation between component differences is even stronger than that of the steric and eustatic components themselves for either site. All of this suggests that margin-parallel eustatic and steric gradients are in balance with one another, so differences in SSH are compensated by a restructuring of the water column rather than inducing a volumetric flow.

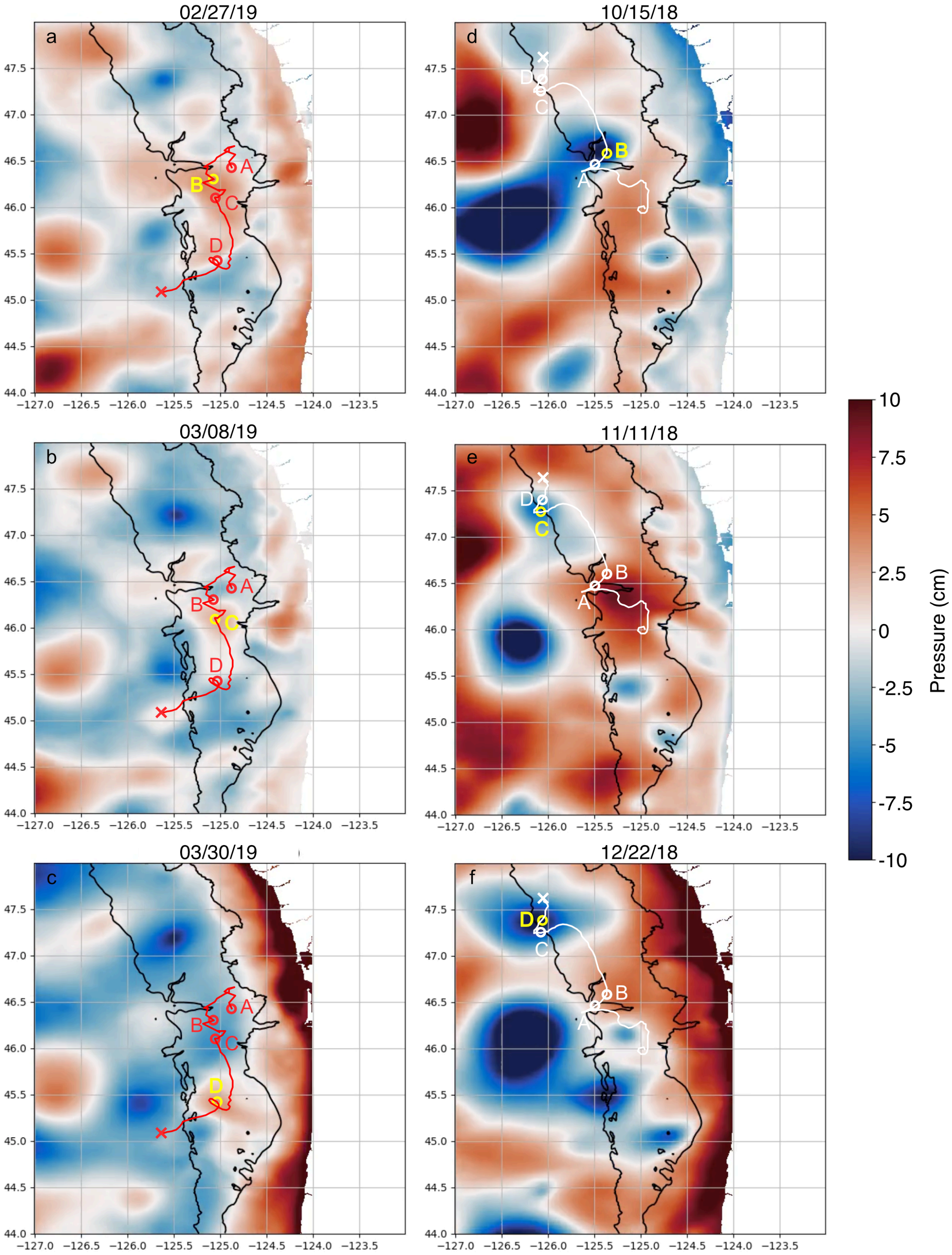

Figure 4.5 Maps of the model's sea surface height field at the times indicated above each panel, corresponding to the passage of the warm-core eddy in a) Figure 4.3b, b) Figure 4.3c, and c)

Figure 4.3d, and the passage of the cold-core eddy in d) Figure 4.4b, e) Figure 4.4c, and f) Figure 4.4d. In each panel, the corresponding extraction location and letter are colored gray.

4.4.3 Relevance for SSE studies

The eddies examined in this study suggest that these mesoscale features are capable of generating SSE-like ramps that persist through differencing with a depth-matched location, with the sign of the eustatic difference determining the sign of the ramp. Positive eustatic difference excursions generate positive ramps, indicative of subsidence if misinterpreted as tectonic deformation. Negative eustatic difference excursions generate negative ramps, indicative of uplift. The numerical modeling from Fredrickson et al. (2019) shows that SSE deformation causes uplift nearer the trench and subsidence closer to shore, from which one can envision several false detection scenarios (Chapter 2). At near-trench sites, a passing eddy could induce uplift-like signals if the matched-depth reference station is influenced by a warm-core eddy or if the other station(s) is influenced by a cold-core eddy. At mid-upper slope sites, an eddy could induce a subsidence-like signal if the depth-matched reference station is influenced by a cold-core eddy or if the other station(s) is influenced by a warm-core eddy. More complex situations, such as a single eddy overlying both reference and observation stations, can be avoided by requiring a spacing away from the reference location greater than the diameter of these features (~100 km).

The eddies studied here suggest a characteristic time for which an eddy produces a ramp-like signal in the pressure differences. When an eddy passes through a given region over a period of 1~3 weeks, ramps often result, while longer durations are more often characterized by relatively flat pressure differences. This indicates that the margin-parallel eustatic and steric gradients discussed above require a finite period to recover after perturbation but that they are able to do so for slower-moving eddies even during their passage.

As demonstrated previously in SSE pressure studies (Fredrickson et al., 2019; Inoue et al., 2021), there are depth-dependent along-strike separation and depth-difference scales for which differencing two given bottom pressure anomaly time series yields a signal amplitude below a given threshold (i.e., spatial relationships for which the technique works well). Though only a few examples are considered in this study, we can nonetheless see in the pressure differences (Figures 4.3e-g & 4.4e-g) that the eustatic and steric components have very different scales than those seen in the total pressure anomaly. Additionally, from our investigation of eddy pressure signatures, we can infer that these relationships are largely controlled by eddy spatial and temporal scales. Though a comprehensive analysis is not within the scope of this study, these relationships could be used to determine depth-dependent characteristic scales of processes that inhibit the effectiveness of depth matched differencing (namely eddies) and compare these scales to those expected from SSE deformation.

4.5 Conclusions

Though modest in scope, the eddy case studies presented here demonstrate a link between mesoscale eddies on the continental margin and seafloor pressure perturbations of great interest for tectonic studies. Without obvious restrictions in time and space, these eddies are capable of generating ramp-like signals much like those expected of SSE deformation, particularly when considering pressure differences, as is a common practice in the field. These examples also suggest a link between the eustatic expression of the eddy and the sign of the ensuing ramp, which shows promise for identifying regional eddies in satellite altimetry data and using them to corroborate or contradict the inference of SSE deformation. Further work in this direction has the potential to characterize key identifiers for the generation of other tectonic-like pressure signals. Of particular interest are features such as internal tides and coastal trapped waves.

4.6 Acknowledgements

We thank Elizabeth Brasseale of Scripps Institution of Oceanography and Jake Steinberg of Woods Hole Oceanographic Institution for their discussion and suggestions in early iterations of this analysis. We likewise thank Susan Hautala of the University of Washington for her input and ideas for expansion on a draft of this manuscript.

Chapter 5:

A Method for Observing Tilt and Correcting Drift with a Triaxial Accelerometer

Erik Fredrickson[1], William Wilcock[1], Michael Harrington[2], Geoff Cram[2], James Tilley[2], Derek Martin[2] and Justin Burnett[2]

[1]School of Oceanography, University of Washington, Seattle, Washington, USA
[2]Applied Physics Lab, University of Washington, Seattle, Washington, USA

5.0 Abstract

We present observations from two field deployments of a calibrated tiltmeter that we name the Self-Calibrating Tilt Accelerometer (SCTA). The tiltmeter is based upon a triaxial quartz crystal accelerometer; the horizontal channels used to measure tilt are periodically rotated into the vertical to obtain a measurement of the acceleration of gravity. Changes in the measured total acceleration are ascribed to drift in the vertical sensor and used as calibrations for removing that same drift from the tilt time series observed between calibrations. Changes in the span (sensitivity) of the accelerometer channels can also be measured but calibrating them pointing up and down. A 3-year test on the seafloor at Axial Seamount show that the calibrations are consistent with a linear-exponential model of drift to ~0.5 μg (μrad). A 15-month test in a stable vault at Piñon Flat Observatory was complicated by seasonal temperature variations of >5°C; the calibrations are consistent with a linear-exponential model of drift to ~2 μg when temperature and temperature time-derivative dependence is included. At Axial Seamount the calibrated tilt time series was impacted by platform settling for the first 2 years. After repositioning the tiltmeter, the calibrated observations were consistent for the final year with the tilt observed on a nearby LILY tiltmeter. At Piñon Flat Observatory, the calibrated tilt observations were impacted by thermal deformation of the SCTA assembly. A future test in a thermally and tectonically stable borehole will be required to assess the accuracy of the SCTA.

5.1 Introduction

Geodetic measurements complement seismic observations, because together they provide a comprehensive view of tectonic processes (e.g., Bevis et al., 2001; Bock et al., 1993; Feigl et al., 1993; Kreemer et al., 2014; Massonnet et al., 1993; McCaffrey, 2005). On land, spaced-based Global Navigation Satellite System (GNSS) and Interferometric Synthetic Aperture Radar (InSAR) geodetic techniques have revolutionized studies of plate boundary and volcanic deformation by providing observations with spatial and temporal resolutions unattainable with other approaches (Burgman and Thatcher, 2013; Poland and Zebker, 2022). However, this revolution does not extend to the seafloor because the oceans do not transmit the electromagnetic waves on which the spaced-based techniques are based. Thus, the challenge of seafloor geodesy provides impetus for continued development of traditional geodetic measurements that are presently of relatively minor importance on land (Burgmann and Chadwell, 2014).

One long established geodetic measurement is tilt, the change in attitude of a surface. There are two broad classes of tiltmeters (Agnew 1986). Long baseline units measure the relative change in elevation of two connected liquid surfaces up to hundreds of meters apart. Short baseline units measure change in the tilt of a small platform, either by sensing the movement of a bubble within a conductive fluid trapped beneath a convex surface with electrical techniques or by measuring the deflection of a vertical pendulum using electrical or optical approaches.

By nature of their size, long baseline tiltmeters are relatively unsusceptible to hyper local effects like platform settling and small block motion, making them suitable for observations of secular strain. They have high resolution and can achieve low drift rates on the order of 1 μrad/yr (Wyatt et al., 1984). However, there are many applications in which long-baseline instruments are impractical because of their cost, size, and installation needs, such as for rapid response, difficult-to-access locations, and settings where many sensors are required to resolve complex deformation. On the seafloor, only one long-baseline tiltmeter deployment has been attempted (Anderson et al., 1997). Over two months in 1994, an installation at Axial Seamount measured variable long-period signals of several µrad/day that could not be categorized between endpoint settling, instrumental drift, and volcanic inflation. While the authors identified approaches to improve the stability of future deployments, no further experiments were attempted.

Short baseline tiltmeters are easier to deploy but the cheaper bubble tiltmeters experience significant instrumental drift of 10-100 µrad/yr that is unique to each individual instrument and can vary significantly over the deployment interval. They are most frequently deployed to monitor rapidly deforming volcanoes (e.g., Dvorak & Dzurisin, 1997). High-resolution tiltmeters with lower inherent drift rates have also been developed for borehole applications (Chawah et al., 2015; Jahr et al., 2006) but the technology is expensive, and drift can result from temperature dependence and the mechanical leveling systems needed for instruments with a small dynamic range.

Significant efforts have been made to develop short baseline tiltmeters for the seafloor (Sakata and Shimada, 1984; Shimamura and Kanazawa, 1988; Anderson et al., 1997; Tolstoy et al., 1998; Fabian and Villager, 2007; Takamori et al., 2011; Shiobara et al., 2021; Hensch, 2009) and they have detected short-term geological signals. Fabian and Villanger (2008) describe a 1-year experiment with a single tiltmeter in the Logachev hydrothermal field that recorded large changes in tilt of up to 10 mrads, possibly resulting from of earthquakes and nearby mass wasting. Cabled tiltmeters on the Ocean Observatories Initiative (OOI) Regional Cabled Array

(RCA) measured signals of 100s μrads during the 2015 eruption of Axial Seamount that constrained the timing and direction of dike propagation (Nooner & Chadwick, 2016). Shiobara et al. (2021) observed tilt signals of up to a few 10s of μrads associated with shallow slow-slip events offshore Japan. However, as on land, drift limits the capabilities to measure longer term signals. For example, at the end of a 2-month deployment at Axial Seamount, the combined drift and settling rates of four short period sensors were ~1 μrad/day, sufficiently low to detect volcanic events but not to measure inflation (Tolstoy et al., 1998). Likewise, the longer-term volcano inflation tilt signals on the OOI RCA tiltmeters have proved challenging to interpret (Fredrickson et al., 2019), possibly because of instrumental drift.

Several short baseline tiltmeters have also been developed for seafloor boreholes (Duennebier et al., 1987; Sacks et al., 2000; Kitada et al. 2013; McGuire et al., 2018). A tiltmeter is included in the geophysical packages deployed in the NanTroSEIZE boreholes in Nankai Trough subduction zone offshore Japan (Kitada et al., 2013), but did not detect signals from the small slow slip events that were observed with formation pressure measurements (Araki et al., 2017). Data from a borehole tiltmeter deployed in the Cascadia subduction zone showed no evidence that slow slip events were triggered by the dynamic stress from teleseismic earthquakes (McGuire et al., 2018).

The experiences from past deployments of short baseline tiltmeter provide clear motivation for continued development of approaches to detect small transient and secular signals. Statistical techniques are available to isolate drift from physical tilt signals, but they require initially low drift rates on the order of a few μrad/yr (Furst et al., 2019). Because of drift, short-baseline tiltmeters are often considered reliable only for measuring short-period and/or large-amplitude signals, despite the nanoradian resolution of modern sensors (Jahr et al., 2009).

Eliminating drift from these instruments opens up significant opportunity for observing subtle deformation signals, particularly if they can be deployed in stable boreholes where environmental signals are damped.

Here we present a new approach to reducing the drift in tilt time series measured by the horizontal channels of a high-resolution quartz crystal three component accelerometer. In our instrument, the Self-Calibrating Triaxial Accelerometer (SCTA), the horizontal channels are periodically calibrated against local gravity (*g*) by temporarily rotating them into the vertical. We describe the SCTA and evaluate its capabilities with two deployments: one on the seafloor of a submarine volcano and the other on land in a vault at a geophysical observatory.

5.2 Instrumental Approach

5.2.1 Calibration principle

The SCTA uses a Quartz Seismic Sensors, Inc. triaxial accelerometer with a full scale of ± 3*g* and a resolution of parts per billion. The accelerometer works by measuring changes in the oscillation frequency of three quartz crystal resonators as they are strained by accelerations in orthogonal directions. The oscillation frequency of a fourth unstrained quartz resonator measures temperature and is used to provide temperature corrections to the frequency outputs of the accelerometers. In the absence of other signals, the accelerometer's three channels measure *g*. A factory calibration internally corrects the outputs of the three accelerometers for small orientation offsets from orthogonality so that the scalar value of *g* is independent of orientation. Although quartz crystal resonators are remarkably sensitive to changes in load, they are well known to undergo significant instrumental drift (Polster et al., 2009; Watts & Kontoyiannia, 1990). This drift is often characterized by a combination of linear and exponential functions, but the amplitudes and time constants vary between sensors and between deployments of the same sensor, so cannot be predicted.

To avoid ambiguity, we will refer to the SCTA's three accelerometer channels as capital X, Y, and Z, and refer to coordinate system axes as lowercase x, y, and z, with x and X, and y and Y, in vertical planes. When X and Y are nearly horizontal and Z thus, nearly vertical – the measurement orientation (Figure 5.1a) – the horizontal channels will measure accelerations

$$a_X(t) = g\sin\theta_X(t) + \sigma_X(t) \approx g\,\theta_X(t) + \sigma_X(t) \tag{1}$$

$$a_Y(t) = g\sin\theta_Y(t) + \sigma_Y\,(t) \approx g\,\theta_Y(t) + \sigma_Y\,(t)$$

where θ_X is the angle between X and x, θ_Y is the angle between Y and y, σ_X and σ_Y are the drift for each channel and t is time. For small tilts, these channels are linearly dependent on tilt but are also sensitive to drift. Conversely, the channel in the vertical measures

$$a_Z(t) = g\cos\theta_Z\,(t) + \sigma_Z(t) \tag{2}$$

where θ_Z is the angle between Z and z. The total acceleration, a_T can be written from the three orthogonal accelerations as

$$a_T(t) = \sqrt{a_X^2 + a_Y^2 + a_Z^2} \approx g + \cos\theta_Z\,(t)\,\sigma_Z(t) \approx g + \sigma_Z(t) \tag{3}$$

Provided the Z channel is within a few degrees of vertical, it will, to a good approximation, be the sum of the magnitude of g and the accumulated drift of the vertical channel since the factory calibration.

If a horizontal channel is temporarily rotated into the vertical at the start and end of a measurement interval, then provided g is constant, the change in the total accelerations between the two rotations will following equation (3), be a measure of the drift of that channel, σ, over the measurement interval. This can be expressed for the two horizontal channels

$$a_T^X(t_k) = g + \sigma_X(t_k) \tag{4}$$

$$a_T^Y(t_k) = g + \sigma_Y(t_k)$$

where the superscripts X and Y indicate the vertical channel when the measurement of total acceleration is obtained and t_k is the time of the k^{th} calibration. This drift, measured in the vertical orientation, but can be applied to measurements in the horizontal by making assumption that the drift is independent of orientation, that is that the measurement span of the accelerometer does not change with time.

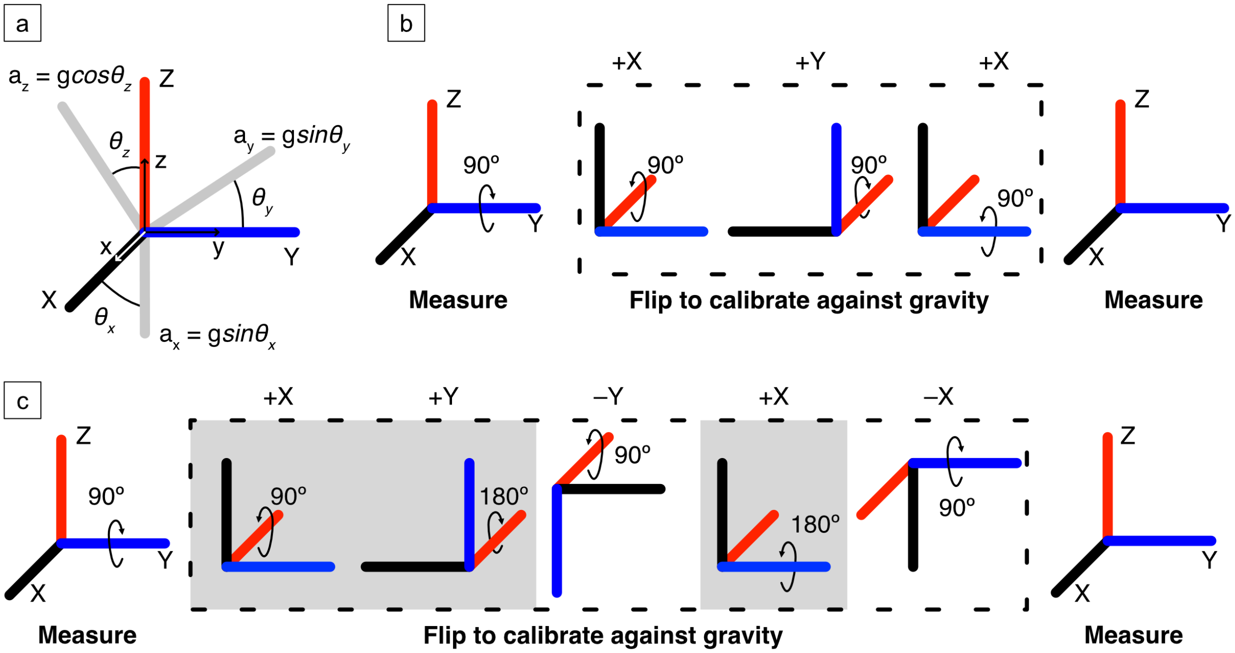

Figure 5.1. (a) Notation used to indicate accelerometer orientations when making tilt measurements (b) Schematic of the 3-orientation rotation sequence used during calibrations prior to August 9, 2021. The colors correspond to the same axes throughout the sequence. Arrows indicate the sense of rotation applied to get to the next orientation. (c) As in (b), but for the 5-orientation rotation sequence used for all calibrations on and after August 9, 2021. Gray shading indicates the orientations common to the sequence shown in (b). We use notation of the form +X and -X to indicate whether the positive or negative X channel is positively upwards.

Considering just one interval between calibrations, the difference between the start and end calibrations can be used to apply a linear drift correction. Since it is impractical to return the horizontal channels to the same orientation after a calibration, it is necessary to stitch the segments together when there are multiple measurement intervals. This can be done by applying simple offsets to linearly corrected segments but also provides an opportunity to fit a more complex linear plus exponential drift model and account for residual temperature sensitivity.

5.2.2 SCTA design

The accelerometer casing is a ~10-cm-long cylinder of radius ~1.5 cm, with the Z axis along the axis of the cylinder and the X and Y axes perpendicular to the cylinder axis in a right-handed configuration. The SCTA houses the accelerometer within a two-axis gimbal system that normally holds the Z channel vertical (Figure 5.2a-b). The axis of the inner gimbal is parallel to the Z channel and that of the outer gimbal parallel to the X channel. The outer gimbal is used to rotate the Z channel into the horizontal while the rotation of the inner gimbal controls whether the X channel or Y channel is vertical. The rotations are driven by stepper motors from Lin Engineering and the accelerometer held in place between rotations by electromagnetic brakes from Stock Drive Products. Heat generation is minimized by powering off the motors between calibrations and setting the brakes to power-off engage.

In our testing we employed two rotational sequences (Figure 5.1). The first comprises a quarter rotation of the outer gimbal, a quarter rotation of the inner gimbal, and then a reversal of the rotations of the inner and outer gimbals (Figure 5.1b). This results in a 3-orientation calibration sequence in which +X, +Y, and +X are sequentially moved into the vertical for calibrations before the accelerometer returns to the measurement orientation. The second rotational sequence is a 5-orientation sequence in which +X, +Y, -Y, +X, and -X, are sequentially rotated into the vertical before returning to the measurement orientation (Figure

5.1c). This more complex sequence enables a calibration of the accelerometer span by measuring acceleration with each horizontal channel pointing both up and down. The ordering is imposed by the geometry of the SCTA's internal wiring which limits the rotations of each gimbal to ±90°. Because changes in the accelerometer orientation lead to repeatable short-term transients in the accelerometer output, it is important to maintain a consistent timing for the calibration sequences. For both sequences, the accelerometer is held in each orientation for 110 seconds and the gimbals rotated at a quarter turn per 10 seconds. As a check on consistency, both sequences include a two calibrations in the +X orientation which we term +X1 and +X2.

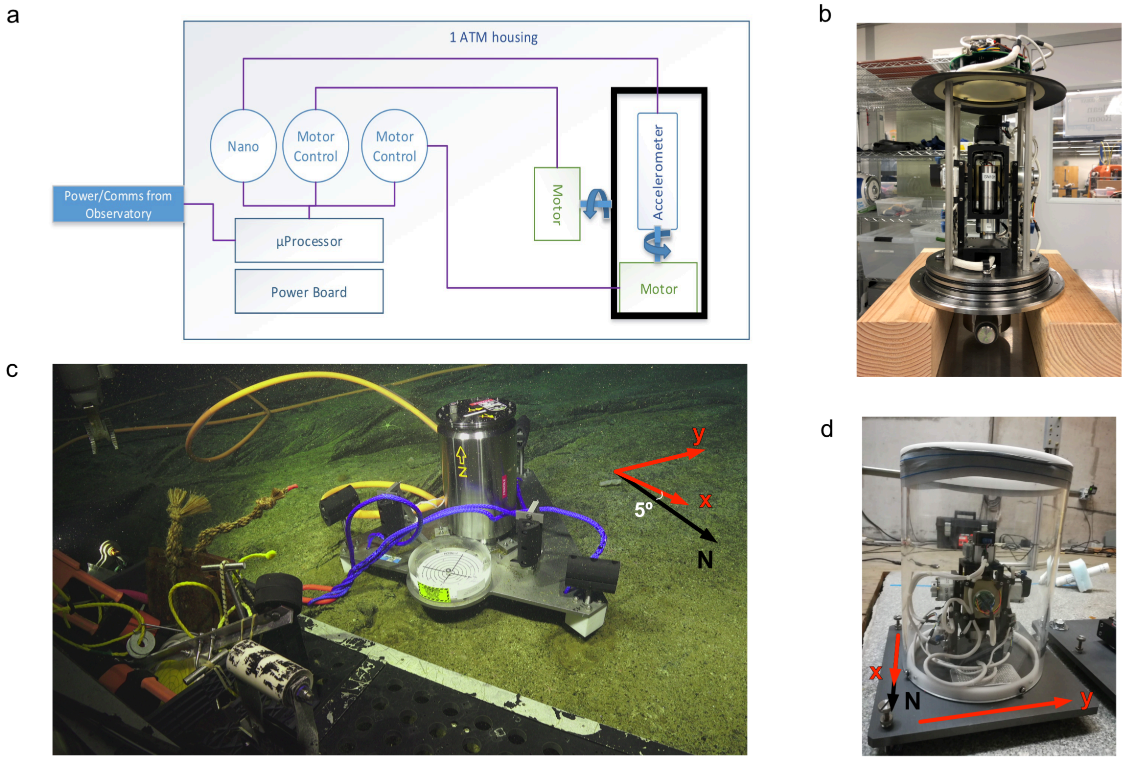

Figure 5.2. (a) Schematic of SCTA design showing the stepping motors that rotate the accelerometer, the motor control, Paroscientific Nano-Resolution frequency counting, the microprocessor and power boards. (b) Axial Seamount SCTA attached to the end cap before insertion into the pressure housing, (c) Axial Seamount SCTA on the seafloor at Location 1 showing the orientation of the X and Y channels (X at an azimuth of 355°). The leg that we inferred to be subsiding is on the left. At Location 2, the X channel was at an azimuth of 340° (d) Piñon Flat SCTA in the vault showing the orientations (X is north).

5.3 Field Tests

5.3.1 Axial Seamount

On July 6, 2018, the seafloor version of the SCTA was connected to the OOI RCA cabled observatory at the central caldera site of Axial Seamount at 45.955° N, 130.008° W (Figures 5.2c and 3b) using a remotely operated vehicle (ROV). Axial Seamount is an active undersea volcano on the Juan de Fuca Ridge and the current eruptive edifice for the Cobb Hotspot. The summit of the seamount is characterized by a 100-m-deep 8-km-by-3-km horseshoe-shaped caldera whose wall demarks an inward-dipping ring fault that meets a conjugate outward-dipping fault at 0.5–1 km depth (Wilcock et al., 2016). The volcanic system is characterized by a 14 km x 3 km central magma chamber at 1.1–2.3 km depth, with up to 1 km thickness (Arnulf et al., 2014). The main magma body is surrounded by several other shallow magma bodies and is underlain by a 3–5 km diameter region of stacked reflectors extending to 5 km depth that are interpreted to be a series of melt sills within a column of mush that feeds the upper crustal magma chamber.

Geodetic efforts have been ongoing here since 1987, starting with intermittent deployments of a bottom pressure recorder (Fox, 1993). There is a near continuous time series of calibrated bottom pressure observations that spans the three most recent eruptions in 1998, 2011, and 2015 (Chadwick et al., 2006; Nooner and Chadwick, 2009; Chadwick et al., 2012; Nooner and Chadwick, 2016). Each eruption is accompanied by several meters of subsidence and the eruptions occur when the caldera floor has reinflated back to a predictable level (Nooner & Chadwick, 2016). The most recent observations show that the caldera has recovered most of the deflation that occurred in 2015 but is presently inflating slowly with the next eruption predicted to be years away (Chadwick et al., 2022). The OOI RCA operates four cabled bottom pressure and tilt sensors that include a Jewell Instruments LILY tiltmeter with a dynamic range of 330 μrad and a resolution of 5 nrad. One of these instruments is located 40 m from the SCTA deployment site at a heading of 252° (Figure 5.3c).

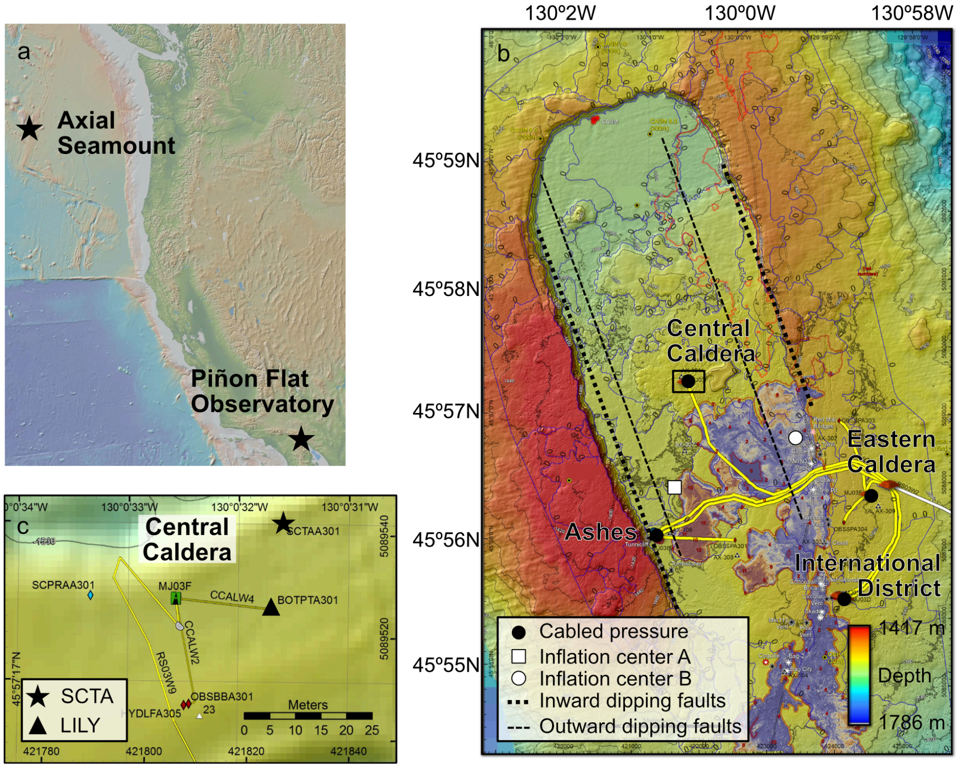

Figure 5.3. (a) Map showing the location of Axial Seamount and Piñon Flat Observatory. (b) Bathymetric map of the Axial Seamount summit caldera (courtesy of Deborah Kelley) showing the location the OOI RCA cables (white for the trunk line to the red primary node and yellow lines for cables to secondary infrastructure), cabled pressure sites (black circles), the approximate surface locations of inward and outward dipping faults (Hefner et al., 2021), and the center of inflation for two models of volcano/inflation deflation; inflation center A assumes no fault motion (Nooner & Chadwick, 2016) and inflation center B assume motion on an outward dipping ring fault (Hefner et al., 2020). A square box about the Central Caldera site shows the area of (c). (c) Map of the OOI RCA infrastructure at the Central Caldera site (courtesy of the OOI RCA) showing the deployment location of the SCTA and LILY tiltmeter.

The SCTA at Axial was housed within a titanium cylinder that was oriented vertically and attached to a triangular metal platform with three leveling feet that were adjusted by the ROV to level the housing within 1° (Figure 5.2c). Data from Axial were initially collected from

August 06, 2018 – September 10, 2020 (data streaming into the IRIS DMC did not start until October 10, 2018). We then moved the SCTA a few meters and resumed data collection from September 11, 2020 – August 27, 2021. The instrument was repositioned because one of the SCTA platform's feet appeared to be settling; there was an anomalously large, ongoing tilt signal on the Y channel and we found evidence of loose sediments after reinspecting the deployment video. Settling was supported by observations of sediment erosion around the subsiding foot when the sensor was moved. We refer to the initial deployment location as "Location 1" and the re-positioned location as "Location 2". Data were streamed to shore at 40 Hz and 8 Hz, with the high-rate data occasionally sequestered by the U.S. Navy, and archived in near-real time at the Incorporated Research Institutions for Seismology Data Management Center (IRIS DMC) as station AXCC2 on network OO.

At Axial Seamount Location 1, the SCTA did not collect data for 27 days of the 689 deployment, while at Location 2, data is missing for only 4 of the 350 days. The data gaps resulted from OOI Cabled Array outages and loss of software connectivity to the SCTA. Figure 5.4 shows representative examples of the observed acceleration and power spectra for the SCTA while in its measurement orientation for both Axial Seamount locations. The secondary microseism peak is clearly visible at both locations, for all channels, between 0.1–1 Hz . At Location 1, there is a pronounced peak in power at 0.05-0.06 Hz which we attribute to rocking due to the unstable footing (Figure 5.4b). The horizontal channels are also noisier at frequencies above the microseism which again may be indicative of platform instability. At Location 2, peaks at 2-3 Hz and just below 5 Hz may be related to mechanical resonances of the gimbal system. Bottom temperatures at Axial Seamount are very stable with internal temperature of the housing characterized by seasonal variations of 0.15°C (5.60-5.75°C) and a daily standard deviation of <0.05°C

In total, 125 calibrations of the SCTA were obtained at Axial Seamount; 65 at Location 1 (of which the first 24 were 3-orientation sequences before August 13, 2019, and the remaining 41 5-orientation sequences) (Table A3.1) and 60 calibrations at Location 2 (all 5-orientation sequences) (Table A3.2). The time between calibrations varied from a day to a month, with occasional longer intervals when communication with the SCTA was lost.

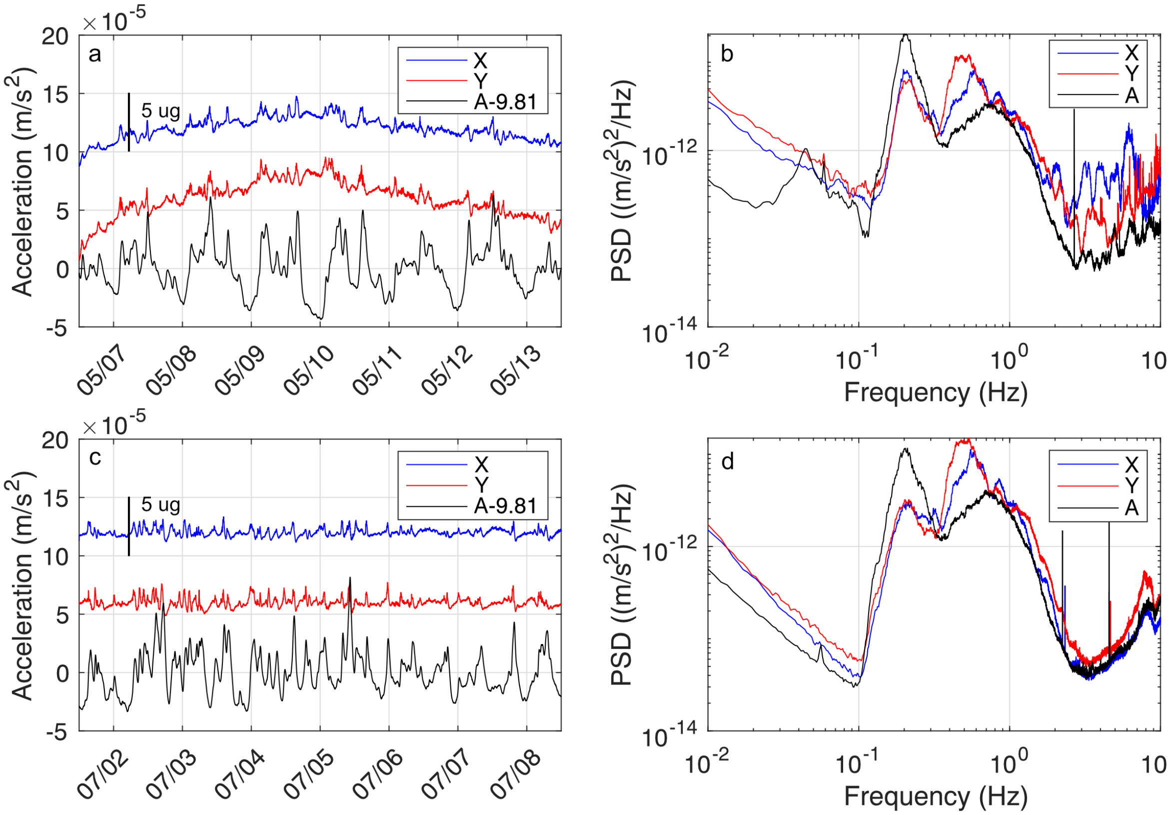

Figure 5.4. (a) Representative 6-days of data from Axial Seamount with the SCTA in the measurement orientation (with the Z channel in the vertical) at Location 1 (before relocating the instrument) starting 05/06/2019 12:00 GMT, showing X-, Y-, and Z-channel observations are plotted in blue, red, and black, respectively, after removing the mean and linear trend and decimating to 1 sample/minute. Vertical offsets are for display purposes only. (b) Associated power spectral density for the three channels, calculated without decimating the data and plotted with the same colors. (c-d) As in (a-b), but at Location 2 (after relocating the instrument) starting from 7/01/2018 12:00 GMT.

5.3.2 Piñon Flat Observatory

A second SCTA was operated at a terrestrial site, the Scripps Institution of Oceanography's Cecil and Ida Green Piñon Flat Observatory (PFO) at 33.611 N, 116.455 W (Figure 5.3a). PFO is located at the northern end of the Santa Rosa Mountains, some 30 km southwest of the city of Palm Desert, California. This site has relatively smooth topography (Wyatt, 1982) and is composed of granodiorite that grades from weathered sediment to crystalline rock within the first few meters of the surface (Foster, 1976). Though seismic activity is frequent due to the proximity of the San Andreas and San Jacinto fault systems, local deformation rates are low. Numerous deployments over several decades indicate tilt rates $\ll 1$ µrad/yr and strain rates $\ll 1$ µstrain/yr (Agnew, 2007; Wyatt et al., 1994), even during periods of high seismic activity (Agnew et al., 1989).

The SCTA operated at PFO was the prototype of the seafloor version. The configuration of the gimbals, stepper motors and brakes were identical to the instrument deployed at Axial Seamount but it was attached to a square plate with three leveling feet and shielded by an acrylic housing (Figure 5.2d). We deployed the SCTA in a sealed vault several meters beneath the surface, on a concrete slab and enclosed under a box of rigid foam insulation. Within the vault there are large seasonal temperature variations of >5°C (24.4-30.1°C) but after removing the seasonal trend, the daily variations have a standard deviation of ~0.001°C.

Data were collected from October 18, 2018 – January 16, 2020 at 40 Hz, stored on a local drive, and uploaded daily to the University of Washington for archiving. There were five data outages: one from February 14 – March 28, 2019 that was the result of a failure of the local computer (during this interval the instrument continued to run but no calibrations were performed), and four from March 31 – April 3, 2019, April 27 – 29, 2019, September 8, 2019, and December 25 – 29, 2019 that were each the result of local power outages at the site. Figure A3.1 shows a representative week of data in time and frequency space while the SCTA was in measurement orientation. In this quiet setting, Earth tides are visible in the time domain. The spectrogram is dominated by the microseism peak and shows increased amplitudes above 1 Hz which is a result of frequency counting noise (Webb and Nooner, 2016). A peak at 6-7 Hz a may be related to a mechanical resonance of the gimbals. A total of 32 calibrations were conducted at PFO (Table A3.3), of which the first 20 were 3-orientation sequences and the remaining 12 on and after August 9, 2019, were 5-orientation sequences.

5.4 Results

5.4.1 Calibrations Measurements

Figure 5.5a shows a representative 5-orientation calibration sequence from Axial Seamount Location 2. There are noticeable short-term transients immediately following the change in orientation (Figure 5.5b); the transients differ for each orientation and position in the calibration sequence but are repeatable between calibration sequences. We present calibrations obtained by averaging the acceleration over 30 s starting 60 s after the sensor has reached the calibration orientation, thus excluding the interval immediately after the accelerometer has moved when the transients are largest. However, because the transients are repeatable, the measurements of drift are not strongly sensitive to the interval selected.

Calibrations for the full deployment period at Locations 1 and 2 are shown in Figure A3.2 and Figure 5.6, respectively. These plots exclude occasional anomalous calibrations that are scattered throughout the deployment at Axial Seamount. The cause of the anomalous calibrations is unknown, but they may be a result of an intermittent mechanical problem in the sensor. They are easily identified because the total acceleration a_T is inconsistent with that obtained at other times. They are discussed further in Appendix 3 and shown in Figures A3.3-A3.5.

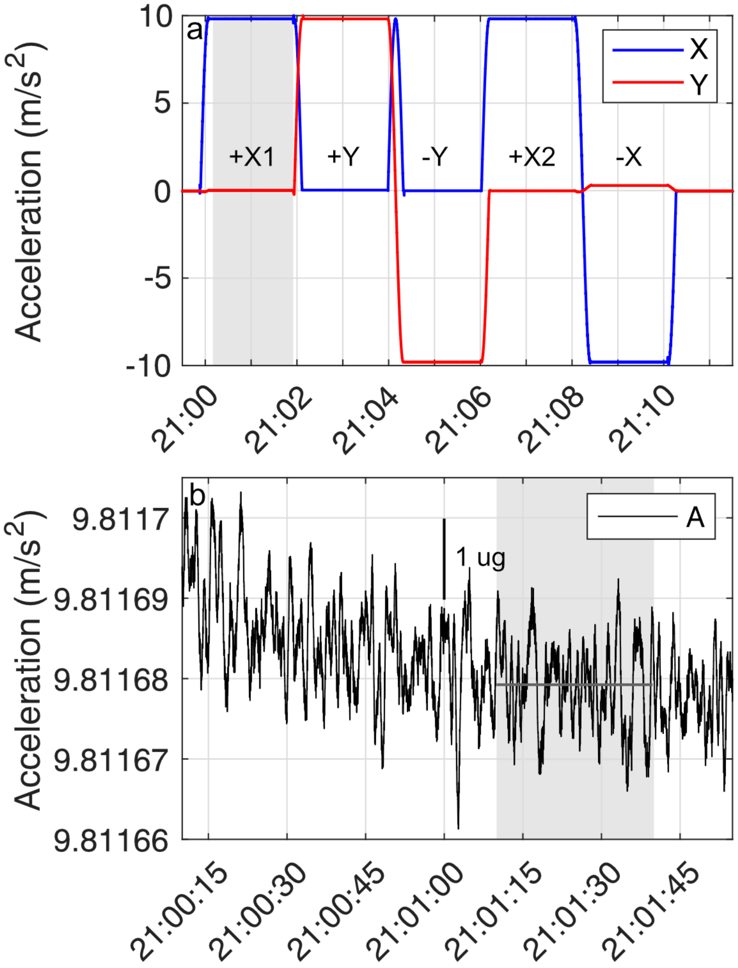

Figure 5.5. (a) X (blue) and Y channel (red) acceleration observations during a 5-orientation calibration sequence at Axial Seamount Location 2, with calibration orientations labeled. Gray shaded area indicates the time interval plotted in (b). (b) Total acceleration observed during the interval indicated in (a), after the sensor has stabilized in the +X1 orientation and prior to beginning the next rotation. Gray shaded area indicates the interval over which the acceleration is averaged to get a calibration value. The dark gray horizontal line indicates the calculated calibration value during the interval.

To characterize the drift on each channel for each location, we fit a simple exponential-linear model (Polster et al., 2009; Watts & Kontoyiannia, 1990) to each set of calibrations of the form

$$a_T^i(t) = b + ct + f \exp\left(\frac{-t}{h}\right) \tag{5}$$

where superscript i indicates the sensor orientation and position in the calibration sequence (i.e., +X1, +Y, +X2, -X, -Y), t is time, and the terms b, c, f, and h are constants determined by a least squares inversion. For Location 1, the switch from the 3-orientation to 5-orientation sequence leads to a change in timing of the +X2 calibration relative to the onset of the sequence (Figure 5.1), so we solve for different values of b on either side of this change.

Table 5.1 presents the calibration values and model misfits for Axial Locations 1 and 2 while the model misfits for each calibration are shown in Figures A3.2d, h and Figures 5.6d and h. The drift for all channels at both locations is characterized by the calibrations to better than 1 μg/yr. At Location 1, the span change over the period of 5-orientation calibrations is ~5 μg/yr for each channel while at Location 2 the change in span for the X channel is < 1 μg/yr, while the change in span for the Y channel is ~2.5 μg/yr.

Table 5.1. Calibration model parameters for equations (5) and (6) and misfit by location and orientation

		***b* - *g* (μg)**	***c* (μg/yr)**	***d* (μg/C)**	***e* (μg/(C/d))**	***f* (μg)**	***h* (day)**	**RMS misfit (μg)**
Axial Seamount Location 1	+X1	0.19	21.72	-	-	-26.50	2.40	0.37
	+X2	14.38 30.52[a]	21.97	-	-	-24.50	2.07	0.36
	-X	-226.15	20.08	-	-	-	-	0.97
	X1 span	-	5.40	-	-	-	-	0.67[c]
	X2 span	-	5.30	-	-	-	-	0.61[c]
	+Y	-131.10	45.63	-	-	-30.40	1.22	0.75
	-Y	9.09	40.88	-	-	-	-	0.70
	Y span	-	5.15	-	-	-	-	0.44[c]
Axial Seamount Location 2	+X1	42.17	16.61	-	-	-	-	0.30
	+X2	72.59	16.72	-	-	-	-	0.31
	-X	-247.24	17.34	-	-	-	-	0.44
	X1 span	-	-0.72	-	-	-	-	0.4[c]
	X2 span	-	-0.68	-	-	-	-	0.39[c]
	+Y	-28.54	31.86	-	-	-	-	0.36
	-Y	-44.05	29.60	-	-	-	-	0.58
	Y span	-	2.41	-	-	-	-	0.41[c]
Pinon Flat Observatory	+X1	-2029.0 -2034.56[b]	87.97	5.30	300.00	14.00	2.36	1.46
	+X2	-2008.98 -2015.74[b] -1992.07[a]	86.87	5.30	300.00	13.80	2.28	2.01
	-X	-1769.32	81.40	5.30	300.00	-	-	2.27
	X1 span	-	-1.86	-	-	-	-	2.29[c]
	X2 span	-	0.48	-	-	-	-	2.48[c]
	+Y	-1986.68 -1990.08[b]	100.38	8.44	260.00	14.90	4.53	1.01
	-Y	-1806.26	93.81	8.44	260.00	-	-	2.51
	Y span	-	3.43	-	-	-	-	1.7[c]

[a] The value for after the calibration switched from the 3-orientation to the 5-orientation sequence.
[b] At Piñon Flat Observatory, the constants for the 3-sequence calibration changed after the communication was restored following a laptop failure.

An example 3-orientation calibration sequence from PFO is shown in Figure A3.6. The SCTAs at PFO and Axial Seamount have transients with similar amplitudes but the noise levels are much higher at Axial Seamount (compare Figure A3.6b and Figure 5.5b). The calibrations from the PFO SCTA are shown in Figure 5.7 and have a visually apparent temperature dependence and initial exponential transient. We account for temperature dependence by fitting the calibrations with an expression of the form

$$a_T^i(t) = b + ct + dT + e\frac{dT}{dt} + f\exp\left(\frac{-t}{h}\right) \tag{6}$$

where T is temperature and *d* and *e* are additional constant obtained from the least squares inversion; we found that the temperature derivative term, with the derivative averaged over one day, was necessary to get a reasonable fit. As before, we allow *b* to have different value for the +X2 calibrations on either side of the transition from 3- to 5-calibration sequences. We also found that the data was fitted better with different values of *b* either side of the 43-day interval of lost connectivity, likely because the instrument was disturbed thermally when the insulating cover was removed for inspection.

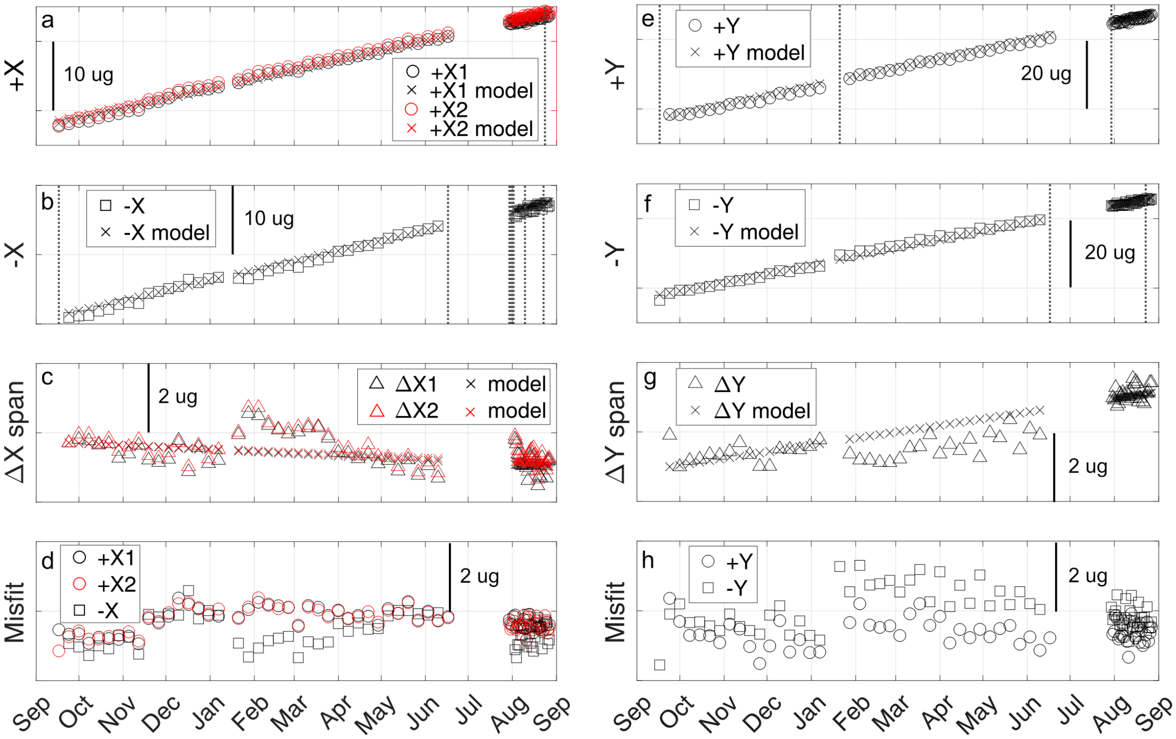

Figure 5.6. Calibration observations and model values for the Axial Seamount SCTA at Location 2. (a) Calibration results for +X1 (black) and +X2 (red). (b) Calibrations results for -X. (c) Span defined as +X1 or +X2 minus -X. (d) Misfit of the exponential linear model

(equation 5) for the +X1, +X2 and -X calibrations. (e-h) As for (a-d) except for Y calibrations. Vertical dotted lines in (a-b) and (e-f) indicate where anomalous calibrations have been excluded (see text).

Figure 5.7d and h shows the model misfits after applying the model of equation (6), and Table 5.1 lists the model parameters. The SCTA deployed at PFO was an entirely separate unit from that deployed at Axial and did not experience any anomalous calibrations. At PFO, the drift on each channel is characterized to ~2 µg/yr and the span change over the period of 5-orientation calibrations is < 3 µg/yr for each channel.

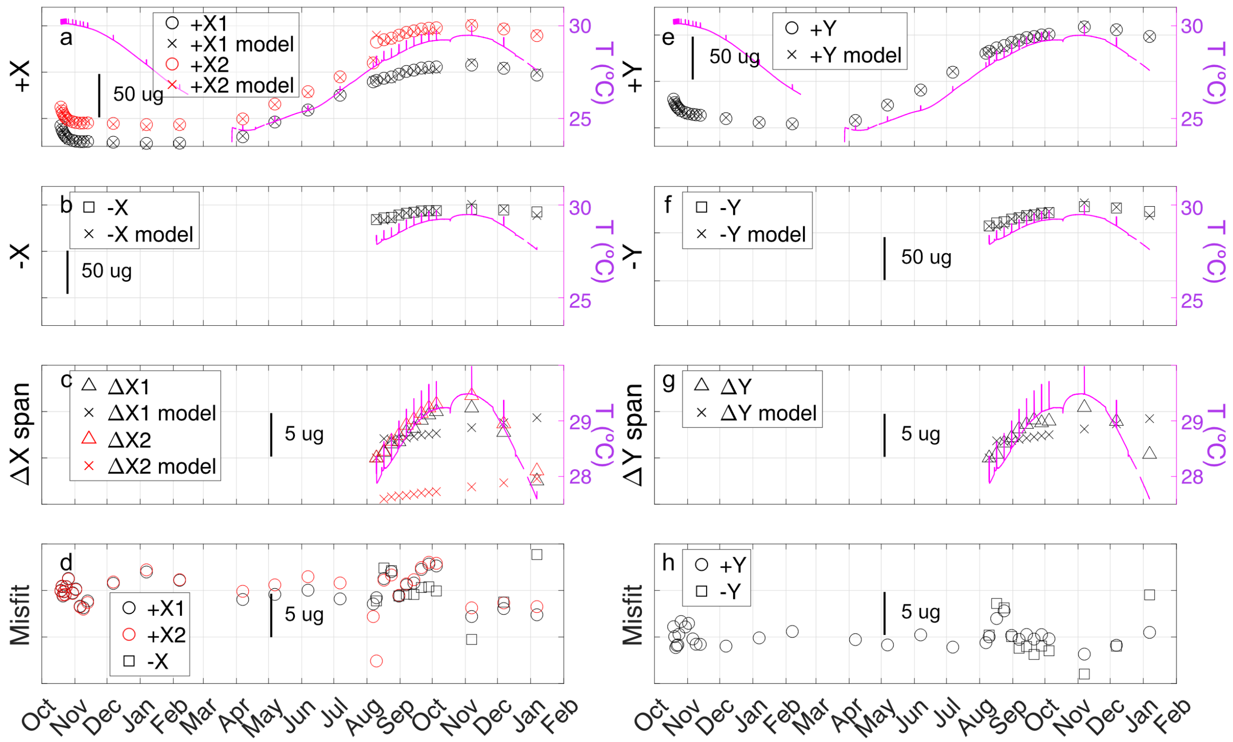

Figure 5.7. Calibration observations and model values, and temperatures for Piñon Flat Observatory. (a) Calibration results for +X1 (black) and +X2 (red) with temperature shown by purple on the righthand axis. (b) Calibrations results for -X. (c) Span defined as +X1 or +X2 minus -X. (d) Misfit of the exponential linear model (equation 5) for the +X1, +X2 and -X calibrations. (e-h) As for (a-d) except for Y calibrations.

5.4.2 Applying Calibrations and Data stitching

To generate calibrated accelerations for the measurement interval between two calibrations it is necessary to correct for the sensor drift. The drift for the X channel σ_X at the time of the k^{th} calibration t_k, can be written for a 3-orientation calibration sequence as

$$\sigma_X(t_k) = a_T^{+X}(t_k) - a_T^{+X}(t_1) \tag{7}$$

where the superscript $+X$ indicates the channel that is vertically oriented, and drift is relative to the first calibration. For a 5-orientation calibration sequence, a drift that accounts for changes in span be written based on calibrations with the channel pointing up ($+X$) and down ($-X$) as

$$\sigma_X(t_k) = \frac{a_T^{+X}(t_k)+a_T^{-X}(t_k)}{2} - \frac{a_T^{+X}(t_1)+a_T^{-X}(t_1)}{2} \tag{8}$$

To remove the drift from a measurement interval, one can either subtract a linear interpolation between the end point drifts measured by the calibration or subtract a smooth fit to the calibration data obtained by fitting a drift model such as those described in equations (5)-(6).

The calibration method employed in the SCTA yields small gaps and offsets in the calibrated tilt measurements. These are analogous to those seen for a bubble tiltmeter when it re-levels after going out of range (Agnew, 1986). For the SCTA they arise from periods of non-observation during calibrations, small changes in orientation when the instrument is returned to the measurement orientation, and transients seen in the measured acceleration after changing the orientation quartz accelerometer. To stich the calibrated segments of tilt data together, as shown schematically in Figure 5.8, it is first necessary to interpolate the calibrated tilt measurements for one measurement across the calibration interval while taking into account the acceleration transients at the start of the segment. The linear extrapolation of the k^{th} measurement interval, which we define as starting at the end of the k^{th} calibration, can be written as

$$a'_{X,k}(t) = \left[a_{X,k}(t_{s,k} + \delta t) - \delta a_X(\delta t)\right]\left(\frac{t_{e,k} - t}{t_{e,k} - t_{s,k} - \delta t}\right) - a_{X,k}(t_{e,k})\left(\frac{t_{s,k} + \delta t - t}{t_{e,k} - t_{s,k} - \delta t}\right) \tag{9}$$

where the prime indicates a linearly extrapolated and transient corrected acceleration, $t_{s,k}$ and $t_{e,k}$ are the start and end time of the measurement interval, respectively, δa_X is a time dependent transient referenced in time to the start of the measurement interval, and δt can be set to a non-zero value if the transient correction is unknown or a has a large uncertainty immediately after the calibration.

To stitch data, we use equation (9) to extrapolate an acceleration for the k^{th} measurement interval back in time to the end time of the previous measurement interval to give $a_{X,k}(t_{e,k-1})$. The measurement intervals can then be stitched together iteratively be calculating the end point tilts, θ_X for each segment iteratively according to

$$\begin{aligned}
&\theta_X(t_{e,0}) = 0 \\
&\theta_X(t_{e,1}) = [a_{X,1}(t_{e,1}) - a'_{X,1}(t_{e,0}) - \sigma_X(t_{e,1})]/g \qquad (10) \\
&\theta_X(t_{e,k+1}) = \theta_X(t_{e,k}) + [a_{X,k+1}(t_{e,k+1}) - a'_{X,k+1}(t_{e,k}) - \sigma_X(t_{e,k+1}) + \sigma_X(t_{e,k})]/g
\end{aligned}$$

Stitching involves working with each calibrated measurement interval to remove the transient acceleration if it is known, linearly interpolating the acceleration back to the start of the prior calibration, converting acceleration to a tilt by dividing by g, and applying a fixed offset to match the extrapolated tilt to the end point tilt of the prior measurement interval given by equation (10).

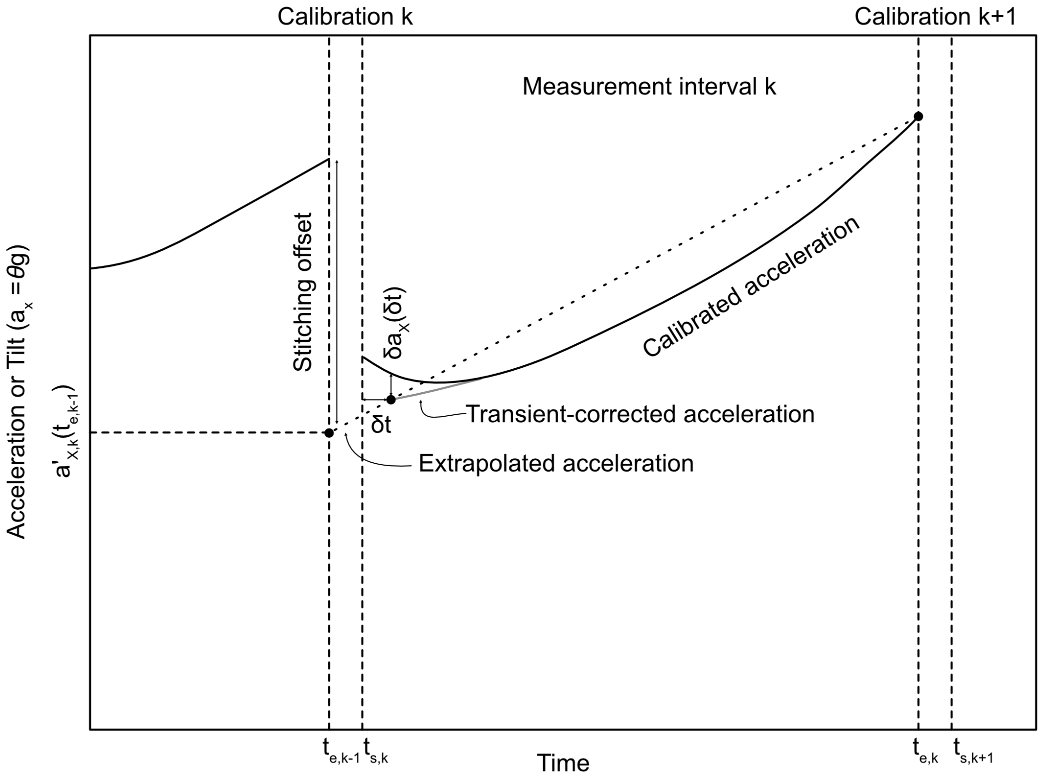

Figure 5.8. Demonstration of the stitching process with scale exaggerated for display purposes. There are three key components to stitching a continuous tilt time series: the tilt offset between data segments, the time offset between data segments (i.e., the calibration interval $t_{s,k}$–$t_{e,k-1}$) and the post-calibration transient (δa_X (δt)). Each data segment is corrected for its transient, extrapolated to time $t_{e,k-1}$, and then corrected for the tilt offset.

At Piñon Flat Observatory the data is sufficiently quiet that the transient following the calibration can be estimated by averaging the acceleration measurements for the time immediately after the calibration sequence (Figure 5.9), after subtracting out the slope of the acceleration from 2-24 hours after the calibration. The transient accelerations differ between the 3- and 5-orientation calibration sequences and the X and Y channels since they reflect a different history of orientations. The initial transient amplitudes are ~20 µg but they decrease to absolute values of ~1 µg within about an hour and to ~0.1 µg after 5 hours (Figure 5.9).

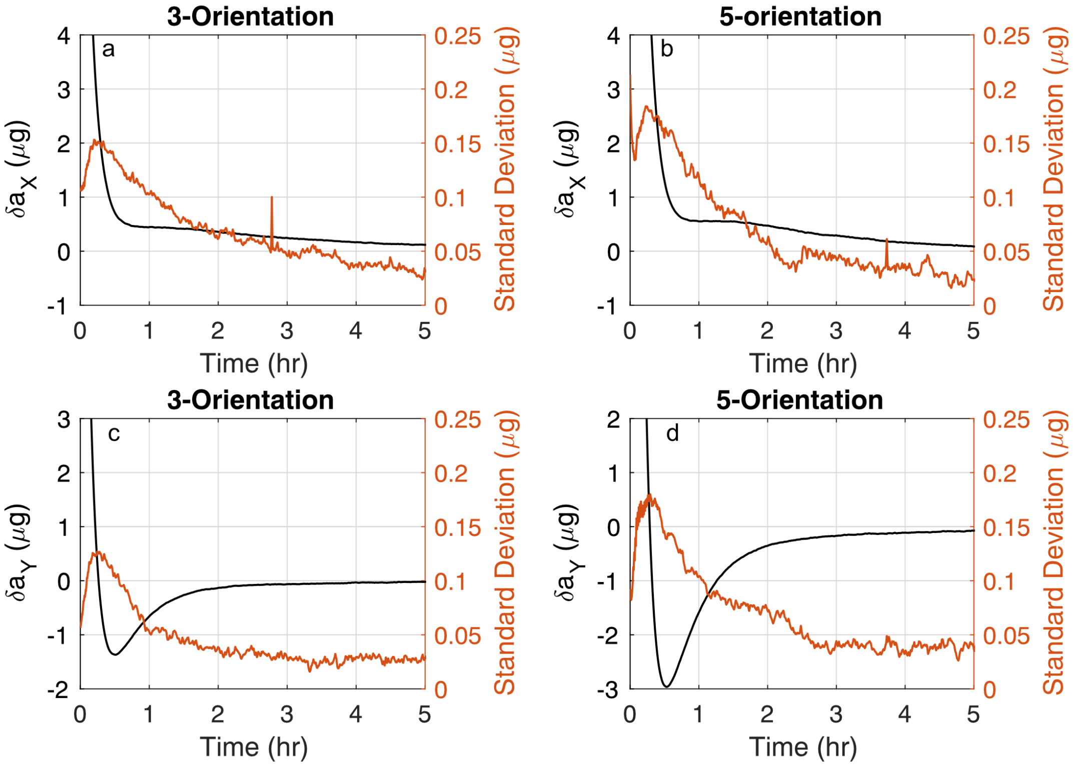

Figure 5.9. Transient accelerations (black lines) observed after the calibrations for (a) the X channel and the three-orientation sequence, (b) the X channel and the five-orientation sequence, (c) the Y channel and the three-orientation sequence and (d) the Y channel and the five-orientation sequence. The transients determined after first decimating the observed accelerations to a 1-minute time series and then by averaging the detrended accelerations observations after each calibration type. The standard deviation (red lines) will be a combination of any variation in the post-calibration transient and environmental variations in the 1-minute averaged acceleration.

Figure 5.10 shows the results of stitching the data at Piñon Flat Observatory including a extrapolation over the 43-day gap. Here the data have been stitched by setting $\delta t = 0$ hours in equation (9) to avoid a significant offset from the post-flip transients. Setting $\delta t = 5$ hours and correcting with the average of all the post-calibration transients leads to a 1-2 μrad difference in the accumulated tilt over the experiment. The calibrated tilt time series shows a strong temperature dependence, particularly on the Y channel (red lines Figure 5.10). Since, the temperature dependence of the accelerometer output should be removed by calibrations, we infer that this may reflect thermal deformation of the SCTA apparatus. Solving for a least squares linear temperature correction significantly flattens the tilt time-series (black lines in Figure 5.10) leaving a residual signal that suggests about 20 μrad of tilt down to the SW over the 16-month experiment.

At Axial Seamount the data is too noisy to measure the post-calibration transients well, but they appear to be significantly shorter in duration, so we stitch by setting δt = 2 hours to minimize their impact. The results are shown along with the tilt data from the nearby LILY tiltmeter for Location 1 in the SCTA X-Y coordinates in Figure A3.8 and for Location 2 in geographic coordinates in Figure 5.11. At Location 1 (Figure A3.8), the results are inconsistent with the LILY tiltmeter, and difference suggests subsidence of the southeast leg of the SCTA platform. At Location 2, the SCTA shows ~25 μrad of downward tilt to the east over the year, while the LILY sensor indicates ~40 μrad of downward tilt (Figure 5.11a). On the north channel the SCTA initially tilts to the north for about a month, possibly indicating platform settling. Following this there is very little net tilt while LILY shows about 10 μrads of tilt down to the south.

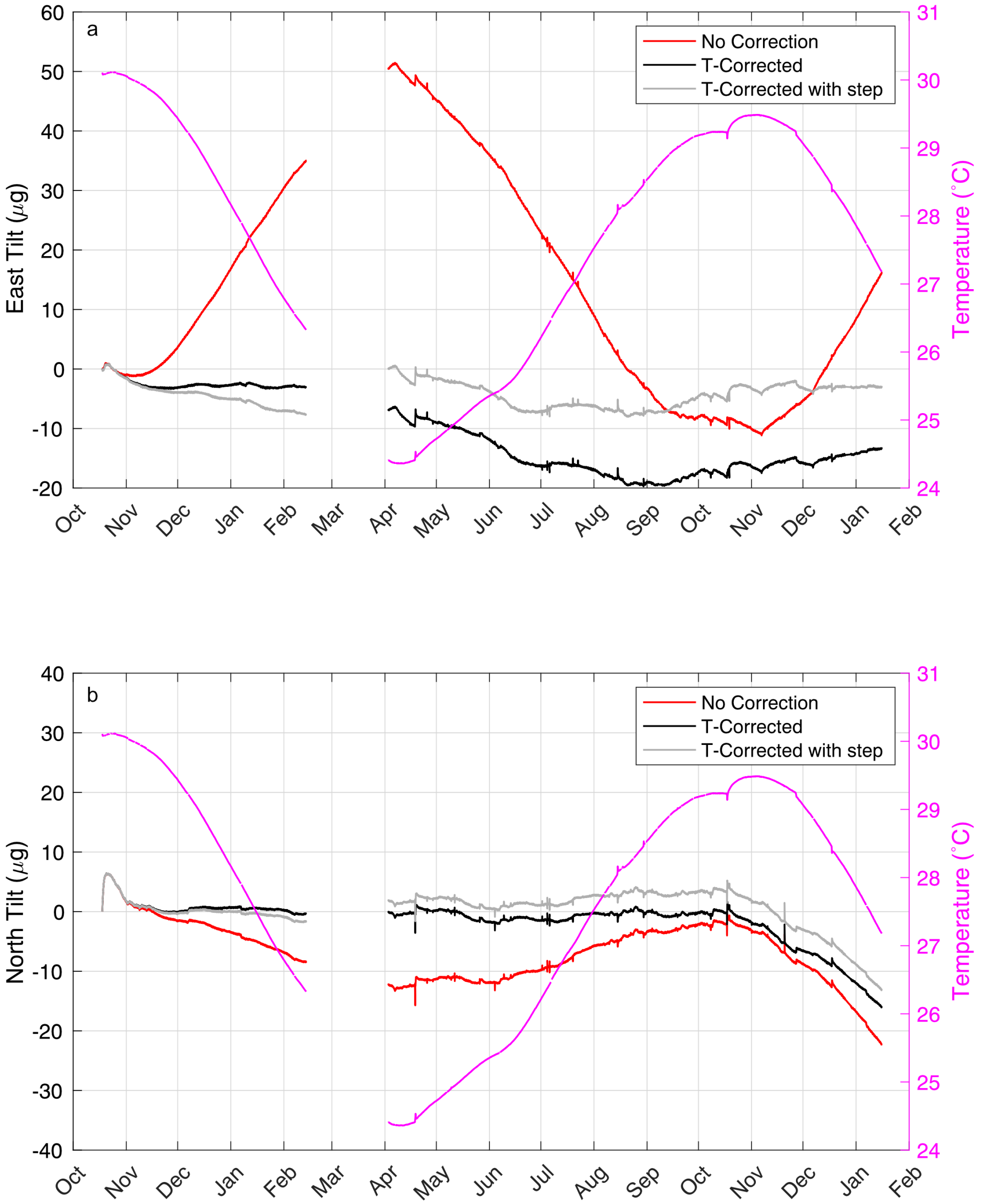

Figure 5.10. Time series of one-minute averaged tilt for Piñon Flat Observatory from 2018 to 2020 for the (a) east (-Y) and (b) north (+X) directions. The curves show the drift-corrected stitched data with δt = 0 hours in equation (9) (red) and the stitched data fit after adjusting for linear temperature dependence (black) and with both a linear temperature dependence and a step at the 46-day gap (gray). The temperature is also shown (purple). The sign convention is positive for a downward tilt.

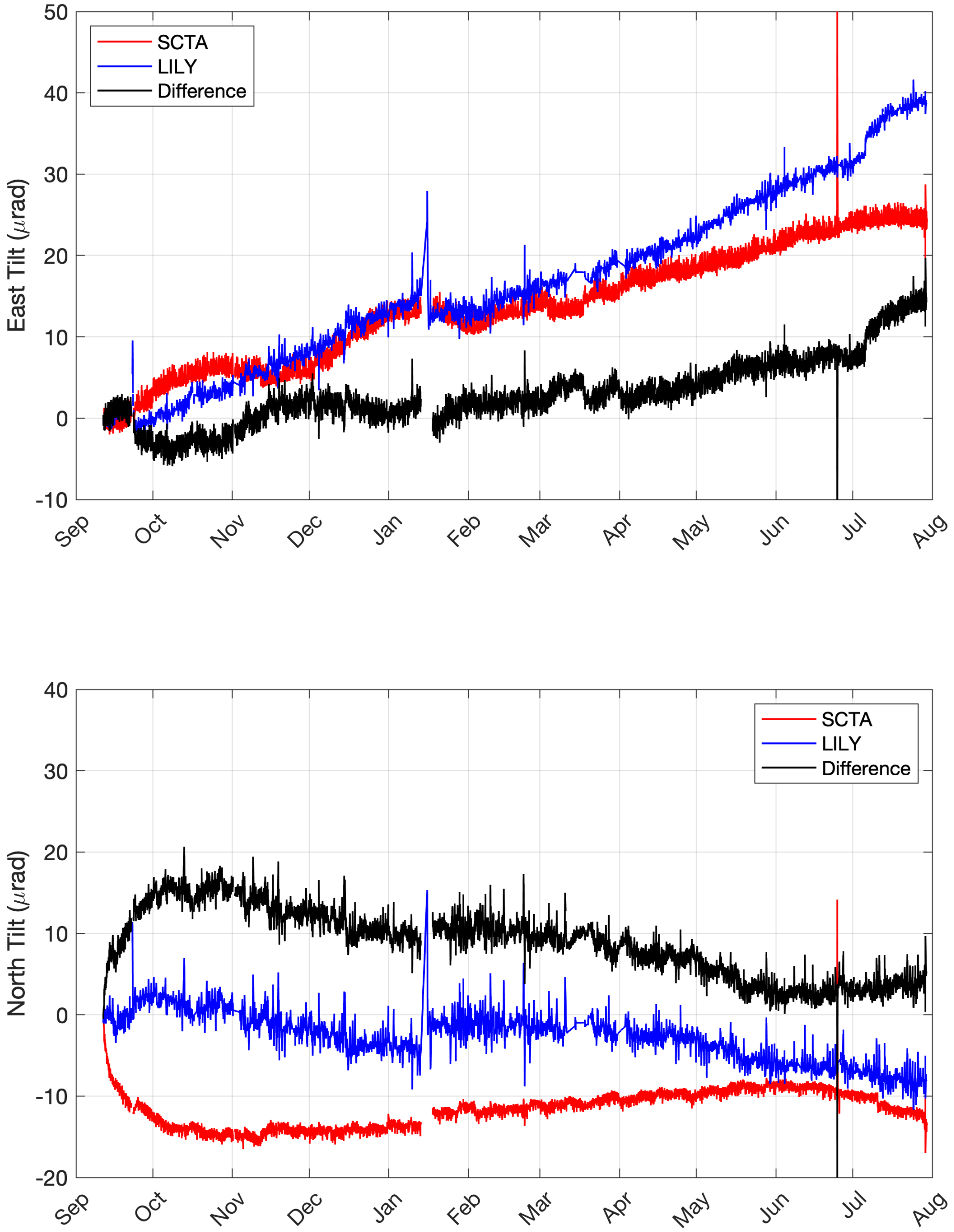

Figure 5.11. Time series of 1-minute averaged tilt for Axial Seamount Location 2 from 2020 to 2021 for the (a) east and (b) north directions. Each plot shows the drift corrected stitched SCTA data with $\delta t = 2$ hours in equation (9) with the assumption of no transient acceleration after 5 hours (red), the LILY tile meter data (blue) and the difference (LILY – SCTA) (black). The sign convention is positive for a downward tilt.

5.5 Discussion

5.5.1 Calibration Technique

The calibration data collected at Axial Seamount (Figures 5.6 and A3.5) and PFO (Figure 5.7) suggest that the rotational calibration approach is a valid method for measuring sensor drift. A small proportion of calibrations at Axial Seamount exhibit anomalous behavior for unknown reasons (see Appendix 3 Text A3.1), but these anomalous calibrations are readily identifiable and thus, easily excluded. The remaining calibrations at Axial Seamount are well fit to RMS residuals of ~0.5 μg (Table 5.1), with the exponential-linear drift that is commonly used for quartz sensors (Polster et al., 2009; Watts & Kontoyiannia, 1990). At Piñon Flat Observatory where there were seasonal temperature variations of > 5°C, the calibration data are fit to RMS residuals of ~2 μg (Table 5.1) when additional terms are added for linear dependence on temperature and the time derivative of temperature. The results show a linear sensor drift for the SCTA at Axial Seamount that is a few tens of μg/yr (Table 5.1) on both channels and that decreases between Location 1 and Location 2, consistent with decreasing drift rates with sensor age. At Piñon Flat Observatory, the linear drift rates of ~100 μg/yr are larger than Axial Seamount, likely because the accelerometer was newer.

By rotating each horizontal channel for calibrations pointing up and down, it is also possible to measure changes in the accelerometer span and thus correct for changes is both drift and sensitivity. For all the deployments, the rate of change of span is ≤ ~ 5 μg/yr and is typically an order of magnitude lower than the drift rate.

Each calibration sequence leads to a transient response lasting several hours that is very consistent to ≤ ~0.1 μg/yr for a given channel and calibration sequence (Figure 5.9). This memory effect in the accelerometer output means that it is important to keep the calibration rotational sequence consistent in terms of order and timing and to make the calibration measurements over a consistent time interval after each rotation.

5.5.2 Axial Seamount Tilt Observations

The tilt data collected at Location 1 at Axial Seamount central caldera site (Figure A3.8) was impacted by settling by one leg of the tripod platform which was accidentally deployed on a thin layer of sediment. At Axial Seamount Location 2 (Figure 5.11), the calibrated and stitched tilt observations show a tilt to downwards to the east at about 40 μrad /yr. On both channels the tilt time series at Location 2 is except for the first month when there may be a settling signal on the SCTA, consistent with the annual signal on LILY tiltmeter to within ~15 μrad /yr on both channels. Kitada et al. (2013) conducted multiyear testing on LILY tiltmeters that demonstrated linear drift rates on these sensors as large as ~70 μrad/yr even in deep, cemented borehole environments. The SCTA observations are thus consistent with the LILY tiltmeter.

There have been various efforts to model the Axial volcano inflation source from the available observational data (Nooner & Chadwick, 2016; Hefner et al., 2020, 2021; Slead et al., 2022) that includes both bottom pressure observations (e.g., Nooner & Chadwick, 2016) and repeat mapping with an autonomous underwater vehicle (AUV) (Caress et al., 2020). Though the system is underdetermined, recent models by Hefner et al. (2021) posit two potential sources that best fit the pressure and AUV altimetry data, individually. Neither model is consistent with the SCTA and LILY tilt observations at the central caldera site, with the pressure-based model suggesting tilt oriented ~180° from observed and the altimetry-based model suggesting tilt oriented ~90° clockwise from observed. The discrepancy between the models and the SCTA observations may be attributed localized block tilting given that the caldera floor is composed of relatively poorly consolidated and fragmented material (Arnulf et al., 2014; Baillard et al., 2019). In addition, the AUV repeat data suggests that inflation is more symmetric about the central caldera with more inflation to the north (Caress et al., 2020), so the earlier models that are based on pressure data in and around the southern half of the caldera may not be accurate at the central caldera site.

5.5.3 Piñon Flat Observatory Tilt Observations

The deployment at Axial Seamount does not provide a means to assess the accuracy of the SCTA because the volcano is deforming, and the true tilt signal is unknown. At PFO, the expected tilt signal is << 1µrad/yr (Agnew, 2007; Wyatt et al., 1994) so is a good site to assess the accuracy of SCTA. Unfortunately, the large seasonal temperature variations observed with in the vault are not ideal. To fit the calibration data, it was necessary to include not only a temperature dependent term but also a term dependent on the time derivative of temperature, and the resulting exponential-linear drift model fits had an RMS about four times worse than Axial. After applying the calibrations, the resulting stitched tilt records show a strong temperature dependence, even though this should be removed from the accelerometer by the calibrations. We infer that the SCTA apparatus deformed thermally. Correcting for this with a linear temperature-dependent term and also allowing an unknown step during a 43-day period when connections were lost significantly flattens the stitched tilt time series. For the east direction the tilt still varies by ~10 µrad over the 15-month deployment. For the north direction, the tilt signal is much smaller except near the very start and near then end when there is ~15 µrad of apparent tilt to the south over 3 months. This latter signal could indicate slip of the breaking mechanism since the north direction corresponds to the X-axis which should be sensitive to slip on the outer gimbal on which there is more mechanical leverage.

5.5.4. Future steps

While the SCTA tests at both Axial Seamount and PFO demonstrate promising results for the rotational calibration method, neither is provides a good test of the accuracy of resulting time series. At Axial Seamount the true signal is unknown while at Piñon Flat Observatory, the large seasonal temperature variations proved quite challenging. In addition, for these initial tests we performed more calibrations than necessary to understand their consistency which increases the challenges associated with stitching the tilt time series together. The SCTA would clearly benefit from a long deployment in a tectonically stable setting with much smaller temperature fluctuations than the vault at Piñon Flat Observatory. This could be accomplished by deployment at moderate depths in a borehole where the temperature fluctuations might be expected to be three orders of magnitude smaller than observed in the vault at Piñon Flat Observatory vault (e.g., Kinoshita et al., 2009).

5.6 Acknowledgements

We thank the OOI RCA field team, the ROV *Jason* and the captains and crews of the *R/V Roger Revelle* and *R/V Thomas G. Thompson* for deploying and recovering the Axial Seamount SCTA, Bill Chadwick and colleagues for providing the opportunity to move the Axial Seamount SCTA during a *R/V Thomas G. Thompson* and ROV *Jason* cruise, and Mark Zumberge and Glenn Sasagawa for providing space in the vault, internet connectivity and field assistance for the test at

Piñon Flat Observatory. This work was supported by National Science Foundation grant 1634103.

Chapter 6:
Summary and Future Work

Plate boundaries are complex, dynamic systems from which we stand to learn much about Earth's tectonic processes. However, most plate boundaries are entirely or partially offshore, where they suffer from a historic deficit of observation. Our current state of knowledge of these settings thus lags significantly behind that of processes observable from land. In particular, subduction zone earthquake and tsunami hazards are of great concern but cannot be fully understood without a shoreline-crossing view of the entire system. Megathrust earthquakes are only one part of the complex dynamics of subduction and taking a broader view on these systems allows us to better understand the conditions that lead to and follow large damaging earthquakes. The offshore is a challenging work environment, but an essential part of the subduction system; everything that enters the subduction zone does so here and in subduction zones worldwide most of the locked region is offshore and the dynamics in the shallowest reaches of the plate interface play crucial roles in determine the extent of megathrust rupture and tsunamigenesis. There is increasing attention and demand for observations in the offshore, which is increasingly being broadly recognized as the next frontier in solid-Earth geophysics.

This dissertation encompasses a body of work that demonstrates the observational gains that can be achieved by developing seafloor-specific techniques and by utilizing state of the art oceanographic models to gain a deeper understanding of how circulation processes impact geodetic measurements. In Chapter 2, I showed that in Cascadia seafloor pressure is remarkably coherent along isobaths over hundreds of kilometers separation and that depth-matched differencing can be used to greatly reduce oceanographic pressure signals without eliminating the desired slow slip signals. In Chapter 3, I expanded this line of inquiry to show that in Alaska further processing utilizing a combination of Complex Empirical Orthogonal Functions (CEOFs) and depth-matched differencing corrections further reduced the oceanographic signal and allowed for the statistically repeatable detection of 4 cm SSE signals on the shelf and 2 cm signals on the slope. In Chapter 4, I used hindcast seafloor pressure from a Cascadia regional oceanographic model to demonstrate the generation of SSE-like signals in pressure differences by the passage of mesoscale eddies through the region and explored the water column structural changes that cause these signals. Finally, in Chapter 5, I presented observations from two field tests of a self-calibrating tiltmeter (the SCTA) – in many ways analogous to A-0-A calibrations on pressure sensors – that shows promise for reducing drift-induced uncertainty by an order of magnitude, thereby allowing the observation of increasingly small-amplitude and long-period tectonic signals.

The tectonics community is increasingly trying to address the observational shortcomings in offshore systems and a number of efforts are being made to cross the shoreline and obtain seafloor seismic and geodetic measurements. In the last decade, there have been ambitious geodetic and tectonic deployments aimed to increase the spatial coverage and/or longevity of seafloor measurements. Real-time observatories like the OOI Cabled Array (Smith et al., 2018), Ocean Networks Canada NEPTUNE (Heesemann et al., 2014), and the Japanese DONET (Kawaguchi et al., 2015) and S-NET (Kanazawa, 2013) systems, as well as continued installments of borehole observatories (Davis et al., 1992), provide opportunities for multi-year or even decadal-scale observations. Community driven experiments like the Cascadia Initiative (Toomey et al., 2014) and Alaska Amphibious Community Seismic Experiment (AACSE; Abers et al., 2019), though not explicitly geodetic in nature, included pressure sensors and can be used as test beds for the capabilities and limitations of seafloor pressure geodesy over large spatial scales. Most recently, the actively expanding U.S. Global Navigation Satellite System-Acoustic network, which includes pressure sensors, is demonstrative of the will and momentum in rapidly bringing seafloor geodetic efforts up to scale.

Looking forward, there is still a great deal we do not yet know or have not properly characterized about the ocean's impact on our observations. In many seafloor observation systems, oceanographic circulation processes generate signals that conflate with the desired solid-Earth observations, so this need extends well beyond the bounds of seafloor pressure alone. There is great opportunity while the field of seafloor geodesy is in this nascent stage to ensure that we are getting the most out of our observations and expanding our efforts meaningfully and effectively, and approaching our science in a way that anticipates and makes room for emerging technologies. This dissertation highlights the need for sustained observational networks, which would alleviate challenges presented by seasonal fluctuations and increase the likelihood of an SSE occurring during the observation period, as well as provide essential data to better understand the ocean circulation. Additionally, the modeling and detectability efforts presented herein underscore the need for having reliable SSE timing information, highlighting the benefit of multi-sensor deployments and of increasing coastal GPS station density. The payoff for this observational endeavor would be significant, as the detection and characterization of shallow SSEs may lead to a better understanding of the mechanical properties of the plate boundary and the stress release process leading up to large magnitude megathrust earthquakes. There is a wealth of information to be mined out of oceanographic circulation models, of which this dissertation has made only a modest start. As these models improve in resolution and validation, particularly off the continental shelf, they are likely to become increasingly useful in assessing the comparability of bottom pressure between locations and may become practical for use as a correction to oceanographic pressure effects.

Bibliography

Abers, G., Adams, A., Haeussler, P., Roland, E., Shore, P., Wiens, D., Schwartz, S., Sheehan, A., Shillington, D., Webb, S., & Worthington, L. (2019). Examining Alaska's Earthquakes on Land and Sea. *Eos*, *100*. https://doi.org/10.1029/2019EO117621

Agata, R., Hori, T., Ariyoshi, K., & Ichimura, T. (2019). Detectability analysis of interplate fault slips in the Nankai subduction thrust using seafloor observation instruments. *Marine Geophysical Research*, *40*(4), 453–466. https://doi.org/10.1007/s11001-019-09380-y

Agnew, D. C. (2007). Before PBO: An Overview of Continuous Strain and Tilt Measurements in the United States. *Journal of the Geodetic Society of Japan*, *53*(2), 157–182.

Agnew, D. C. (1986). Strainmeters and tiltmeters. *Reviews of Geophysics*, *24*(3), 579–624. https://doi.org/10.1029/RG024i003p00579

Agnew, D. C., & Wyatt, F. K. (1989). The 1987 Superstition Hills earthquake sequence: Strains and tilts at Piñon Flat Observatory. *Bulletin of the Seismological Society of America*, *79*(2), 480–492. https://doi.org/10.1785/BSSA0790020480

Anderson, G., Constable, S., Staudigel, H., Wyatt, F. K., Et, A., & Seafloor, A. L. (1997). A seafloor longsbaseline tiltmeter inflation of Axial Seamount to be below. *Geophysics*, *102*.

Andres, M., Siegelman, M., Hormann, V., Musgrave, R., Merrifield, S., Rudnick, D., Merrifield, M., Alford, M., Voet, G., Wijesekera, H., MacKinnon, J., Centurioni, L., Nash, J., & Terrill, E. (2019). Eddies, Topography, and the Abyssal Flow by the Kyushu-Palau Ridge Near Velasco Reef. *Oceanography*, *32*(4), 46–55. https://doi.org/10.5670/oceanog.2019.410

Androsov, A., Boebel, O., Schröter, J., Danilov, S., Macrander, A., & Ivanciu, I. (2020). Ocean Bottom Pressure Variability: Can It Be Reliably Modeled? *Journal of Geophysical Research: Oceans*, *125*(3). https://doi.org/10.1029/2019JC015469

Arai, K., Naruse, H., Miura, R., Kawamura, K., Hino, R., Ito, Y., Inazu, D., Yokokawa, M., Izumi, N., Murayama, M., & Kasaya, T. (2013). Tsunami-generated turbidity current of the 2011 Tohoku-Oki earthquake. *Geology*, *41*(11), 1195–1198. https://doi.org/10.1130/G34777.1

Araki, E., Kimura, T., Machida, Y., Yokobiki, T., Nishida, S., Kawaguchi, K., Kyo, M., Saruhashi, T., Toczko, S., Saffer, D., & Kopf, A. (2017). Deep seafloor borehole observatories for seismogenic zone monitoring. *Techno-Ocean 2016: Return to the Oceans*, 656–659. https://doi.org/10.1109/Techno-Ocean.2016.7890737

Araki, E., Saffer, D. M., Kopf, A. J., Wallace, L. M., Kimura, T., Machida, Y., Ide, S., & Davis, E. (2017). Recurring and triggered slow-slip events near the trench at the Nankai Trough subduction megathrust. *Science*, *356*(6343), 1157–1160. https://doi.org/10.1126/science.aan3120

Araki, E., Shinohara, M., Sacks, S., Linde, A., Kanazawa, T., Shiobara, H., Mikada, H., & Suyehiro, K. (2004). Improvement of seismic observation in the ocean by use of seafloor boreholes. *Bulletin of the Seismological Society of America*, *94*(2), 678–690. https://doi.org/10.1785/0120020088

Ariyoshi, K., Nakata, R., Matsuzawa, T., Hino, R., Hori, T., Hasegawa, A., & Kaneda, Y. (2014). The detectability of shallow slow earthquakes by the Dense Oceanfloor Network system for Earthquakes and Tsunamis (DONET) in Tonankai district, Japan. *Marine Geophysical Research*, *35*(3), 295–310. https://doi.org/10.1007/s11001-013-9192-6

Arnoso, J., Vieira, R., Velez, E., Weixin, C., Shihng, T., Jun, J., & Venedikov, A. (2001). Monitoring Tidal and Non-tidal Tilt Variations in Lanzarote Island (Spain). *Journal of the Geodetic Society of Japan*, *47*(1), 456–462.

Arnulf, A. F., Harding, A. J., Kent, G. M., Carbotte, S. M., Canales, J. P., & Nedimović, M. R. (2014). Anatomy of an active submarine volcano. *Geology*, *42*(8), 655–658. https://doi.org/10.1130/G35629.1

Ashi, J., Sawada, R., Omura, A., & Ikehara, K. (2014). Accumulation of an earthquake-induced extremely turbid layer in a terminal basin of the Nankai accretionary prism. *Earth, Planets, and Space*, *66*(51), 1–9.

Atwater, B. F., Carson, B., Griggs, G. B., Johnson, H. P., Salmi, M. S., & Survey, U. S. G. (2014). Rethinking turbidite paleoseismology along the Cascadia subduction zone. *Geology*, *42*(9), 827–830. https://doi.org/10.1130/G35902.1

Baba, T., Hirata, K., Hori, T., & Sakaguchi, H. (2006). Offshore geodetic data conducive to the estimation of the afterslip distribution following the 2003 Tokachi-oki earthquake. *Earth and Planetary Science Letters*, *241*(1–2), 281–292. https://doi.org/10.1016/j.epsl.2005.10.019

Baillard, C., Wilcock, W. S. D., Arnulf, A. F., Tolstoy, M., & Waldhauser, F. (2019). A Joint Inversion for Three-dimensional P and S Wave Velocity Structure and Earthquake

Locations Beneath Axial Seamount. *Journal of Geophysical Research: Solid Earth*, *124*(12), 12997–13020. https://doi.org/10.1029/2019JB017970

Barcheck, G., Abers, G. A., Adams, A. N., Bécel, A., Collins, J., Gaherty, J. B., Haeussler, P. J., Li, Z., Moore, G., Onyango, E., Roland, E., Sampson, D. E., Schwartz, S. Y., Sheehan, A. F., Shillington, D. J., Shore, P. J., Webb, S., Wiens, D. A., & Worthington, L. L. (2020). The Alaska amphibious community seismic experiment. *Seismological Research Letters*, *91*(6), 3054–3063. https://doi.org/10.1785/0220200189

Bécel, A., Shillington, D. J., Delescluse, M., Nedimović, M. R., Abers, G. A., Saffer, D. M., Webb, S. C., Keranen, K. M., Roche, P. H., Li, J., & Kuehn, H. (2017). Tsunamigenic structures in a creeping section of the Alaska subduction zone. *Nature Geoscience*, *10*(8), 609–613. https://doi.org/10.1038/NGEO2990

Bevis, M., Kendrick, E., Smalley, R., Brooks, B., Allmendinger, R., & Isacks, B. (2001). On the strength of interplate coupling and the rate of back arc convergence in the central Andes: An analysis of the interseismic velocity field. *Geochemistry, Geophysics, Geosystems*, *2*(11), n/a-n/a. https://doi.org/10.1029/2001GC000198

Bingham, R. J., & Hughes, C. W. (2008). The relationship between sea-level and bottom pressure variability in an eddy permitting ocean model. *Geophysical Research Letters*, *35*(3), 1–5. https://doi.org/10.1029/2007GL032662

Bock, Y., Agnew, D. C., Fang, P., Genrich, J. F., Hager, B. H., Herring, T. A., Hudnut, K. W., King, R. W., Larsen, S., Minster, J.-B., Stark, K., Wdowinski, S., & Wyatt, F. K. (1993). Detection of crustal deformation from the Landers earthquake sequence using continuous geodetic measurements. *Nature*, *361*(6410), 337–340. https://doi.org/10.1038/361337a0

Bock, Y., & Melgar, D. (2016). Physical applications of GPS geodesy: a review. *Reports on Progress in Physics*, *79*(10), 106801. https://doi.org/10.1088/0034-4885/79/10/106801

Brown, J. R., Beroza, G. C., Ide, S., Ohta, K., Shelly, D. R., Schwartz, S. Y., Rabbel, W., Thorwart, M., & Kao, H. (2009). Deep low-frequency earthquakes in tremor localize to the plate interface in multiple subduction zones. *Geophysical Research Letters*, *36*, 1–5. https://doi.org/10.1029/2009GL040027

Brown, J. R., Prejean, S. G., Beroza, G. C., Gomberg, J. S., & Haeussler, P. J. (2013). Deep low-frequency earthquakes in tectonic tremor along the Alaska-Aleutian subduction zone.

Journal of Geophysical Research: Solid Earth, *118*(3), 1079–1090. https://doi.org/10.1029/2012JB009459

Bürgmann, R., & Chadwell, D. (2014). Seafloor geodesy. *Annual Review of Earth and Planetary Sciences*, *42*(May), 509–534. https://doi.org/10.1146/annurev-earth-060313-054953

Bürgmann, R., & Thatcher, W. (2013). Space geodesy: A revolution in crustal deformation measurements of tectonic processes. In *The Web of Geological Sciences: Advances, Impacts, and Interactions*. Geological Society of America. https://doi.org/10.1130/2013.2500(12)

Buurman, H., Nye, C. J., West, M. E., & Cameron, C. (2014). Geochemistry, Geophysics, Geosystems. *Geochemistry, Geophysics, Geosystems*, *15*, 1147–1163. https://doi.org/10.1002/2013GC005101.Received

Capotondi, A., Combes, V., Alexander, M. A., Di Lorenzo, E., & Miller, A. J. (2009). Low-frequency variability in the Gulf of Alaska from coarse and eddy-permitting ocean models. *Journal of Geophysical Research*, *114*(C1), C01017. https://doi.org/10.1029/2008JC004983

Carbotte, S. M., Arnulf, A., Spiegelman, M., Lee, M., Harding, A., Kent, G., Canales, J. P., & Nedimović, M. (2020). Stacked sills forming a deep melt-mush feeder conduit beneath axial seamount. *Geology*, *48*(7), 693–697. https://doi.org/10.1130/G47223.1

Carrere, L., & Lyard, F. (2003). Modeling the barotropic response of the global ocean to atmospheric wind and pressure forcing - comparisons with observations. *Geophysical Research Letters*, *30*(6), 1275–1278. https://doi.org/10.1029/2002GL016473

Chadwell, C. D., Hildebrand, J. A., Spiess, F. N., Morton, J. L., Normark, W. R., & Reiss, C. A. (1999). No spreading across the southern Juan de Fuca ridge axial cleft during 1994-1996. *Geophysical Research Letters*, *26*(16), 2525–2528. https://doi.org/10.1029/1999GL900570

Chadwick, W. W., Embley, R. W., Milburn, H. B., Meinig, C., & Stapp, M. (1999). Evidence for deformation associated with the 1998 eruption of Axial Volcano, Juan de Fuca Ridge, from acoustic extensometer measurements. *Geophysical Research Letters*, *26*(23), 3441–3444. https://doi.org/10.1029/1999GL900498

Chadwick, W. W., Nooner, S. L., Zumberge, M. A., Embley, R. W., & Fox, C. G. (2006). Vertical deformation monitoring at Axial Seamount since its 1998 eruption using deep-sea pressure sensors. *Journal of Volcanology and Geothermal Research*, *150*(1–3), 313–327. https://doi.org/10.1016/j.jvolgeores.2005.07.006

Chadwick, W. W., Wilcock, W. S. D., Nooner, S. L., Beeson, J. W., Sawyer, A. M., & Lau, T. K. (2022). Geodetic Monitoring at Axial Seamount Since Its 2015 Eruption Reveals a Waning Magma Supply and Tightly Linked Rates of Deformation and Seismicity. *Geochemistry, Geophysics, Geosystems*, *23*(1). https://doi.org/10.1029/2021GC010153

Chaudhuri, K., & Ghosh, A. (2022). Widespread Very Low Frequency Earthquakes (VLFEs) Activity Offshore Cascadia. *Geophysical Research Letters*, *49*(13). https://doi.org/10.1029/2022GL097962

Chawah, P., Chéry, J., Boudin, F., Cattoen, M., Seat, H. C., Plantier, G., Lizion, F., Sourice, A., Bernard, P., Brunet, C., Boyer, D., & Gaffet, S. (2015). A simple pendulum borehole tiltmeter based on a triaxial optical-fibre displacement sensor. *Geophysical Journal International*, *203*(2), 1026–1038. https://doi.org/10.1093/gji/ggv358

Cook, M. J. (2019). *Calibrated Ocean Bottom Pressure Measurements for Marine Geodesy*. University of California San Diego.

Cook, M. J., Sasagawa, G. S., Schmidt, D. A., Roland, E. C., Wilcock, W. S. D., & Zumberge, M. A. (2019). Absolute calibrated seafloor pressure measurements for geodesy in Cascadia.

Coyle, K. O., Hermann, A. J., & Hopcroft, R. R. (2019). Modeled spatial-temporal distribution of productivity, chlorophyll, iron and nitrate on the northern Gulf of Alaska shelf relative to field observations. *Deep-Sea Research Part II: Topical Studies in Oceanography*, *165*(May), 163–191. https://doi.org/10.1016/j.dsr2.2019.05.006

Coyle, K. O., Hermann, A. J., & Hopcroft, R. R. (2019). Modeled spatial-temporal distribution of productivity, chlorophyll, iron and nitrate on the northern Gulf of Alaska shelf relative to field observations. *Deep Sea Research Part II: Topical Studies in Oceanography*, *165*, 163–191. https://doi.org/10.1016/j.dsr2.2019.05.006

Crowell, B. W., & Melgar, D. (2020). Slipping the Shumagin Gap: A Kinematic Coseismic and Early Afterslip Model of the Mw 7.8 Simeonof Island, Alaska, Earthquake. *Geophysical Research Letters*, *47*(19), 1–7. https://doi.org/10.1029/2020GL090308

Davies, J., Sykes, L., House, L., & Jacob, K. (1981). Shumagin Seismic Gap, Alaska Peninsula: History of great earthquakes, tectonic setting, and evidence for high seismic potential. *Journal of Geophysical Research*, *86*(B5), 3821. https://doi.org/10.1029/JB086iB05p03821

Davis, E. E., Villinger, H., & Sun, T. (2015). Slow and delayed deformation and uplift of the outermost subduction prism following ETS and seismogenic slip events beneath Nicoya

Peninsula, Costa Rica. *Earth and Planetary Science Letters*, *410*, 117–127. https://doi.org/10.1016/j.epsl.2014.11.015

Dixon, T. H., Jiang, Y., Malservisi, R., McCaffrey, R., Voss, N., Protti, M., & Gonzalez, V. (2014). Earthquake and tsunami forecasts: Relation of slow slip events to subsequent earthquake rupture. *Proceedings of the National Academy of Sciences*, *111*(48), 17039–17044. https://doi.org/10.1073/pnas.1412299111

Dobashi, Y., & Inazu, D. (2021). Improving Detectability of Seafloor Deformation From Bottom Pressure Observations Using Numerical Ocean Models. *Frontiers in Earth Science*, *8*(January), 1–16. https://doi.org/10.3389/feart.2020.598270

Dragert, G., Wang, K., James, T. S., Dragert, H., Wang, K., & Thomas S. J. (2001). A Silent Slip Event on the Deeper Cascadia Subduction Interface. *Science*, *292*(5521), 1236–1058. https://doi.org/10.1126/science.1060152

Duennebier, F. K., Cessaro, R. K., & Harris, D. (1987). TEMPERATURE AND TILT VARIATION MEASURED FOR 64 DAYS IN HOLE 581C. *Init. Repts. DSDP*, *88*, 161–166.

Dvorak, J. J., & Dzurisin, D. (1997). Volcano geodesy: The search for magma reservoirs and the formation of eruptive vents. *Reviews of Geophysics*, *35*(3), 343–384. https://doi.org/10.1029/97RG00070

Elliott, J. L., Grapenthin, R., Parameswaran, R. M., Xiao, Z., Freymueller, J. T., & Fusso, L. (2022). Cascading rupture of a megathrust. *Science Advances*, *8*(18). https://doi.org/10.1126/sciadv.abm4131

Fabian, M., & Villinger, H. (2007). The Bremen ocean bottom tiltmeter (OBT) - A technical article on a new instrument to monitor deep sea floor deformation and seismicity level. *Marine Geophysical Research*, *28*(1), 13–26. https://doi.org/10.1007/s11001-006-9011-4

Fabian, M., & Villinger, H. (2008). Long-term tilt and acceleration data from the Logatchev Hydrothermal Vent Field, Mid-Atlantic Ridge, measured by the Bremen Ocean Bottom Tiltmeter. *Geochemistry, Geophysics, Geosystems*, *9*(7), 1–12. https://doi.org/10.1029/2007GC001917

Feigl, K. L., Agnew, D. C., Bock, Y., Dong, D., Donnellan, A., Hager, B. H., Herring, T. A., Jackson, D. D., Jordan, T. H., King, R. W., Larsen, S., Larson, K. M., Murray, M. H., Shen, Z. kang, & Webb, F. H. (1993). Space geodetic measurement of crustal deformation in central and southern California, 1984-1992. *Journal of Geophysical Research*, *98*(B12), 1984–1992. https://doi.org/10.1029/93jb02405

Fleck, R. J., & Calvert, A. T. (2015). Geochemistry, Geophysics, Geosystems. *Geochemistry Geophysics Geosystems*, *18*(1–2), 1541–1576. https://doi.org/10.1002/2014GC005684.Key

Foreman, M. G. G., Crawford, W. R., Cherniawsky, J. Y., Henry, R. F., & Tarbotton, M. R. (2000). A high-resolution assimilating tidal model for the northeast Pacific Ocean. *Journal of Geophysical Research: Oceans*, *105*(C12), 28629–28651. https://doi.org/10.1029/1999JC000122

Foster, J. (1976). Geology. In I. P. Ting & W. Jennings (Eds.), *Deep Canyon, a Desert Wilderness for Science* (pp. 90–91). University of California.

Fournier, T. J., & Freymueller, J. T. (2007). Transition from locked to creeping subduction in the Shumagin region, Alaska. *Geophysical Research Letters*, *34*(6), L06303. https://doi.org/10.1029/2006GL029073

Fox, C. G. (1993). Five years of ground deformation monitoring on axial seamount using a bottom pressure recorder. *Geophysical Research Letters*, *20*(17), 1859–1862. https://doi.org/10.1029/93GL01216

Fredrickson, E. K., Wilcock, W. S. D., Schmidt, D. A., MacCready, P., Roland, E., Kurapov, A. L., Zumberge, M. A., & Sasagawa, G. S. (2019). Optimizing Sensor Configurations for the Detection of Slow-Slip Earthquakes in Seafloor Pressure Records, Using the Cascadia Subduction Zone as a Case Study. *Journal of Geophysical Research: Solid Earth*, *124*(12), 13504–13531. https://doi.org/10.1029/2019JB018053

Fredrickson, E. K., Gomberg, J. S., Wilcock, W. S. D., Hautala, S. L., Hermann, A. J., & Johnson, H. P. (2023). Slow Slip Detectability in Pressure Records Offshore Alaska. *Journal of Geophysical Research: Solid Earth*, *128*. https://doi.org/10.1029/2022JB024767

Furst, S., Chéry, J., Mohammadi, B., & Peyret, M. (2019). Joint estimation of tiltmeter drift and volume variation during reservoir monitoring. *Journal of Geodesy*, *93*(8), 1137–1146. https://doi.org/10.1007/s00190-019-01231-3

Giddings, S. N., MacCready, P., Hickey, B. M., Banas, N. S., Davis, K. A., Siedlecki, S. A., Trainer, V. L., Kudela, R. M., Pelland, N. A., & Connolly, T. P. (2014). Hindcasts of potential harmful algal bloom transport pathways on the Pacific Northwest coast. *Journal of*

Geophysical Research: Oceans, *119*(4), 2439–2461. https://doi.org/10.1002/2013JC009622.Received

Goldfinger, C. (2011). Submarine Paleoseismology Based on Turbidite Records. *Annual Review of Marine Science*. https://doi.org/10.1146/annurev-marine-120709-142852

Gomberg, J. (2018). Cascadia onshore-offshore site response, submarine sediment mobilization, and earthquake recurrence. *Journal of Geophysical Research: Solid Earth*, *123*, 1381–1404. https://doi.org/10.1002/2017JB014985

Gomberg, J., Hautala, S., Johnson, P., & Chiswell, S. (2019). Separating Sea and Slow Slip Signals on the Seafloor. *Journal of Geophysical Research: Solid Earth*, 2019JB018285. https://doi.org/10.1029/2019JB018285

Hautala, S. L. (2018). The abyssal and deep circulation of the Northeast Pacific Basin. *Progress in Oceanography*, *160*(January 2017), 68–82. https://doi.org/10.1016/j.pocean.2017.11.011

He, B., Wei, M., Watts, D. R., & Shen, Y. (2020). Detecting Slow Slip Events From Seafloor Pressure Data Using Machine Learning. *Geophysical Research Letters*, *47*(11), 1–8. https://doi.org/10.1029/2020GL087579

Hefner, W. L., Nooner, S. L., Chadwick, W. W., & Bohnenstiehl, D. W. R. (2020). Revised Magmatic Source Models for the 2015 Eruption at Axial Seamount Including Estimates of Fault-Induced Deformation. *Journal of Geophysical Research: Solid Earth*, *125*(4), 1–11. https://doi.org/10.1029/2020JB019356

Hensch, M., Dahm, T., Hort, M., Huebscher, C., & Dehghani, A. (2009). *On the interrelation of fluid-induced seismicity and crustal deformation at Columbo Seamount (Aegean Sea , Greece)*. University of Hamburg.

Hermann, A. J., Curchitser, E. N., Haidvogel, D. B., & Dobbins, E. L. (2009). A comparison of remote vs. local influence of El Niño on the coastal circulation of the northeast Pacific. *Deep-Sea Research Part II: Topical Studies in Oceanography*, *56*(24), 2427–2443. https://doi.org/10.1016/j.dsr2.2009.02.005

Hermann, A. J., Hinckley, S., Dobbins, E. L., Haidvogel, D. B., Bond, N. A., Mordy, C., Kachel, N., & Stabeno, P. J. (2009). Quantifying cross-shelf and vertical nutrient flux in the Coastal Gulf of Alaska with a spatially nested, coupled biophysical model. *Deep Sea Research Part II: Topical Studies in Oceanography*, *56*(24), 2474–2486. https://doi.org/10.1016/j.dsr2.2009.02.008

Hermann, A. J., Hinckley, S., Dobbins, E. L., Haidvogel, D. B., Bond, N. A., Mordy, C., Kachel, N., & Stabeno, P. J. (2009). Quantifying cross-shelf and vertical nutrient flux in the Coastal Gulf of Alaska with a spatially nested, coupled biophysical model. *Deep-Sea Research Part II: Topical Studies in Oceanography*, *56*(24), 2474–2486. https://doi.org/10.1016/j.dsr2.2009.02.008

Hilmo, R., & Wilcock, W. S. D. (2020). Physical Sources of High-Frequency Seismic Noise on Cascadia Initiative Ocean Bottom Seismometers. *Geochemistry, Geophysics, Geosystems*, *21*(10), 1–20. https://doi.org/10.1029/2020GC009085

Hino, R., Inazu, D., Ohta, Y., Ito, Y., Suzuki, S., Iinuma, T., Osada, Y., Kido, M., Fujimoto, H., & Kaneda, Y. (2014). Was the 2011 Tohoku-Oki earthquake preceded by aseismic preslip? Examination of seafloor vertical deformation data near the epicenter. *Marine Geophysical Research*, *35*(3), 181–190. https://doi.org/10.1007/s11001-013-9208-2

Hirose, H., Hirahara, K., Kimata, F., Fujii, N., & Miyazaki, S. (1999). A slow thrust slip event following the two 1996 Hyuganada earthquakes beneath the Bungo Channel, southwest Japan. *Geophysical Research Letters*, *26*(21), 3237–3240. https://doi.org/10.1029/1999GL010999

Homola, K., Johnson, H. P., & Hearn, C. (2015). In situ measurements of thermal diffusivity in sediments of the methane-rich zone of Cascadia Margin, NE Pacific Ocean. *Elementa*, *3*, 1–8. https://doi.org/10.12952/journal.elementa.000039

Hughes, C. W., & Meredith, M. P. (2006). Coherent sea-level fluctuations along the global continental slope. *Philosophical Transactions of the Royal Society A: Mathematical, Physical and Engineering Sciences*, *364*(1841), 885–901. https://doi.org/10.1098/rsta.2006.1744

Hughes, C. W., Williams, J., Blaker, A., Coward, A., & Stepanov, V. (2018). A window on the deep ocean: The special value of ocean bottom pressure for monitoring the large-scale, deep-ocean circulation. *Progress in Oceanography*, *161*, 19–46. https://doi.org/10.1016/j.pocean.2018.01.011

Ikehara, K., Kanamatsu, T., Nagahashi, Y., Strasser, M., Fink, H., Usami, K., Irino, T., & Wefer, G. (2016). Documenting large earthquakes similar to the 2011 Tohoku-oki earthquake from sediments deposited in the Japan Trench over the past 1500 years. *Earth and Planetary Science Letters*, *445*, 48–56. https://doi.org/10.1016/j.epsl.2016.04.009

Inoue, T., Ito, Y., Wallace, L. M., Yoshikawa, Y., Inazu, D., Garcia, E. S. M., Muramoto, T., Webb, S. C., Ohta, K., Suzuki, S., & Hino, R. (2021). Water Depth Dependence of Long-Range Correlation in Nontidal Variations in Seafloor Pressure. *Geophysical Research Letters*, *48*(8). https://doi.org/10.1029/2020GL092173

Ito, Y., Hino, R., Kido, M., Fujimoto, H., Osada, Y., Inazu, D., Ohta, Y., Iinuma, T., Ohzono, M., Miura, S., Mishina, M., Suzuki, K., Tsuji, T., & Ashi, J. (2013). Episodic slow slip events in the Japan subduction zone before the 2011 Tohoku-Oki earthquake. *Tectonophysics*, *600*, 14–26. https://doi.org/10.1016/j.tecto.2012.08.022

Itoh, Y., Nishimura, T., Ariyoshi, K., & Matsumoto, H. (2019). Interplate Slip Following the 2003 Tokachi-oki Earthquake From Ocean Bottom Pressure Gauge and Land GNSS Data. *Journal of Geophysical Research: Solid Earth*, *124*(4), 4205–4230. https://doi.org/10.1029/2018JB016328

Itou, M., Matsumura, I., & Noriki, S. (2000). A large flux of particulate matter in the deep Japan Trench observed just after the 1994 Sanriku-Oki earthquake. *Deep-Sea Research*, *1*(47), 1987–1998.

Jahr, T., Jentzsch, G., & Weise, A. (2009). Natural and man-made induced hydrological signals, detected by high resolution tilt observations at the Geodynamic Observatory Moxa/Germany. *Journal of Geodynamics*, *48*(3–5), 126–131. https://doi.org/10.1016/j.jog.2009.09.011

Jahr, T., Jentzsch, G., Gebauer, A., & Lau, T. (2008). Deformation, seismicity, and fluids: Results of the 2004/2005 water injection experiment at the KTB/Germany. *Journal of Geophysical Research: Solid Earth*, *113*(11), 1–10. https://doi.org/10.1029/2008JB005610

Jahr, T., Letz, H., & Jentzsch, G. (2006). Monitoring fluid induced deformation of the earth's crust: A large scale experiment at the KTB location/Germany. *Journal of Geodynamics*, *41*(1–3), 190–197. https://doi.org/10.1016/j.jog.2005.08.003

Janiszewski, H. A., Eilon, Z., Russell, J. B., Brunsvik, B., Gaherty, J. B., Mosher, S. G., Hawley, W. B., & Coats, S. (n.d.). Broadband Ocean Bottom Seismometer Noise Properties. *Geophysical Journal International*.

Johnson, H. P., Gomberg, J. S., Hautala, S. L., & Salmi, M. S. (2017). Sediment gravity flows triggered by remotely generated earthquake waves. *Journal of Geophysical Research: Solid Earth*, *122*(6), 4584–4600. https://doi.org/10.1002/2016JB013689

Johnson, H. P., Gomberg, J. S., Hautala, S. L., & Salmi, M. S. (2017). Sediment gravity flows triggered by remotely generated earthquake waves. *Journal of Geophysical Research: Solid Earth*, *122*, 4584–4600. https://doi.org/10.1002/2016JB013689

Kato, A., Obara, K., Igarashi, T., Tsuruoka, H., Nakagawa, S., & Hirata, N. (2012). Propagation of Slow Slip Leading Up to the 2011 Mw 9.0 Tohoku-Oki Earthquake. *Science*, *335*(6069), 705–708. https://doi.org/10.1126/science.1215141

Kawaguchi, K., Kaneko, S., Nishida, T., & Komine, T. (2015). Construction of the DONET real-time seafloor observatory for earthquakes and tsunami monitoring. In *SEAFLOOR OBSERVATORIES* (pp. 211–228). Berlin, Heidelberg: Springer Berlin Heidelberg. https://doi.org/10.1007/978-3-642-11374-1_10

Kimura, T., Araki, E., & Kitada, K. (2013). Evaluation tests on tiltmeter and seismometer for the Long-Term Borehole Monitoring System. In *Proceedings of the 11th SEGJ International Symposium, Yokohama, Japan, 18-21 November 2013* (pp. 438–442). Society of Exploration Geophysicists. https://doi.org/10.1190/segj112013-111

Kinoshita, M., Sayanagi, K., Kasaya, T., Araki, E., & Ito, H. (2009). Long-term temperatures measurements at some onland and sub-seafloor boreholes. *JAMSTEC-R IFREE Special Issue*, (November), 21–25.

Kitada, K., Araki, E., Kimura, T., Kinoshita, M., Kopf, A., & Saffer, D. (2013). Long-term monitoring at C0002 seafloor borehole in Nankai Trough seismogenic zone. *2013 IEEE International Underwater Technology Symposium, UT 2013*, 15–17. https://doi.org/10.1109/UT.2013.6519882

Kreemer, C., Blewitt, G., & Klein, E. C. (2014). A geodetic plate motion and Global Strain Rate Model. *Geochemistry, Geophysics, Geosystems*, *15*(10), 3849–3889. https://doi.org/10.1002/2014GC005407

Kühnel, M., Diethold, C., & Fröhlich, T. (2015). Progress of the tu ilmenau dual axis tiltmeter with nanorad resolution. *XXI IMEKO World Congress "Measurement in Research and Industry."*

Ladd, C., Mordy, C. W., Kachel, N. B., & Stabeno, P. J. (2007). Northern Gulf of Alaska eddies and associated anomalies. *Deep-Sea Research I*, *54*, 487–509. https://doi.org/10.1016/j.dsr.2007.01.006

Levin, L. A., Bett, B. J., Gates, A. R., Heimbach, P., Howe, B. M., Janssen, F., … Weller, R. A. (2019). Global Observing Needs in the Deep Ocean. *Frontiers in Marine Science*, *6*(May), 1–32. https://doi.org/10.3389/fmars.2019.00241

Li, J., Shillington, D. J., Becel, A., Nedimović, M. R., Webb, S. C., Saffer, D. M., Keranen, K. M., & Kuehn, H. (2015). Downdip variations in seismic reflection character: Implications for fault structure and seismogenic behavior in the Alaska subduction zone. *Journal of Geophysical Research: Solid Earth*, *120*, 7883–7904. https://doi.org/10.1002/2015JB012338

Li, S., & Freymueller, J. T. (2018). Spatial Variation of Slip Behavior Beneath the Alaska Peninsula Along Alaska-Aleutian Subduction Zone. *Geophysical Research Letters*, *45*, 3453–3460. https://doi.org/10.1002/2017GL076761

Lindsey, E. O., Mallick, R., Hubbard, J. A., Bradley, K. E., Almeida, R. V., Moore, J. D. P., Bürgmann, R., & Hill, E. M. (2021). Slip rate deficit and earthquake potential on shallow megathrusts. *Nature Geoscience*, *14*(5), 321–326. https://doi.org/10.1038/s41561-021-00736-x

Liu, Y., MacCready, P., Hickey, B. M., Dever, E. P., Kosro, P. M., & Banas, N. S. (2009). Evaluation of a coastal ocean circulation model for the Columbia river plume in summer 2004. *Journal of Geophysical Research: Oceans*, *114*(3), 1–23. https://doi.org/10.1029/2008JC004929

Logan, P. D., & Johnson, G. C. (2017). Zonal evolution of Alaskan Stream structure and transport quantified with Argo data. *Journal of Geophysical Research: Oceans*, *122*, 821–833. https://doi.org/10.1002/2016JC012302.Received

Lowry, A. R., Larson, K. M., Kostoglodov, V., & Bilham, R. (2001). Transient fault slip in Guerrero, southern Mexico. *Geophysical Research Letters*, *28*(19), 3753–3756.

Luther, D. S., Chave, A. D., Filloux, J. H., & Spain, P. F. (1990). Evidence for local and nonlocal barotropic responses to atmospheric forcing during BEMPEX. *Geophysical Research Letters*, *17*(7), 949–952.

Luther, D. S., Chave, A. D., Filloux, J. H., & Spain, P. F. (1990). Evidence for local and nonlocal barotropic responses to atmospheric forcing during BEMPEX. *Geophysical Research Letters*, *17*(7), 949–952. https://doi.org/10.1029/GL017i007p00949

Luther, D. S., Chave, A. D., Filloux, J. H., & Spain, P. F. (1990). Evidence for local and nonlocal barotropic responses to atmospheric forcing during BEMPEX. *Geophysical Research Letters*, *17*(7), 949–952. https://doi.org/10.1029/GL017i007p00949

MacCready, P., McCabe, R. M., Siedlecki, S. A., Lorenz, M., Giddings, S. N., Bos, J., Albertson, S., Banas, N. S., & Garnier, S. (2021). Estuarine Circulation, Mixing, and Residence Times in the Salish Sea. *Journal of Geophysical Research: Oceans*, *126*(2), 1–19. https://doi.org/10.1029/2020JC016738

Massonnet, D., Rossi, M., Carmona, C., Adragna, F., Peltzer, G., Feigl, K., & Rabaute, T. (1993). The displacement field of the Landers earthquake mapped by radar interferometry. *Nature*, *364*(6433), 138–142. https://doi.org/10.1038/364138a0

McCaffrey, R., King, R. W., Payne, S. J., & Lancaster, M. (2013). Active tectonics of northwestern U.S. inferred from GPS-derived surface velocities. *Journal of Geophysical Research: Solid Earth*, *118*(2), 709–723. https://doi.org/10.1029/2012JB009473

McGuire, J. J., Collins, J. A., Davis, E., Becker, K., & Heesemann, M. (2018). A Lack of Dynamic Triggering of Slow Slip and Tremor Indicates That the Shallow Cascadia Megathrust Offshore Vancouver Island Is Likely Locked. *Geophysical Research Letters*, *45*(20), 11,095-11,103. https://doi.org/10.1029/2018GL079519

Mchugh, C. M., Kanamatsu, T., Seeber, L., Bopp, R., Cormier, M., & Usami, K. (2016). Remobilization of surficial slope sediment triggered by the A.D. 2011 M w 9 Tohoku-Oki earthquake and tsunami along the Japan Trench. *Geology*, *44*(5), 391–394. https://doi.org/10.1130/G37650.1

Mchugh, C. M., Seeber, L., Braudy, N., Cormier, M., Davis, M. B., Diebold, J. B., Dieudonne, N., Douilly, R., Gulick, S. P. S., Hornbach, M. J., Iii, H. E. J., Ryan, K., Sorlien, C. C., Steckler, M. S., Symithe, S. J., & Templeton, J. (2011). Offshore sedimentary effects of the 12 January 2010 Haiti earthquake. *Geology*, *39*(8), 723–726. https://doi.org/10.1130/G31815.1

Mungov, G., Eblé, M., & Bouchard, R. (2013). DART® Tsunameter Retrospective and Real-Time Data: A Reflection on 10 Years of Processing in Support of Tsunami Research and Operations. *Pure and Applied Geophysics*, *170*(9–10), 1369–1384. https://doi.org/10.1007/s00024-012-0477-5

Muramoto, T., Ito, Y., Inazu, D., Wallace, L. M., Hino, R., Suzuki, S., Webb, S. C., & Henrys, S. (2019). Seafloor Crustal Deformation on Ocean Bottom Pressure Records With Nontidal Variability Corrections: Application to Hikurangi Margin, New Zealand. *Geophysical Research Letters*, *46*(1), 303–310. https://doi.org/10.1029/2018GL080830

Nagano, A., Yamashita, Y., Ariyoshi, K., Hasegawa, T., Matsumoto, H., & Shinohara, M. (2021). Seafloor Pressure Change Excited at the Northwest Corner of the Shikoku Basin by the Formation of the Kuroshio Large-Meander in September 2017. *Frontiers in Earth Science*, *8*(January), 1–16. https://doi.org/10.3389/feart.2020.583481

Noguchi, T., Tanikawa, W., Hirose, T., Lin, W., Kawagucci, S., Yoshida-Takashima, Y., Honda, M. C., Takai, K., Kitizato, H., & Okamura, K. (2012). Dynamic process of turbidity generation triggered by the 2011 Tohoku-Oki earthquake. *Geochemistry, Geophysics, Geosystems*, *13*(11), 1–7. https://doi.org/10.1029/2012GC004360

Nooner, S. L., & Chadwick, W. W. (2016). Inflation-predictable behavior and co-eruption deformation at Axial Seamount. *Science*, *354*(6318), 1399–1403. https://doi.org/10.1126/science.aah4666

Obara, K. (2002). Nonvolcanic Deep Tremor Associated with Subduction in Southwest Japan. *Science*, *296*(5573), 1679–1682. https://doi.org/10.1126/science.1070378

Oguri, K., Kawamura, K., Sakaguchi, A., Toyofuku, T., Kasaya, T., Murayama, M., Fujikura, K., Glud, R. N., & Kitazato, H. (2013). Hadal disturbance in the Japan Trench induced by the 2011 Tohoku-Oki earthquake. *Scientific Reports*, *3*(1915), 1–6. https://doi.org/10.1038/srep01915

Ozawa, S., Suito, H., & Tobita, M. (2007). Occurrence of quasi-periodic slow-slip off the east coast of the Boso peninsula, central Japan. *Earth, Planets and Space*, *59*(12), 1241–1245. https://doi.org/10.1186/BF03352072

Party, S. S. (2000). *Proceedings of the Ocean Drilling Program, 186 Initial Reports*. (I. S. Sacks, K. Suyehiro, G. D. Acton, & E. Al., Eds.), *Proceedings of the Ocean Drilling Program, 186 Initial Reports* (Vol. 186). Ocean Drilling Program. https://doi.org/10.2973/odp.proc.ir.186.2000

Party, S. S. (2000). Borehole Instrument Package. In I. S. Sacks, K. Suyehiro, G. D. Acton, & E. Al. (Eds.), *Proceedings of the Ocean Drilling Program, 186 Initial Reports* (Vol. 186). https://doi.org/10.2973/odp.proc.ir.186.2000

Pickart, R. S., & Watts, D. R. (1990). Deep Western Boundary Current variability at Cape Hatteras. *Journal of Marine Research*, *48*(4), 765–791. https://doi.org/10.1357/002224090784988674

Piper, D. J. W., Tripsanas, E., Mosher, D. C., & Mackillop, K. (2019). Paleoseismicity of the continental margin of eastern Canada: Rare regional failures and associated turbidites in Orphan Basin. *Geosphere*, *15*(1), 85–107. https://doi.org//10.1130/GES02001.1

Poland, M. P., & Zebker, H. A. (2022). Volcano geodesy using InSAR in 2020: the past and next decades. *Bulletin of Volcanology*, *84*(3). https://doi.org/10.1007/s00445-022-01531-1

Polster, A., Fabian, M., & Villinger, H. (2009). Effective resolution and drift of paroscientific pressure sensors derived from long-term seafloor measurements. *Geochemistry, Geophysics, Geosystems*, *10*(8). https://doi.org/10.1029/2009GC002532

Radiguet, M., Perfettini, H., Cotte, N., Gualandi, A., Valette, B., Kostoglodov, V., Lhomme, T., Walpersdorf, A., Cabral Cano, E., & Campillo, M. (2016). Triggering of the 2014 Mw 7.3 Papanoa earthquake by a slow slip event in Guerrero, Mexico. *Nature Geoscience*, *9*(11), 829–833. https://doi.org/10.1038/ngeo2817

Reece, R. S., Gulick, S. P. S., Horton, B. K., Christeson, G. L., & Worthington, L. L. (2011). Tectonic and climatic influence on the evolution of the Surveyor Fan and Channel system, Gulf of Alaska. *Geosphere*, *7*(4), 830–844. https://doi.org/10.1130/GES00654.1

Reed, R. K., & Stabeno, P. J. (1989). Recent observations of variability in the path and vertical structure of the Alaskan Stream. *Journal of Physical Oceanography*, *19*, 1634–1642.

Rousset, B., Fu, Y., Bartlow, N., & Bürgmann, R. (2019). Weeks-Long and Years-Long Slow Slip and Tectonic Tremor Episodes on the South Central Alaska Megathrust. *Journal of Geophysical Research: Solid Earth*, *124*(12), 13392–13403. https://doi.org/10.1029/2019JB018724

Ruiz, S., Métois, M., Fuenzalida, A., Ruiz, J., Leyton, F., Grandin, R., Vigny, C., Madariaga, R., & Campos, J. (2014). Intense foreshocks and a slow slip preceded the 2014 Iquique Mw 8.1 earthquake. *Science*, *345*(6201), 1165–1169. https://doi.org/10.1126/science.1256074

Ryan, H., Von Huene, R., Scholl, D., & Kirby, S. (2012). Tsunami Hazards to U.S. Coasts From Giant Earthquakes in Alaska. *EOS, Transactions, American Geophysical Union*, *93*(19), 185–186. https://doi.org/10.1111/j.1365-246X.2006.02899.x.von

Sakata, S., & Shimada, S. (1984). Development of the Ocean Bottom Tiltmeter (2). *Journal of the Geodetic Society of Japan*, *30*(1), 50–58. https://doi.org/10.11366/sokuchi1954.30.50

Salmi, M. S., Johnson, H. P., & Harris, R. N. (2017). Thermal environment of the Southern Washington region of the Cascadia subduction zone. *Journal of Geophysical Research: Solid Earth*, *122*(8), 5852–5870. https://doi.org/10.1002/2016JB013839

Sasagawa, G., Cook, M. J., & Zumberge, M. A. (2016). Drift-corrected seafloor pressure observations of vertical deformation at Axial Seamount 2013-2014. *Earth and Space Science*, *3*(9), 381–385. https://doi.org/10.1002/2016EA000190

Sawyer, D. E., Reece, R. S., Gulick, S. P. S., & Lenz, B. L. (2017). Submarine landslide and tsunami hazards offshore southern Alaska: Seismic strengthening versus rapid sedimentation. *Geophysical Research Letterse*, *44*, 8435–8442. https://doi.org/10.1002/2017GL074537

Scharroo, R., Bonekamp, H., Ponsard, C., Parisot, F., Von Engeln, A., Tahtadjiev, M., De Vriendt, K., & Montagner, F. (2016). Jason continuity of services: Continuing the Jason altimeter data records as Copernicus Sentinel-6. *Ocean Science*, *12*(2), 471–479. https://doi.org/10.5194/os-12-471-2016

Shchepetkin, A. F., & McWilliams, J. C. (2005). The regional oceanic modeling system (ROMS): a split-explicit, free-surface, topography-following-coordinate oceanic model. *Ocean Modelling*, *9*(4), 347–404. https://doi.org/10.1016/j.ocemod.2004.08.002

Shillington, D. J., Becel, A., Nedimovic, M. R., Kuehn, H., Webb, S. C., Abers, G. A., Keranen, K. M., Li, J., Delescluse, M., & Mattei-Salicrup, G. A. (2015). Link between plate fabric, hydration and subduction zone seismicity in Alaska. *Nature Geoscience*, *8*(12), 961–964. https://doi.org/10.1038/ngeo2586

Shimamura, H., & Kanazawa, T. (1988). Ocean bottom tiltmeter with acoustic data retrieval system implanted by a submersible. *Marine Geophysical Researches*, *9*(3), 237–254. https://doi.org/10.1007/BF00309975

Shiobara, H., Ito, A., Sugioka, H., Shinohara, M., & Sato, T. (2021). Tilt Observations at the Seafloor by Mobile Ocean Bottom Seismometers. *Frontiers in Earth Science*, *8*(March), 1–13. https://doi.org/10.3389/feart.2020.599810

Siegismund, F., Romanova, V., Köhl, A., & Stammer, D. (2011). Ocean bottom pressure variations estimated from gravity, nonsteric sea surface height and hydrodynamic model simulations. *Journal of Geophysical Research: Oceans*, *116*(C7), 2010JC006727. https://doi.org/10.1029/2010JC006727

Stabeno, P. J., Bond, N. A., Hermann, A. J., Kachel, N. B., Mordy, C. W., & Overland, J. E. (2004). *Meteorology and oceanography of the Northern Gulf of Alaska*. *Continental Shelf Research* (Vol. 24). https://doi.org/10.1016/j.csr.2004.02.007

Stabeno, P. J., Bond, N. A., Kachel, N. B., Ladd, C., Mordy, C. W., & Strom, S. L. (2016). Southeast Alaskan shelf from southern tip of Baranof Island to Kayak Island: Currents, mixing and chlorophyll-a. *Deep-Sea Research Part II: Topical Studies in Oceanography*, *132*, 6–23. https://doi.org/10.1016/j.dsr2.2015.06.018

Stabeno, P. J., Bell, S., Cheng, W., Danielson, S., Kachel, N. B., & Mordy, C. W. (2016). Deep-Sea Research II Long-term observations of Alaska Coastal Current in the northern Gulf of Alaska $. *Deep-Sea Research Part II*, *132*, 24–40. https://doi.org/10.1016/j.dsr2.2015.12.016

Stabeno, P. J., & Hristova, H. G. (2014). Deep-Sea Research I Observations of the Alaskan Stream near Samalga Pass and its connection to the Bering Sea: 2001 – 2004. *Deep-Sea Research Part I*, *88*, 30–46. https://doi.org/10.1016/j.dsr.2014.03.002

Stenvold, T., Eiken, O., Zumberge, M. A., Sasagawa, G. S., & Nooner, S. L. (2006). High-precision relative depth and subsidence mapping from seafloor water-pressure measurements. *SPE Journal*, *11*(3), 380–389. https://doi.org/10.2118/97752-PA

Stone, I., Vidale, J. E., Han, S., & Roland, E. (2018). Catalog of Offshore Seismicity in Cascadia: Insights Into the Regional Distribution of Microseismicity and its Relation to Subduction Processes. *Journal of Geophysical Research: Solid Earth*, *123*, 641–652. https://doi.org/10.1002/2017JB014966

Suzuki, K., Araki, E., & Takahashi, N. (2018). Detectability of crustal deformation by using ocean bottom pressure gauges deployed to DONET system. *2018 OCEANS - MTS/IEEE Kobe Techno-Oceans, OCEANS - Kobe 2018*, 12–15. https://doi.org/10.1109/OCEANSKOBE.2018.8559470

Taburet, G., Sanchez-Roman, A., Ballarotta, M., Pujol, M.-I., Legeais, J.-F., Fournier, F., Faugere, Y., & Dibarboure, G. (2019). DUACS DT2018: 25 years of reprocessed sea level altimetry products. *Ocean Science*, *15*(5), 1207–1224. https://doi.org/10.5194/os-15-1207-2019

Takamori, A., Bertolini, A., Desalvo, R., Araya, A., Kanazawa, T., & Shinohara, M. (2011). Novel compact tiltmeter for ocean bottom and other frontier observations. *Measurement Science and Technology*, *22*(11). https://doi.org/10.1088/0957-0233/22/11/115901

Talling, P. J., Allin, J., Armitage, D. A., Arnott, R. W. C., Cartigny, M. J. B., Clare, M. A., … Xu, J. (2015). Key future directions for research on turbidity currents and their deposits. *Journal of Sedimentary Research*, *85*, 153–169. https://doi.org//10.2110/jsr.2015.03

Talling, P. J., Paull, C. K., & Piper, D. J. W. (2013). How are subaqueous sediment density flows triggered, what is their internal structure and how does it evolve? Direct observations from monitoring of active flows. *Earth Science Reviews*, *125*, 244–287. https://doi.org/10.1016/j.earscirev.2013.07.005

ten Brink, U. S., Lee, H. J., Geist, E. L., & Twichell, D. (2009). Assessment of tsunami hazard to the U.S. East Coast using relationships between submarine landslides and earthquakes. *Marine Geology*, *264*(1–2), 65–73. https://doi.org/10.1016/j.margeo.2008.05.011

Thomson, R. E., Davis, E. E., Heesemann, M., & Villinger, H. (2010). Observations of long-duration episodic bottom currents in the Middle America Trench: Evidence for tidally initiated turbidity flows. *Journal of Geophysical Research*, *115*, 1–23. https://doi.org/10.1029/2010JC006166

Thomson, R. E., & Emery, W. J. (2014). *Data Analysis Methods in Physical Oceanography*. Elsevier. https://doi.org/10.1016/C2010-0-66362-0

Todd, E. K., Schwartz, S. Y., Mochizuki, K., Wallace, L. M., Sheehan, A. F., Webb, S. C., Williams, C. A., Nakai, J., Yarce, J., Fry, B., Henrys, S., & Ito, Y. (2018). Earthquakes and Tremor Linked to Seamount Subduction During Shallow Slow Slip at the Hikurangi Margin, New Zealand. *Journal of Geophysical Research: Solid Earth*, *123*(8), 6769–6783. https://doi.org/10.1029/2018JB016136

Tolstoy, M., Constable, S., Orcutt, J., Staudigel, H., Wyatt, F. K., & Anderson, G. (1998). Short and long baseline tiltmeter measurements on axial seamount, Juan de Fuca Ridge. *Physics of the Earth and Planetary Interiors*, *108*(2), 129–141. https://doi.org/10.1016/S0031-9201(98)00091-0

Tolstoy, M., Vernon, F. L., Orcutt, J. A., & Wyatt, F. K. (2002). Breathing of the seafloor: Tidal correlations of seismicity at Axial volcano. *Geology*, *30*(6), 503. https://doi.org/10.1130/0091-7613(2002)030<0503:BOTSTC>2.0.CO;2

Toomey, D. R., Allen, R. M., Barclay, A. H., Samuel, W., Bromirski, P. D., Carlson, R. L., … Wilcock, W. S. D. (2014). The Cascadia Initiative: A Sea Change In Seismological Studies of Subduction Zones. *Oceanography*, *27*(2), 138–150.

Tripsanas, E. K., Bryant, W. R., & Phaneuf, B. A. (2004). Slope-instability processes caused by salt movements in a complex deep-water environment, Bryant Canyon area, northwest Gulf of Mexico. *American Association of Petroleum Geologists Bulletin*, *88*(6), 801–823. https://doi.org/10.1306/01260403106

Uchida, N., Iinuma, T., Nadeau, R. M., Bürgmann, R., & Hino, R. (2016). Periodic slow slip triggers megathrust zone earthquakes in northeastern Japan. *Science*, *351*(6272), 488–492. https://doi.org/10.1126/science.aad3108

Vallée, M., Nocquet, J. M., Battaglia, J., Font, Y., Segovia, M., Régnier, M., Mothes, P., Jarrin, P., Cisneros, D., Vaca, S., Yepes, H., Martin, X., Béthoux, N., & Chlieh, M. (2013). Intense interface seismicity triggered by a shallow slow slip event in the Central Ecuador subduction zone. *Journal of Geophysical Research: Solid Earth*, *118*(6), 2965–2981. https://doi.org/10.1002/jgrb.50216

Vinogradova, N. T., Ponte, R. M., & Stammer, D. (2007). Relation between sea level and bottom pressure and the vertical dependence of oceanic variability. *Geophysical Research Letters*, *34*(3), 1–5. https://doi.org/10.1029/2006GL028588

von Huene, R., Miller, J. J., & Weinrebe, W. (2012). Subducting plate geology in three great earthquake ruptures of the western Alaska margin, Kodiak to Unimak. *Geosphere*, *8*(3), 628–644. https://doi.org/10.1130/GES00715.1

Wallace, L. M., & Beavan, J. (2010). Diverse slow slip behavior at the Hikurangi subduction margin, New Zealand. *Journal of Geophysical Research: Solid Earth*, *115*(12), 1–20. https://doi.org/10.1029/2010JB007717

Wallace, L. M., Webb, S. C., Ito, Y., Mochizuki, K., Hino, R., Henrys, S., Schwartz, S. Y., & Sheehan, A. (2016). Slow slip near the trench at the Hikurangi subduction zone, New Zealand. *Science*, *352*(6286), 701–704. https://doi.org/10.1126/science.aaf2349 704

Wang, D.-P., & Mooers, C. N. K. (1976). Coastal-Trapped Waves in a Continuously Stratified Ocean. *Journal of Physical Oceanography*, *6*(6), 853–863. https://doi.org/10.1175/1520-0485(1976)006<0853:CTWIAC>2.0.CO;2

Wang, K., & Tréhu, A. M. (2016). Invited review paper: Some outstanding issues in the study of great megathrust earthquakes—The Cascadia example. *Journal of Geodynamics*, *98*, 1–18. https://doi.org/10.1016/j.jog.2016.03.010

Warren, B. A., Owens, W. B., Hole, W., & Hole, W. (1985). Some Preliminary Results Concerning Deep Northern-Boundary Currents in the North Pacific. *Progress in Oceanography*, *14*, 537–551.

Warren, B. A., & Owens, W. B. (1988). Deep Currents in the Central Subarctic Pacific Ocean. *Journal of Physical Oceanography*, *18*(4), 529–551. https://doi.org/10.1175/1520-0485(1988)018<0529:DCITCS>2.0.CO;2

Warren, B. A., & Owens, W. B. (1988). Deep currents in the Central Subarctic Pacific Ocean. *Journal of Physical Oceanography*, *18*, 529–551.

Watts, D. R., & Kontoyiannis, H. (1990). Deep-Ocean Bottom Pressure Measurement: Drift Removal and Performance. *Journal of Atmospheric and Oceanic Technology*. https://doi.org/10.1175/1520-0426(1990)007<0296:dobpmd>2.0.co;2

Watts, D. R., Wei, M., Tracey, K. L., Donohue, K. A., & He, B. (2021). Seafloor Geodetic Pressure Measurements to Detect Shallow Slow Slip Events: Methods to Remove Contributions From Ocean Water. *Journal of Geophysical Research: Solid Earth*, *126*(4), 1–15. https://doi.org/10.1029/2020JB020065

Webb, S. C., & Nooner, S. L. (2016). High-resolution seafloor absolute pressure gauge measurements using a better counting method. *Journal of Atmospheric and Oceanic Technology*, *33*(9), 1859–1874. https://doi.org/10.1175/JTECH-D-15-0114.1

Wilcock, W. S. D., Manalang, D. A., Fredrickson, E. K., Harrington, M. J., Cram, G., Tilley, J., Burnett, J., Martin, D., Kobayashi, T., & Paros, J. M. (2021). A Thirty-Month Seafloor Test of the A-0-A Method for Calibrating Pressure Gauges. *Frontiers in Earth Science*, *8*. https://doi.org/10.3389/feart.2020.600671

Wilcock, W. S. D., Tolstoy, M., Waldhauser, F., Garcia, C., Tan, Y. J., Bohnenstiehl, D. R., Caplan-Auerbach, J., Dziak, R. P., Arnulf, A. F., & Mann, M. E. (2016). Seismic constraints on caldera dynamics from the 2015 Axial Seamount eruption. *Science*, *354*(6318), 1395–1399. https://doi.org/10.1126/science.aah5563

Wilcock, W. S. D., Manalang, D. A., Harrington, M. J., Fredrickson, E. K., Cram, G., Tilley, J., Burnett, J., Martin, D., Kobayashi, T., & Paros, J. M. (2018). New approaches to in situ calibration for seafloor geodetic measurements. *2018 OCEANS - MTS/IEEE Kobe Techno-Oceans, OCEANS - Kobe 2018*. https://doi.org/10.1109/OCEANSKOBE.2018.8559178

Woods, K., Webb, S. C., Wallace, L. M., Ito, Y., Collins, C., Palmer, N., Hino, R., Savage, M. K., Saffer, D. M., Davis, E. E., & Barker, D. H. N. (2022). Using Seafloor Geodesy to Detect Vertical Deformation at the Hikurangi Subduction Zone: Insights From Self-Calibrating Pressure Sensors and Ocean General Circulation Models. *Journal of Geophysical Research: Solid Earth*, *127*(12), 1–22. https://doi.org/10.1029/2022JB023989

Wunsch, C. (2016). Global Ocean Integrals and Means, with Trend Implications. *Annual Review of Marine Science*, *8*, 1–33. https://doi.org/10.1146/annurev-marine-122414-034040

Wyatt, F. K., Agnew, D. C., & Gladwin, M. (1994). Continuous measurements of crustal deformation for the 1992 Landers earthquake sequence. *Bulletin - Seismological Society of America*, *84*(3), 768–779. https://doi.org/10.1016/0148-9062(95)94488-5

Wyatt, F., Bilham, R., Beavan, J., Sylvester, A. G., Owen, T., Harvey, A., Macdonald, C., Jackson, D. D., & Agnew, D. C. (1984). Comparing tiltmeters for crustal deformation measurement - A preliminary report. *Geophysical Research Letters*, *11*(10), 963–966. https://doi.org/10.1029/GL011i010p00963

Wyatt, F. (1982). Displacement of surface monuments: Horizontal motion. *Journal of Geophysical Research: Solid Earth*, *87*(B2), 979–989. https://doi.org/10.1029/JB087iB02p00979

Yamashita, Y., Yakiwara, H., Asano, Y., Shimizu, H., Uchida, K., Hirano, S., Umakoshi, K., Miyamachi, H., Nakamoto, M., Fukui, M., Kamizono, M., Kanehara, H., Yamada, T., Shinohara, M., & Obara, K. (2015). Migrating tremor off southern Kyushu as evidence for slow slip of a shallow subduction interface. *Science*, *348*(6235), 676–679. https://doi.org/10.1126/science.aaa4242

Yarce, J., Sheehan, A. F., Nakai, J. S., Schwartz, S. Y., Mochizuki, K., Savage, M. K., Wallace, L. M., Henrys, S. A., Webb, S. C., Ito, Y., Abercrombie, R. E., Fry, B., Shaddox, H., & Todd, E. K. (2019). Seismicity at the Northern Hikurangi Margin, New Zealand, and Investigation of the Potential Spatial and Temporal Relationships With a Shallow Slow Slip Event. *Journal of Geophysical Research: Solid Earth*, *124*(5), 4751–4766. https://doi.org/10.1029/2018JB017211

Yuan, L., Tian, F., Xu, S., Zhou, C., & Chen, J. (2021). Three-dimensional mesoscale eddy identification and tracking algorithm based on pressure anomalies. *Journal of Oceanology and Limnology*, *39*(6), 2153–2166. https://doi.org/10.1007/s00343-021-0309-5

Zhang, Z., Zhang, Y., Wang, W., & Huang, R. X. (2013). Universal structure of mesoscale eddies in the ocean. *Geophysical Research Letters*, *40*(14), 3677–3681. https://doi.org/10.1002/grl.50736

Zhang, Z., Tian, J., Qiu, B., Zhao, W., Chang, P., Wu, D., & Wan, X. (2016). Observed 3D Structure, Generation, and Dissipation of Oceanic Mesoscale Eddies in the South China Sea. *Scientific Reports*, *6*(1), 24349. https://doi.org/10.1038/srep24349

Appendix 1: Supplementary Material for Chapter 2

Introduction

The included materials provide detailed information about the pressure data used in our analysis, our processing of those pressure data, and the comparability of the two oceanographic models. We also present additional figures of slow slip modeling scenarios discussed in the main text.

Text A1.1

In each year there are pressure records with significant quality issues that render the data unusable for this study. These issues include off-scale/flatline output and the presence of high-amplitude, long-period signals, that could not realistically be produced at the seafloor. Additionally, in the 2013-2014 experiment year, there were systematic mechanical failures in all but one of the pressure sensors, possibly related to air bubbles in the oil-filled inlet tubing (personal communication, Andrew Barclay, Lamont-Doherty Earth Observatory), that lead to increased noise across all frequencies above 0.02 day^{-1} and unpredictable response to pressure perturbations. A single pressure sensor is not sufficient to detect a SSE so we exclude this year from this study. In the 2014-2015 experiment year, 5 instruments yielded pressure data of higher amplitude and increased high-frequency noise relative to instruments from similar locations in this and previous years. This may be due to residual mechanical issues with the sensors and we exclude these data in our assessment of oceanographic signal reduction.

Data from the OOI cabled array came online in 2014 and include 2 high-resolution APG instruments on the margin, all Sea-Bird devices utilizing Paroscientific sensors, which are used to supplement the final year of CI data. A series of seafloor pressure benchmarks with Paroscientific APGs were deployed in 2014 and 2015 across the margin offshore central Oregon as part of an ongoing interseismic deformation experiment (Cook et al., 2017). Data from one of these benchmarks spans the final year of the CI experiment and is included in our analysis.

Text A1.2

The pressure data used in this study are corrected with a 3rd order polynomial, modeled using least-squares, to eliminate instrument drift and long period (i.e. seasonal) oceanographic signals. We elected to use a third-order polynomial after examining the effects of correcting with polynomials order 1-5 as well as a linear trend with an initial exponential, all fit by least squares. A third-order polynomial is the lower order polynomial that successfully removes annual signals that are apparent in much of the data. Some examples of pressure differences from records fit in these ways are shown in Figure A1.1. We determined that a polynomial of 3rd order was the best tradeoff between RMS reduction and avoiding over-fitting the data. Our results are not sensitive to the use of higher-order polynomials.

Text A1.3

Individual pressure records of the LiveOcean and WCOFS oceanographic models are compared at continental shelf, slope, and abyssal plain locations for the 2013-2014 year in time (Figure A1.2a-c) and frequency space (Figure A1.2c-f). The models show the best agreement on or near the continental shelf (Figure A1.2a,d), where the amplitude spectra are broadly comparable and signals are similarly resolved in either model. On the abyssal plain (Figure A1.2c,f), the amplitude spectra remain comparable, but the timing and amplitude of pressure signals do not show good agreement between models. Continental slope locations (Figure

A1.2b,e) fall somewhere between the two, with the most large-amplitude, low-frequency signals similarly resolved but higher-frequency signals varying.

The bottom pressure RMS are highly similar between the two models (Figure A1.3a,b), as are the difference RMS (Figure A1.3c,d). The LiveOcean model generally predicts higher amplitude signals on the inner continental shelf and slightly lower amplitudes on the slope and abyssal plain. Also, the WCOFS model features a region of low RMS near the shelf break not seen in the LiveOcean model. Similarly, difference RMS of the LiveOcean model are larger on the inner continental shelf, but otherwise the two models predict very similar difference amplitudes. The RMS change obtained by subtracting the WCOFS model from LiveOcean at each location within their common domain is contoured in Figure A1.4a. Signal amplitudes are reduced near the coast but are unchanged elsewhere, with the exception of a >0.5 cm increase seen near the shelf break and for a small subset of the abyssal plain. Figure A1.4b contours the R^2 of the fit (equation 1) of the WCOFS model to the LiveOcean model. Most locations show $R^2 > 0.2$, with values as large as 0.75 on the inner continental shelf, while select abyssal plain locations and locations near the shelf break show $R^2 < 0$ and as low as -0.6.

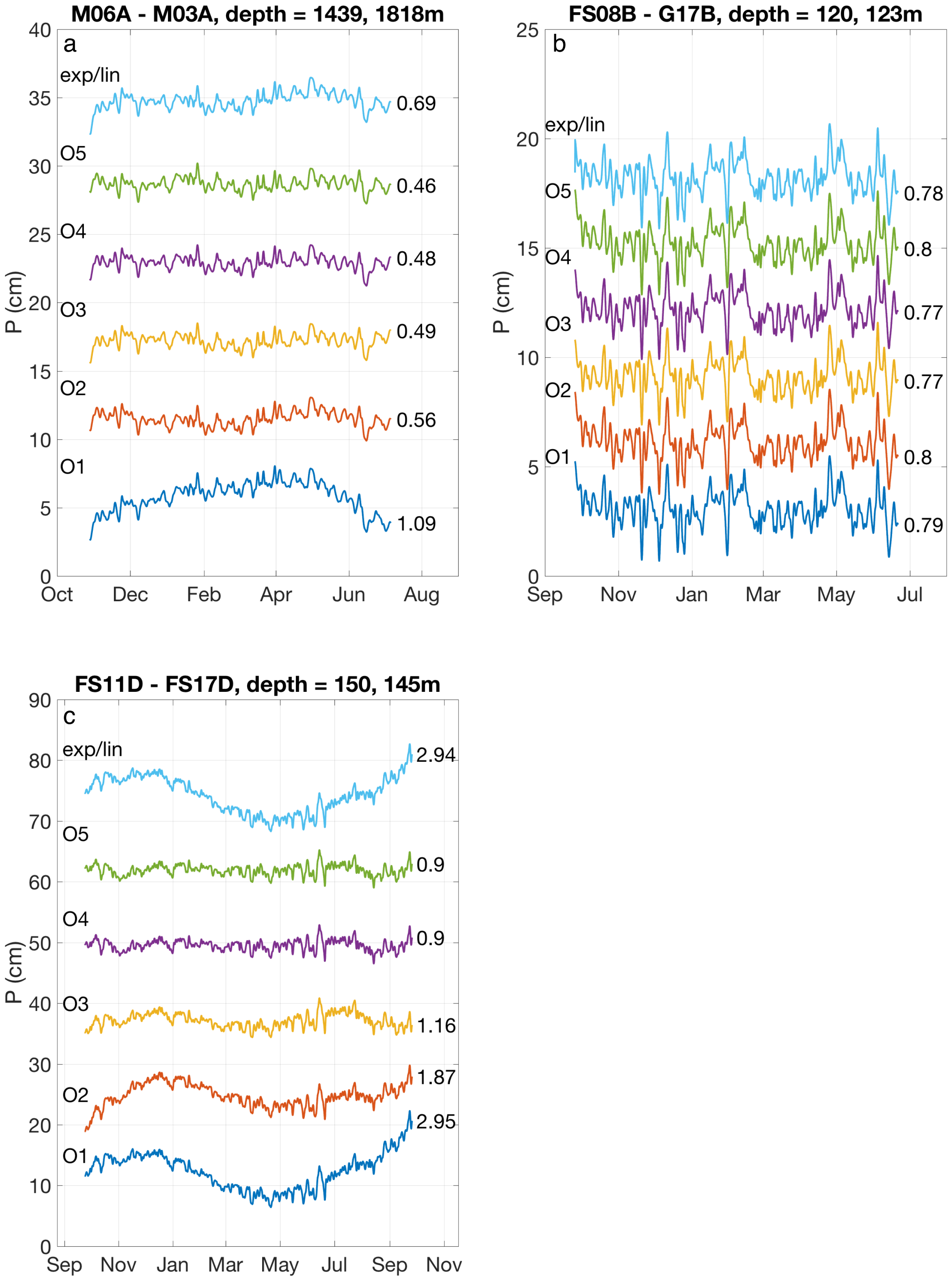

Figure A1.1. Comparison of methods for removing instrument drift for three example pressure differences. From bottom to top, pressure differences were corrected with a polynomial fit of order 1-5 and with a combination linear and exponential fit. Traces are offset for display purposes and RMS values (in cm) are reported next to each. (a) Instruments from the 2011-2012 year on the lower continental slope. (b) Instruments from the 2012-2013 year on the continental shelf. (c) Instruments from the 2014-2015 year on the continental shelf.

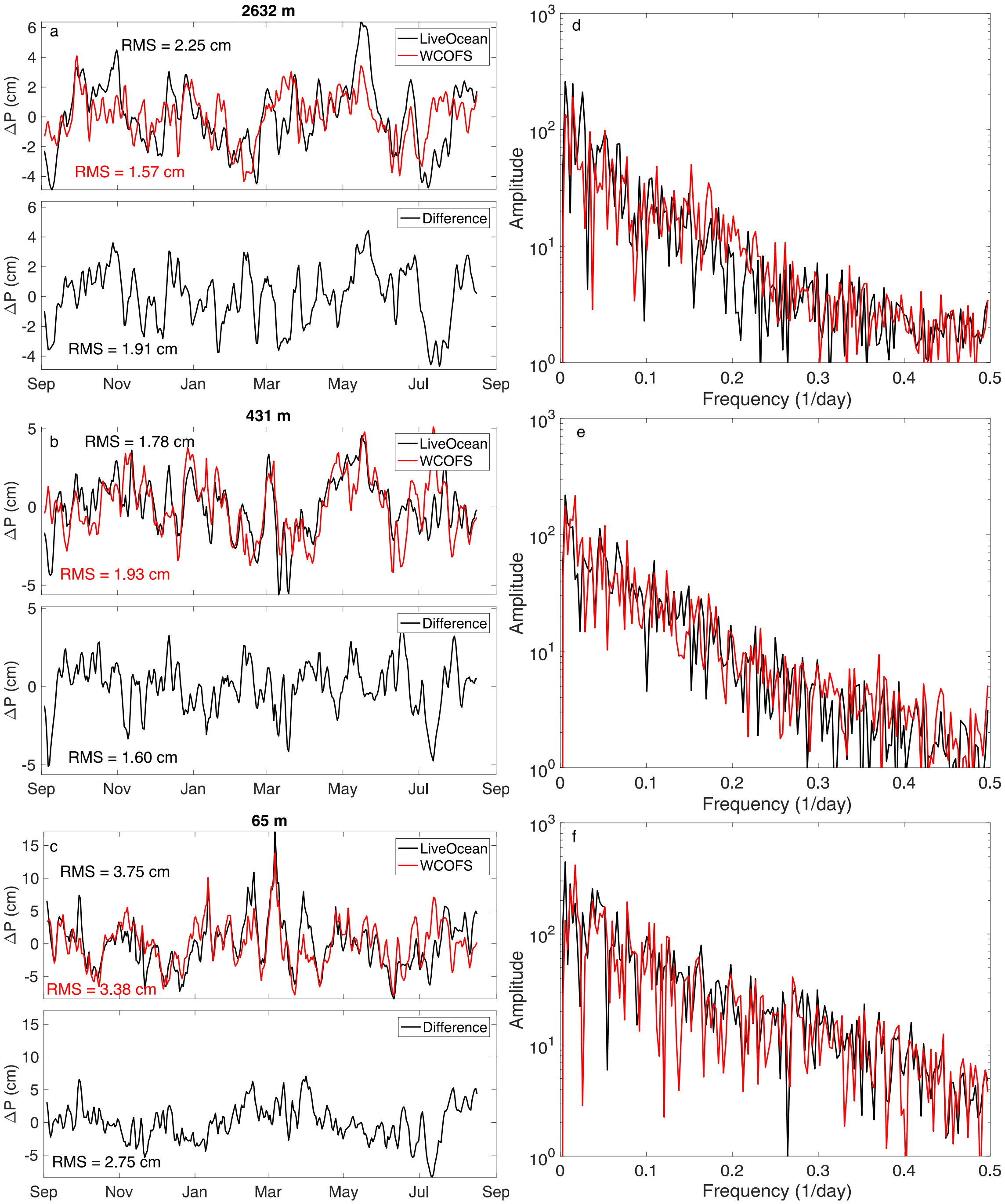

Figure A1.2. Comparison of WCOFS and LiveOcean models in 2013-2014, when the models overlap, for the locations in Figure 6b-d. As with the APG data, these pressures are tidally filtered with a 24-24-25 Godin filter (Godin, 1972). (a-c) Bottom pressure timeseries (upper panels) and differences (lower panels) for a continental shelf, slope, and abyssal plain location. (d-f) Amplitude spectra of the timeseries at the same locations.

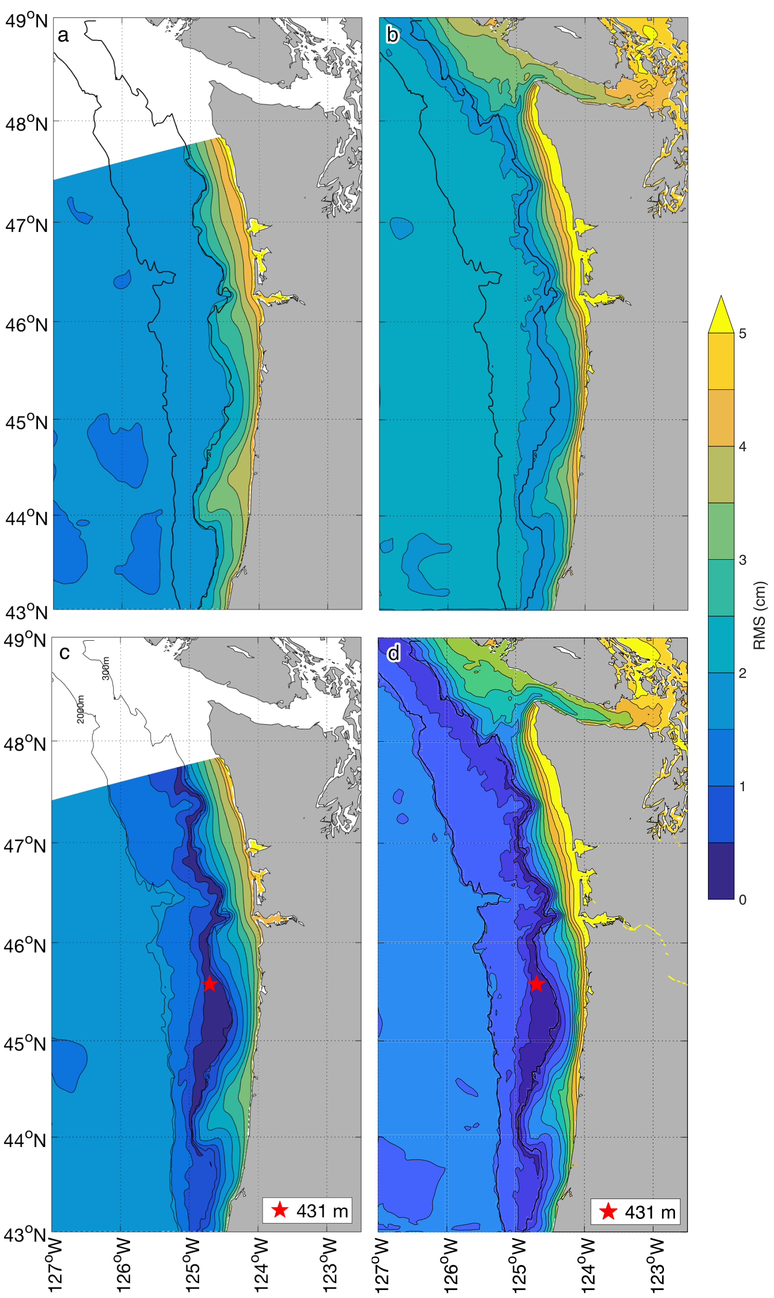

Figure A1.3. Comparison of the seafloor pressure output from the WCOFS and Live Ocean circulation models. (a) Contours of bottom pressure RMS for 2013-2014 for the WCOFS model, with a Godin 24-24-25 filter (Godin, 1972) applied and a 3rd order polynomial fit removed. (b) Contours of RMS for the 2013-2014 LiveOcean model, processed the same way. (c) Contours of pressure difference RMS against a reference location at 500 m depth, as indicated by the red star, from the WCOFS model. (d) Contours of pressure difference RMS from the LiveOcean model, for the same reference location. Black lines show the 300 m and 2000 m isobaths.

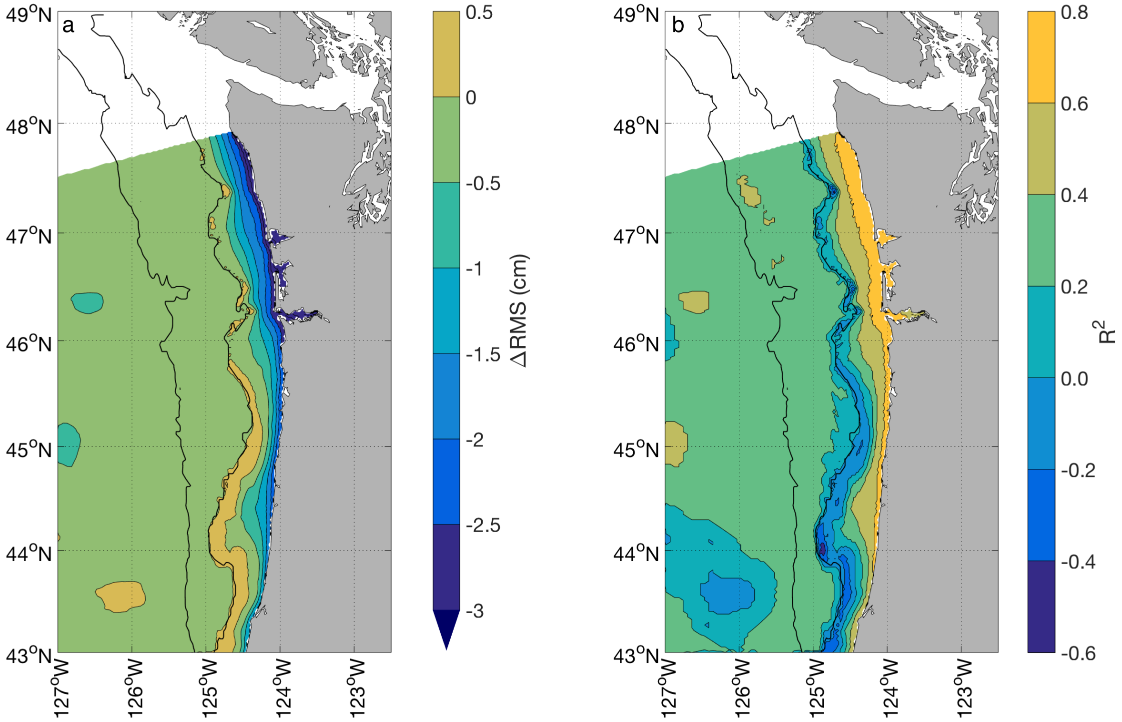

Figure A1.4. (a) Contours of change in bottom pressure RMS when subtracting the WCOFS model from the LiveOcean model, after applying to both a Godin 24-24-25 filter (Godin, 1972) and removing a 3rd order polynomial fit. (b) Contours of the R^2 of the fit of the WCOFS model to the LiveOcean model for every location in their shared domain. Black lines show the 300 m and 2000 m isobaths.

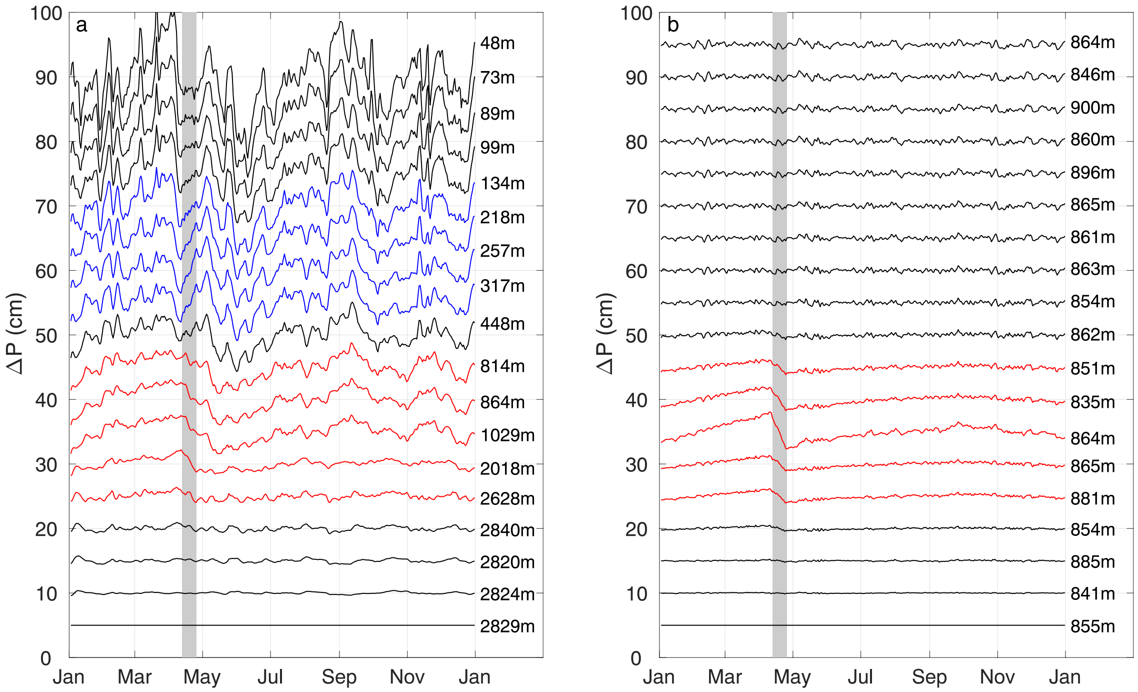

Figure A1.5. As for Figure 2.9, but for an earlier onset time of the SSE, now beginning on 12 April 2013. (a) As for Figure 2.9b. (b) As for Figure 2.9c.

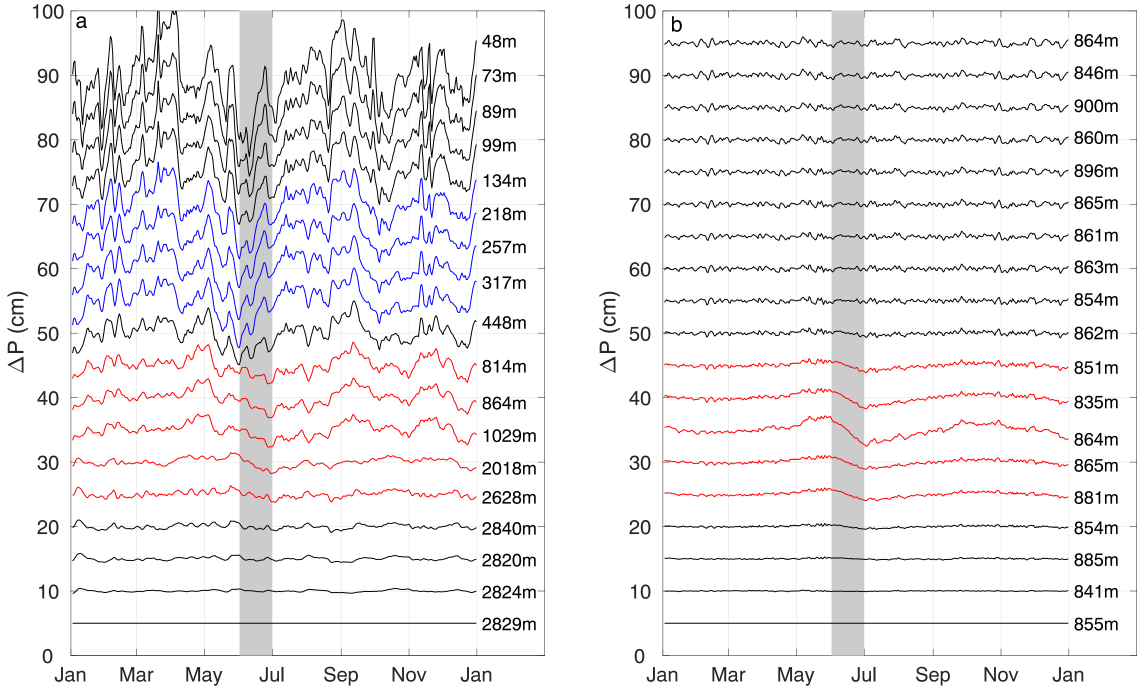

Figure A1.6. As for Figure 2.9, but for a 30-day SSE. (a) As for Figure 2.9b. (b) As for Figure 2.9c.

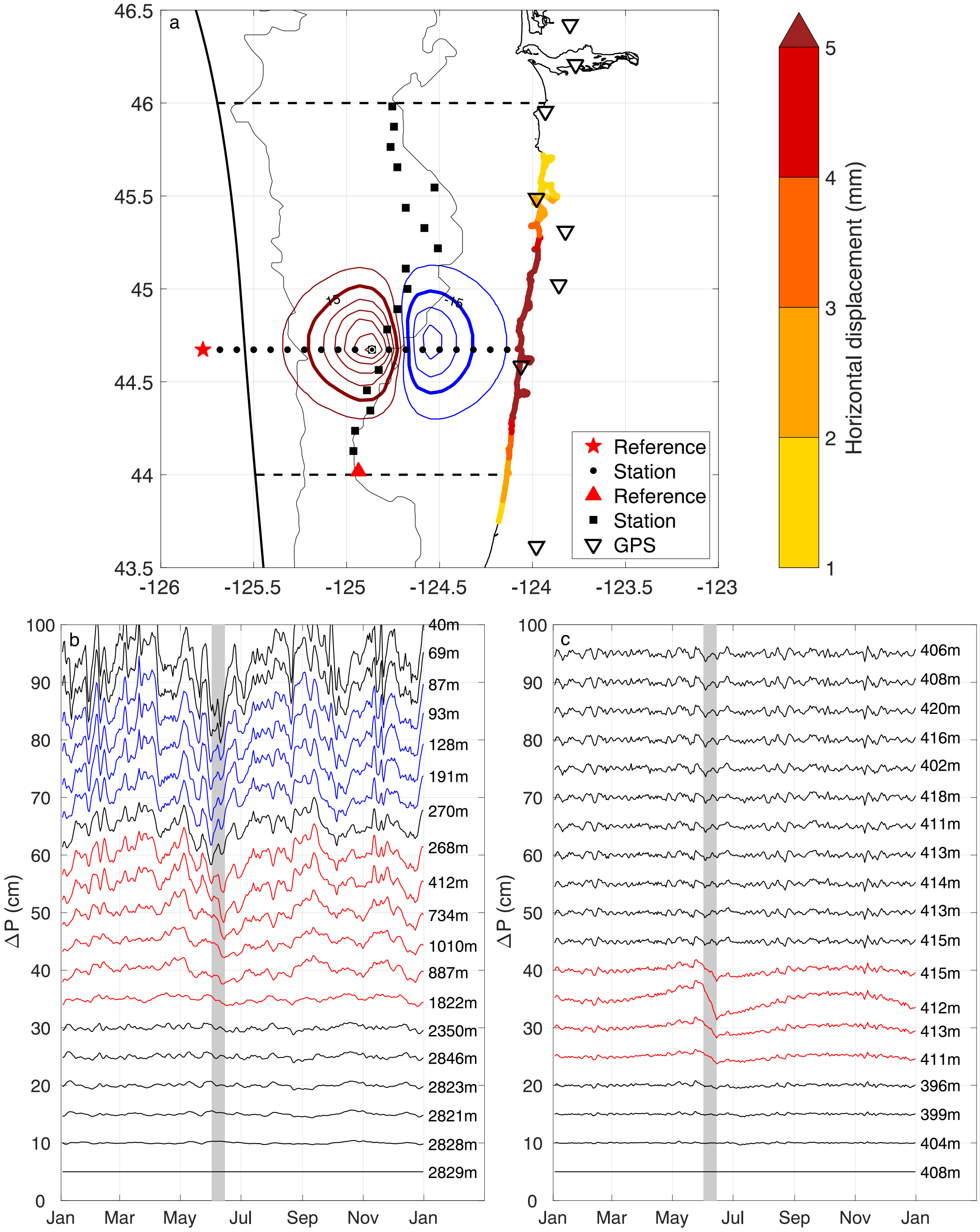

Figure A1.7. As for Figure 2.9, but for a SSE located near the shelf break.

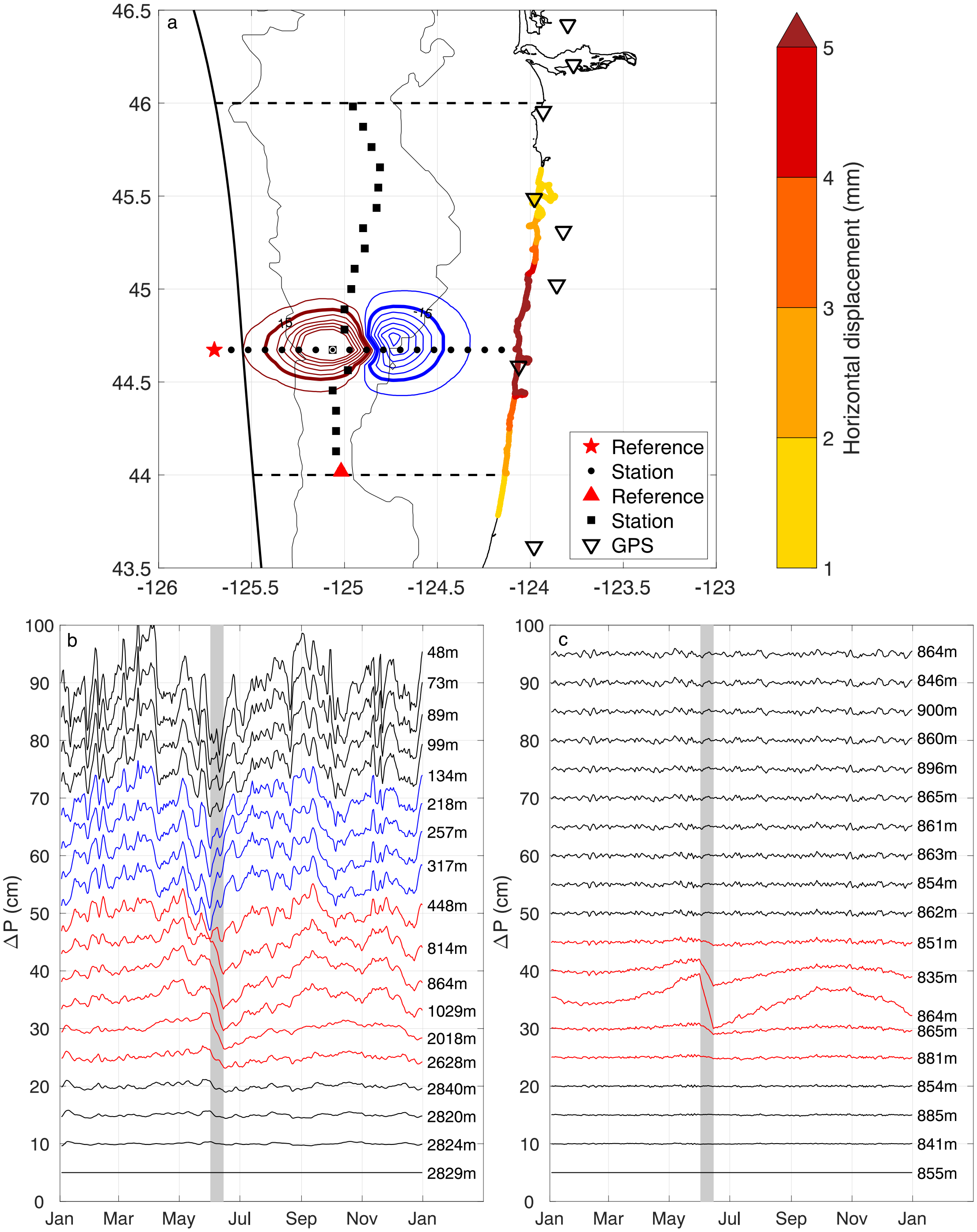

Figure A1.8. As for Figure 2.9, but for a SSE with $\Delta\sigma_E = 0.217$ MPa ($\Delta\sigma_M = 0.104$ MPa).

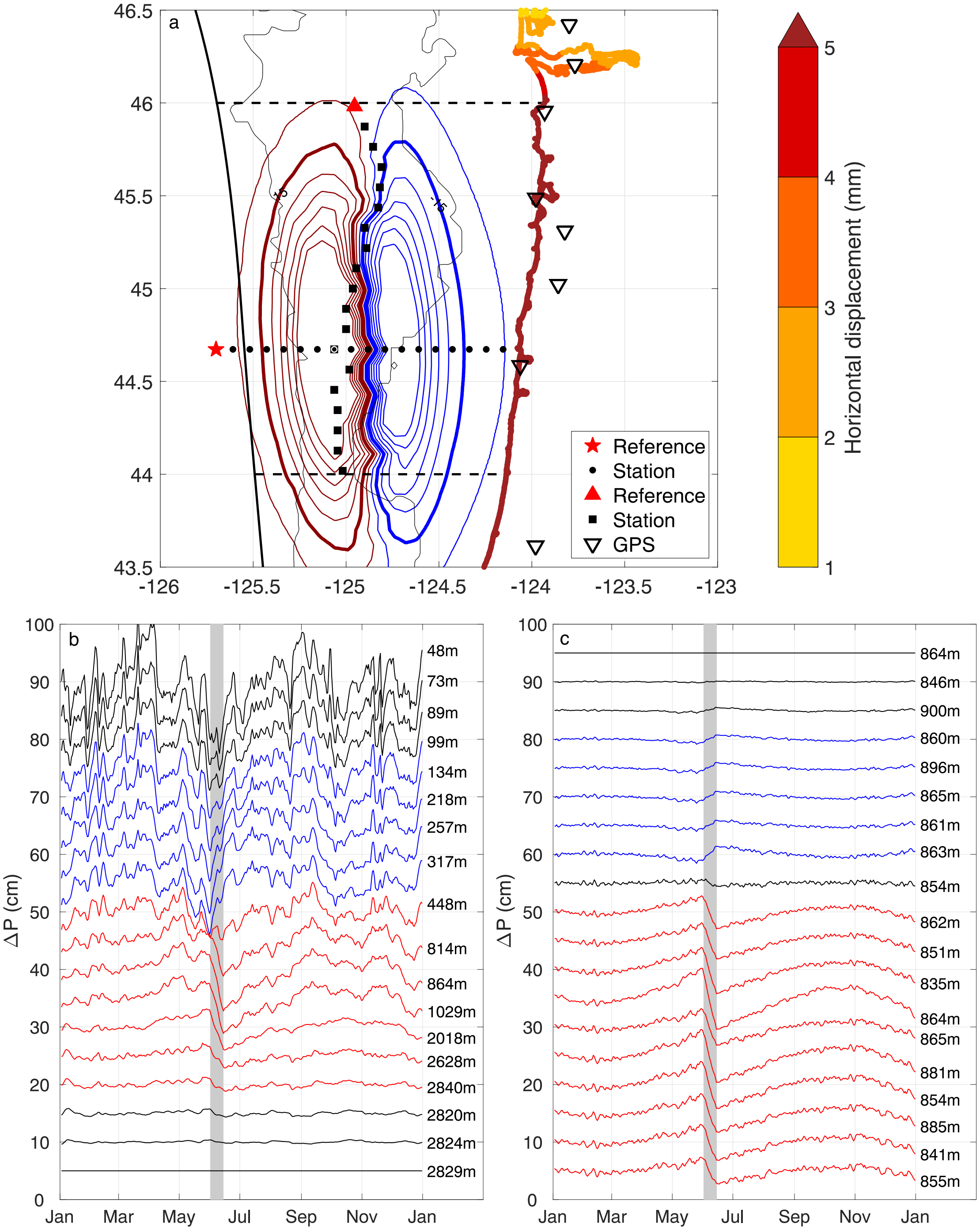

Figure A1.9. As for Figure 2.9, but for a M_w 6.9 SSE.

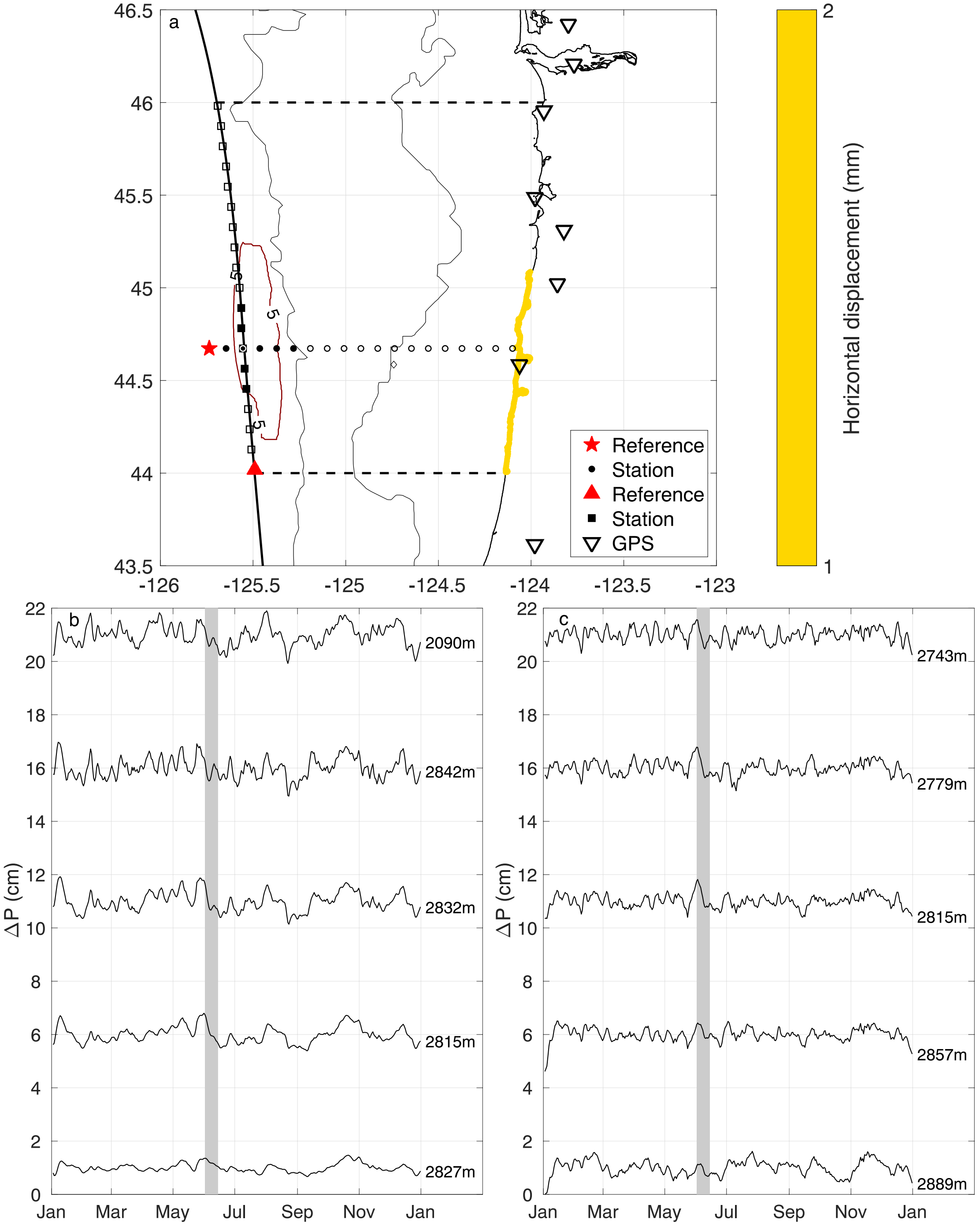

Figure A1.10. As for Figure 2.9, but for a M_w 6.2, $\Delta\sigma_E = 0.006$ ($\Delta\sigma_M = 0.005$ MPa) MPa SSE with 4 cm peak slip.

Table S1 Comprehensive list of depth matched differences

Depth Range	Year	Station	Depth	Depth dif.	Separation	Observations		Model		Model corrected obs.	
			z (m)	Δ z (m)	Δ xy (km)	RMS (cm)	Dif. RMS (cm)	RMS (cm)	Dif. RMS (cm)	RMS (cm)	Dif. RMS (cm)
>1400 m (Figure 5a)	2011-2012	**J26A**	**2864**	**--**	**--**	**1.5**	**--**	**1.3**	**--**	**1.6**	**--**
		J51A	2610	-254	244	1.7	0.8	1.4	0.4	1.9	0.8
		J34A	2574	-290	72	1.5	0.6	1.4	0.2	1.8	0.6
		J59A	2371	-493	326	1.8	0.7	1.4	0.5	1.8	0.5
		M03A	1818	-1046	363	1.7	0.7	n/a [a]	n/a [a]	n/a [a]	n/a [a]
		J42A	1540	-1810	143	1.5	0.5	1.4	0.3	1.7	0.5
		M06A	1439	-1425	106	1.5	0.7	1.4	0.4	1.6	0.6
		J51A	**2610**	**--**	**--**	**1.7**	**--**	**1.4**	**--**	**1.9**	**--**
		J34A	2574	-36	176	1.5	0.7	1.4	0.4	1.8	0.7
		J59A	2371	-239	81	1.8	0.5	1.4	0.3	1.8	0.5
		M03A	1818	-792	121	1.7	0.5	n/a [a]	n/a [a]	n/a [a]	n/a [a]
		J42A	1540	-1070	117	1.5	0.6	1.4	0.4	1.7	0.6
		M06A	1439	-1171	170	1.5	0.7	1.4	0.4	1.6	0.7
		J34A	**2574**	**--**	**--**	**1.5**	**--**	**1.4**	**--**	**1.8**	**--**
		J59A	2371	-203	257	1.8	0.7	1.4	0.5	1.8	0.6
		M03A	1818	-756	292	1.7	0.8	n/a [a]	n/a [a]	n/a [a]	n/a [a]
		J42A	1540	-1034	70	1.5	0.7	1.4	0.3	1.7	0.7
		M06A	1439	-1135	45	1.5	0.9	1.4	0.4	1.6	0.8
		J59A	**2371**	**--**	**--**	**1.8**	**--**	**1.4**	**--**	**1.8**	**--**
		M03A	1818	-553	48	1.7	0.4	n/a [a]	n/a [a]	n/a [a]	n/a [a]
		J42A	1540	-831	195	1.5	0.6	1.4	0.4	1.7	0.4
		M06A	1439	-932	248	1.5	0.7	1.4	0.4	1.6	0.5
		M03A	**1818**	**--**	**--**	**1.7**	**--**	**n/a [a]**	**--**	**n/a [a]**	**--**
		J42A	1540	-287	226	1.5	0.4	1.4	n/a [a]	1.7	n/a [a]
		M06A	1439	-379	277	1.5	0.5	1.4	n/a [a]	1.6	n/a [a]
		J42A	**1540**	**--**	**--**	**1.5**	**--**	**1.4**	**--**	**1.7**	**--**
		M06A	1439	-101	53	1.5	0.4	1.4	0.2	1.6	0.4

Table S1 cont.

Depth Range	Year	Station	Depth	Depth dif.	Separation	Observations		Model		Model corrected obs.	
			z (m)	Δ z (m)	Δ xy (km)	RMS (cm)	Dif. RMS (cm)	RMS (cm)	Dif. RMS (cm)	RMS (cm)	Dif. RMS (cm)
>1400 m (Figure 5a)	2012-2013	**G34B**	**2954**	--	--	**1.2**	--	**1.2**	--	**1.4**	--
		FS20B	2378	-576	241	1.3	0.5	1.2	0.3	1.4	0.5
		G26B	2357	-597	70	1.3	0.4	1.2	0.2	1.4	0.4
		FS20B	**2378**	--	--	**1.3**	--	**1.2**	--	**1.4**	--
		G26B	2357	-21	171	1.3	0.3	1.2	0.3	1.4	0.3
	2014-2015	**MJ01A**	**2908**	--	--	**1.4**	--	**2.7**	--	**2.6**	--
		O2	1909	-999	12	1.6	0.8	2.4	0.8	2.5	1.2
500 – 1400 m (Figure 5b)	2012-2013	**FS07B**	**1297**	--	--	**1.5**	--	**1.1**	--	**1.6**	--
		FS16B	1073	-224	23	1.4	0.6	1.1	0.1	1.4	0.6
		G09B	842	-455	36	1.5	0.6	1.1	0.1	1.4	0.6
		M18B	720	-577	506	1.8	1.5	1.4	0.7	1.5	1.3
		M10B	675	-622	366	1.5	1.1	1.3	0.5	1.4	1.1
		FS16B	**1073**	--	--	**1.4**	--	**1.1**	--	**1.4**	--
		G09B	842	-231	13	1.5	0.3	1.1	0.1	1.4	0.2
		M18B	720	-353	484	1.8	1.3	1.4	0.7	1.5	1.1
		M10B	675	-398	344	1.5	0.8	1.3	0.5	1.4	0.8
		G09B	**842**	--	--	**1.5**	--	**1.1**	--	**1.4**	--
		M18B	720	-122	471	1.8	1.2	1.4	0.6	1.5	1.1
		M10B	675	-167	331	1.5	0.8	1.3	0.5	1.4	0.8
		M18B	**720**	--	--	**1.8**	--	**1.4**	--	**1.5**	--
		M10B	675	-45	140	1.5	0.7	1.3	0.3	1.4	0.7
	2014-2015	**M15D**	**933**	--	--	**1.7**	--	**1.8**[b]	--	**2.1**[b]	--
		LJ01B	775	-158	263	1.6	1.0	1.9[b]	0.4[b]	2.0[b]	1.0[b]

Table S1 cont.

Depth Range	Year	Station	Depth	Depth dif.	Separation	Observations		Model		Model corrected obs.	
			z (m)	Δ z (m)	Δ xy (km)	RMS (cm)	Dif. RMS (cm)	RMS (cm)	Dif. RMS (cm)	RMS (cm)	Dif. RMS (cm)
250 – 500 m (Figure 5c)	2012-2013	**G25B**	**430**	--	--	**2.0**	--	**1.5**	--	**1.7**	--
		J33B	350	-80	354	1.9	1.3	1.7	0.9	1.6	1.4
		FS03B	345	-85	183	1.8	1.2	1.3	0.5	1.5	1.2
		J17B	286	-144	208	2.3	1.3	1.8	0.9	1.8	1.3
		J33B	**350**	--	--	**1.9**	--	**1.7**	--	**1.6**	--
		FS03B[c]	345	-5	537	1.8	1.3	1.3	1.1	1.5	1.2
		J17B	286	-64	146	2.3	0.9	1.8	0.5	1.8	0.9
		FS03B	**345**	--	--	**1.8**	--	**1.3**	--	**1.5**	--
		J17B	286	-59	391	2.3	1.7	1.8	1.2	1.8	1.4
	2014-2015	**J17D**	**285**	--	--	**2.8**	--	**1.8**	--	**2.6**	--
		J09D	252	-32	71	3.0	1.1	1.8	0.4	2.9	1.1
100 – 250 m (Figure 5d)	2011-2012	**FN08A**	**177**	--	--	**2.6**	--	**1.8**	--	**2.3**	--
		J41A	175	-2	123	3.1	1.7	2.5	1.1	2.7	1.7
		FN14A	173	-4	16	2.7	0.4	1.7	0.2	2.5	0.5
		FN07A	154	-23	8	3.3	1.0	2.5	1.0	2.5	0.6
		FN06A	134	-43	12	3.1	0.9	3.0	1.6	2.2	1.1
		J49A	120	-57	61	4.3	2.3	3.5	2.1	2.7	1.5
		J41A	**175**	--	--	**3.1**	--	**2.5**	--	**2.7**	--
		FN14A	173	-2	139	2.7	1.7	1.7	1.2	2.5	1.8
		FN07A	154	-21	118	3.3	1.8	2.5	0.8	2.5	1.7
		FN06A	134	-41	124	3.1	1.6	3.0	1.1	2.2	1.5
		J49A	120	-55	70	4.3	2.7	3.5	1.4	2.7	2.2
		FN14A	**173**	--	--	**2.7**	--	**1.7**	--	**2.5**	--
		FN07A	154	-19	23	3.3	0.9	2.5	1.1	2.5	0.6
		FN06A	134	-39	21	3.1	1.0	3.0	1.7	2.2	1.3
		J49A	120	-53	77	4.3	2.3	3.5	2.2	2.7	1.6

Table S1 cont.

Depth Range	Year	Station	Depth	Depth dif.	Separation	Observations		Model		Model corrected obs.	
			z (m)	Δ z (m)	Δ xy (km)	RMS (cm)	Dif. RMS (cm)	RMS (cm)	Dif. RMS (cm)	RMS (cm)	Dif. RMS (cm)
100 – 250 m (Figure 5d)	2011-2012	**FN07A**	**154**	--	--	**3.3**	--	**2.5**	--	**2.5**	--
		FN06A	134	-20	8	3.1	0.7	3.0	0.6	2.2	1.0
		J49A	120	-34	54	4.3	1.7	3.5	1.2	2.7	1.4
		FN06A	**134**	--	--	**3.1**	--	**3.0**	--	**2.2**	--
		J49A	120	-14	59	4.3	1.7	3.5	0.7	2.7	1.5
	2012-2013	**FS17B**	**146**	--	--	**3.0**	--	**2.1**	--	**2.1**	--
		FS11B	132	-14	15	2.7	0.9	1.6	0.9	2.2	1.2
		G17B	123	-23	83	2.9	1.0	2.4	0.6	1.9	1.0
		FS08B	120	-26	27	3.0	1.0	1.8	0.5	2.2	1.1
		FS11B	**132**	--	--	**2.7**	--	**1.6**	--	**2.2**	--
		G17B	123	-9	97	2.9	0.9	2.4	1.4	1.9	1.4
		FS08B	120	-12	14	3.0	0.6	1.8	0.5	2.2	0.7
		G17B	**123**	--	--	**2.9**	--	**2.4**	--	**1.9**	--
		FS08B	120	-3	106	3.0	0.7	1.8	1.0	2.2	1.1
	2014-2015	**FS11D**	**150**	--	--	**3.2**	--	**2.2**[b]	--	**3.1**[b]	--
		FS17D	145	-5	15	2.9	1.1	2.9[b]	1.1[b]	2.7[b]	1.7[b]
		J25D[c]	136	-14	448	3.6	2.0	3.6[b]	2.1[b]	4.1[b]	2.6[b]
		FS17D	**145**	--	--	**2.9**	--	**2.9**[b]	--	**2.7**[b]	--
		J25D[c]	136	-9	433	3.6	2.2	3.6[b]	1.6[b]	4.1[b]	2.6[b]
<100 m (Figure 5e)	2011-2012	**FN03A**	**90**	--	--	**5.3**	--	**4.2**	--	**3.4**	--
		FN19A	75	-15	21	7.1	3.8	4.8	0.8	5.2	3.8
		FN01A	54	-36	14	6.9	2.5	5.5	1.6	3.3	1.9
		FN19A	**75**	--	--	**7.1**	--	**4.8**	--	**5.2**	--
		FN01A	54	-21	17	6.9	3.5	5.5	0.9	3.3	3.5

Table S1 cont.

Depth Range	Year	Station	Depth	Depth dif.	Separation	Observations		Model		Model corrected obs.	
			z (m)	Δ z (m)	Δ xy (km)	RMS (cm)	Dif. RMS (cm)	RMS (cm)	Dif. RMS (cm)	RMS (cm)	Dif. RMS (cm)
<100 m (Figure 5e)	2012-2013	**FS19B**	**87**	**--**	**--**	**3.9**	**--**	**2.1**	**--**	**2.9**	**--**
		FS12B	60	-27	21	3.7	1.5	3.1	1.5	2.3	2.3
		FS15B	52	-35	15	5.8	3.7	2.9	1.3	4.5	3.4
		FS12B	**60**	**--**	**--**	**3.7**	**--**	**3.1**	**--**	**2.3**	**--**
		FS15B	52	-8	6	5.8	3.6	2.9	0.3	4.5	3.6
	201 4-	**FS42D**	**95**	**--**	**--**	**3.5**	**--**	**3.3**[b]	**--**	**3.3**[b]	**--**
		FS12D	55	-40	30	4.2	1.2	3.9[b]	0.8[b]	4.1[b]	1.2[b]

Note. We include here all differences for each year within the depth bins used in Figure 5. Bold font indicates the reference against which subsequent stations were differenced (“Observations”). Values from the WCOFS model at the same locations are also included (“Model”), as are those obtained by applying the model as a correction to the data prior to differencing (“Model corrected obs.”). In the 2014-2015 year, the LiveOcean model is used for those instruments within its domain, while the remainder use a truncated WCOFS model (which ends in December 2014). z – depth, Δxy – horizontal separation, RMS – RMS of pressure time series, Dif. RMS – RMS of difference.

[a] Model unavailable for station M03A

[b] WCOFS model available only until 12/31/2014

[c] Difference excluded from Figure 5 for display purposes

Appendix 2: Supplementary Materials for Chapter 3

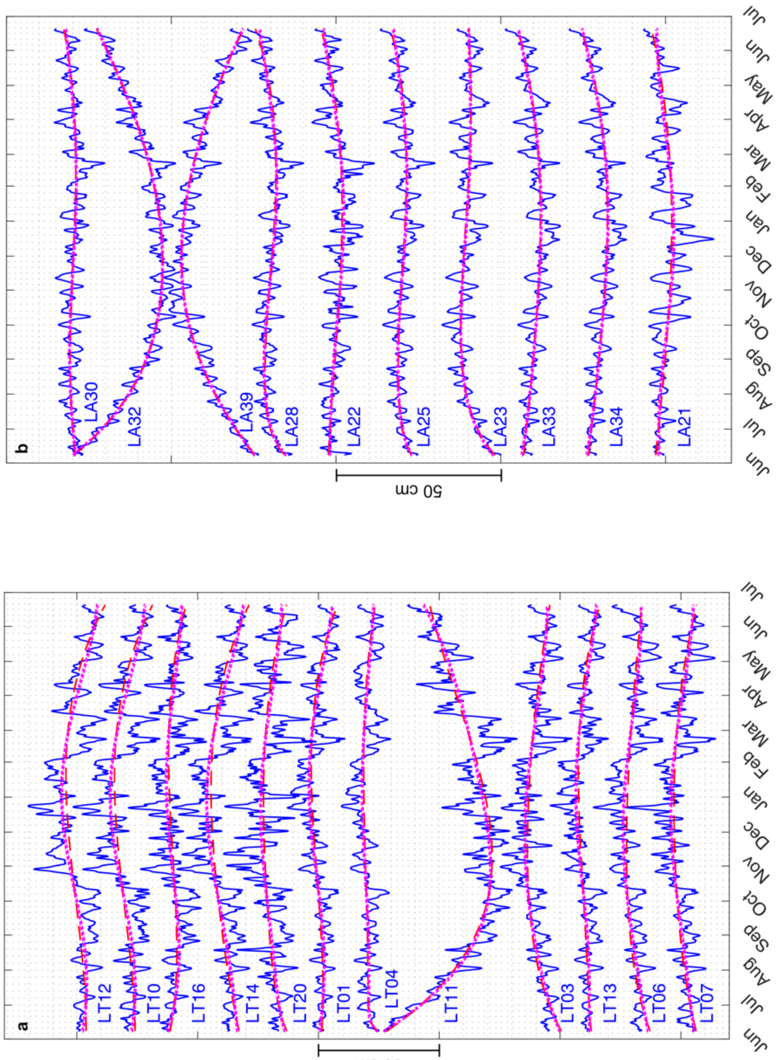

Figure A2.1. Time series of tidally filtered, detrended, and artificially offset pressure data (blue) along with the least-squares sinusoidal + exponential fit (pink, dotted) and 3rd order polynomial + exponential fit (red, dashed) for the shelf (a) and slope (b).

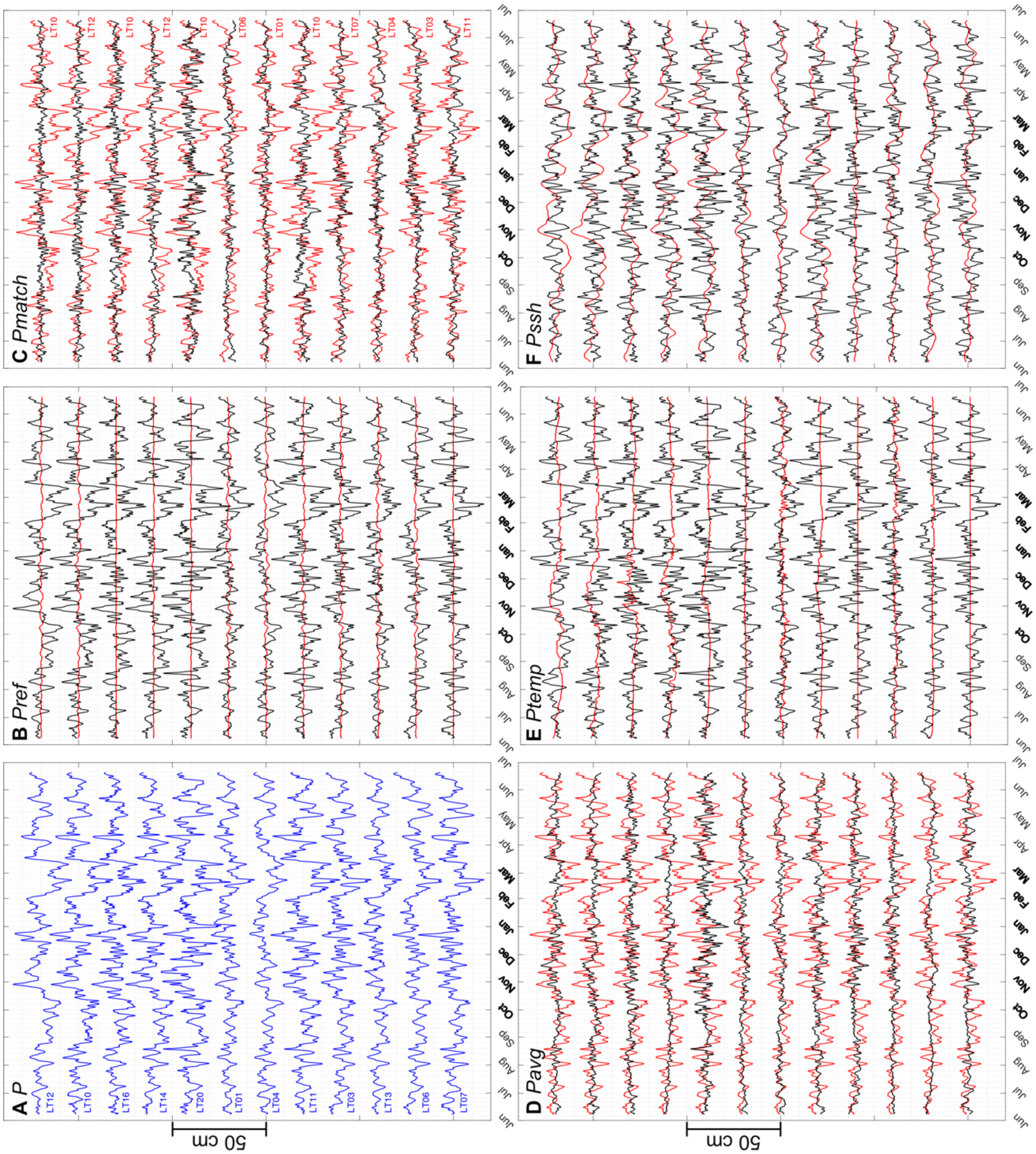

Figure A2.2. Time series of tidally filtered, drift and sinusoidal-corrected shelf pressure data (blue), scaled proxies (red), and proxy-corrected data (black), vertically offset with shallowest station at the top for display purposes. Winter months, when signals are anomalously large across observables, are labeled in bold. A) No proxy. B) Scaled reference station pressure (P_{ref}). C) Scaled depth-matched pressure (P_{match}), with matched station labeled in red text. D) Scaled network average pressure (P_{avg}). E) Scaled temperatures, lagged to maximize correlation (P_{temp}). F) Scaled sea surface height (P_{SSH}).

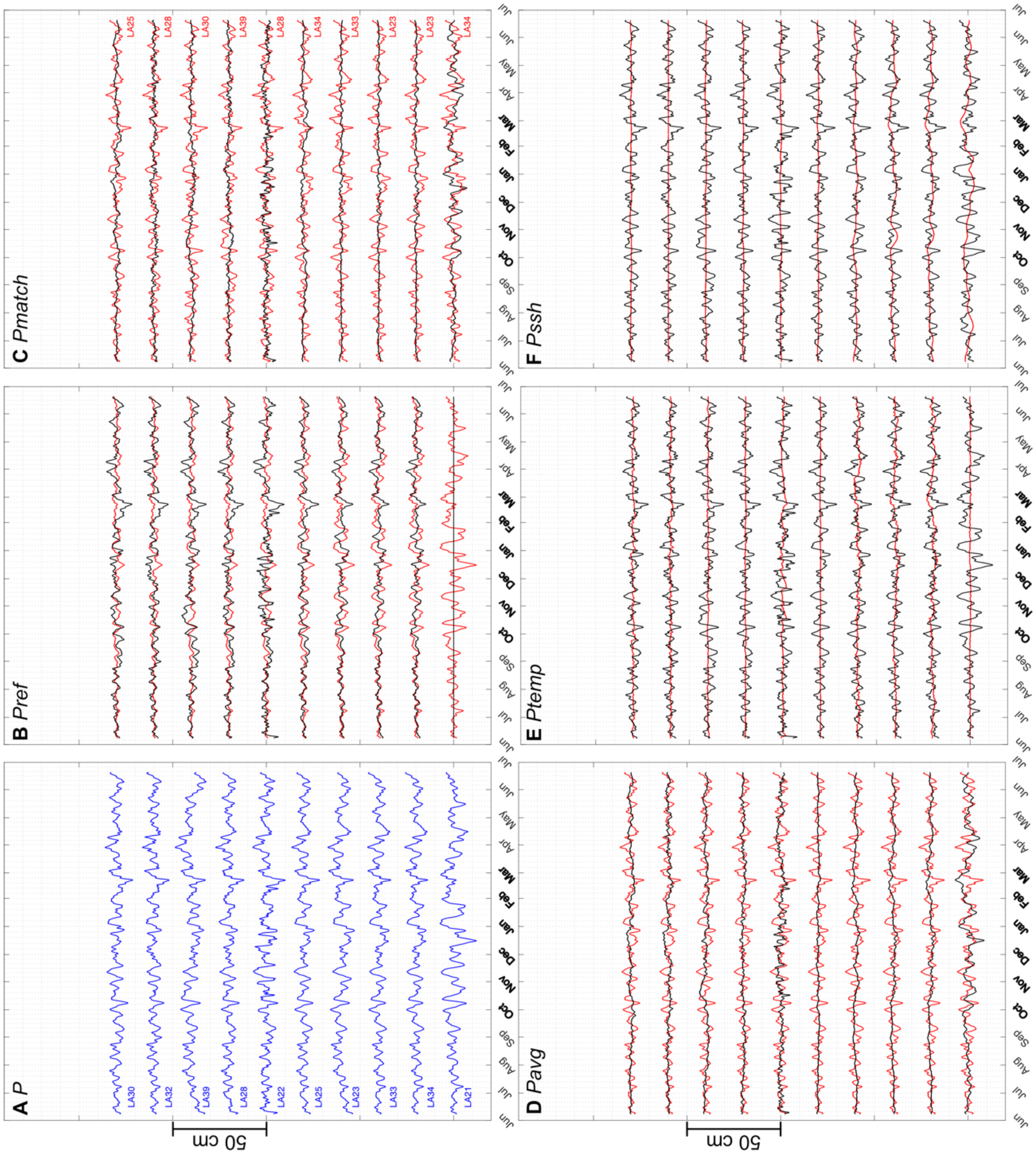

Figure A2.3. Time series of tidally filtered, drift and sinusoidal-corrected slope pressure data (blue), scaled proxies (red), and proxy-corrected data (black), vertically offset with shallowest station at the top for display purposes. Winter months, when signals are anomalously large across observables, are labeled in bold. A) No proxy. B) Scaled reference station pressure (P_{ref}). C) Scaled depth-matched pressure (P_{match}), with matched station labeled in red text. D) Scaled network average pressure (P_{avg}). E) Scaled temperatures, lagged to maximize correlation (P_{temp}). F) Scaled sea surface height (P_{SSH}).

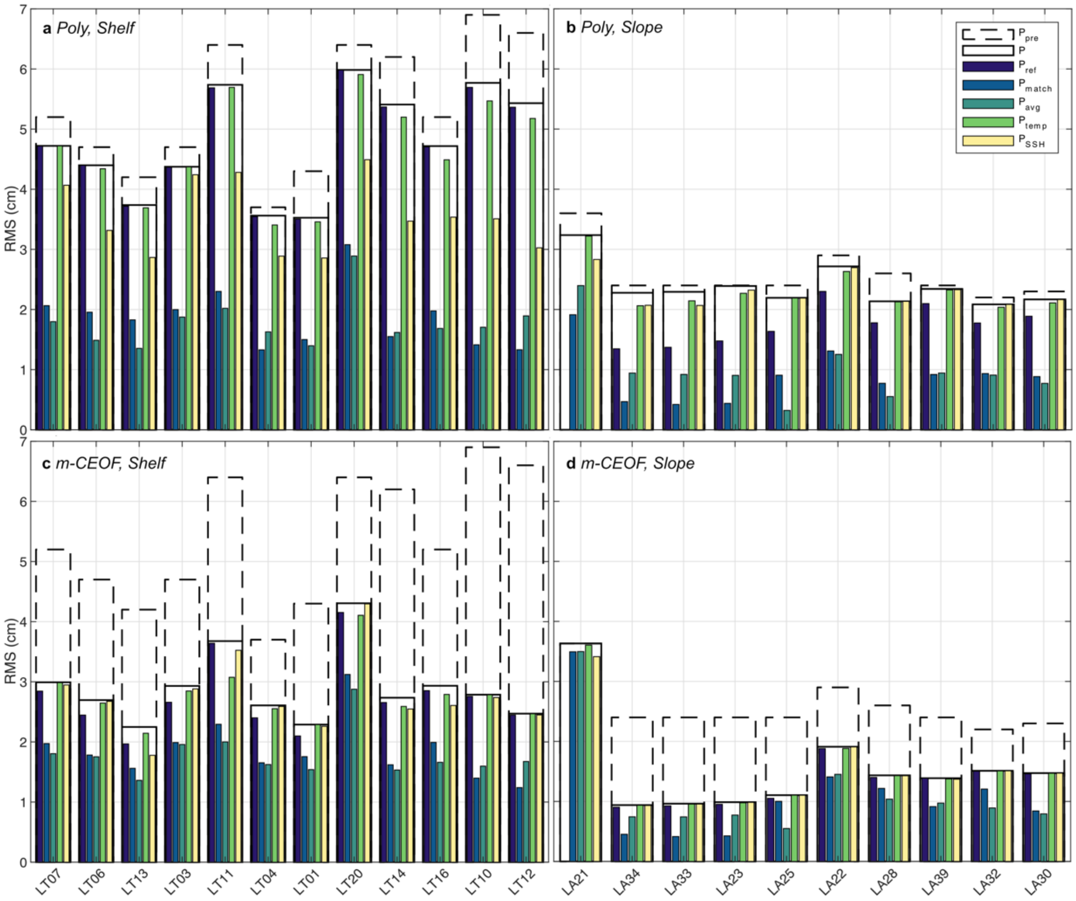

Figure A2.4. Proxy-corrected pressure RMS improvements for A) polynomially corrected shelf data, B) polynomially corrected slope data, C) multivariate-CEOF (m-CEOF) corrected shelf data, and D) multivariate-CEOF corrected slope data. The empty, black-outlined bars in the background show the RMS of the seasonally corrected pressure record prior to applying any proxy, while the thin colored bars show the RMS of each proxy corrected time series.

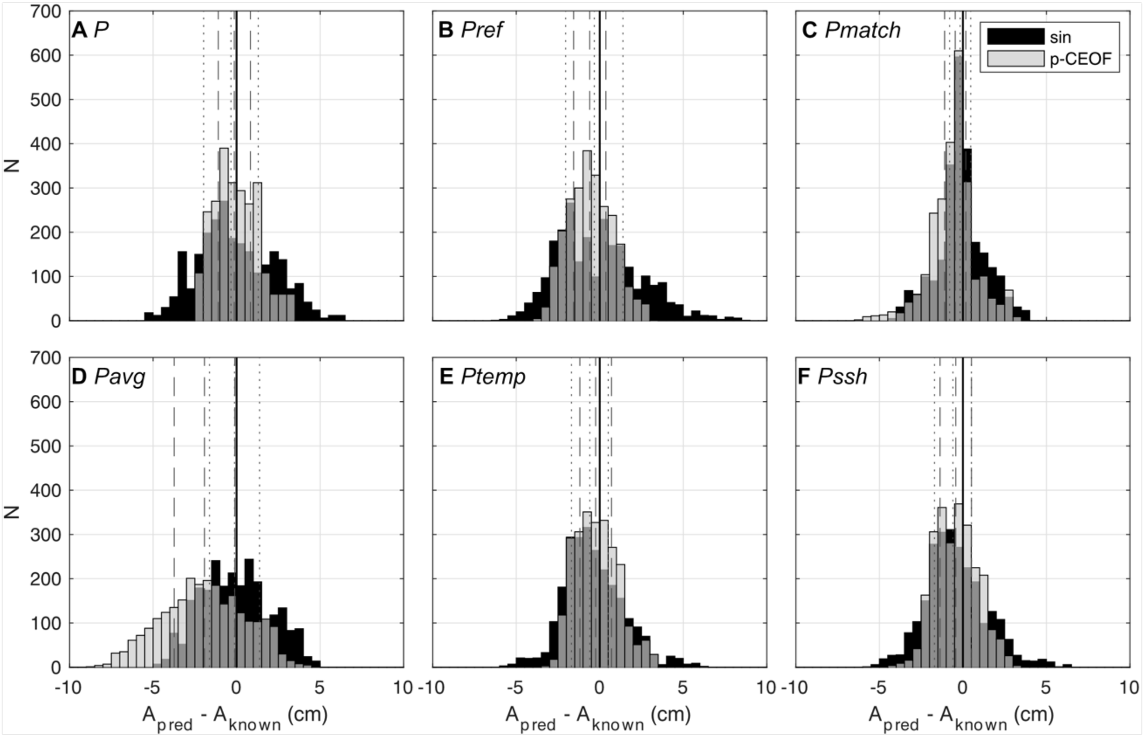

Figure A2.5. Amplitude recovery from synthetic detection analysis on the continental slope, when known onset time is assumed, sinusoidal (black), and pressure-CEOF (p-CEOF, translucent gray) seasonal corrections, for each of the proxies considered. The results from all synthetic ramp amplitude considered (0, 2, 4, 6, 8, and 10 cm) were combined, with ramp duration held at 14 days and onset times varied weekly from August 2018 through April 2019. A) No proxy. B) P_{ref}. C) P_{match}, D) P_{avg}. E) P_{temp}. F) P_{SSH}. Vertical solid lines show the input synthetic amplitude, vertical dotted lines show the median and ±MAD for the sinusoidal case, and vertical dashed lines show the same for the pressure-CEOF case.

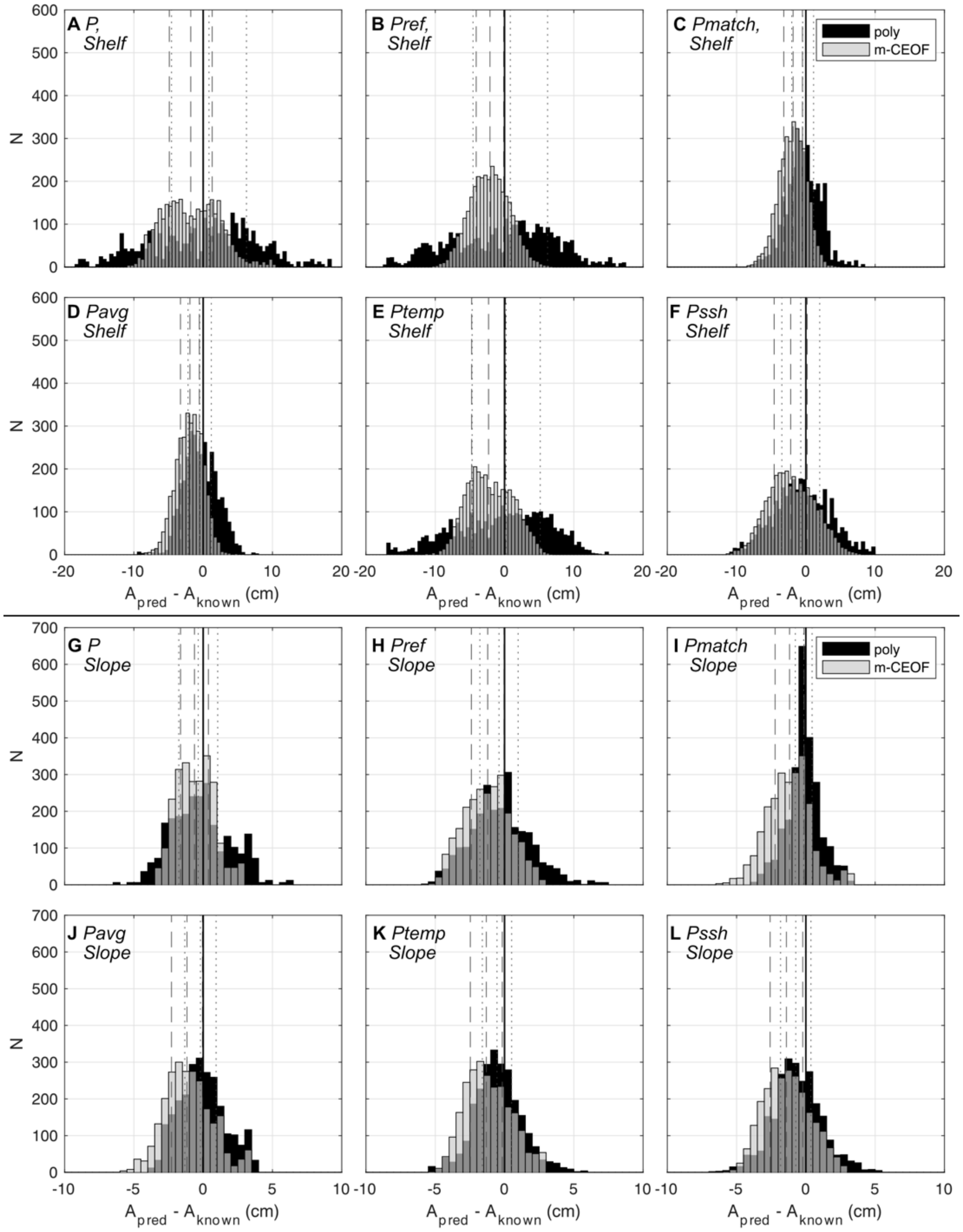

Figure A2.6. Amplitude recovery from synthetic detection analysis, when known onset time is assumed, for polynomial (black) and multivariate-CEOF (m-CEOF, translucent gray) seasonal corrections, for each of the proxies considered. A-F) Shelf amplitude predictions for no proxy, P_{ref}, P_{match}, P_{avg}, P_{temp}, and P_{SSH}, respectively. G-L) Slope amplitude predictions for no proxy, P_{ref}, P_{match}, P_{avg}, P_{temp}, and P_{SSH}, respectively. The results from all synthetic ramp amplitude considered (0, 2, 4, 6, 8, and 10 cm) were combined, with ramp duration held at 14 days and onset times varied weekly from August 2018 through April 2019. Vertical solid lines show the input synthetic amplitude, vertical dotted lines show the median and ±MAD for the polynomial case, and vertical dashed lines show the same for the multivariate-CEOF case.

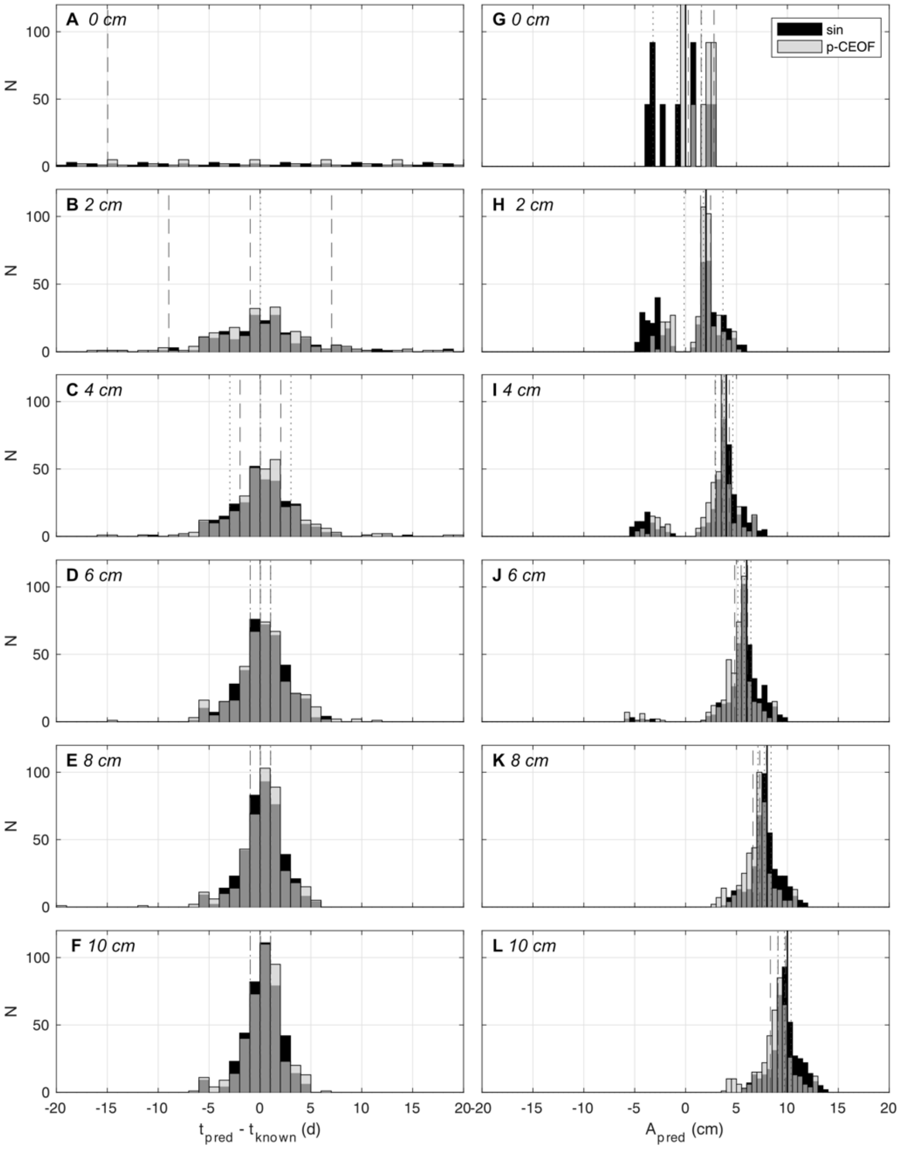

Figure A2.7. Histograms displaying SSE onset and amplitude prediction results from synthetic detection analysis on the slope, when unknown onset time is assumed, for sinusoidal (black) and pressure-CEOF (p-CEOF, translucent gray) seasonal corrections, using only our best-preforming proxy, P_{match}. Synthetic ramp duration was held constant at 14 days and onset times were varied weekly from August 2018 through April 2019 to generate the composite distributions shown. A-F) Timing recovery for synthetic ramps of 0, 2, 4, 6, 7, and 10 cm amplitude. Vertical dotted lines show the median and ±MAD for the sinusoidal case, while vertical dashed lines show the same for the pressure-CEOF case. G-L) Amplitude recovery for synthetic ramps of 0, 2, 4, 6, 8, and 10 cm amplitude. Vertical solid lines show the input synthetic amplitude, vertical dotted lines show the median and ±MAD, for the sinusoidal case, and vertical dashed lines show the same for the pressure-CEOF case.

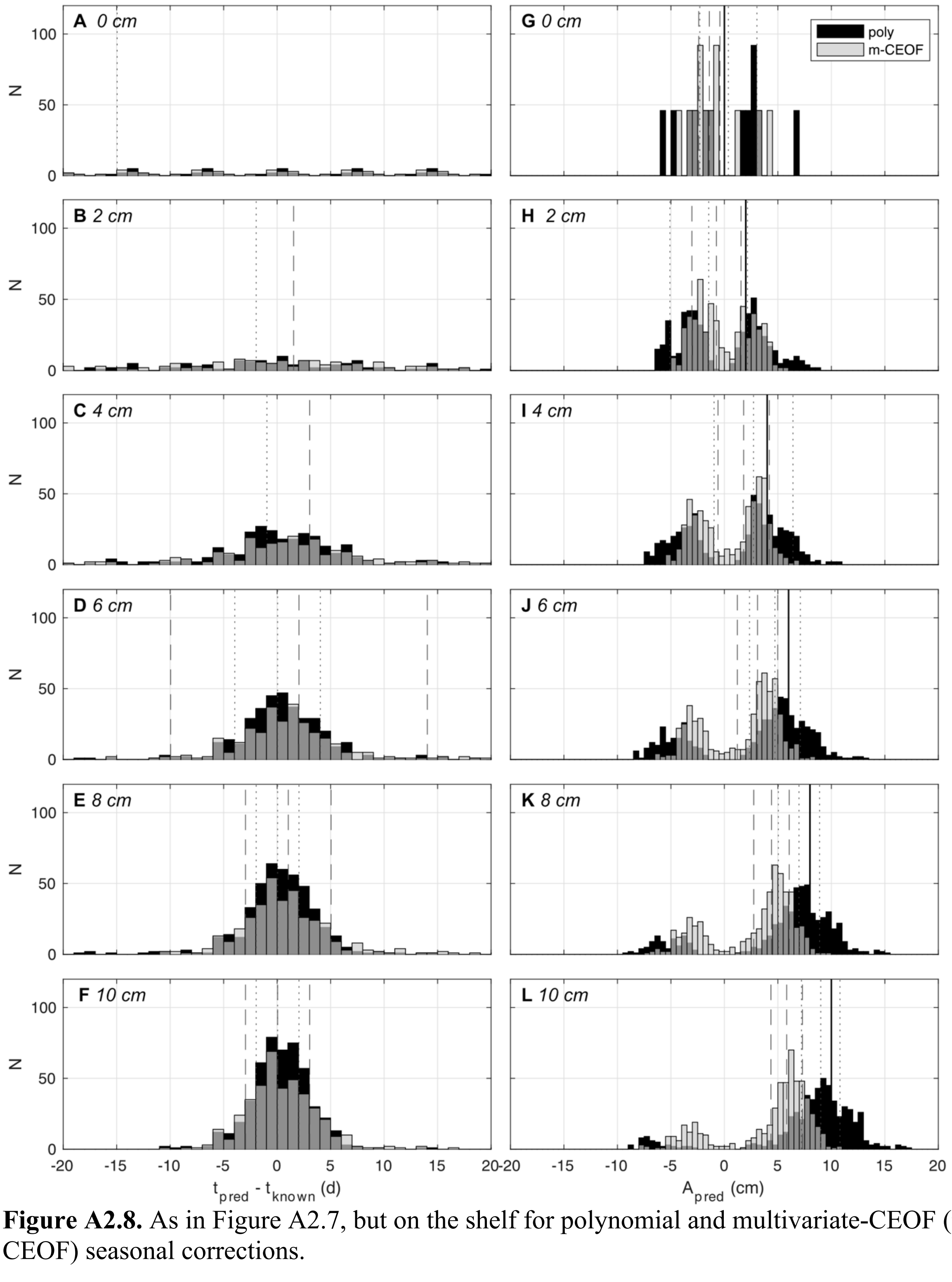

Figure A2.8. As in Figure A2.7, but on the shelf for polynomial and multivariate-CEOF (m-CEOF) seasonal corrections.

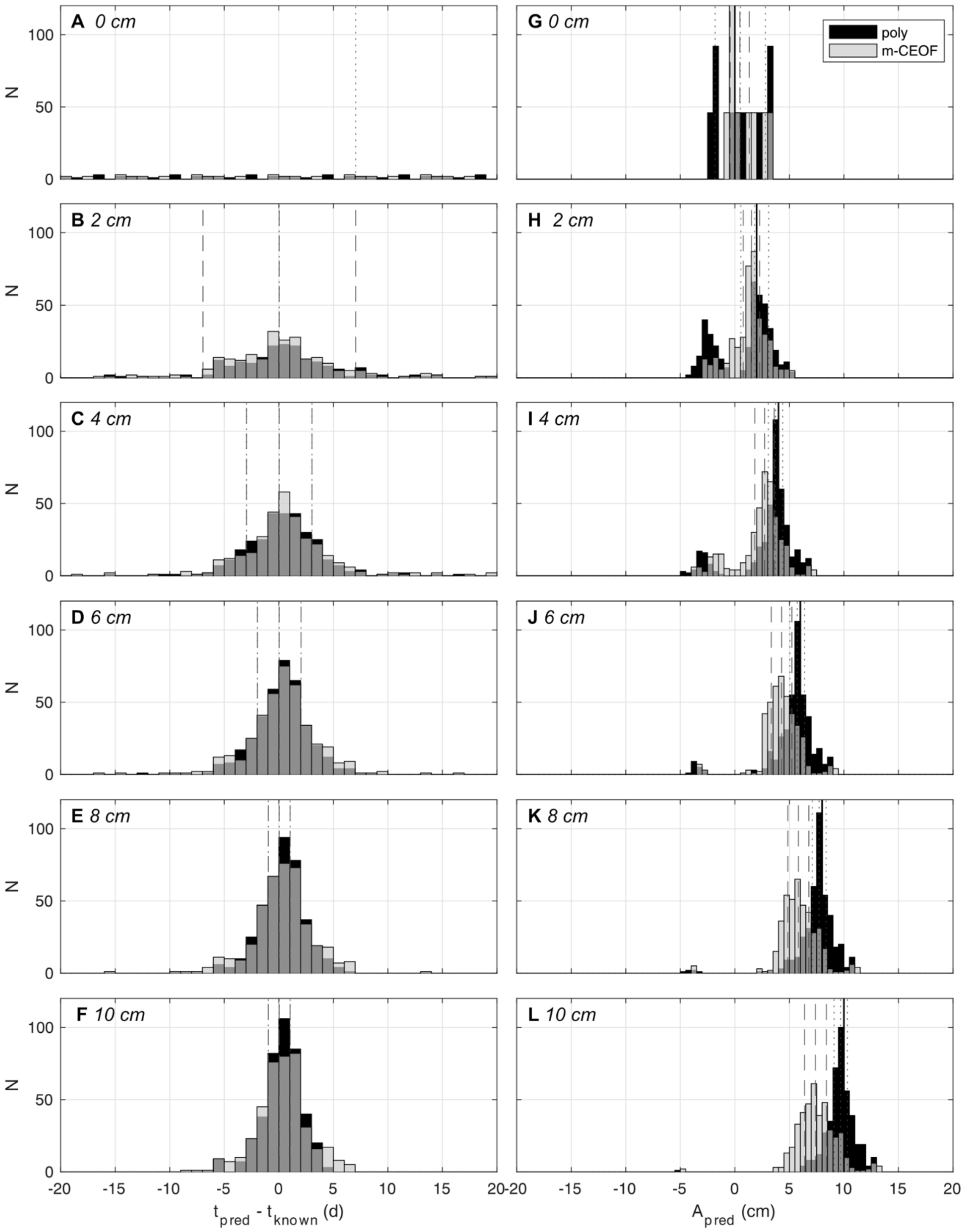

Figure A2.9. As in Figure 3.8, but on the slope.

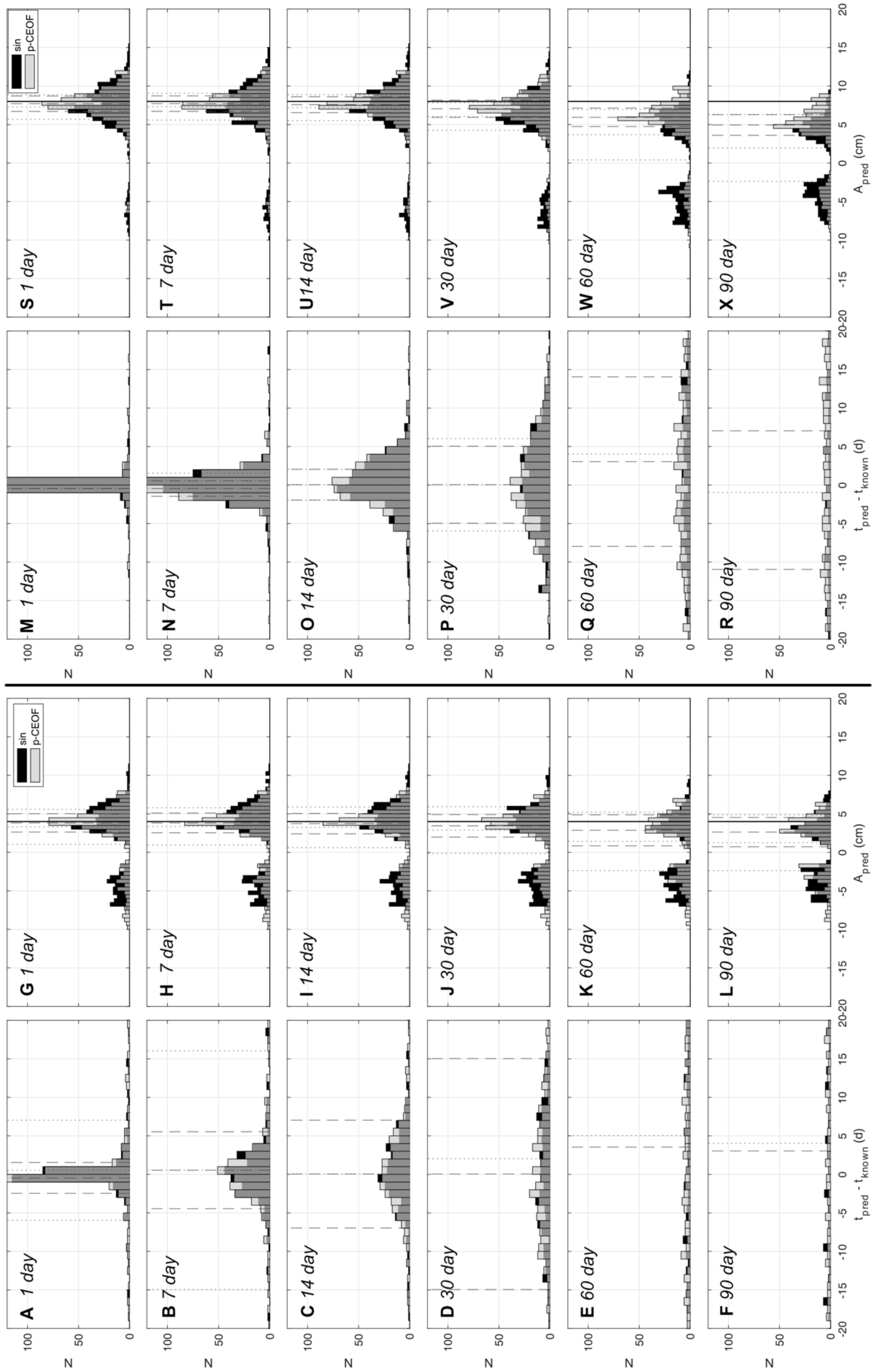
A 1 day
B 7 day
C 14 day
D 30 day
E 60 day
F 90 day
G 1 day
H 7 day
I 14 day
J 30 day
K 60 day
L 90 day
M 1 day
N 7 day
O 14 day
P 30 day
Q 60 day
R 90 day
S 1 day
T 7 day
U 14 day
V 30 day
W 60 day
X 90 day
sin
p-CEOF
N
0
50
100
-20
-15
-10
-5
0
5
10
15
20
$t_{pred} - t_{known}$ (d)
A_{pred} (cm)

Figure A2.10. Histograms displaying SSE onset and amplitude prediction results as a function of input ramp duration from synthetic detection analysis on the shelf, when unknown onset time is assumed, for sinusoidal (black) and pressure-CEOF (p-CEOF, translucent gray) seasonal corrections, using only our best-preforming proxy, P_{match}. A-F) Timing recovery for synthetic ramps of 1, 7, 14, 30, 60, and 90 day duration with amplitude held constant at 8 cm and onset times were varied weekly from August 2018 through April 2019. Vertical dotted lines show the median and ±MAD for the sinusoidal case, while vertical dashed lines show the same for the pressure-CEOF case. G-L) Amplitude recovery for the same suite of synthetics. Vertical solid lines show the input synthetic amplitude, vertical dotted lines show the median and ±MAD for the sinusoidal case, and vertical dashed lines show the same for the pressure-CEOF case. M-R) As for (A-F) but with amplitude held constant at 4 cm. S-X) Amplitude recovery for the same suite of synthetics.

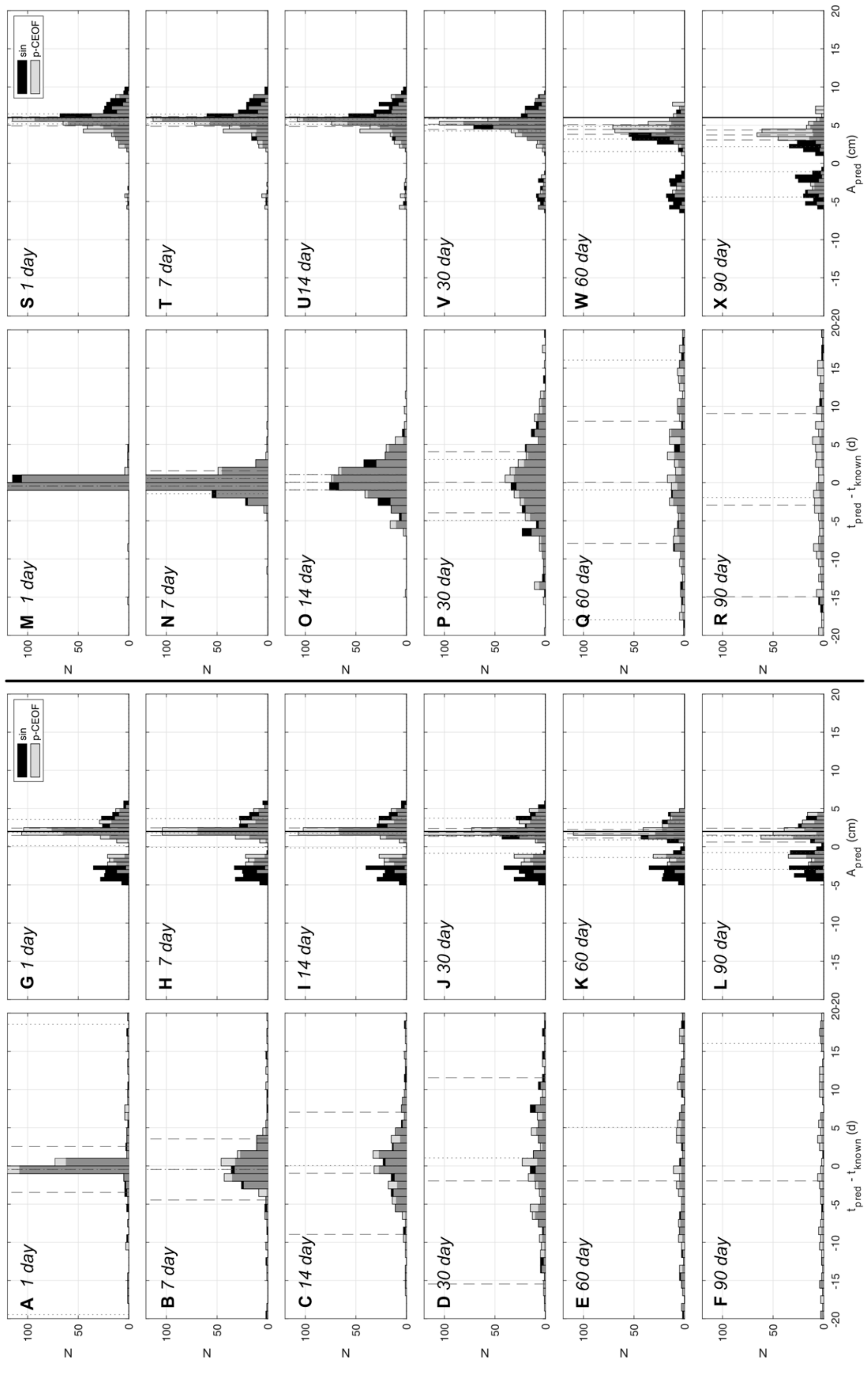

Figure A2.11. As for Figure A2.10, but for slope detections.

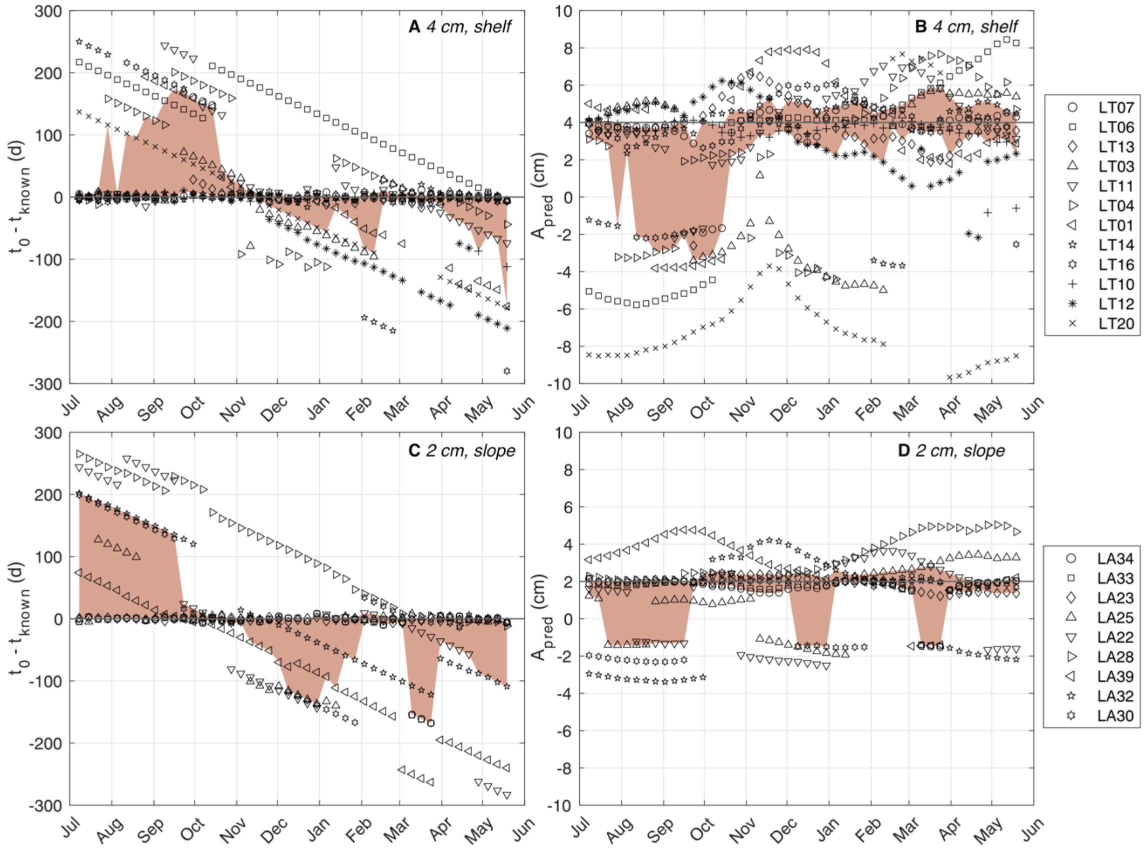

Figure S12. Scatter plots showing onset and amplitude prediction accuracy from pressure-CEOF corrected data with P_{match} applied. A) Timing prediction accuracy and B) amplitude prediction accuracy as a function of onset time for a 4 cm, 14-day ramp on the shelf. Pink infilled region contains the middle 50% (6/12 stations) of the detections for each synthetic onset considered. C) Timing prediction accuracy and D) amplitude prediction accuracy as a function of onset time for a 2 cm, 14-day ramp on the slope. Pink infilled region contains the middle 55% (5/9 stations) of the detections for each synthetic onset considered. Black horizontal lines indicate the known synthetic onset time and ramp amplitude, respectively. Symbols correspond to stations, as indicated in the legend, using the same shapes as in Figure 5.

Table A2.1. Shelf station parameters and RMS of difference for every possible pair.

Name	Depth (m)	Depth Dif (m)	Range (km)	RMS (cm)	Dif RMS (cm)
LT07	**262**	**–**	**–**	**4.5**	**–**
LT06	225	37	51.1	4.1	2.1
LT13	203	59	246.3	3.5	2.6
LT03	202	60	177.4	4.2	2.1
LT11	162	100	96.7	5.6	2.0
LT04	157	105	120.4	3.5	2.9
LT01	156	106	219.7	3.3	2.7
LT20	150	112	389.1	5.8	2.9
LT14	125	137	160.1	5.0	2.4
LT16	125	137	202.2	4.5	2.6
LT10	98	164	138.2	5.4	2.5
LT12	83	179	192.8	5.0	2.7
LT07	262	-37	51.1	4.5	1.9
LT06	**225**	**–**	**–**	**4.1**	**–**
LT13	203	22	212.5	3.5	2.0
LT03	202	23	214.3	4.2	1.9
LT11	162	63	83.5	5.6	2.4
LT04	157	68	96.9	3.5	2.1
LT01	156	69	222.1	3.3	2.0
LT20	150	75	373.3	5.8	2.7
LT14	125	100	138.9	5.0	2.3
LT16	125	100	181.4	4.5	2.3
LT10	98	127	105.7	5.4	2.4
LT12	83	142	158.2	5.0	2.5
LT07	262	-59	246.3	4.5	2.0
LT06	225	-22	212.5	4.1	1.7
LT13	**203**	**–**	**–**	**3.5**	**–**
LT03	202	1	423.3	4.2	2.2
LT11	162	41	155.6	5.6	2.0
LT04	157	46	283.4	3.5	1.7
LT01	156	47	422.4	3.3	1.8
LT20	150	53	194.0	5.8	2.3
LT14	125	78	97.3	5.0	1.8
LT16	125	78	73.8	4.5	1.8
LT10	98	105	108.4	5.4	1.8
LT12	83	120	54.3	5.0	1.8
LT07	262	-60	177.4	4.5	2.0
LT06	225	-23	214.3	4.1	2.0
LT13	203	-1	423.3	3.5	2.6
LT03	**202**	**–**	**–**	**4.2**	**–**
LT11	162	40	273.0	5.6	2.5
LT04	157	45	195.9	3.5	2.4
LT01	156	46	156.4	3.3	2.1
LT20	150	52	559.6	5.8	2.6
LT14	125	77	336.7	5.0	2.6
LT16	125	77	378.2	4.5	2.7
LT10	98	104	314.9	5.4	2.6
LT12	83	119	369.4	5.0	2.8
LT07	262	-100	96.7	4.5	2.5
LT06	225	-63	83.5	4.1	3.2
LT13	203	-41	155.6	3.5	3.2
LT03	202	-40	273.0	4.2	3.3
LT11	**162**	**–**	**–**	**5.6**	**–**
LT04	157	5	179.2	3.5	3.6
LT01	156	6	304.6	3.3	3.4
LT20	150	12	293.9	5.8	3.0
LT14	125	37	63.7	5.0	2.5
LT16	125	37	105.6	4.5	2.8
LT10	98	64	55.1	5.4	2.2
LT12	83	79	105.3	5.0	2.6
LT07	262	-105	120.4	4.5	2.3
LT06	225	-68	96.9	4.1	1.8
LT13	203	-46	283.4	3.5	1.7
LT03	202	-45	195.9	4.2	2.0
LT11	162	-5	179.2	5.6	2.3
LT04	**157**	**–**	**–**	**3.5**	**–**
LT01	156	1	139.3	3.3	1.3
LT20	150	7	460.4	5.8	2.5
LT14	125	32	228.1	5.0	2.2
LT16	125	32	268.7	4.5	2.2
LT10	98	59	187.7	5.4	2.1
LT12	83	74	232.0	5.0	2.1

Name	Depth (m)	Depth Dif (m)	Range (km)	RMS (cm)	Dif RMS (cm)
LT07	262	-106	219.7	4.5	2.0
LT06	225	-69	222.1	4.1	1.6
LT13	203	-47	422.4	3.5	1.7
LT03	202	-46	156.4	4.2	1.7
LT11	162	-6	304.6	5.6	2.1
LT04	157	-1	139.3	3.5	1.3
LT01	**156**	**–**	**–**	**3.3**	**–**
LT20	150	6	594.9	5.8	2.3
LT14	125	31	360.6	5.0	2.1
LT16	125	31	402.6	4.5	1.9
LT10	98	58	323.3	5.4	2.0
LT12	83	73	370.3	5.0	2.1
LT07	262	-112	389.1	4.5	3.7
LT06	225	-75	373.3	4.1	3.9
LT13	203	-53	194.0	3.5	3.9
LT03	202	-52	559.6	4.2	3.7
LT11	162	-12	293.9	5.6	3.1
LT04	157	-7	460.4	3.5	4.2
LT01	156	-6	594.9	3.3	4.0
LT20	**150**	**–**	**–**	**5.8**	**–**
LT14	125	25	234.4	5.0	3.1
LT16	125	25	192.3	4.5	3.4
LT10	98	52	272.7	5.4	3.0
LT12	83	67	233.8	5.0	3.4
LT07	262	-137	160.1	4.5	2.7
LT06	225	-100	138.9	4.1	2.8
LT13	203	-78	97.3	3.5	2.6
LT03	202	-77	336.7	4.2	3.1
LT11	162	-37	63.7	5.6	2.3
LT04	157	-32	228.1	3.5	3.2
LT01	156	-31	360.6	3.3	3.1
LT20	150	-25	234.4	5.8	2.7
LT14	**125**	**–**	**–**	**5.0**	**–**
LT16	125	0	42.7	4.5	2.0
LT10	98	27	45.0	5.4	1.5
LT12	83	42	57.1	5.0	1.6
LT07	262	-137	202.2	4.5	2.6
LT06	225	-100	181.4	4.1	2.6
LT13	203	-78	73.8	3.5	2.4
LT03	202	-77	378.2	4.2	2.9
LT11	162	-37	105.6	5.6	2.2
LT04	157	-32	268.7	3.5	2.9
LT01	156	-31	402.6	3.3	2.6
LT20	150	-25	192.3	5.8	2.7
LT14	125	0	42.7	5.0	1.8
LT16	**125**	**–**	**–**	**4.5**	**–**
LT10	98	27	81.6	5.4	2.0
LT12	83	42	60.9	5.0	2.1
LT07	262	-164	138.2	4.5	3.0
LT06	225	-127	105.7	4.1	3.2
LT13	203	-105	108.4	3.5	2.8
LT03	202	-104	314.9	4.2	3.4
LT11	162	-64	55.1	5.6	2.2
LT04	157	-59	187.7	3.5	3.3
LT01	156	-58	323.3	3.3	3.3
LT20	150	-52	272.7	5.8	2.8
LT14	125	-27	45.0	5.0	1.6
LT16	125	-27	81.6	4.5	2.4
LT10	**98**	**–**	**–**	**5.4**	**–**
LT12	83	15	54.6	5.0	1.4
LT07	262	-179	192.8	4.5	3.1
LT06	225	-142	158.2	4.1	3.1
LT13	203	-120	54.3	3.5	2.5
LT03	202	-119	369.4	4.2	3.4
LT11	162	-79	105.3	5.6	2.4
LT04	157	-74	232.0	3.5	3.1
LT01	156	-73	370.3	3.3	3.2
LT20	150	-67	233.8	5.8	2.9
LT14	125	-42	57.1	5.0	1.6
LT16	125	-42	60.9	4.5	2.3
LT10	98	-15	54.6	5.4	1.3
LT12	**83**	**–**	**–**	**5.0**	**–**

Note. The bolded row for each set indicates the station of interest, against which all others are differenced. The shaded row in each set indicates the choice of P_{match} for the bolded station used in this study (See Methods section 3.3, Proxies for oceanographic pressure, P_O). Pressure records were de-tided, de-drifted, and corrected with a sinusoidal seasonal correction prior to differencing.

Table A2.2. Slope station parameters and RMS of difference for every possible pair.

Name	Depth (m)	Depth Dif (m)	Range (km)	RMS (cm)	Dif RMS (cm)
LA21	**5113**	–	–	**3.2**	–
LA34	4612	501	231.4	2.3	1.9
LA33	4478	635	198.9	2.3	2.0
LA23	3977	1136	61.8	2.4	2.0
LA25	2622	2491	80.4	2.2	2.4
LA22	2130	2983	98.9	2.7	2.7
LA28	1852	3261	114.7	2.1	2.6
LA39	1628	3485	378.7	2.3	2.8
LA32	1595	3518	180.3	2.1	2.7
LA30	1564	3549	155.2	2.2	2.8
LA21	5113	-501	231.4	3.2	1.4
LA34	**4612**	–	–	**2.3**	–
LA33	4478	134	33.1	2.3	0.1
LA23	3977	635	237.1	2.4	0.5
LA25	2622	1990	195.2	2.2	1.0
LA22	2130	2482	258.8	2.7	1.6
LA28	1852	2760	159.5	2.1	1.4
LA39	1628	2984	572.5	2.3	1.5
LA32	1595	3017	69.5	2.1	1.6
LA30	1564	3048	102.9	2.2	1.6
LA21	5113	-635	198.9	3.2	1.4
LA34	4612	-134	33.1	2.3	0.1
LA33	**4478**	–	–	**2.3**	–
LA23	3977	501	204.1	2.4	0.4
LA25	2622	1856	162.5	2.2	1.0
LA22	2130	2348	226.4	2.7	1.6
LA28	1852	2626	128.0	2.1	1.4
LA39	1628	2850	540.6	2.3	1.5
LA32	1595	2883	42.0	2.1	1.6
LA30	1564	2914	73.2	2.2	1.6
LA21	5113	-1136	61.8	3.2	1.5
LA34	4612	-635	237.1	2.3	0.5
LA33	4478	-501	204.1	2.3	0.4
LA23	**3977**	–	–	**2.4**	–
LA25	2622	1355	45.1	2.2	0.9
LA22	2130	1847	38.3	2.7	1.6
LA28	1852	2125	87.3	2.1	1.4
LA39	1628	2349	342.8	2.3	1.5
LA32	1595	2382	174.3	2.1	1.6
LA30	1564	2413	142.5	2.2	1.6
LA21	5113	-2491	80.4	3.2	1.6
LA34	4612	-1990	195.2	2.3	0.9
LA33	4478	-1856	162.5	2.3	0.9
LA23	3977	-1355	45.1	2.4	0.8
LA25	**2622**	–	–	**2.2**	–
LA22	2130	492	64.7	2.7	1.1
LA28	1852	770	42.4	2.1	0.7
LA39	1628	994	379.3	2.3	0.9
LA32	1595	1027	130.3	2.1	1.1
LA30	1564	1058	97.9	2.2	0.9

Name	Depth (m)	Depth Dif (m)	Range (km)	RMS (cm)	Dif RMS (cm)
LA21	5113	-2983	98.9	3.2	2.3
LA34	4612	-2482	258.8	2.3	1.9
LA33	4478	-2348	226.4	2.3	1.9
LA23	3977	-1847	38.3	2.4	1.8
LA25	2622	-492	64.7	2.2	1.4
LA22	**2130**	–	–	**2.7**	–
LA28	1852	278	100.6	2.1	1.3
LA39	1628	502	314.7	2.3	1.5
LA32	1595	535	192.2	2.1	1.5
LA30	1564	566	158.7	2.2	1.3
LA21	5113	-3261	114.7	3.2	1.7
LA34	4612	-2760	159.5	2.3	1.3
LA33	4478	-2626	128.0	2.3	1.3
LA23	3977	-2125	87.3	2.4	1.2
LA25	2622	-770	42.4	2.2	0.7
LA22	2130	-278	100.6	2.7	1.1
LA28	**1852**	–	–	**2.1**	–
LA39	1628	224	413.0	2.3	0.8
LA32	1595	257	91.8	2.1	0.9
LA30	1564	288	58.1	2.2	0.6
LA21	5113	-3485	378.7	3.2	2.1
LA34	4612	-2984	572.5	2.3	1.6
LA33	4478	-2850	540.6	2.3	1.5
LA23	3977	-2349	342.8	2.4	1.5
LA25	2622	-994	379.3	2.2	1.0
LA22	2130	-502	314.7	2.7	1.3
LA28	1852	-224	413.0	2.1	0.9
LA39	**1628**	–	–	**2.3**	–
LA32	1595	33	504.3	2.1	1.3
LA30	1564	64	470.4	2.2	0.9
LA21	5113	-3518	180.3	3.2	1.8
LA34	4612	-3017	69.5	2.3	1.5
LA33	4478	-2883	42.0	2.3	1.4
LA23	3977	-2382	174.3	2.4	1.4
LA25	2622	-1027	130.3	2.2	1.0
LA22	2130	-535	192.2	2.7	1.2
LA28	1852	-257	91.8	2.1	0.9
LA39	1628	-33	504.3	2.3	1.2
LA32	**1595**	–	–	**2.1**	–
LA30	1564	31	33.9	2.2	0.8
LA21	5113	-3549	155.2	3.2	1.9
LA34	4612	-3048	102.9	2.3	1.5
LA33	4478	-2914	73.2	2.3	1.5
LA23	3977	-2413	142.5	2.4	1.4
LA25	2622	-1058	97.9	2.2	0.9
LA22	2130	-566	158.7	2.7	1.1
LA28	1852	-288	58.1	2.1	0.7
LA39	1628	-64	470.4	2.3	0.9
LA32	1595	-31	33.9	2.1	0.8
LA30	**1564**	–	–	**2.2**	**0.0**

Note. As for Table A2.1, but for slope stations. The lone abyss station, LA21, is included for the sake of comparison.

Table A2.3. Pressure RMS and RMS reduction after sinusoidal and proxy corrections.

	Depth (m)	Tides + Drift	Seasonal		Pref			Pmatch			Pavg			Ptemp			Pssh		
		RMS (cm)	RMS (cm)	Reduction (%)	RMS (cm)	Reduction (%)	Net Reduction (%)	RMS (cm)	Reduction (%)	Net Reduction (%)	RMS (cm)	Reduction (%)	Net Reduction (%)	RMS (cm)	Reduction (%)	Net Reduction (%)	RMS (cm)	Reduction (%)	Net Reduction (%)
LA21	5113	3.6	3.2	12%	0.0	100%	100%	1.9	39%	46%	2.4	26%	35%	3.2	0%	12%	2.8	12%	23%
LA34	4612	2.4	2.3	3%	1.4	39%	41%	0.5	79%	80%	1.0	58%	59%	2.1	9%	12%	2.1	9%	12%
LA33	4478	2.4	2.3	3%	1.4	38%	40%	0.4	81%	82%	0.9	59%	60%	2.2	6%	9%	2.1	10%	13%
LA23	3977	2.4	2.4	2%	1.5	37%	38%	0.4	81%	82%	0.9	61%	62%	2.3	5%	7%	2.3	3%	5%
LA25	2622	2.4	2.2	11%	1.6	26%	34%	0.9	57%	61%	0.3	84%	86%	2.2	0%	11%	2.2	1%	11%
LA22	2130	2.9	2.7	8%	2.3	14%	21%	1.3	50%	54%	1.2	54%	57%	2.6	3%	11%	2.7	0%	8%
LA28	1852	2.6	2.1	17%	1.7	17%	32%	0.8	63%	69%	0.6	72%	77%	2.1	0%	17%	2.1	0%	17%
LA39	1628	2.4	2.3	2%	2.1	11%	13%	0.9	60%	61%	0.9	60%	61%	2.3	1%	3%	2.3	0%	2%
LA32	1595	2.2	2.1	3%	1.8	16%	18%	0.9	56%	57%	0.9	57%	59%	2.0	2%	5%	2.1	0%	3%
LA30	1564	2.3	2.2	6%	1.9	13%	19%	0.9	59%	62%	0.8	64%	66%	2.1	3%	9%	2.1	1%	7%
Minimum		2.2	2.1	2%	1.4	11%	13%	0.4	50%	54%	0.3	54%	57%	2.0	0%	3%	2.1	0%	2%
Maximum		3.6	3.2	17%	2.3	39%	41%	1.3	81%	82%	1.2	84%	86%	2.6	9%	17%	2.7	10%	17%
Median		2.4	2.3	3%	1.7	17%	32%	0.9	60%	62%	0.9	60%	61%	2.2	3%	9%	2.1	1%	8%
LT07	262	5.2	4.5	13%	4.5	0%	13%	2.0	55%	60%	1.8	60%	65%	4.5	0%	13%	4.1	10%	21%
LT06	225	4.7	4.1	13%	4.1	1%	14%	1.9	53%	59%	1.6	62%	67%	4.1	1%	14%	3.5	14%	26%
LT13	203	4.2	3.5	17%	3.4	2%	18%	1.7	51%	59%	1.3	62%	68%	3.4	2%	19%	2.9	18%	32%
LT03	202	4.7	4.2	11%	4.1	1%	12%	2.0	53%	58%	1.8	56%	60%	4.2	0%	11%	4.1	1%	12%
LT11	162	6.4	5.6	13%	5.5	0%	13%	2.2	60%	65%	2.0	64%	69%	5.5	1%	14%	4.2	24%	34%
LT04	157	3.7	3.5	6%	3.4	1%	7%	1.3	62%	64%	1.6	54%	57%	3.3	6%	11%	2.9	16%	21%
LT01	156	4.3	3.3	22%	3.3	2%	23%	1.6	52%	62%	1.4	58%	67%	3.3	0%	22%	2.8	15%	34%
LT20	150	6.4	5.8	8%	5.8	0%	8%	3.0	49%	53%	2.8	51%	55%	5.8	1%	9%	4.4	24%	30%
LT14	125	6.2	5.0	19%	5.0	0%	19%	1.6	68%	74%	1.6	68%	74%	4.7	6%	23%	3.6	28%	41%
LT16	125	5.2	4.5	14%	4.5	0%	14%	2.0	56%	62%	1.7	63%	68%	4.3	5%	18%	3.5	22%	33%
LT10	98	6.9	5.4	22%	5.4	1%	22%	1.4	74%	79%	1.7	68%	75%	5.1	5%	25%	3.5	35%	49%
LT12	83	6.6	5.0	24%	5.0	0%	25%	1.3	74%	80%	1.9	63%	72%	4.7	5%	28%	3.0	40%	54%
Minimum		3.7	3.3	6%	3.3	0%	7%	1.3	49%	53%	1.3	51%	55%	3.3	0%	9%	2.8	1%	12%
Maximum		6.9	5.8	24%	5.8	2%	25%	3.0	74%	80%	2.8	68%	75%	5.8	6%	28%	4.4	40%	54%
Median		5.2	4.5	14%	4.5	0%	14%	1.8	55%	62%	1.7	62%	68%	4.4	2%	16%	3.5	20%	32%

Note. For each station, RMS and RMS reduction are summarized after correction with a sinusoidal seasonal fit and each proxy considered in this study. For the proxy corrections, 'Net Reduction' indicates the RMS reduction relative to the detided and de-drifted input signal. The lone abyss station, LA21 (highlighted in gray), is included for comparison but is excluded from the minimum, maximum, and median calculations.

Table A2.4. Pressure RMS and RMS reduction after pressure-CEOF and proxy corrections.

	Depth (m)	Tides + Drift	Seasonal		Pref			Pmatch			Pavg			Ptemp			Pssh		
		RMS (cm)	RMS (cm)	Reduction (%)	RMS (cm)	Reduction (%)	Net Reduction (%)	RMS (cm)	Reduction (%)	Net Reduction (%)	RMS (cm)	Reduction (%)	Net Reduction (%)	RMS (cm)	Reduction (%)	Net Reduction (%)	RMS (cm)	Reduction (%)	Net Reduction (%)
LA21	5113	3.6	3.6	0%	0.0	100%	100%	3.5	4%	4%	3.5	3%	3%	3.6	1%	1%	3.5	5%	5%
LA34	4612	2.4	1.0	59%	0.9	4%	61%	0.5	51%	80%	1.0	1%	60%	1.0	0%	59%	0.8	19%	67%
LA33	4478	2.4	0.9	60%	0.9	4%	62%	0.4	55%	82%	0.9	1%	60%	0.9	1%	61%	0.8	13%	66%
LA23	3977	2.4	1.0	61%	0.9	3%	62%	0.4	55%	83%	0.9	2%	61%	0.9	1%	61%	0.9	1%	61%
LA25	2622	2.4	0.5	80%	0.5	3%	81%	0.5	0%	80%	0.2	62%	93%	0.5	1%	80%	0.5	0%	80%
LA22	2130	2.9	1.4	53%	1.4	0%	53%	1.3	4%	55%	1.4	0%	53%	1.3	4%	54%	1.4	1%	53%
LA28	1852	2.6	0.9	63%	0.9	0%	63%	0.9	0%	63%	0.8	18%	70%	0.9	1%	64%	0.9	6%	65%
LA39	1628	2.4	1.0	58%	0.9	8%	61%	0.9	6%	60%	0.9	6%	60%	1.0	0%	58%	1.0	0%	58%
LA32	1595	2.2	1.0	56%	0.9	3%	57%	1.0	0%	56%	0.9	3%	57%	0.9	1%	56%	1.0	0%	56%
LA30	1564	2.3	0.8	66%	0.8	4%	67%	0.8	0%	66%	0.8	1%	66%	0.8	1%	66%	0.8	0%	66%
Minimum		2.2	0.5	53%	0.5	0%	53%	0.4	0%	55%	0.2	0%	53%	0.5	0%	54%	0.5	0%	53%
Maximum		3.6	3.6	80%	1.4	8%	81%	1.3	55%	83%	1.4	62%	93%	1.3	4%	80%	1.4	19%	80%
Median		2.4	1.0	60%	0.9	3%	62%	0.8	4%	66%	0.9	2%	60%	0.9	1%	61%	0.9	1%	65%
LT07	262	5.2	1.7	67%	1.7	0%	67%	1.7	3%	68%	1.7	1%	67%	1.7	3%	68%	1.7	0%	67%
LT06	225	4.7	1.7	64%	1.7	2%	65%	1.6	8%	67%	1.5	10%	68%	1.7	1%	64%	1.6	7%	66%
LT13	203	4.2	1.4	68%	1.3	4%	69%	1.3	2%	69%	1.4	0%	68%	1.3	4%	69%	1.3	0%	68%
LT03	202	4.7	1.9	59%	1.9	4%	60%	1.8	5%	61%	1.6	18%	66%	1.9	0%	59%	1.9	0%	59%
LT11	162	6.4	2.0	69%	1.9	3%	70%	2.0	2%	69%	2.0	2%	69%	2.0	0%	69%	2.0	0%	69%
LT04	157	3.7	1.7	54%	1.6	6%	57%	1.6	8%	58%	1.4	15%	61%	1.7	2%	55%	1.6	6%	57%
LT01	156	4.3	1.6	63%	1.5	1%	64%	1.6	0%	64%	1.6	0%	64%	1.5	1%	64%	1.5	7%	66%
LT20	150	6.4	2.9	54%	2.9	0%	54%	2.9	0%	54%	2.9	3%	55%	2.9	2%	55%	2.9	2%	55%
LT14	125	6.2	1.7	73%	1.6	5%	74%	1.3	22%	79%	1.2	27%	80%	1.6	1%	73%	1.5	10%	76%
LT16	125	5.2	1.7	68%	1.7	0%	68%	1.6	1%	69%	1.5	13%	72%	1.7	1%	68%	1.7	1%	68%
LT10	98	6.9	1.8	73%	1.6	16%	77%	1.2	36%	83%	1.3	27%	80%	1.8	0%	73%	1.7	9%	76%
LT12	83	6.6	2.1	69%	1.8	14%	73%	1.3	36%	80%	1.6	23%	76%	2.1	0%	69%	1.9	9%	72%
Minimum		3.7	1.4	54%	1.3	0%	54%	1.2	0%	54%	1.2	0%	55%	1.3	0%	55%	1.3	0%	55%
Maximum		6.9	2.9	73%	2.9	16%	77%	2.9	36%	83%	2.9	27%	80%	2.9	4%	73%	2.9	10%	76%
Median		5.2	1.7	67%	1.7	4%	68%	1.6	4%	68%	1.5	11%	68%	1.7	1%	68%	1.7	4%	68%

Note. As for Table A2.3, but for the pressure-CEOF seasonal correction.

Table A2.5. Summary of synthetic detectability results when onset is assumed unknown, for only 1.5 cm amplitude synthetic ramp on the slope and 3.5 cm amplitude synthetic ramp on the shelf.

Aknown (cm)	Proxy		Shelf				Slope			
			Onset Recovery Error (d)		Amplitude Recovery (cm)		Onset Recovery Error (d)		Amplitude Recovery (cm)	
			median	mad	median	mad	median	mad	median	mad
1.5	**POLY**	P	--	--	--	--	22.0	65.5	2.5	1.1
		Pmatch	--	--	--	--	0.0	46.0	1.3	1.8
		Pavg	--	--	--	--	3.0	62.0	3.0	1.0
	SIN	P	--	--	--	--	12.0	61.5	2.8	1.3
		Pmatch	--	--	--	--	1.0	45.0	1.2	2.3
		Pavg	--	--	--	--	-2.0	58.0	3.1	1.8
	m-CEOF	P	--	--	--	--	-14.0	90.5	-0.3	1.7
		Pmatch	--	--	--	--	-1.0	20.0	1.1	0.9
		Pavg	--	--	--	--	11.5	81.0	1.3	1.5
	p-CEOF	P	--	--	--	--	-14.0	90.5	-0.4	2.3
		Pmatch	--	--	--	--	-1.0	22.0	1.5	0.7
		Pavg	--	--	--	--	-5.0	100.0	0.2	1.7
3.5	**POLY**	P	32.0	81.0	-12.5	2.4	--	--	--	--
		Pmatch	-1.0	50.0	2.2	4.0	--	--	--	--
		Pavg	-2.0	62.0	3.2	2.3	--	--	--	--
	SIN	P	36.0	84.0	-11.5	2.8	--	--	--	--
		Pmatch	1.0	47.5	2.8	2.9	--	--	--	--
		Pavg	-1.0	58.5	3.5	2.8	--	--	--	--
	m-CEOF	P	17.5	81.5	4.4	2.1	--	--	--	--
		Pmatch	3.0	52.0	1.1	2.6	--	--	--	--
		Pavg	3.0	52.5	0.9	2.3	--	--	--	--
	p-CEOF	P	0.0	26.0	3.6	1.7	--	--	--	--
		Pmatch	0.0	18.0	3.2	1.3	--	--	--	--
		Pavg	0.0	26.0	2.3	3.6	--	--	--	--

Note. Onset recovery error and amplitude recovery for the unknown onset case is summarized as median and MAD errors for each ramp amplitude considered herein for all seasonal corrections, and the proxy corrections P, P_{match}, and P_{avg}, with shelf and slope presented separately. m-CEOF = multivariate-CEOF, p-CEOF = pressure-CEOF.

Appendix 3: Supplementary Materials for Chapter 5

Text A3.1 Anomalous calibrations at Axial Seamount

A total of 43 anomalous calibrations were identified throughout the Axial Seamount SCTA deployment: 26 at Location 1 and 17 at Location 2. As an example, the acceleration data for 5 good calibrations and one anomalous calibration in the +X1 orientation at Location 1 are shown in Figure A3.3. The primary indication of an anomalous calibration is that the total acceleration, a_T, lies well outside the normal bounds. Usually, most of the anomalous contribution to a_T arises from the Z channel with other channels contributing smaller amounts. When anomalous calibrations occur, they can be seen on one or several calibrations within a sequence and in only one instance comprised all the calibrations in a sequence. Anomalous calibrations are sometimes accompanied by higher noise levels on some channels (Figure A3.3b). We do not understand the cause of anomalous calibrations. They are most likely a mechanical problem but have been unable to reproduce them after recovering the SCTA from Axial because the accelerometer performed normally during a post-experiment factory recalibration – most of the anomalous calibrations occurred early in the deployment. Because the anomalous calibrations are readily identifiable from the offset in a_T, they are easily removed prior to characterizing and correcting sensor drift by inspecting plots of the calibrations against time (Figures A3.4 and A3.5).

Table A3.1. Details of calibrations at Axial Seamount Location 1 indicating the date, calibration values relative to the first calibration, and the rate of drift over the previous measurement interval obtained from differencing the calibration values. Gray shading indicates anomalous calibrations that are evident by unreasonable apparent rates of drift.

Date	+X1 (ug)	∂+X1 / ∂t (ug/yr)	+Y (ug)	∂+Y / ∂t (ug/yr)	-Y (ug)	∂-Y / ∂t (ug/yr)	+X2 (ug)	∂+X2 / ∂t (ug/yr)	-X (ug)	∂-X / ∂t (ug/yr)	Comment
2018-08-08	0.00		0.00				0.00				
2018-08-09	0.04	14	0.34	125			0.06	23			
2018-08-10	0.42	138	1.13	286			0.43	134			
2018-08-18	1.70	59	3.94	128			1.80	62			
2018-08-22											OOI power loss
2018-08-24											OOI power return
2018-09-10	5.92	67	12.90	142			5.97	66			
2018-09-17	7.43	79	16.09	166			7.84	98			
2018-09-24	8.37	49	16.99	47			8.39	29			
2018-10-08	10.62	58	21.87	127			11.15	72			
2018-10-15	11.44	43	22.69	43			11.58	23			
2018-10-22	12.08	33	24.10	74			12.27	36			
2018-10-29	13.23	60	25.78	88			13.46	62			
2018-11-05	14.37	59	27.65	97			14.42	50			
2018-11-12	15.00	33	29.13	77			15.13	37			
2018-11-19	16.47	76	31.57	127			16.56	74			
2018-11-26	16.91	23	32.27	37			16.93	19			
2018-12-03	17.70	41	33.57	68			17.77	44			
2019-01-01	20.84	40	38.99	68			21.05	41			
2019-02-01	24.64	45	45.37	75			24.84	45			
2019-03-01	27.33	35	50.10	62			27.44	34			
2019-04-01	30.60	38	55.60	65			30.81	40			
2019-05-01	33.62	37	61.09	67			33.77	36			
2019-06-01	36.15	30	65.30	50			36.46	32			
2019-07-01	38.84	33	70.11	58			39.18	33			
2019-08-01	42.02	37	73.53	40			42.28	37			
2019-08-13	43.28	38	75.59	63	0.00		58.40		0.00		
2019-08-20	43.84	30	76.32	38	-1.63	-85	59.12	37	1.22	64	
2019-08-27	44.41	30	76.90	30	-1.87	-13	59.77	34	0.83	-21	

2019-09-03	45.20	41	78.29	72	-3.07	-63	60.44	35	0.59	-12	
2019-09-10	45.34	7	78.66	19	-3.27	-10	60.68	13	-0.32	-48	
2019-10-15	48.67	35	86.47	81	-9.22	-62	63.95	34	-4.56	-44	
2019-11-01	49.80	24	87.41	20	-10.68	-31	65.18	26	-0.23	93	
2019-12-01	259.89	2556	202.64	1402	77.42	1072	84.64	237	0.43	8	
2020-01-08	89.15	-1640	99.18	-994	28.18	-473	74.26	-100	-7.84	-79	
2020-01-15	63.86	-1319	96.68	-131	-12.58	-2125	72.00	-117	-9.60	-91	
2020-01-22	57.92	-310	98.07	72	-15.69	-162	71.74	-14	-10.96	-71	
2020-01-29	61.98	212	98.54	25	-20.75	-264	71.87	7	-10.79	9	
2020-02-05	57.19	-250	99.84	68	-21.81	-56	72.36	26	-11.12	-18	
2020-02-12	57.47	15	100.18	18	-22.44	-33	72.86	26	-11.74	-32	
2020-02-19	58.28	42	101.61	75	-20.44	104	73.48	32	-11.70	2	
2020-02-26	58.47	10	101.82	11	-23.83	-177	73.92	23	-12.58	-46	
2020-03-04	58.71	12	102.53	37	-24.37	-28	74.18	14	-12.33	13	
2020-03-11	59.21	26	103.86	69	-26.02	-86	74.70	27	-12.44	-6	
2020-03-18	59.95	38	104.60	39	17.38	2263	75.34	33	-12.96	-27	
2020-03-25	60.25	16	105.65	54	-27.45	-2337	75.60	14	-13.28	-17	
2020-04-01	60.84	31	106.15	26	-27.56	-6	76.34	39	-13.71	-22	
2020-04-08	60.99	8	106.85	37	-28.56	-52	76.33	-1	-14.07	-19	
2020-04-15	61.59	31	107.48	33	-28.79	-12	77.00	35	-14.32	-13	
2020-04-22	61.66	4	108.26	41	-29.87	-56	76.97	-2	-14.27	3	
2020-04-29	63.05	72	110.19	100	-31.23	-71	84.66	401	-14.92	-34	
2020-05-06	62.51	-28	109.85	-18	-31.00	12	77.67	-365	-14.88	2	
2020-05-09											OOI power loss
2020-06-02											OOI power return
2020-06-03	65.33	37	117.88	105	-36.80	-76	80.56	38	-16.59	-22	
2020-06-10	65.59	13	115.72	-112	-35.70	57	80.79	12	-16.02	30	
2020-06-17	66.25	35	116.86	59	-4.39	1633	80.82	2	-16.61	-31	
2020-06-24	66.30	2	117.01	8	-36.93	-1697	81.54	38	-17.05	-23	
2020-07-01	66.56	13	117.50	25	-37.75	-42	81.87	17	-17.37	-17	
2020-07-08	67.05	26	118.04	29	-38.31	-30	82.35	25	-18.09	-37	
2020-07-15	67.47	22	119.25	63	-39.33	-53	82.83	25	-18.17	-4	
2020-07-22	67.92	23	119.82	30	-40.07	-39	83.26	22	-18.95	-40	
2020-07-29	68.44	27	120.76	49	-40.69	-32	83.52	14	-18.66	15	
2020-08-05	68.98	28	120.88	7	-40.93	-13	83.78	14	-19.25	-31	

2020-08-12	69.71	38	121.74	45	-41.62	-36	84.47	36	-19.37	-6	
2020-08-19	69.54	-9	122.67	48	-42.79	-61	85.01	28	-20.46	-57	
2020-08-26	69.91	19	122.98	16	-42.59	10	85.28	14	-20.62	-8	
2020-09-02	70.09	9	125.00	105	-42.96	-19	90.65	280	5.43	1358	
2020-09-09	74.46	228	127.09	109	212.20	13305	85.84	-251	-21.12	-1384	

Table A3.2. Details of calibrations at Axial Seamount Location 2 indicating the date, calibration values relative to the first calibration, and the rate of drift over the previous measurement interval obtained from differencing the calibration values. Gray shading indicates anomalous calibrations that are evident by unreasonable apparent rates of drift.

Date	+X1 (ug)	∂+X1 / ∂t (ug/yr)	+Y (ug)	∂Δ+Y / ∂t (ug/yr)	-Y (ug)	∂Δ-Y / ∂t (ug/yr)	+X2 (ug)	∂Δ+X2 / ∂t (ug/yr)	-X (ug)	∂Δ-X / ∂t (ug/yr)	Comment
2020-09-16	0.00		0.00		0.00		0.00		0.00		
2020-09-22											OOI power loss
2020-09-23											OOI power return
2020-09-23	0.19	10	3.80	198	-2.03	-106	0.73	38	1.50	78	
2020-09-30	0.52	17	3.75	-3	-2.88	-45	1.21	25	1.27	-12	
2020-10-07	0.57	2	3.96	11	-2.92	-2	1.30	5	1.18	-5	
2020-10-14	1.06	26	4.59	33	-3.51	-31	1.63	17	0.57	-32	
2020-10-21	1.34	15	5.18	31	-3.96	-24	2.02	20	0.32	-13	
2020-10-28	1.64	15	5.59	21	-4.39	-23	2.37	18	-0.39	-37	
2020-11-04	2.05	21	6.73	60	-5.43	-54	2.79	22	-0.68	-15	
2020-11-11	2.15	5	7.20	25	-5.64	-11	2.85	3	-0.52	8	
2020-11-18	3.19	54	7.31	6	-6.10	-24	3.86	53	-2.00	-77	
2020-11-25	3.38	10	7.43	6	-6.56	-24	4.05	10	-2.26	-13	
2020-12-02	3.90	27	8.55	58	-7.67	-58	4.63	30	-2.68	-22	
2020-12-09	4.74	44	9.89	70	-8.51	-44	5.21	30	-2.98	-16	
2020-12-16	4.88	7	9.60	-15	-8.23	14	5.56	18	-4.01	-54	
2020-12-23	5.09	11	10.57	50	-9.21	-51	5.70	7	-3.53	25	
2020-12-30	5.20	5	10.81	13	-9.36	-8	5.87	9	-4.10	-30	
2021-01-06	5.49	15	11.43	33	-9.79	-23	6.34	24	-4.31	-10	
2021-01-13											OOI power loss
2021-01-18											OOI power return
2021-01-20	6.09	16	14.61	83	-13.04	-85	6.70	10	-4.17	4	
2021-01-27	6.64	28	14.11	-26	-12.88	8	7.35	34	-4.10	3	
2021-02-03	7.17	27	15.27	60	-14.21	-69	7.94	31	-4.69	-31	
2021-02-10	7.43	14	15.27	0	-14.21	0	8.05	5	-5.24	-28	
2021-02-17	7.70	14	15.81	28	-14.82	-32	8.27	12	-5.64	-21	
2021-02-24	7.97	14	16.47	34	-15.48	-35	8.63	19	-6.03	-20	

2021-03-03	7.75	-12	16.80	17	-15.71	-12	8.44	-10	-5.75	15	
2021-03-10	8.67	48	18.03	64	-16.62	-47	9.28	44	-6.54	-41	
2021-03-17	8.94	14	18.94	47	-17.49	-45	9.52	12	-6.81	-14	
2021-03-24	9.02	4	18.92	-1	-17.14	19	9.63	6	-7.20	-20	
2021-03-31	9.47	24	19.80	46	-18.56	-75	10.16	27	-8.06	-45	
2021-04-07	9.56	5	19.64	-8	-18.13	23	10.24	4	-8.17	-6	
2021-04-14	9.98	21	20.64	52	-19.31	-61	10.60	19	-8.74	-30	
2021-04-21	10.27	16	21.02	20	-19.36	-3	11.07	25	-8.90	-8	
2021-04-28	10.33	3	21.87	44	-20.74	-72	11.09	1	-9.25	-18	
2021-05-05	11.13	41	22.27	21	-20.42	17	11.75	35	-9.95	-36	
2021-05-12	11.32	10	23.12	44	-21.42	-52	11.98	12	-10.44	-26	
2021-05-19	11.97	34	23.82	37	-21.59	-9	12.61	33	-10.76	-17	
2021-05-26	11.76	-11	23.89	4	-22.53	-49	12.40	-11	-11.01	-13	
2021-06-02	12.33	30	24.71	43	-22.76	-12	12.98	30	-11.30	-15	
2021-06-09	12.37	2	24.94	12	-23.16	-21	13.07	5	-11.70	-21	
2021-06-16	12.78	22	25.91	51	-11.59	603	13.50	23	-10.71	51	
2021-07-29	14.68	16	30.91	42	-27.28	-133	15.28	15	-12.43	-15	
2021-07-30	14.61	-28	29.85	-386	-27.00	100	15.15	-48	-11.65	287	
2021-07-31	14.63	7	30.02	61	-27.23	-82	15.25	36	-12.15	-185	
2021-08-01	14.91	104	30.56	196	-27.41	-67	15.47	81	-12.72	-207	
2021-08-02	15.00	32	30.56	2	-27.96	-198	15.64	59	-13.20	-176	
2021-08-03	14.69	-114	30.07	-182	-27.38	208	15.32	-115	-13.02	66	
2021-08-04	14.81	45	30.22	57	-27.26	47	15.46	51	-13.45	-155	
2021-08-05	14.81	2	30.38	57	-27.48	-82	15.48	6	-13.48	-11	
2021-08-06	14.89	28	30.41	11	-27.41	26	15.60	43	-13.82	-126	
2021-08-07	14.89	0	30.48	26	-27.55	-51	15.56	-14	-13.86	-14	
2021-08-08	15.15	93	31.10	226	-28.33	-286	15.95	143	-14.11	-90	
2021-08-09	14.92	-81	30.52	-211	-27.52	296	15.65	-111	-5.86	3010	
2021-08-10	14.65	-100	30.16	-133	-27.27	93	15.35	-110	-13.67	-2850	
2021-08-11	15.26	223	31.29	412	-28.23	-351	16.06	261	-14.66	-360	
2021-08-12	15.48	79	31.58	107	-28.75	-191	16.08	6	-14.13	191	
2021-08-13	15.18	-109	31.30	-103	-27.89	315	15.93	-54	-13.92	79	
2021-08-14	15.25	25	31.52	82	-28.28	-142	15.90	-12	-13.85	23	
2021-08-15	15.09	-58	31.15	-136	-27.82	167	15.87	-9	-13.78	25	
2021-08-16	15.38	106	31.44	105	-28.17	-127	16.11	87	-14.24	-167	
2021-08-17	15.52	50	31.69	93	-28.96	-288	16.35	88	-14.62	-138	
2021-08-18	15.34	-65	31.28	-149	-28.44	189	16.07	-104	-14.89	-98	
2021-08-19	15.41	28	31.71	157	-28.68	-86	16.22	55	-14.68	74	
2021-08-20	15.41	-3	31.36	-127	-28.63	16	16.16	-21	-14.72	-13	

2021-08-21	15.39	-6	31.54	63	-28.86	-81	16.09	-26	-14.13	213	
2021-08-22	15.64	91	31.84	110	20.00	17833	16.18	32	-16.65	-919	
2021-08-23	55.94	14710	32.31	170	-29.32	-18001	16.64	168	-15.06	580	
2021-08-24	15.72	-14682	31.84	-170	-28.80	187	16.50	-51	-15.05	5	
2021-08-25	15.63	-32	32.17	119	-28.88	-29	16.23	-97	-14.47	209	
2021-08-26	15.82	66	32.41	90	-29.12	-89	16.42	68	-14.63	-56	

Table S3. Details of calibrations at Piñon Flat Observatory indicating the date, calibration values relative to the first calibration, and the the rate of drift over the previous measurement interval obtained from differencing the calibration values.

Date	+X1 (ug)	Δ+X1 (ug/yr)	+Y (ug)	Δ+Y (ug/yr)	-Y (ug)	Δ-Y (ug/yr)	+X2 (ug)	Δ+X2 (ug/yr)	-X (ug)	Δ-X (ug/yr)	Comment
2018-10-18	0.00		0.00				0.00				
2018-10-19	-4.15	-1514	-3.69	-1348			-4.10	-1498			
2018-10-20	-6.91	-1010	-5.90	-805			-6.92	-1028			
2018-10-21	-9.11	-802	-8.00	-766			-9.07	-785			
2018-10-22	-10.69	-576	-9.27	-465			-10.75	-613			
2018-10-23	-12.06	-501	-10.48	-441			-12.07	-483			
2018-10-25	-13.96	-346	-12.36	-342			-13.97	-346			
2018-10-29	-15.84	-172	-14.42	-188			-15.75	-163			
2018-11-01	-16.64	-97	-15.60	-144			-16.61	-104			
2018-11-05	-17.19	-49	-16.42	-75			-17.15	-49			
2018-11-08	-17.11	9	-16.86	-53			-17.14	2			
2018-11-12	-16.98	13	-17.39	-48			-16.95	17			
2018-12-06	-17.72	-11	-20.93	-54			-17.55	-9			
2019-01-06	-19.00	-15	-25.21	-50			-18.83	-15			
2019-02-06	-18.76	3	-26.64	-17			-18.85	0			
2019-02-14											Local computer failure
2019-03-28											Computer replaced
2019-03-31											PFO power outage (?)
2019-04-03											PFO power restored (?)

2019-04-06	-11.93	42	-23.00	22			-12.68	38			
2019-04-27											PFO power outage (?)
2019-04-29											PFO power restored (?)
2019-05-06	4.02	194	-6.40	202			3.32	195			
2019-06-06	17.00	153	9.86	191			16.65	157			
2019-07-06	32.88	193	29.09	234			32.68	195			
2019-08-06	47.31	170	49.54	241			47.66	176			
2019-08-09	48.80	182	51.54	243	0.00		70.16	2738	0.00	0	
2019-08-16	51.22	126	55.29	195	-3.34	-174	72.69	132	-1.82	-95	
2019-08-23	52.70	77	57.77	130	-4.62	-67	74.34	86	-2.38	-29	
2019-08-30	55.58	150	61.24	181	-7.51	-151	77.63	171	-5.02	-138	
2019-09-06	58.52	154	63.60	123	-8.92	-74	80.60	155	-6.90	-98	
2019-09-08											PFO power outage (1 day)
2019-09-13	59.96	75	66.40	146	-11.24	-121	82.25	86	-7.97	-55	
2019-09-20	62.19	116	67.57	61	-11.93	-36	84.29	106	-9.32	-71	
2019-09-27	63.05	45	69.22	86	-13.88	-102	85.17	46	-9.60	-15	
2019-10-04	63.46	21	69.95	38	-14.43	-29	85.62	24	-9.66	-3	
2019-11-06	65.41	22	77.94	88	-20.95	-72	88.12	28	-11.22	-17	
2019-12-06	61.99	-42	74.85	-38	-19.37	19	84.28	-47	-10.43	10	
2019-12-25											PFO power outage (?)
2019-12-29											PFO power restored (?)
2020-01-06	54.67	-86	67.62	-85	-15.69	43	77.12	-84	-8.35	25	

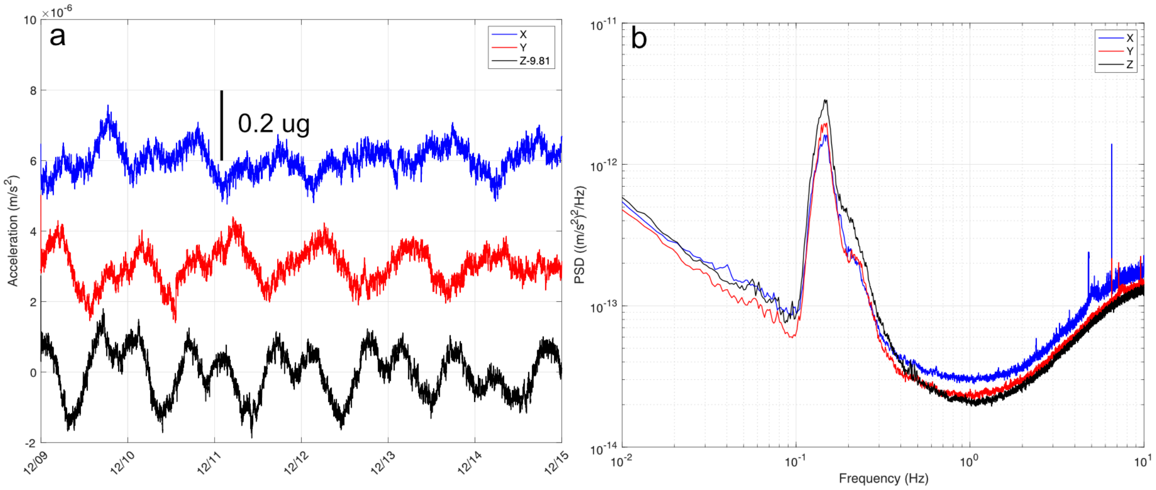

Figure A3.1. (a) Representative 6-days of data from Piñon Flab Observatory with the SCTA in the measurement orientation (the Z channel vertical) from 12/09/2018–12/15/2018. X-, Y-, and Z channel observations are plotted in blue, red, and black, respectively, after removing the mean and linear trend and decimating to 1 sample/minute. Vertical offsets are for display purposes only. (b) Associated power spectral density for the three channels, calculated without decimating the data and plotted with the same colors.

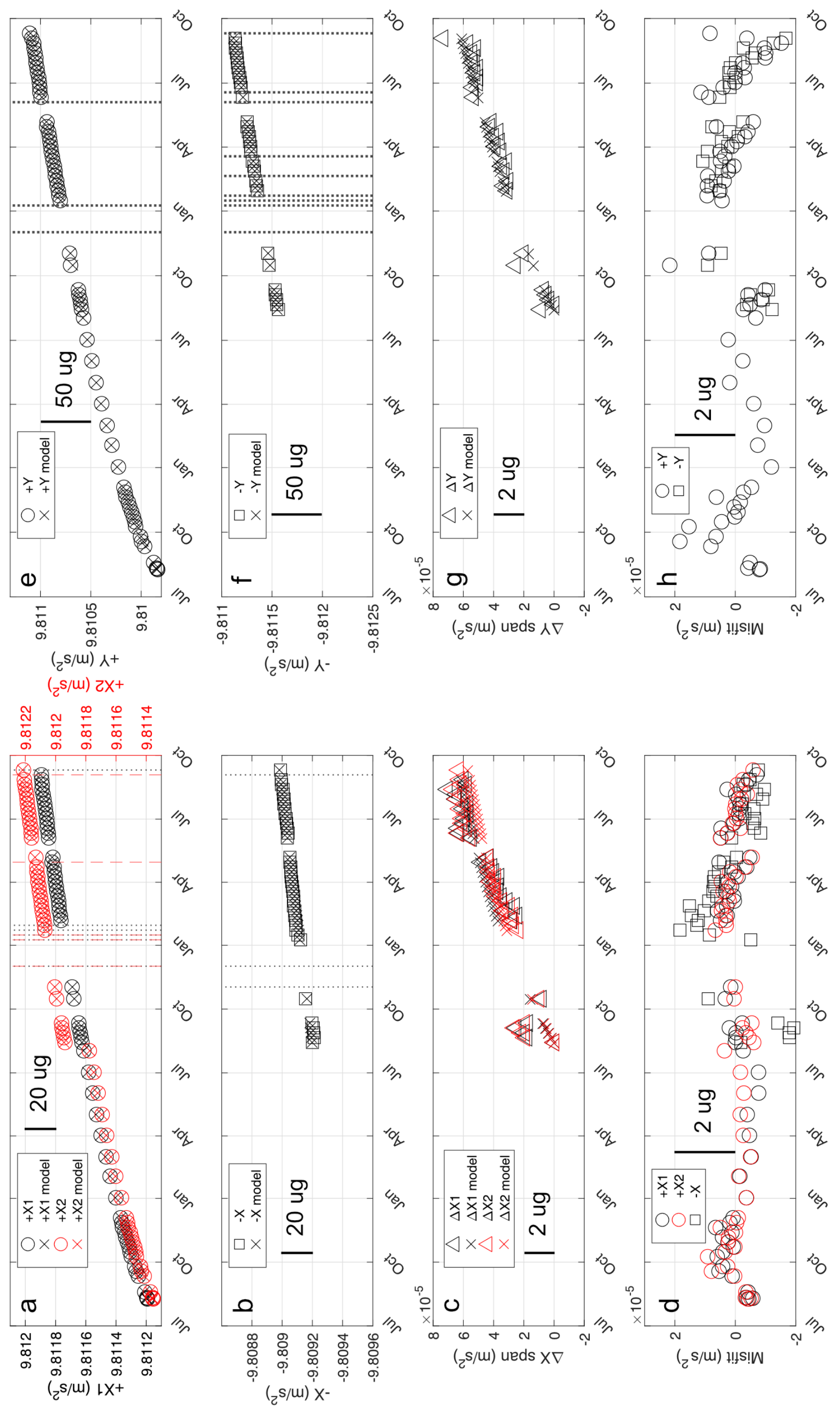

Figure A3.2. Calibration results for the Axial Seamount SCTA at Location 1. (a) Calibration values for +X1 (black) and +X2 (red). (b) Calibration values for -X. (c) Span defined as +X1 or +X2 minus -X. (d) Misfit of the exponential linear model (equation 5) for the +X1, +X2 and -X calibrations. (e-h) As for (a-d) except for Y calibrations. Vertical dotted lines in (a-b) and (e-f) indicate where anomalous calibrations have been excluded (see text).

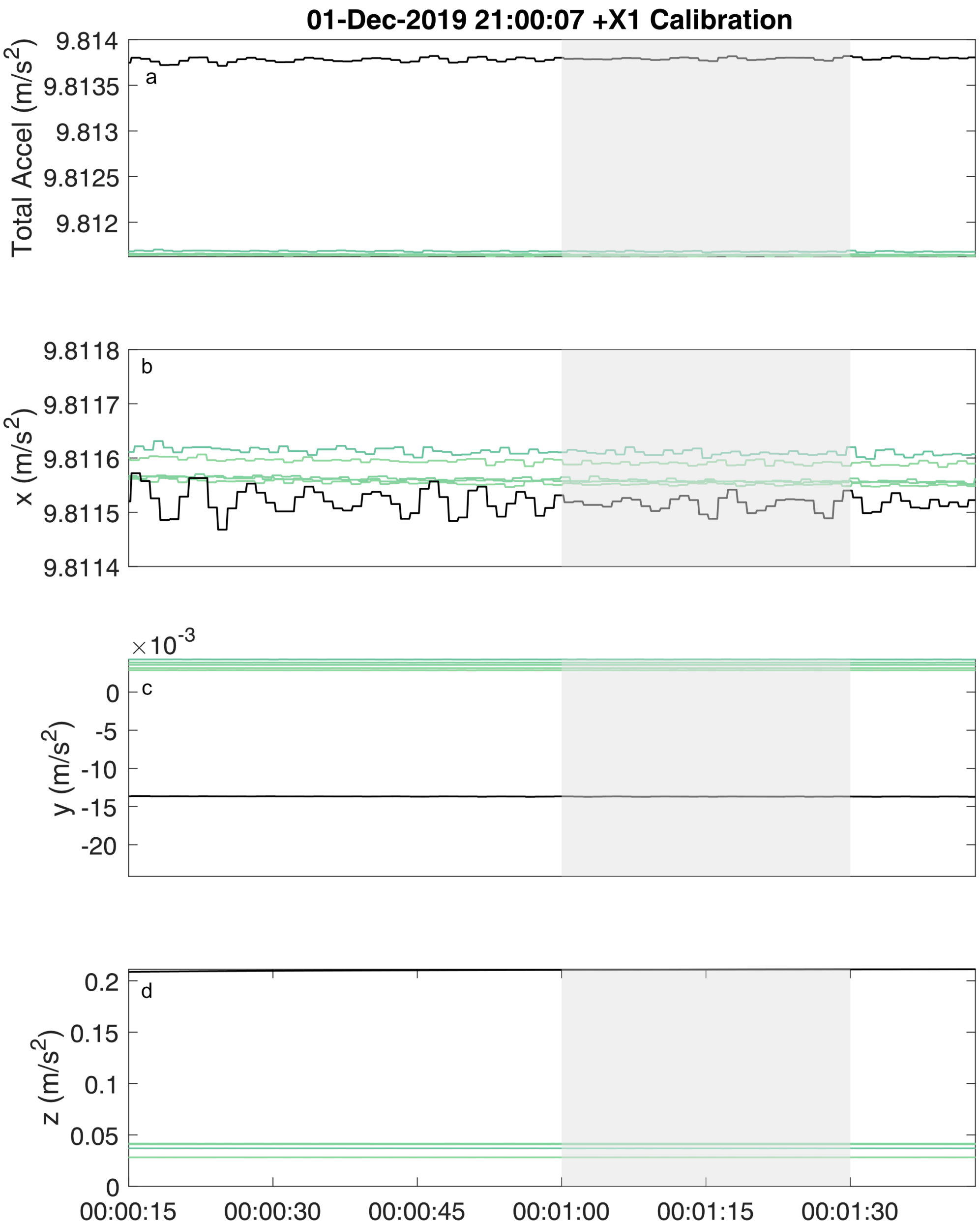

Figure A3.3. Acceleration observed during 6 +X1 calibrations on the SCTA at Axial Seamount Location 1 from August 20 – December 1, 2019 showing an anomalous calibration at the end of the interval. (a) Total (b) X channel, (c) Y channel, and (d) Z channel acceleration. Time is referenced to the start the calibration interval and the curves are color coded by time of the calibration from pale teal at the early on to black at the end. Light gray shading shows the time interval used to obtain calibration values. The final calibration is clearly inconsistent with the drift observed for other calibrations.

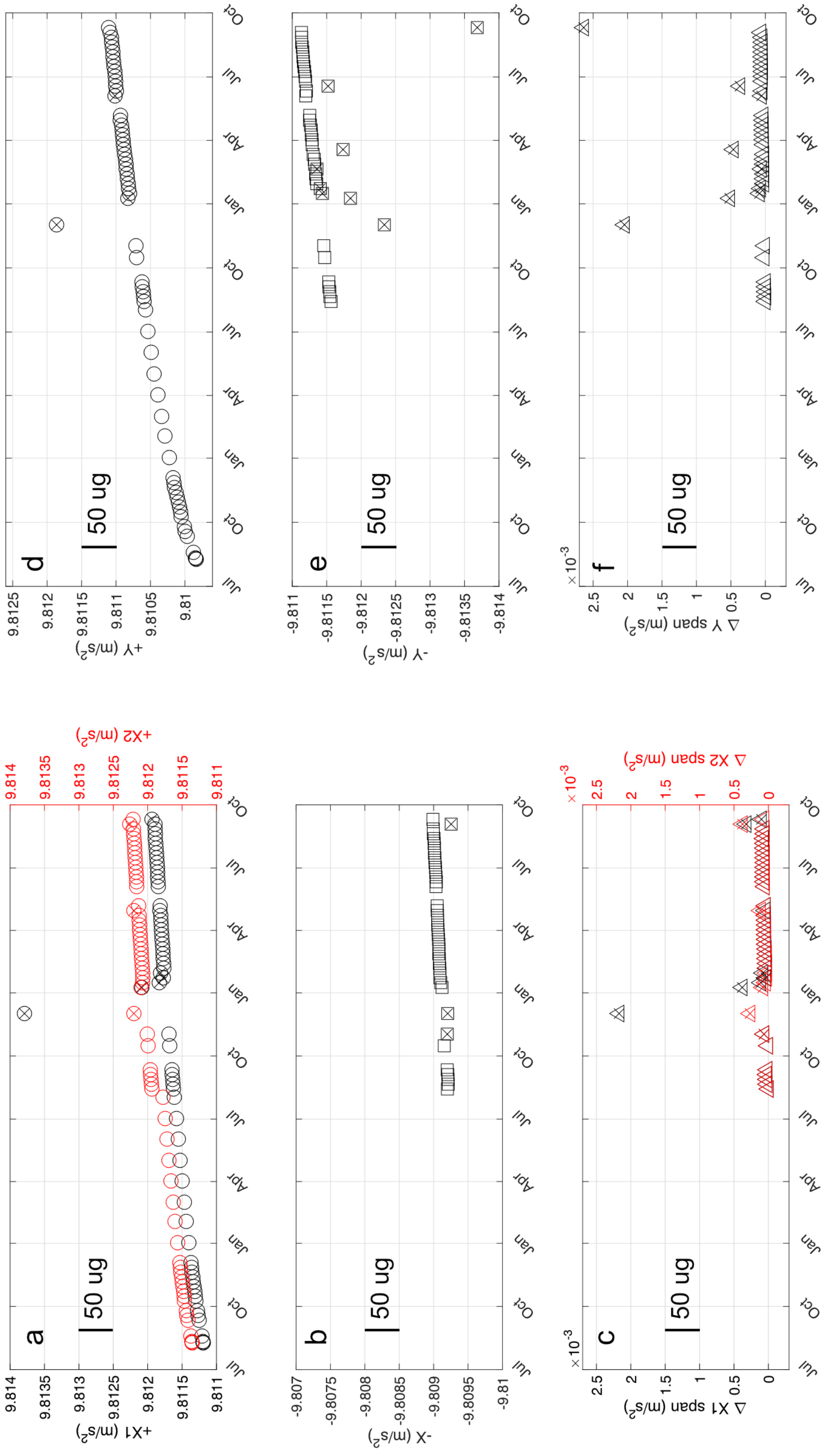

Figure A3.4. Calibration values for Axial Location 1 with anomalous calibrations plotted. (a-c) As for Figure A3.2a-c but also plotting the anomalous calibration values. (d-f) As for Figure A3.2e-h but also plotting the anomalous calibration values.

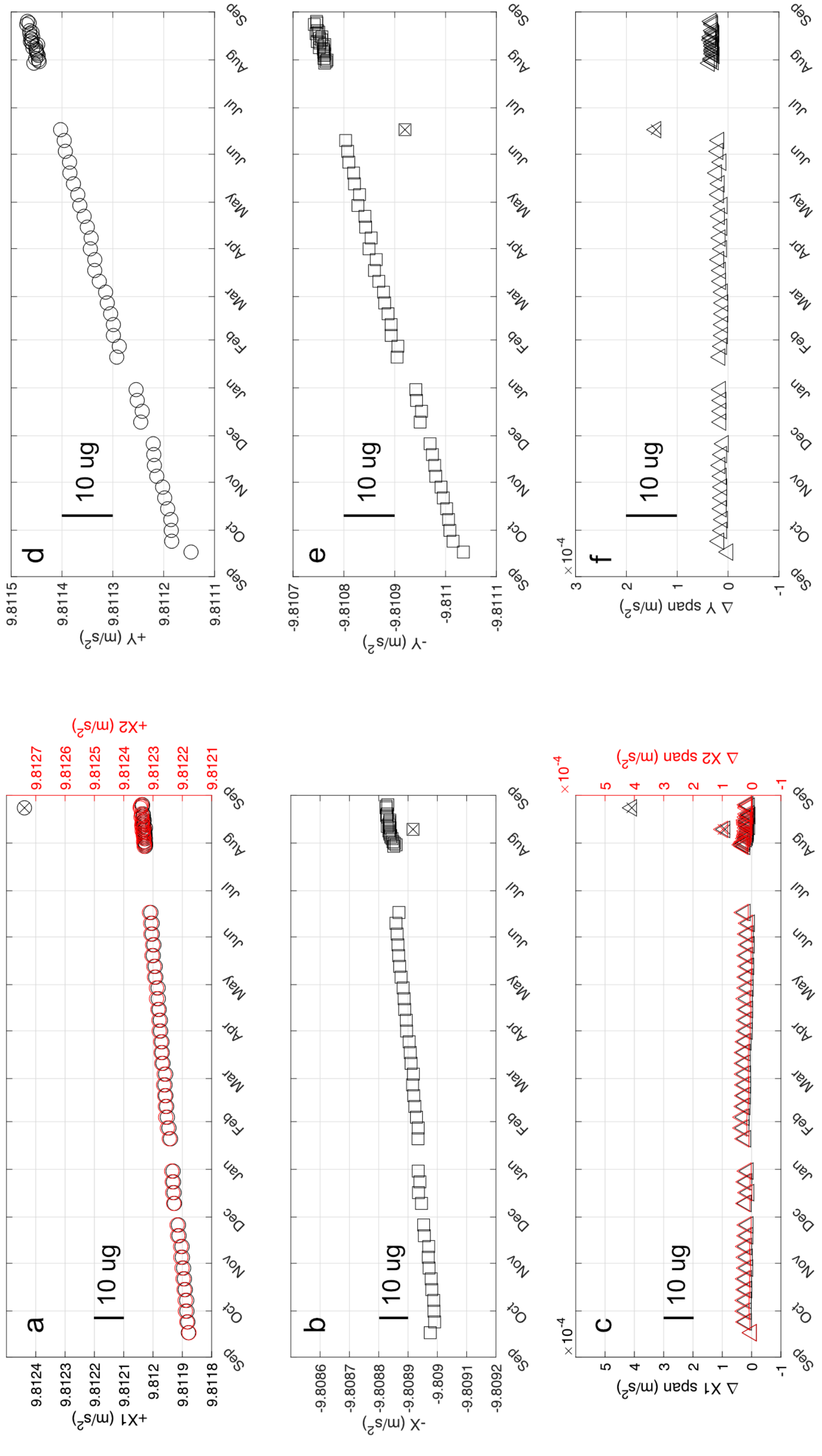

Figure A3.5. Calibration values for Axial Location 2 with anomalous calibrations plotted. (a-c) As for Figure 6a-c but also plotting the anomalous calibration values. (d-f) As for Figure 6e-h but also plotting the anomalous calibration values.

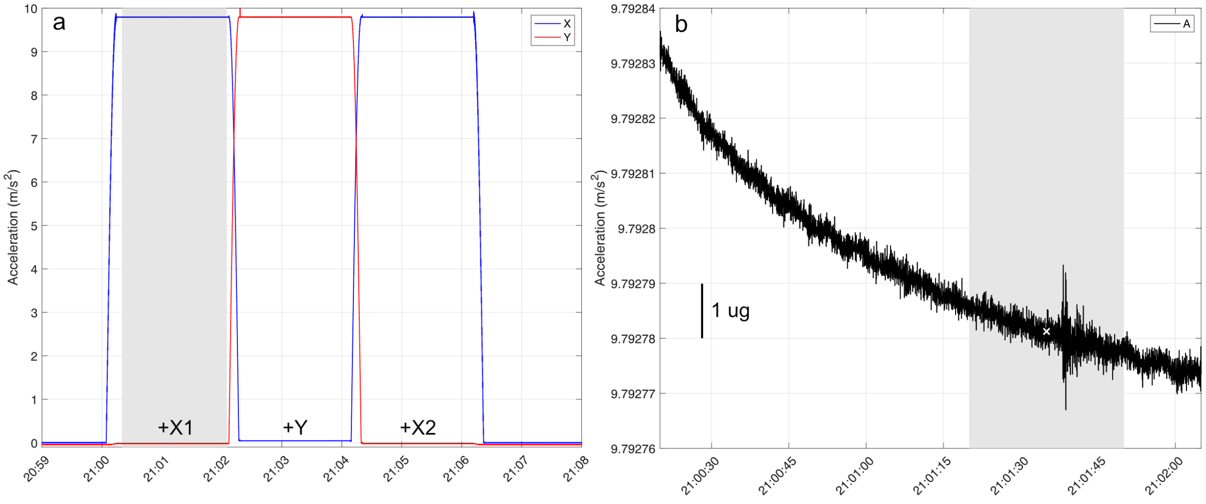

Figure A3.6. (a) X (blue) and Y channel (red) acceleration observations during a 3-orientation calibration sequence at PFO, with calibration orientations labeled. Gray shading indicates the time interval plotted in (b). (b) Total acceleration during the interval indicated in (a), after the sensor has stabilized in the +X1 orientation and prior to beginning the next rotation. Gray shaded area indicates the interval over which the acceleration is averaged to get a calibration value. White X indicates the calculated calibration value and nominal time.

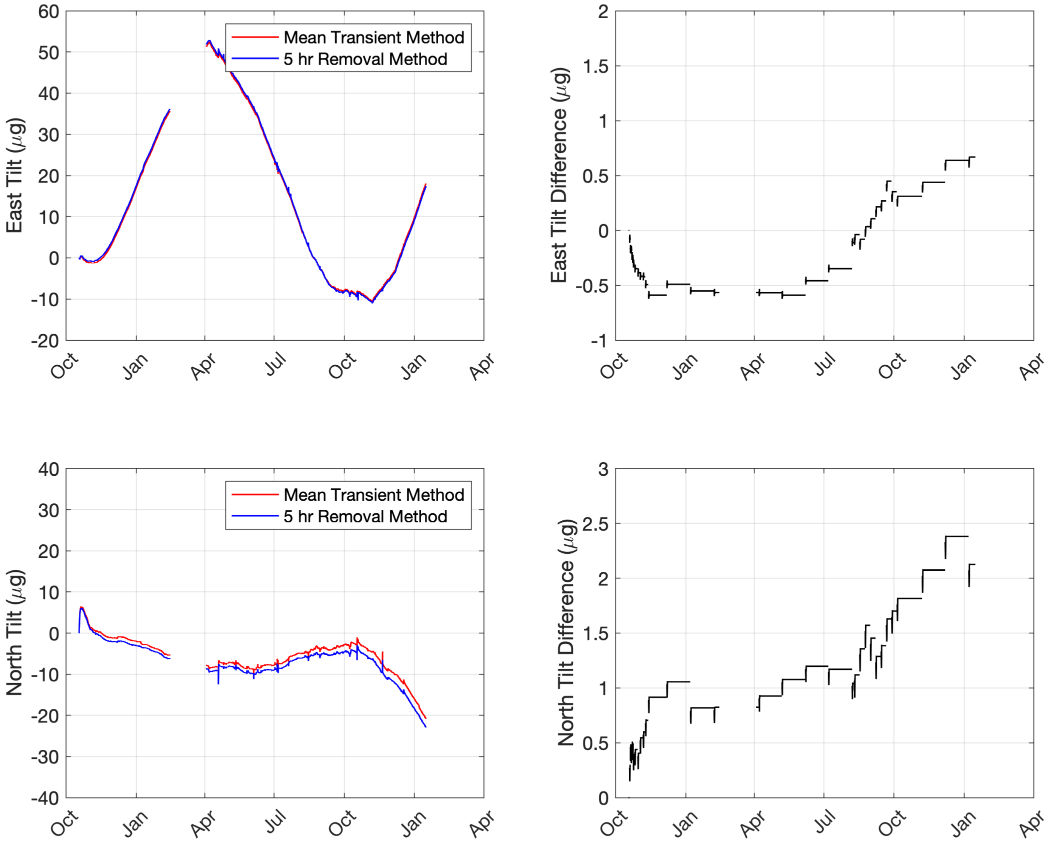

Figure A3.7. (a-b) Time series of one-minute averaged drift-corrected stitched tilt for Piñon Flat Observatory for 2018 to 2020 for (a) the east direction (-Y) and (b) the north direction (+X) obtained using $\delta t = 0$ (red) and $\delta t = 5$ hours (blue) in equation (9). (c-d) The resulting difference in the tilt time series ($\delta t = 0$ minus $\delta t = 5$ hours) showing an accumulated offset for the two interpolation methods.

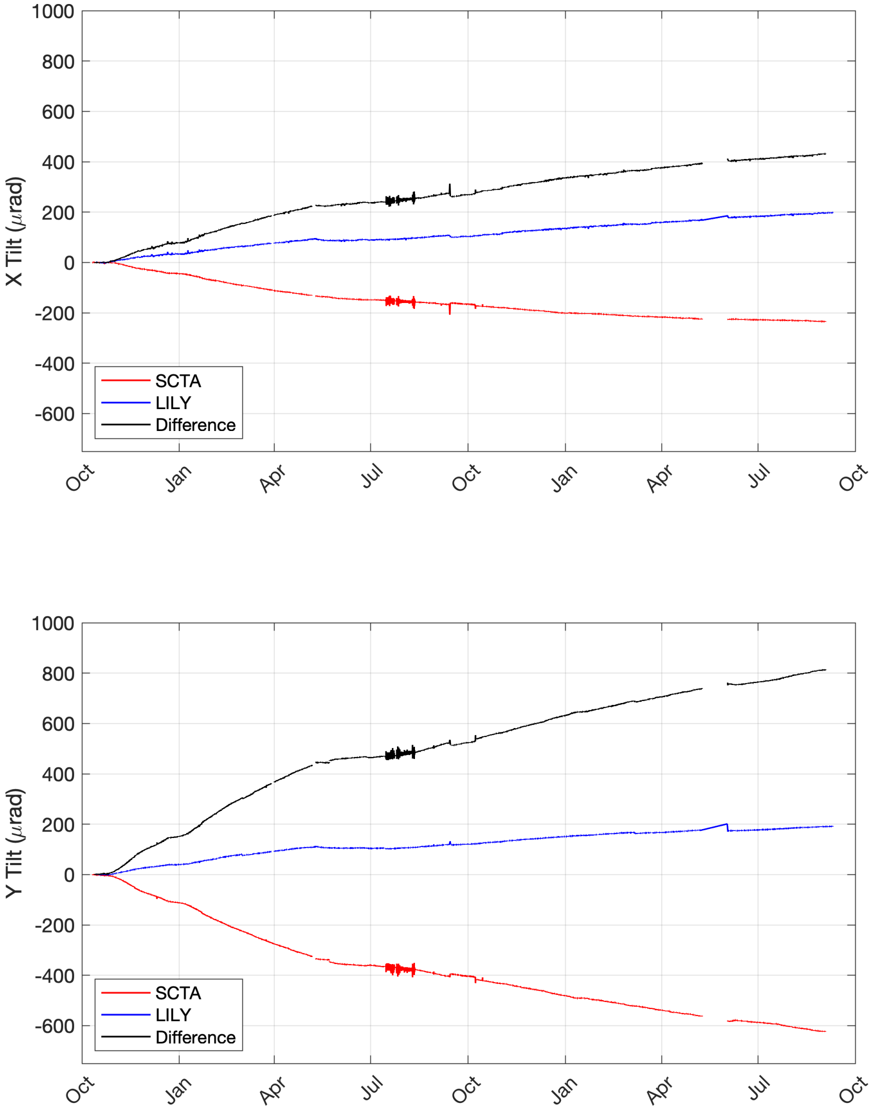

Figure A3.8. Time series of 1-minute averaged tilt for Axial Seamount Location 1 from 2018 to 2020 for the SCTA (a) X (approximately north) and (b) Y directions (approximately west). Each plot shows the drift corrected stitched SCTA data with $\delta t = 2$ hours in equation (9) with the assumption of no transient acceleration after 5 hours (red), the LILY tiltmeter data (blue) and the difference (LILY – SCTA) (black). The sign convention is positive for a downward tilt.